Noise Modelling for GRACE Follow-On Observables in the Celestial Mechanics Approach

Inauguraldissertation
der Philosophisch-naturwissenschaftlichen Fakultät
der Universität Bern

vorgelegt von

Martin Lasser

aus Österreich

Leiter der Arbeit:

Prof. Dr. Adrian Jäggi
Astronomisches Institut der Universität Bern

Noise Modelling for GRACE Follow-On Observables in the Celestial Mechanics Approach

Inauguraldissertation
der Philosophisch-naturwissenschaftlichen Fakultät
der Universität Bern

vorgelegt von

Martin Lasser

aus Österreich

Leiter der Arbeit:

Prof. Dr. Adrian Jäggi
Astronomisches Institut der Universität Bern

Von der Philosophisch-naturwissenschaftlichen Fakultät angenommen.

Bern, 3. Juni 2022

Der Dekan

Prof. Dr. Zoltan Balogh

Year: 2022
Title: Noise Modelling for GRACE Follow-On Observables in the Celestial Mechanics Approach
Author: Martin Lasser

To all who contributed to this work

A sincere
THANK YOU!

Contents

List of Figures

List of Tables

Acronyms

AC Analysis Centre. 6–8, 10, 106–108
ACC Accelerometer. 3–5, 10, 42, 53–61, 64, 65, 77, 83, 85, 96–100, 110
ACT Accelerometer Transplant. 56–59
AIUB Astronomical Institute of the University of Bern. 2, 6, 8, 44, 46, 53, 55, 84, 96, 100, 106–111
AOD Atmospheric and Oceanic De-aliasing. 50, 51, 55
ASD Amplitude Spectral Density. 27, 43, 62–65, 87, 88, 90, 95, 97–99, 104, 106
ATT Attitude. 5, 56, 60, 64

BIQUE Best Invariant Quadratic Unbiased Estimate. 24
BLAS Basic Linear Algebra Subprograms. 9, 66–69, 110
BSW Bernese GNSS Software. 8, 9, 32, 44, 53, 59, 66, 68, 72

CHAMP Challenging Minisatellite Payload. 1, 5, 46, 60
CMA Celestial Mechanics Approach. 2, 8, 19, 33, 35, 41, 53–56, 64, 69, 70, 72, 76, 85–87, 89, 93, 96, 109, 110
CODE Center for Orbit Determination Europe. 53
CoM Centre of Mass. 3, 5, 31, 34, 35, 37, 38, 40
COST-G International Combination Service for Time-variable Gravity Fields. 6–8, 10, 107, 108, 110
CPU Central Processing Unit. 68
CRF Celestial Reference Frame, *Glossary:* CRF. 7, 8, 32, 50, 94
CSR Center for Space Research at the University of Texas at Austin. 3, 6, 24, 44, 62, 84, 89, 100, 104, 106–108

DFT Discrete Fourier Transform. 27
DIFF Difference of orbit parameters, *Glossary:* DIFF. 41, 42, 60, 64, 65, 75, 79–83
DORIS Doppler Orbitography and Radiopositioning Integrated by Satellite. 8
DOWR Dual One-Way Ranging. 5, 97

EGSIEM European Gravity Service for Improved Emergency Management. 6
EPOS Earth Parameter and Orbit System. 8

FES Finite Element Solution. 49, 55
FFT Fast Fourier Transform. 27
FSM Fitted Signal Model. 6

GF1 GRACE Follow-On 1. 3, 5, 39, 40, 56, 60
GF2 GRACE Follow-On 2. 3, 5, 39, 40, 56–60

GFZ German Research Centre for Geosciences. 3, 6, 8
GINS Géodésie par Intégrations Numériques Simultanées. 8
GLONASS Globalnaja Nawigazionnaja Sputnikowaja Sistema. 4
GMST Greenwich Mean Sidereal Time. 48
GNSS Global Navigation Satellite System. 4, 5, 8, 9, 21, 35–37
GOCE Gravity field and steady state Ocean Circulation Explorer. 1, 46
GPS Global Positioning System. 3, 4, 8, 34, 38, 40, 53, 62, 85, 86, 88, 89, 91, 94, 96
GRACE Gravity Recovery And Climate Experiment. 1–8, 10, 24, 25, 38, 44–46, 50, 53–55, 85, 87, 89, 93, 94, 96–98, 103
GRACE Follow-On Gravity Recovery And Climate Experiment Follow-On. 1–9, 24, 35, 38, 43, 44, 46, 50, 53–56, 58, 59, 64, 69, 70, 74, 76, 81, 83–85, 96, 100, 102, 106–110
GRACE-SIGMA GRACE-Satellite Orbit Integration and Gravity Field Analysis in MATLAB. 8
GRASP Gravity Satellite Processing Engine. 8, 9
GRGS Groupe de Recherche de Géodésie Spatiale. 6, 8
GROOPS Gravity Recovery Object Oriented Programming System. 7–9

hl-SST High-Low Satellite-to-Satellite Tracking. 3, 4, 35, 36

IAG International Association of Geodesy. 6
ICGEM International Centre for Global Earth Models. 53
IERS International Earth Rotation and Reference Systems Service. 44–51, 55
IGFS International Gravity Field Service. 6
IGS International GNSS Service. 6
ILRS International Laser Ranging Service. 6
IMU Inertial Measurement Unit. 5

JPL Jet Propulsion Laboratory. 3, 4, 6, 46, 53, 56–59

KBR K-band Ranging. 3–5, 40, 41, 53, 55, 64, 70, 75, 76, 85, 88, 90, 91, 94, 95, 97, 110
KBRR K-band Range-Rate. 43, 53, 60–62, 65, 69, 74–76, 78, 80–84, 96–107, 109, 110
KIN Kinematic Positions. 35, 62, 69

LAPACK Linear Algebra Package. 9, 66, 68, 69, 83, 110
LEO Low Earth Orbiter. 6, 8, 25, 85
ll-SST Low-Low Satellite-to-Satellite Tracking. 3, 4
LoS Line of Sight. 40
LRI Laser Ranging Interferometry. 3–5, 40, 55
LSQ Least-Squares. 11, 13, 14, 17, 18, 41, 42, 91, 95
LSQA Least-Squares Adjustment. 2, 12, 13, 15–17, 20–23, 26, 27, 33, 34, 37, 40, 41, 43, 68, 69, 77, 86, 93, 95, 96, 100, 103, 109
LUH Leibniz University Hannover. 6, 8, 9

MAD Median Absolute Deviation. 102
MINQUE Minimum Norm Quadratic Unbiased Estimate. 25
MJD Modified Julian Date, *Glossary:* MJD. 48
MKL Math Kernel Library. 66
MPI Message Passing Interface. 9

NASA National Aeronautics and Space Administration. 1, 3
NEQ Normal Equation. 6, 8, 13, 19, 20, 25, 26, 41–43, 60–63, 66–70, 72–75, 77–83, 97

ONERA Office National d'Études et de Recherches Aérospatiales. 5
op operational. 53

PC Partner Analysis Centre. 6
PCA Piecewise-Constant Acceleration. 35, 54, 62, 64–66, 74, 78–84, 86, 87, 89, 93, 94, 96, 100, 103, 106, 109
POD Precise Orbit Determination. 4–6, 8, 9
PPP Precise Point Positioning. 36, 39, 85, 109
PSD Power Spectral Density. 27–29, 98, 109

RAM Random-Access Memory. 69
RL Release. 50, 51, 55
RMS Root Mean Square, *Glossary:* RMS. 58, 59, 81, 84, 88, 91, 95, 100, 105–108, 110
RSS Residual Sum of Squares. 15, 25
RSW Local Orbit Frame, *Glossary:* RSW. 54–56, 87, 90, 94

SCA Star Camera Assembly. 4, 5, 53, 56, 93
SDS Science Data System. 3, 4, 61
SLR Satellite Laser Ranging. 4, 8, 110
SRF Science Reference Frame, *Glossary:* SRF. 56
SUM Sum of orbit parameters,*Glossary:* SUM. 41, 42, 60, 61, 64, 65, 75, 79–81, 83

TRF Terrestrial Reference Frame, *Glossary:* TRF. 7, 8, 35, 47
TUG Graz University of Technology. 6–9, 49, 56–59, 85, 93, 107, 108

VCE Variance Component Estimation. 2, 20, 24–26, 53, 62, 67–76, 78–84, 93, 101, 102, 106, 107, 109, 110
VLBI Very Long Baseline Interferometry. 8

Glossary

CRF The Celestial Reference Frame (CRF) is a (quasi-)inertial Cartesian coordinate system with its origin in the centre of mass of the Earth, where the x-axis is pointing to the direction of the vernal equinox (the intersection between the equatorial and ecliptic plane), the z-axis is following the Earth's rotational axis to the North and the y-axis being orthogonal to the x- and z-axis forming a right-handed system. 7

DIFF Difference of orbit parameters after a parameter transformation. 41

MJD The Modified Julian Date (MJD) gives the time in days since the epoch 17^{th} of November 1858, 00:00 Universal Time (UT). 48

RMS The Root Mean Square (RMS) denotes the quadratic mean formed as the square root of the mean square for a set of $\{x_1, ..., x_N\}$ by $m_{\text{RMS}} = \sqrt{\frac{1}{N}\sum_{n=1}^{N} x_n^2}$. 58

RSW R, S and W are defining the axes of a right-handed Cartesian coordinate system called local orbit frame, where the axes are pointing in radial (R), along-track (S) and cross-track (W) direction with its origin in the satellite's centre of mass. 54

SRF Science Reference Frame (SRF) originating in the centre of mass of the satellite with its axes pointing along the accelerometer measurement axes, where x points to the K-band horn, z is roughly nadir pointing and the y-axis completing a right-handed cartesian coordinate system.. 56

SUM Sum of orbit parameters after a parameter transformation. 41

TRF The Terrestrial Reference Frame (TRF) is a Cartesian coordinate system with its origin in the long-term centre of mass of the Earth, where the x-axis is located in the equatorial plane pointing towards the prime meridian, the z-axis being defined as the axis pointing from the South Pole to the North Pole and the y-axis being orthogonal to the x- and z-axis completing a right-handed system. 7

Chapter 1

Introduction

A key to understanding the dynamic system Earth in its current state is the continuous observation of its time-variable gravity field. Mass re-distributions on the Earth's surface or interior induced by the continental water cycle or the melting of the ice sheets cause a change in the potential, which is ultimately reflected in a change of orbital trajectories of Earth orbiting satellites. Precisely measuring the fingerprints of these variations in satellite trajectories to recover the underlying gravity field is the task of satellite gravimetry.

With the age of the first satellites the concept of satellite gravimetry became feasible, significantly improving the knowledge about the Earth's gravity field [Flechtner et al., 2021]. Already with the first geodetic satellite launched in 1962 by the US Army, Navy, National Aeronautics and Space Administration (NASA) and Air Force, ANNA-1B, the low degree spherical harmonics of the gravity field could be resolved. Since the beginning of the new millennium several satellite mission dedicated to the observation and continuous monitoring of the Earth's gravity field have been launched. Starting with the Challenging Minisatellite Payload [CHAMP, Reigber et al., 1998] in the year 2000, the Gravity Recovery And Climate Experiment (GRACE) satellite mission [Tapley et al., 2004] in 2002, the Gravity field and steady state Ocean Circulation Explorer [GOCE, Drinkwater et al., 2006] and the Gravity Recovery And Climate Experiment Follow-On (GRACE Follow-On) satellite mission [Landerer et al., 2020], there has been an almost uninterrupted monitoring of the Earth's gravity field for more than two decades. Additionally, non-dedicated missions equipped with adequate instruments such as Swarm [Friis-Christensen et al., 2006] are suited for the determination of the large-scale gravity field variations as well. Among these missions, GRACE and GRACE Follow-On play an exceptional role because of their unique measuring concept being particularly sensitive to the time-variable component of the gravity field. The measurement principle of obtaining distance changes between a pair of satellites separated by a few hundred kilometres chasing each other along the same orbital trajectory was proposed already by Wolff [1969], however, it took three more decades to be realised by GRACE and continued by GRACE Follow-On.

The observations collected by GRACE and GRACE Follow-On are commonly accumulated to monthly snapshots of the Earth's gravity field, providing a resolution of about 300 km on the Earth's surface in the sense of a global average. An accurate and comprehensive description of the different observation characteristics is crucial for the quality, robustness and reliability of thereof derived gravity field solutions. In addition, the recovery of

time-variable gravity field signal implies a sufficient knowledge about the non-gravitational forces perturbing the satellites orbits and about mass flux which cannot be captured by the monthly snapshots. Both effects have to be treated either by auxiliary observations, such as the onboard accelerometer measurements, or by a priori known background models.

In this work an attempt is made to introduce different kinds of stochastic models for the observation noise and to study their impact on monthly gravity field solutions. The noise models include a priori observation noise models from pre-launch simulations, models co-estimated with the gravity field solution and noise models iteratively derived in the estimation process from the emerging residuals.

The thesis is comprised of the following chapters:

Chapter 2 *GRACE Follow-On,* which introduces the satellite mission, the goals and objectives, core principles and measuring concepts.

Chapter 3 *Mathematical Fundamentals,* gives an overview about the basic mathematical concepts used for the research in this thesis, the Least-Squares Adjustment, the method of Variance Component Estimation and fundamental time series analysis, including essential implications for the orbit and gravity field recovery process.

Chapter 4 *Orbit and Gravity Field Determination,* recapitulates the orbit and gravity field determination process of the Celestial Mechanics Approach in the context of the GRACE and GRACE Follow-On observables.

Chapter 5 *GRACE Follow-On Data Processing,* details the steps taken for GRACE Follow-On gravity field recovery. This chapter shows the operational AIUB GRACE Follow-On gravity field solutions, the absorption of noise with pseudo-stochastic parameters, the use of Variance Component Estimation for outlier detection and weighting, as well as the determination of constraints for the pseudo-stochastic parameters. Furthermore, the derivation, use and performance of empirical models based on post-fit residuals is discussed in this chapter for kinematic positions and K-band range-rate observations.

Chapter 6 *Summary,* concluding the thesis by summarising the main results and findings.

Chapter 2

GRACE Follow-On

GRACE Follow-On is a satellite mission dedicated to sensing the time-variable gravity field of the Earth. It was launched on 22nd of May, 2018, from Vandenberg Air Force Base aboard a SpaceX Falcon 9 rocket, half a year after its predecessor GRACE was decommissioned after more than 15 years in orbit. GRACE Follow-On is a joint US–German effort where NASA's Jet Propulsion Laboratory (JPL), the Center for Space Research at the University of Texas at Austin (CSR) and the German Research Centre for Geosciences (GFZ) form the Science Data System (SDS), which is responsible for operating the satellites and providing science data [Landerer et al., 2020].

GRACE Follow-On consists of a pair of satellites, GRACE Follow-On 1 (GF1) and GRACE Follow-On 2 (GF2), flying in a polar orbit configuration in an altitude of about 480 km, with an orbital period of about 94 min. The separation between the two spacecraft is actively controlled by small orbital manoeuvres and kept between 170–270 km [Landerer et al., 2020]. The primary science objective is to continue the monitoring of the Earth's time variable gravity field inherited from the GRACE satellite mission. This is achieved by precise measurements of the satellites' orbits, thus, the spacecrafts themselves may be be considered as the main scientific instrument. The fundamental measuring concept of GRACE and GRACE Follow-On is shown in Fig. 2.1. The satellite pair continuously observes the high-flying satellites of the Global Positioning System (GPS) to obtain the absolute satellite positions in the High-Low Satellite-to-Satellite Tracking (hl-SST) mode. This enables the recovery of the long wavelength components of the Earth's gravity field. When the spacecraft pass a sufficiently large mass anomaly, the relative distance and velocity between the two satellites changes because the leading satellite first experiences a stronger attraction. This variation in the distance between the two satellites is the main observable of the Low-Low Satellite-to-Satellite Tracking (ll-SST) of GRACE Follow-On and is realised by two measuring systems, the K-band Ranging (KBR) and Laser Ranging Interferometry (LRI) instruments. It allows a precise deduction of the long to medium wavelengths of the gravity field. Non-gravitational forces perturbing the satellite orbit are measured by the onboard Accelerometer (ACC) with its proof mass located in the Centre of Mass (CoM) of the satellite.

Such a measuring system is capable of sensing the effects of the perturbing accelerations caused by the Earth's gravity field, and by providing monthly snapshots the dynamic system of mass re-distribution on the Earth's surface and interior is observed. The mea-

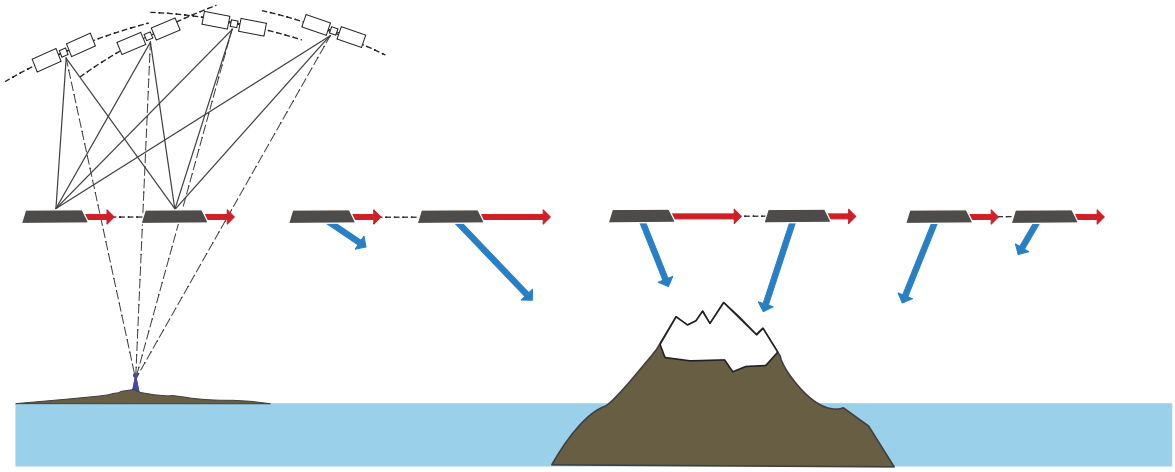

Figure 2.1: Basic measurement principle of GRACE and GRACE Follow-On with hl-SST to the high flying GPS constellation and ll-SST tracking between the mission's satellite pair.

surements, however, cannot distinguish between different sources of mass flux and interpretations of the results rest upon additional, independent observations and models.

The data flow of GRACE Follow-On is realised by the GRACE Follow-On SDS, which converts the raw data transmitted by the satellites (Level-0) to Level-1 data. These then consists of time tagged and down-sampled measurements in engineering units [Wen et al., 2019]. The latter are introduced as observations to the orbit and gravity field recovery processes to obtain Level-2 gravity field solutions.

2.1 GRACE Follow-On instrumentation

This section gives a brief outline of the most important science instruments of GRACE Follow-On to measure the Earth's gravity field. The main instrument for sensing the Earth's gravity field is the spacecraft itself, however, several other instruments are needed to collect the necessary science data. These are the Global Navigation Satellite System (GNSS) receiver for absolute positioning through Precise Orbit Determination (POD), the instruments for measuring the inter-satellite distance changes: The KBR and the LRI systems. Furthermore, the ACC to measure non-gravitational perturbing forces acting on the satellite, the Star Camera Assembly (SCA) to provide attitude information and a Laser retroreflector for Satellite Laser Ranging (SLR). The instrument system design and specifications may be found in Kornfeld et al. [2019].

GNSS Receiver GRACE Follow-On carries a TriG-RO (GPS, Galileo, GLONASS and Radio Occultation) receiver built by Moog Broad Reach to provide capabilities for a POD. The receiver is an offshoot of the BlackJack GPS receiver developed by the JPL, which was mounted on GRACE [Dunn et al., 2003]. Even though the TriG receiver is capable of multi-GNSS tracking on all L-band based frequencies, only GPS is currently used for

POD of GRACE Follow-On. In addition, the GNSS receiver provides the time system for all other instruments.

Inter-satellite link The inter-satellite link is the key observable for temporal gravity field recovery with GRACE Follow-On. It is established in two ways: With K-band Ranging (KBR) and with Laser Ranging Interferometry (LRI). The first employs Dual One-Way Ranging (DOWR) on K- and Ka-band to measure the inter-satellite distance. Each satellite transmits a carrier signal while the other receives it and obtains the phase shift by correlating with a generated reference signal. A change in the phase shift is proportional to a change in distance between the satellites. The measured range between the satellites refers to the distance between the two KBR antenna horns. As a consequence for processing these measurements in orbit and gravity field recovery, the phase centre offset to the CoM of the satellites has to be taken into account. The precision of the KBR is about 1 µm.
The LRI on the other hand uses Nd:YAG non-planar ring oscillators operating at a wavelength of 1064.5 nm to create a laser beam which makes a round trip between the two satellites and then interferes with a wave generated by the local oscillator to derive the range between the satellites. The LRI observations directly refer to the CoM of the satellites due to the positioning of the mirrors of the triple mirror assembly, which directs the laser beam through the spacecraft. The LRI is a technology demonstrator instrument, providing the first optical interferometry between two spacecraft, and does not serve as the main instrument for the mission's objectives. However, its performance is outstanding, reaching a precision of 10 nm at 40 mHz [Abich et al., 2019].

Accelerometer The electrostatic space accelerometer [Christophe et al., 2015] mounted on GRACE Follow-On is supposed to measure the accelerations caused by non-gravitational forces which are acting on the satellite when orbiting the Earth. It is an improved accelerometer developed by the Office National d'Études et de Recherches Aérospatiales (ONERA) compared to the SuperSTAR accelerometer integrated to GRACE. The measurement principle is based on precise position and attitude control of a proof mass in the centre of an electrode cage, which in located in the CoM of the satellite. The latter is realised and maintained by small but frequent in-orbit manoeuvres. Linear and angular accelerations along three axes are derived from the voltage needed to keep the proof mass centred. The precision is about $1 \times 10^{-10}\,\mathrm{m\,s^{-2}}$. However, the accelerometer mounted on GF2 is not able to reach this level due to bias jumps and highly correlated noise emerging on all ACC axes. The data has to be blended with measurements from GF1 to provide calibrated observations which are suited for the orbit and gravity field recovery [Landerer et al., 2020, Bandikova et al., 2019].

Star Camera Assembly The SCA precisely measures the satellite attitude. It consists of three star camera heads viewing the sky from each side of the spacecraft. The SCA technique of GRACE Follow-On stems from CHAMP and GRACE and is used for scientific purposes and position control. The Attitude (ATT) data derived from the SCA observations is combined with angular rate measurements from an Inertial Measurement Unit (IMU) by Kalman filtering [Harvey and Sakumura, 2019].

2.2 COST-G

The International Combination Service for Time-variable Gravity Fields (COST-G) [Jäggi et al., 2020] operationally provides consolidated state-of-the-art monthly global gravity models from GRACE, GRACE Follow-On and Swarm [Meyer et al., 2020a,b, Teixeira Encarnação et al., 2019]. In addition, a Fitted Signal Model (FSM) [Peter et al., 2022] is published to enable a few months of prediction of the gravity signal for operational Low Earth Orbiter (LEO) POD. COST-G is a product centre under the umbrella of the International Gravity Field Service (IGFS) of the International Association of Geodesy (IAG).

Following the example of several services, e.g, the International GNSS Service [IGS, Johnston et al., 2017] and the International Laser Ranging Service [ILRS, Pearlman et al., 2002], of combining solutions from various institutions, which are computed by different and independent software packages, the combination service COST-G continues the works from the EGSIEM [European Gravity Service for Improved Emergency Management, Jäggi et al., 2019] project in combining existing gravity field solutions to obtain a product of improved quality, robustness and reliability. The individual solutions are computed by the COST-G Analysis Centres (ACs) and additional Partner Analysis Centres (PCs). The combination process takes place either on solution level or, as envisaged for the future, on Normal Equation (NEQ) level. The COST-G Analysis Centres (ACs) make use of different gravity field recovery strategies but apply agreed-upon consistent processing standards [Jäggi et al., 2020].

The COST-G consortium consists at the time of writing (Spring 2022) of five ACs, which are the Astronomical Institute of the University of Bern (AIUB), the GFZ, the Groupe de Recherche de Géodésie Spatiale (GRGS), the Institute of Geodesy of the Leibniz University Hannover (LUH) and the Institute of Geodesy of Graz University of Technology (TUG). Furthermore, there are two PCs (CSR, JPL).

2.2.1 Software comparisons

Nowadays various institutions which perform orbit and gravity field determination have set up their own processing schemes based on their in-house developed software packages. In order to minimise systematic differences between different software caused by a diverse handling of e.g., background force models, the effort of comparing software implementations is conducted regularly. Such an attempt was made for the software packages available within the COST-G consortium to detect inconsistencies and learn about the level of agreement.

The following results of the software comparisons between the software from the COST-G ACs are published in Lasser et al. [2020c].

Benchmark data set

The benchmark data set, compiled by TUG, is intended to be used as a reference data set and provides the opportunity to test the implementation of various background force models in software packages. It consists of several accelerations a spacecraft experiences,

which are commonly used in orbit and gravity field determination. The models that describe the accelerations are evaluated along a one day GRACE orbit arc (integrated for 3rd of July, 2008, using Encke's method, see Ellmer and Mayer-Gürr [2017] for more information on the integration) using the Gravity Recovery Object Oriented Programming System (GROOPS) software [Mayer-Gürr et al., 2021]. The orbit is provided with 30 s sampling and is given in cartesian coordinates expressed in both the Terrestrial Reference Frame (TRF) ITRF2014 [Altamimi et al., 2016], and the Celestial Reference Frame (CRF) ICRF2 [Fey et al., 2009]. The evaluations yield three dimensional accelerations for each sampling point at the location of the spacecraft. These accelerations are the main product of the benchmark data set. The underlying models correspond with the models applied in the GRACE Follow-On processing described in Chapter 5 and are listed in Table 5.2. In addition, the benchmark data set contains the evaluation of the EOT11a ocean tide model [Savcenko and Bosch, 2011].

All resulting accelerations are expressed in the CRF, the accelerations caused by the gravity field are also given in the TRF. In an attempt to also make the handling of the TRF and the CRF comprehensible, the orbit is also given in both frames. Furthermore, some auxiliary physical quantities are appended to the data set to enable a better understanding of the different models. The complete data set may be found at the ftp server of TUG[1] including a description of the data and how the models are employed (see file `00README_simulation.txt`).
Moreover, the data set is formulated as benchmark for new ACs, which are interested to contribute to the COST-G products.

Application of the benchmark data set

The main goal of the data set is to create a reference for basic software comparisons. It allows to compare the background force model implementations, and may serve as a reference for the use of celestial and terrestrial reference frames in scientific software packages. The most straight forward approach of comparison is to evaluate the force models at the given orbital positions with a space geodesy software package and to print the resulting accelerations. By subtracting the obtained accelerations from the benchmark data (Eq. 2.1), differences $\boldsymbol{d}$ may be revealed as

$$\begin{bmatrix} d_x \\ d_y \\ d_z \end{bmatrix} = \begin{bmatrix} r_x \\ r_y \\ r_z \end{bmatrix} - \begin{bmatrix} s_x \\ s_y \\ s_z \end{bmatrix}. \tag{2.1}$$

where $\boldsymbol{r}$ denote the reference accelerations and $\boldsymbol{s}$ the accelerations resulting from the software evaluation. Large differences to the reference accelerations may indicate potential implementation problems. It is very unlikely to obtain zero differences. Oscillating patterns around zero, however, are to be expected, most commonly manifesting as once- or twice-per-revolution signals.

[1] `ftp://ftp.tugraz.at/outgoing/ITSG/COST-G/softwareComparison/`

Comparisons within COST-G

The benchmark data set was created, used and examined within the COST-G initiative to augment the combination effort, and in particular, to rule out large systematic differences in the implementations of background force models. Each AC tried to reproduce the reference accelerations as closely as possible when using their own software package and by introducing the also provided rotation between TRF and CRF. The GROOPS software suite from TUG serves as a reference as it was used to compute the benchmark data set. The software packages follow different approaches of modelling gravity fields from satellite data, however, a high level of agreement is expected with the benchmark data for background model handling. The six software packages examined are:

- The Bernese GNSS Software [BSW, Dach et al., 2009], a scientific software package featuring space geodetic applications, mainly high-precision multi-GNSS data processing for ground networks [e.g., Prange et al., 2017], SLR data processing [e.g., Arnold et al., 2019], as well as precise LEO satellite orbit determination and thereof derived gravity field solutions [e.g., Meyer et al., 2016]. The software is developed, maintained and distributed by the AIUB. In its core it employs the Celestial Mechanics Approach (CMA) of orbit determination Beutler [2005], be it for high or low flying Earth orbiting satellites or planetary geodetic applications [Arnold et al., 2015, Bertone et al., 2021]. The software is written in Fortran and used by more than 700 institutions around the world.
- EPOS [Earth Parameter and Orbit System[2], Zhu et al., 2004], a software package designed and applied for operational POD, developed, maintained and used at GFZ. It is based on the dynamic approach of orbit modelling and consists of tools for orbit data analysis, orbit integration, orbit improvement, orbit predictions, NEQ handling and simulation of observations, as well as for gravity field computation. It served and serves numerous satellite missions and is able process SLR, GPS, Doppler Orbitography and Radiopositioning Integrated by Satellite (DORIS), radar altimeter data or inter-satellite ranging observations. Current applications are for example the computation of operational monthly GRACE Follow-On gravity field solutions [Dahle et al., 2019].
- GINS (Géodésie par Intégrations Numériques Simultanées), a software used for operational processing of all space geodetic observation techniques, capable of processing data from GNSS, SLR, Very Long Baseline Interferometry (VLBI), DORIS and inter-satellite ranging. It is developed and maintained by the GRGS.
- GRACE-SIGMA (GRACE-Satellite Orbit Integration and Gravity Field Analysis in MATLAB), a recent development, specifically designed for the processing of GRACE and GRACE Follow-On data, developed at the LUH. It is written in MATLAB and uses heavily vectorised modules for the modelling of perturbing forces, orbit propagation and orbit improvement. The software is applied for the computation of monthly GRACE and GRACE Follow-On gravity field solutions [Koch et al., 2020].
- GRASP (Gravity Satellite Processing Engine), a software dedicated to gravity field recovery from kinematic positions of satellites [Weigelt et al., 2013] using the accel-

[2] https://www.gfz-potsdam.de/en/section/global-geomonitoring-and-gravity-field/topics/earth-system-parameters-and-orbit-dynamics/earth-parameter-and-orbit-system-software-epos/

eration approach of orbit modelling. GRASP is developed at the LUH and written in MATLAB.

- GROOPS (Gravity Recovery Object Oriented Programming System), software suite for geodetic applications used at TUG. Its feature set includes the determination of GNSS orbits, clocks and ground station networks [Strasser et al., 2019], methods for POD [Süsser-Rechberger et al., 2022, Zehentner and Mayer-Gürr, 2016] static and time-variable gravity field solutions from satellite data [Kvas et al., 2021, 2019, Zehentner, 2017], and regional gravity field modelling with terrestrial data. GROOPS is written in C++ and makes heavy use of low level BLAS and LAPACK subroutines. It uses the Message Passing Interface (MPI) communication protocol for parallelisation and is capable to run on large distributed systems. GROOPS is available as an open source software [Mayer-Gürr et al., 2021]. It serves as a reference within these software comparisons as the benchmark data set was compiled using the capabilities of GROOPS. Recent applications are the computation of the ITSG-Grace2018 time series [Mayer-Gürr et al., 2018] and operational processing of GRACE Follow-On data.

Results using the Bernese GNSS Software

The functionalities of the BSW were used to evaluate the provided force models along the reference orbit. All formulae to compute the accelerations caused by each force may be found in Sect. 4.6. Based on the resulting accelerations Eq. 2.1 is applied and its norm is taken to obtain the results shown in Fig. 2.2. The magnitude of the differences is supposed

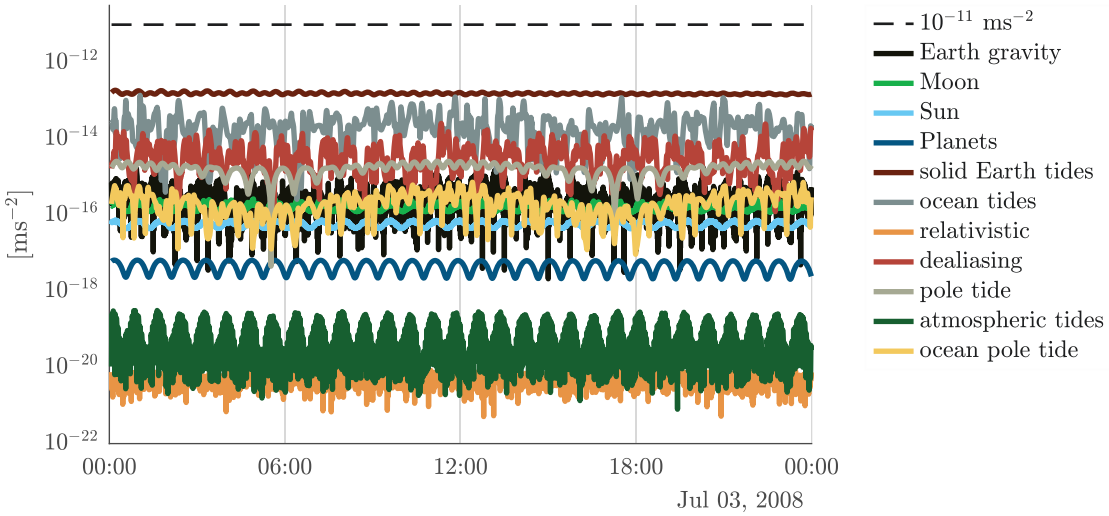

Figure 2.2: Results of the software comparison for the BSW expressed for each force model as the norm of the difference between the evaluation with the BSW and the benchmark data.

to be small since the handling of the background forces should yield compatible results. Altogether, the magnitude of differences is close to the numerical precision of 64-bit arithmetic of about 16 decimal places [IEEE-754, 1985] or even below.

Results from COST-G

Each of the institutions contributing to COST-G performed the software comparison with the benchmark data set. An absolute threshold of $1 \times 10^{-11}\,\mathrm{m\,s^{-2}}$ was set to indicate that a software package agrees with the benchmark data sufficiently well. Such a limit does not take into account that each forces influences the orbit and gravity field recovery in a different way and a relatively large difference does not necessarily map to a final solution. The threshold is chosen to be at least one order of magnitude lower than the ACC noise in the high-precision axes of GRACE [see e.g., Touboul et al., 1999]. For the representation, the maximum absolute deviation from the reference d_{max} is adopted to summarise the comparisons of several software packages

$$d_{max} = \max\left(|\boldsymbol{r} - \boldsymbol{s}|\right). \tag{2.2}$$

The performance is depicted in Fig. 2.3, the dashed black line marks the threshold. All

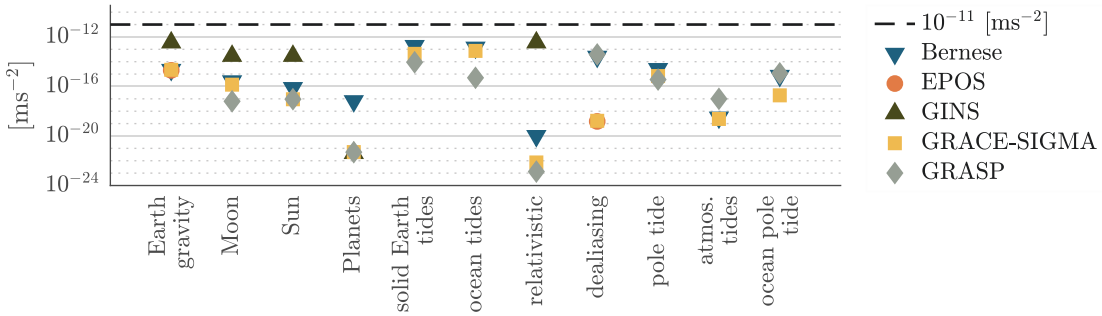

Figure 2.3: Maximum absolute deviation of the difference between the reference from the benchmark data set and the evaluation by the respective software of the COST-G ACs.

COST-G ACs fulfil the requirement of $1 \times 10^{-11}\,\mathrm{m\,s^{-2}}$ for force models in the benchmark data set. Consequently, systematic errors related to the implementation of the application of background forces are considered to be reduced to the extent possible when compared to the GRACE observation precision.

Chapter 3

Mathematical Fundamentals

This chapter introduces the mathematical methods on which the investigations in this thesis rely. Most fundamental is the treatment of an over-determined system of equations with the Least-Squares (LSQ) method (Sect. 3.2) and its implications. The following sections are deepening the application of the LSQ method for the specific problems posed in the context of gravity field determination and observation noise modelling. Comprehensive information about the essential resources may be taken from Koch [1997] or Niemeier [2008].

3.1 Covariance propagation

Covariance propagation is a method to estimate the uncertainties of a set of variables $\boldsymbol{l}$ depending on a set of stochastic variables $\boldsymbol{x}$ with known covariance information. Generally, the covariance matrix (or dispersion matrix) of a set of variables $\boldsymbol{x}$ may be written as the expectation of the outer product of its deviation from the mean

$$\begin{aligned} \mathbf{C}_{xx} &= \mathbb{D}(\boldsymbol{x}) \\ &= \mathbb{E}\left([\boldsymbol{x}-\mu] \wedge [\boldsymbol{x}-\mu]\right) \\ &= \mathbb{E}\left([\boldsymbol{x}-\mu]\,[\boldsymbol{x}-\mu]^{\mathrm{T}}\right) \quad , \end{aligned} \tag{3.1}$$

with $\mathbb{E}$ as the expectation operator, $\mathbb{D}$ being the dispersion operator and μ denoting the expected value of $\boldsymbol{x}$ by

$$\mu := \mathbb{E}(\boldsymbol{x}) \quad . \tag{3.2}$$

The covariance matrix is composed of variances on the main diagonal and covariances occupying the off-diagonal elements.
Introducing a functional relation given by $\boldsymbol{f}(\boldsymbol{x})$ between N dependent variables in $\boldsymbol{l}$ and M variables in $\boldsymbol{x}$ reads as

$$\begin{aligned} \boldsymbol{l} &= \boldsymbol{f}(\boldsymbol{x}) \\ &= \mathbf{A}\boldsymbol{x} \quad , \end{aligned} \tag{3.3}$$

where the relation is expressed in a coefficient matrix $\mathbf{A}$, also called design-matrix or data-matrix, which forms linear combinations between $\boldsymbol{x}$ and $\boldsymbol{l}$. Each entry of the design-matrix is reflecting these linear combination. Inserting Eq. 3.3 into Eq. 3.1 yields the covariance

matrix for $\boldsymbol{l}$

$$\begin{aligned}\mathbf{C}_{ll} &= \mathbb{E}\left(\left[\mathbf{A}\boldsymbol{x} - \mathbb{E}\left(\mathbf{A}\boldsymbol{x}\right)\right]\left[\mathbf{A}\boldsymbol{x} - \mathbb{E}\left(\mathbf{A}\boldsymbol{x}\right)\right]^{\mathrm{T}}\right) \\ &= \mathbb{E}\left(\left[\mathbf{A}\boldsymbol{x} - \mathbf{A}\mathbb{E}\left(\boldsymbol{x}\right)\right]\left[\mathbf{A}\boldsymbol{x} - \mathbf{A}\mathbb{E}\left(\boldsymbol{x}\right)\right]^{\mathrm{T}}\right) \\ &= \mathbb{E}\left(\mathbf{A}\left[\boldsymbol{x} - \mu\right]\left[\boldsymbol{x} - \mu\right]^{\mathrm{T}}\mathbf{A}^{\mathrm{T}}\right) \\ &= \mathbf{A}\mathbb{E}\left(\left[\boldsymbol{x} - \mu\right]\left[\boldsymbol{x} - \mu\right]^{\mathrm{T}}\right)\mathbf{A}^{\mathrm{T}} \\ &= \mathbf{A}\mathbf{C}_{xx}\mathbf{A}^{\mathrm{T}} \ ,\end{aligned} \tag{3.4}$$

hence, propagating the known covariance matrix $\mathbf{C}_{xx}$ of the vector $\boldsymbol{x}$ to the covariance matrix $\mathbf{C}_{ll}$ of the vector $\boldsymbol{l}$.

Non-linear relations between $\boldsymbol{l}$ and $\boldsymbol{x}$ may be taken into account in the covariance propagation as well. In order to make use of the same approach as for a linear model, the non-linear function is developed into a Taylor series

$$T(\boldsymbol{f}, \boldsymbol{x}_0) = \sum_{n=0}^{\infty} \frac{\partial \boldsymbol{f}^n(\boldsymbol{x}_0)}{\partial \boldsymbol{x}^n n!}(\boldsymbol{x} - \boldsymbol{x}_0)^n \ . \tag{3.5}$$

Neglecting all terms higher than $n = 1$ leads to a linear equation which consists of an offset given by the Taylor development point $\boldsymbol{x}_0$ and the linear term

$$T(\boldsymbol{f}, \boldsymbol{x}_0) = \boldsymbol{f}(\boldsymbol{x}_0) + \frac{\partial \boldsymbol{f}(\boldsymbol{x}_0)}{\partial \boldsymbol{x}}(\boldsymbol{x} - \boldsymbol{x}_0) \ . \tag{3.6}$$

This formulation may then be used to relate the dependent variables in the vector $\boldsymbol{l}$ with the vector $\boldsymbol{x}$ by

$$\begin{aligned}\boldsymbol{l} = \boldsymbol{f}(\boldsymbol{x}_0) \ &+ \ \frac{\partial \boldsymbol{f}(\boldsymbol{x}_0)}{\partial \boldsymbol{x}}(\boldsymbol{x} - \boldsymbol{x}_0) \\ = \ \boldsymbol{l}_0 \ &+ \ \mathbf{A} \ (\boldsymbol{x} - \boldsymbol{x}_0) \ ,\end{aligned} \tag{3.7}$$

with $\boldsymbol{l}_0$ denoting the functional relation evaluated at the Taylor point $\boldsymbol{x}_0$ and the design-matrix being the Jacobian matrix

$$\mathbf{A} = \frac{\partial \boldsymbol{l}}{\partial \boldsymbol{x}}\Big|_{\boldsymbol{x}_0} = \frac{\partial \boldsymbol{f}(\boldsymbol{x}_0)}{\partial \boldsymbol{x}} = \begin{bmatrix} \frac{\partial f_1(\boldsymbol{x}_0)}{\partial x_1} & \cdots & \frac{\partial f_1(\boldsymbol{x}_0)}{\partial x_M} \\ \vdots & \ddots & \vdots \\ \frac{\partial f_N(\boldsymbol{x}_0)}{\partial x_1} & \cdots & \frac{\partial f_N(\boldsymbol{x}_0)}{\partial x_M} \end{bmatrix} \ . \tag{3.8}$$

Using the linearised functional model in Eq. 3.7 for the computation of the dependent variables' variances and covariances (Eq. 3.1), again yields $\mathbf{C}_{ll} = \mathbf{A}\mathbf{C}_{xx}\mathbf{A}^{\mathrm{T}}$ (Eq. 3.4), where the constant dependent variables in $\boldsymbol{l}_0$ do not influence the uncertainty estimation.

3.2 Least-squares adjustment

The Least-Squares Adjustment (LSQA) is a method of solving a system of equations in which the number of observations exceeds the number of unknown parameters. It was first developed by Carl Friedrich Gauß, see Gauß [1809], and first published by Adrien-Marie Legendre [Legendre, 1805], to fit a Keplerian orbit to observations of the newly discovered

dwarf planet Ceres.
The idea is to extend a functional model $\boldsymbol{f}(\boldsymbol{x})$, which consists of a relationship between unknown parameters $\boldsymbol{x}$ and the observations $\boldsymbol{\ell}$, with an unobserved error term $\boldsymbol{e}$

$$\begin{aligned} \boldsymbol{\ell} &= \boldsymbol{f}(\boldsymbol{x}) + \boldsymbol{e} \\ &= \mathbf{A}\boldsymbol{x} + \boldsymbol{e} \end{aligned} \tag{3.9}$$

and to compute the unknown parameters $\boldsymbol{x}$ such that the sum of the weighted squared errors $\boldsymbol{e}$ becomes minimal

$$\Omega := \boldsymbol{e}^{\mathrm{T}}\mathbf{P}\boldsymbol{e} \rightarrow \min. \tag{3.10}$$

The metric $\mathbf{P}$ is a weight matrix, assigning each error a certain weight based on the expected precision of the respective observation, i.e., based on the a priori stochastic model. It may be defined by

$$\mathbf{P} := \mathbf{Q}_{\ell\ell}^{-1} \ , \tag{3.11}$$

where $\mathbf{Q}_{\ell\ell}$ is the cofactor matrix of the observations, connected to the covariance matrix of the observations $\mathbf{C}_{\ell\ell}$ by the arbitrarily selectable variance of unit weight σ_0^2 with

$$\mathbf{Q}_{\ell\ell} := \frac{1}{\sigma_0^2}\mathbf{C}_{\ell\ell} \ . \tag{3.12}$$

Hence, the LSQ method is based on a system of linear equations (Eq. 3.3), extended by errors $\boldsymbol{e}$, which link the observations $\boldsymbol{\ell}$, treated as stochastic variables, to the unknown and sought-after parameters $\boldsymbol{x}$. Several types of observations may be processed in one common LSQA as long as a functional model $\boldsymbol{f}$ exists. The design-matrix $\mathbf{A}$ has a dimension of N rows (number of observations) and M columns (number of unknown parameters). For over-determined systems, as they are considered in this work, $N > M$ holds.

Using the minimum condition from Eq. 3.10 and solving the extremum problem for the minimum [see e.g., Koch, 1997] results in the so called Normal Equations (NEQs) as unique solution for the formulated problem. Using the abbreviations

$$\mathbf{N} := \mathbf{A}^{\mathrm{T}}\mathbf{P}\mathbf{A} \ , \qquad \boldsymbol{b} := \mathbf{A}^{\mathrm{T}}\mathbf{P}\boldsymbol{\ell} \qquad \text{and} \qquad \Lambda := \boldsymbol{\ell}^{\mathrm{T}}\mathbf{P}\boldsymbol{\ell} \ , \tag{3.13}$$

with $\mathbf{N}$ being the normal equation matrix, $\boldsymbol{b}$ the right-hand side, and Λ the sum of the weighted observations squared, the normal equation system reads as

$$\mathbf{N}\hat{\boldsymbol{x}} = \boldsymbol{b} \ , \tag{3.14}$$

and the solution for the unknown parameters may be computed with

$$\hat{\boldsymbol{x}} = \mathbf{N}^{-1}\boldsymbol{b} \ , \tag{3.15}$$

under the condition that $\mathbf{N}$ is nondegenerate, thus no linear dependencies between parameters exist. The hat ($\hat{\cdot}$) over the solution vector indicates that it is an estimated quantity.

As a consequence of Eq. 3.9, the estimation for $\boldsymbol{x}$ does not allow to reproduce every

single observation, consequently, the residuals $\hat{\boldsymbol{e}}$ to the estimated functional model may be computed as

$$\begin{aligned}\hat{\boldsymbol{e}} &= \boldsymbol{\ell} - \mathbf{A}\hat{\boldsymbol{x}} \\ &= \boldsymbol{\ell} - \hat{\boldsymbol{\ell}} \ ,\end{aligned} \tag{3.16}$$

with $\hat{\boldsymbol{\ell}}$ being the adjusted observations. Note that the residuals $\hat{\boldsymbol{e}}$ are an estimation for the errors $\boldsymbol{e}$ defined with the model in Eq. 3.9.

According to the Gauss-Markov theorem (for a weight matrix $\mathbf{P} = \mathbf{I}$, David and Neyman, 1938) or the Aitken theorem (for a weight matrix derived from a covariance matrix of the errors $\mathbf{P} = 1/\sigma_0^2\mathbf{C}_{ee}$, Aitken, 1936) the LSQ method provides for a Best Linear Unbiased Estimator [BLUE, see Koch, 1997]. This leads to several statistically important characteristics. First, the expectancy value of $\hat{\boldsymbol{x}}$ reads as

$$\mathbb{E}(\hat{\boldsymbol{x}}) = \boldsymbol{x} \ , \tag{3.17}$$

which means that the expectation of the estimated solution vector $\hat{\boldsymbol{x}}$ corresponds with the true solution vector $\boldsymbol{x}$, thus it is *unbiased*. Additionally, the errors feature a zero mean

$$\mathbb{E}(\boldsymbol{e}|\boldsymbol{x}) = \mathbb{E}(\hat{\boldsymbol{e}}) = 0 \ , \tag{3.18}$$

otherwise the estimator is *biased*. As a consequence of $\mathbb{E}(\boldsymbol{e}|\boldsymbol{x}) = 0$, the second-order central moments (a measure for the dispersion) of the errors correspond with the covariances of the observations

$$\mathbb{D}(\boldsymbol{e}|\boldsymbol{x}, \sigma_0^2) = \mathbb{D}(\boldsymbol{\ell}|\sigma_0^2) = \sigma_0^2\mathbf{P}^{-1} \ , \tag{3.19}$$

thus, observation uncertainties and modelling errors cannot be separated from each other in the covariance matrix of the errors [Förstner, 1979], it always contain a superposition of these two sources. In this sense, one may write the weight matrix either as referring to the observations (as in Eq. 3.11) or to the errors

$$\mathbf{P} = \sigma_0^2\mathbf{Q}_{\ell\ell}^{-1} = \sigma_0^2\mathbf{Q}_{ee}^{-1} \ . \tag{3.20}$$

The variance of unit weight may be estimated from the relation between the estimated value for the minimum criterion (Eq. 3.10) and its expected value [Koch, 1997]. It connects of the sum the weighted residuals squared with the degree of freedom $N - M$ by

$$\hat{\sigma}_0^2 = \frac{\hat{\Omega}}{N - M} \ , \tag{3.21}$$

where the estimated sum of the weighted residuals squared $\hat{\Omega}$ reads as

$$\begin{aligned}\hat{\Omega} :&= \hat{\boldsymbol{e}}^{\mathrm{T}}\mathbf{P}\hat{\boldsymbol{e}} \\ &= (\boldsymbol{\ell} - \mathbf{A}\hat{\boldsymbol{x}})^{\mathrm{T}}\,\mathbf{P}\,(\boldsymbol{\ell} - \mathbf{A}\hat{\boldsymbol{x}}) \\ &= \underbrace{\boldsymbol{\ell}^{\mathrm{T}}\mathbf{P}\boldsymbol{\ell}}_{\Lambda} + \hat{\boldsymbol{x}}^{\mathrm{T}}\,\underbrace{\mathbf{A}^{\mathrm{T}}\mathbf{P}\mathbf{A}\hat{\boldsymbol{x}}}_{\mathbf{N}\hat{\boldsymbol{x}}=\boldsymbol{b}} - 2\hat{\boldsymbol{x}}^{\mathrm{T}}\,\underbrace{\mathbf{A}^{\mathrm{T}}\mathbf{P}\boldsymbol{\ell}}_{\boldsymbol{b}} \\ &= \Lambda - \hat{\boldsymbol{x}}^{\mathrm{T}}\boldsymbol{b} \ ,\end{aligned} \tag{3.22}$$

which is also known as the Residual Sum of Squares (RSS), a criterion to designate variations between the observations and the model.

The linear LSQA process may also be viewed as linear filter applied to the observations, where the filter is defined by the functional and stochastic model. The solution $\hat{\boldsymbol{x}}$ shall be expressed by a filter matrix multiplied with the observations. The solution (cf. Eq. 3.15) may be formulated as

$$\hat{\boldsymbol{x}} = \underbrace{\mathbf{N}^{-1}\mathbf{A}^{\mathrm{T}}\mathbf{P}}_{\mathbf{R}}\boldsymbol{\ell} \ , \tag{3.23}$$

where $\mathbf{R}$ defines a filter matrix according to the functional and stochastic model introduced by $\mathbf{A}$ and $\mathbf{P}$, hence,

$$\hat{\boldsymbol{x}} = \mathbf{R}\boldsymbol{\ell} \ . \tag{3.24}$$

Using this kind of filter the cofactor matrix of the unknown parameters $\mathbf{Q}_{\hat{x}\hat{x}}$ might be established by covariance propagation (Sect. 3.1) from the stochastic model of the observations (Eq. 3.11) by

$$\begin{aligned} \mathbf{Q}_{\hat{x}\hat{x}} &= \mathbf{R}\mathbf{Q}_{\ell\ell}\mathbf{R}^{\mathrm{T}} \\ &= \mathbf{N}^{-1}\mathbf{A}^{\mathrm{T}}\underbrace{\mathbf{P}\mathbf{Q}_{\ell\ell}}_{\mathbf{I}}\mathbf{P}^{\mathrm{T}}\mathbf{A}\mathbf{N}^{-1} \\ &= \mathbf{N}^{-1} \ . \end{aligned} \tag{3.25}$$

The cofactor matrix of the unknown parameters is related to the covariance matrix $\mathbf{C}_{\hat{x}\hat{x}}$ by the a priori variance of unit weight with

$$\begin{aligned} \mathbf{C}_{\hat{x}\hat{x}} &= \mathbb{D}(\hat{\boldsymbol{x}}) \\ &= \sigma_0^2\mathbf{Q}_{\hat{x}\hat{x}} \ , \end{aligned} \tag{3.26}$$

or, in case of an estimated a posteriori variance of unit weight $\hat{\sigma}_0$, by

$$\hat{\mathbf{C}}_{\hat{x}\hat{x}} = \hat{\sigma}_0^2\mathbf{Q}_{\hat{x}\hat{x}} \ . \tag{3.27}$$

The cofactor matrix of the unknown parameters can also be taken as a starting point for another covariance propagation, namely to the adjusted observations $\hat{\boldsymbol{\ell}}$, by applying

$$\begin{aligned} \mathbf{Q}_{\hat{\ell}\hat{\ell}} &= \frac{1}{\sigma_0^2}\mathbb{D}(\hat{\boldsymbol{\ell}}) \\ &= \mathbf{A}\underbrace{\mathbf{Q}_{\hat{x}\hat{x}}}_{\mathbf{N}^{-1}}\mathbf{A}^{\mathrm{T}} \\ &= \mathbf{A}\mathbf{R}\mathbf{P}^{-1} \\ &= \mathbf{A}\mathbf{R}\mathbf{Q}_{\ell\ell} \\ &= \boldsymbol{\Pi}_{\mathrm{A}}\mathbf{Q}_{\ell\ell} \ . \end{aligned} \tag{3.28}$$

$\boldsymbol{\Pi}_{\mathrm{A}}$ denotes the influence matrix or hat matrix and is an idempotent matrix, which describes the formal relation between the observations and the adjusted observations (thus, it is a prediction matrix)

$$\begin{aligned} \hat{\boldsymbol{\ell}} &= \mathbf{A}\hat{\boldsymbol{x}} \\ &= \mathbf{A}\mathbf{R}\boldsymbol{\ell} \\ &= \boldsymbol{\Pi}_{\mathrm{A}}\boldsymbol{\ell} \ . \end{aligned} \tag{3.29}$$

The complementary projection ($\mathbf{\Pi}_{\mathrm{A}}^{\mathrm{C}}$), also called residual-maker matrix, may be motivated from Eq. 3.16 by setting

$$\begin{aligned}\hat{\boldsymbol{e}} &= \boldsymbol{\ell} - \mathbf{A}\hat{\boldsymbol{x}} \\ &= \boldsymbol{\ell} - \mathbf{A}\mathbf{R}\boldsymbol{\ell} \\ &= (\mathbf{I} - \mathbf{A}\mathbf{R})\,\boldsymbol{\ell} \\ &= \mathbf{\Pi}_{\mathrm{A}}^{\mathrm{C}}\boldsymbol{\ell} \ .\end{aligned} \tag{3.30}$$

Likewise to the prediction matrix the residual-maker matrix is idempotent. Summing up the two projections returns the original observations

$$\boldsymbol{\ell} = \left(\mathbf{\Pi}_{\mathrm{A}} + \mathbf{\Pi}_{\mathrm{A}}^{\mathrm{C}}\right)\boldsymbol{\ell} \ . \tag{3.31}$$

3.2.1 Non-linear least-squares adjustment

The functional model $\boldsymbol{f}$ which is used to fit the observations, is generally not linear. However, the LSQA as formulated in Sect. 3.2 requires a linear relation between the observations and the parameters. To overcome this problem, a linearisation with a truncated Taylor series is applied, which was already introduced in Eq. 3.7. Reducing the observations with the functional model at the Taylor point yields

$$\boldsymbol{\ell} - \boldsymbol{f}(\boldsymbol{x}_0) = \mathbf{A}\,(\boldsymbol{x} - \boldsymbol{x}_0) \ . \tag{3.32}$$

The left-hand side now contains the *Observed-minus-Computed* $(O-C)$ component, which serves as the 'observations'. $\boldsymbol{f}(\boldsymbol{x}_0)$ is the functional model evaluated at $\boldsymbol{x}_0$, forming a priori or approximated observations

$$\boldsymbol{\ell}_0 := \boldsymbol{f}(\boldsymbol{x}_0). \tag{3.33}$$

The design-matrix is the Jacobian matrix $\mathbf{A}$ evaluated at the Taylor point $\boldsymbol{x}_0$ and the vector of unknowns is split into the a priori values used for the development of the Taylor series and an increment, also known as shift vector,

$$\begin{aligned}\boldsymbol{\ell} - \boldsymbol{\ell}_0 &= \mathbf{A}(\boldsymbol{x} - \boldsymbol{x}_0) \\ \delta\boldsymbol{\ell} &= \mathbf{A}\delta\boldsymbol{x} \ ,\end{aligned} \tag{3.34}$$

which may be estimated following Eq. 3.13 and Eq. 3.15 as

$$\delta\hat{\boldsymbol{x}} = \left(\mathbf{A}^{\mathrm{T}}\mathbf{P}\mathbf{A}\right)^{-1}\mathbf{A}^{\mathrm{T}}\mathbf{P}\delta\boldsymbol{\ell} \ . \tag{3.35}$$

The final solution for the unknown parameters is composed of the a priori values of the Taylor point and the estimated increment

$$\hat{\boldsymbol{x}} = \boldsymbol{x}_0 + \delta\hat{\boldsymbol{x}} \ . \tag{3.36}$$

All further computations follow the formalism of the linear LSQA. Neglecting the higher orders of the Taylor series naturally poses the question about convergence. A first approximation of $\boldsymbol{x}_0$ has to be introduced into the computation, and the Taylor point has to be improved with each solution by setting

$$\boldsymbol{x}_0 = \hat{\boldsymbol{x}} \ , \tag{3.37}$$

and re-iterating the adjustment process.

3.2.2 Parameter constraining

The goal of constraining certain (or all) unknown parameters is to confine the spectrum of values each parameter can attain by introducing conditions through artificial (also called fictious) observations of the parameters and the stochastic model. This is a regularisation of parameters based on a priori information about their systematic and stochastic behaviour in the posed problem. The method used in this thesis is a branch of the generalised Tikhonov regularisation [Tikhonov, 1963] and closely related to the damping factor in the Levenberg–Marquardt algorithm [Levenberg, 1944, Marquardt, 1963] or in ridge regression [Hoerl and Kennard, 1970], with the main difference being that the regularisation is not applied to the full set of parameters but only to a subset. If appropriately applied, parameter constraining introduces a regularisation which is only acting towards independent a priori information, e.g., knowledge about the stochastic behaviour of a parameter.

To apply a constraining, artificial observations $\boldsymbol{h}$ are appended to the vector of observations $\boldsymbol{\ell}$. These artificial observations feature a distinct relation with a (sub)-set of the sought-after parameters, defined by $\mathbf{H}$, and a stochastic behaviour $\mathbf{W}$, which is realised by the constraints, such that

$$\mathbf{W} = \begin{bmatrix} \frac{\sigma_0^2}{\sigma_1^{\mathrm{c}\,2}} & \frac{\sigma_0^2}{\sigma_{21}^{\mathrm{c}}} & \cdots & \frac{\sigma_0^2}{\sigma_{P1}^{\mathrm{c}}} \\ \frac{\sigma_0^2}{\sigma_{21}^{\mathrm{c}}} & \frac{\sigma_0^2}{\sigma_2^{\mathrm{c}\,2}} & & \vdots \\ \vdots & & \ddots & \\ \frac{\sigma_0^2}{\sigma_{P1}^{\mathrm{c}}} & \cdots & & \frac{\sigma_0^2}{\sigma_P^{\mathrm{c}\,2}} \end{bmatrix} \quad . \tag{3.38}$$

$\sigma_p^{\mathrm{c}\,2}$ denotes the a priori variance called *constraint*. The vector $\boldsymbol{h}$ is of dimension $(P \times 1)$ and the matrix $\mathbf{H}$ is $(P \times M)$. Generally, $\mathbf{W}$ is a symmetric matrix, containing the full stochastic model of the artificial observations, i.e., potentially also correlations between the artificial observations. The formulation of the LSQA when using artificial observations changes to

$$\begin{bmatrix} \boldsymbol{\ell} \\ \boldsymbol{h} \end{bmatrix} = \begin{bmatrix} \mathbf{A} \\ \mathbf{H} \end{bmatrix} \boldsymbol{x} \quad . \tag{3.39}$$

Furthermore, the weight matrix is modified to contain $\mathbf{P}$ and $\mathbf{W}$. It is composed of three distinct parts. One assigning weights to the observations trough $\mathbf{P}$, one denoting weights to the pseudo-observations ($\mathbf{W}$), which is defined by the adopted constraints, and a matrix $\mathbf{U}$ which expresses that the observations $\boldsymbol{\ell}$ and pseudo-observations $\boldsymbol{h}$ may also be correlated.

$$\mathbf{P}_{\mathrm{c}} := \begin{bmatrix} \mathbf{P} & \mathbf{U} \\ \mathbf{U}^{\mathrm{T}} & \mathbf{W} \end{bmatrix} \quad . \tag{3.40}$$

Unless the observations have already been used to determine the pseudo-observations this block of the weight matrix equals to zero. Following the LSQ method, the normal equations system expands to

$$\begin{aligned} \mathbf{N}_{\mathrm{c}} &= \begin{bmatrix} \mathbf{A} & \mathbf{H} \end{bmatrix}^{\mathrm{T}} \begin{bmatrix} \mathbf{P} & \mathbf{U} \\ \mathbf{U}^{\mathrm{T}} & \mathbf{W} \end{bmatrix} \begin{bmatrix} \mathbf{A} \\ \mathbf{H} \end{bmatrix} = \mathbf{A}^{\mathrm{T}}\mathbf{P}\mathbf{A} + \mathbf{A}^{\mathrm{T}}\mathbf{U}\mathbf{H} + \mathbf{H}^{\mathrm{T}}\mathbf{U}^{\mathrm{T}}\mathbf{A} + \mathbf{H}^{\mathrm{T}}\mathbf{W}\mathbf{H} \\ \boldsymbol{b}_{\mathrm{c}} &= \begin{bmatrix} \mathbf{A} & \mathbf{H} \end{bmatrix}^{\mathrm{T}} \begin{bmatrix} \mathbf{P} & \mathbf{U} \\ \mathbf{U}^{\mathrm{T}} & \mathbf{W} \end{bmatrix} \begin{bmatrix} \boldsymbol{\ell} \\ \boldsymbol{h} \end{bmatrix} = \mathbf{A}^{\mathrm{T}} \left(\mathbf{P} + \mathbf{U}\right) \boldsymbol{\ell} + \mathbf{H}^{\mathrm{T}} \left(\mathbf{U}^{\mathrm{T}} + \mathbf{W}\right) \boldsymbol{h} \quad . \end{aligned} \tag{3.41}$$

The subscript c stands for *constraining*, hence, referring to a solution which is computed under the condition of constraints.

For the case of $\mathbf{U} = \mathbf{0}$ the normal equations read as

$$\begin{aligned} \mathbf{N}_{\mathrm{c}} &:= \mathbf{A}^{\mathrm{T}}\mathbf{P}\mathbf{A} + \mathbf{H}^{\mathrm{T}}\mathbf{W}\mathbf{H} = \mathbf{N} + \mathbf{H}^{\mathrm{T}}\mathbf{W}\mathbf{H} \\ \boldsymbol{b}_{\mathrm{c}} &:= \mathbf{A}^{\mathrm{T}}\mathbf{P}\boldsymbol{\ell} + \mathbf{H}^{\mathrm{T}}\mathbf{W}\boldsymbol{h} = \boldsymbol{b} + \mathbf{H}^{\mathrm{T}}\mathbf{W}\boldsymbol{h} \ , \end{aligned} \tag{3.42}$$

and the solution $\hat{\boldsymbol{x}}^{\mathrm{c}}$ may be computed with

$$\begin{aligned} \hat{\boldsymbol{x}}^{\mathrm{c}} &= \left(\mathbf{N} + \mathbf{H}^{\mathrm{T}}\mathbf{W}\mathbf{H}\right)^{-1}\left(\boldsymbol{b} + \mathbf{H}^{\mathrm{T}}\mathbf{W}\boldsymbol{h}\right) \\ &= \mathbf{N}_{\mathrm{c}}^{-1}\boldsymbol{b}_{\mathrm{c}} \ . \end{aligned} \tag{3.43}$$

In analogy to the filter in Sect. 3.2, the constraining may be re-written by inserting Eq. 3.14 in Eq. 3.43

$$\begin{aligned} \hat{\boldsymbol{x}}^{\mathrm{c}} &= \left(\mathbf{N} + \mathbf{H}^{\mathrm{T}}\mathbf{W}\mathbf{H}\right)^{-1}\left(\mathbf{N}\hat{\boldsymbol{x}} + \mathbf{H}^{\mathrm{T}}\mathbf{W}\boldsymbol{h}\right) \\ &= \mathbf{N}_{\mathrm{c}}^{-1}\mathbf{N}\hat{\boldsymbol{x}} + \mathbf{N}_{\mathrm{c}}^{-1}\mathbf{H}^{\mathrm{T}}\mathbf{W}\boldsymbol{h} \ . \end{aligned} \tag{3.44}$$

A filter which yields the constrained solution vector $\hat{\boldsymbol{x}}^{\mathrm{c}}$ from the unconstrained solution vector $\hat{\boldsymbol{x}}$ may then be defined by

$$\mathbf{T} := \mathbf{N}_{\mathrm{c}}^{-1}\mathbf{N} \tag{3.45}$$

and the constrained solution may eventually be written as

$$\hat{\boldsymbol{x}}^{\mathrm{c}} = \mathbf{T}\hat{\boldsymbol{x}} + \mathbf{T}\mathbf{N}^{-1}\mathbf{H}^{\mathrm{T}}\mathbf{W}\boldsymbol{h} \ . \tag{3.46}$$

Eq. 3.45 shows that the filter explains a difference between a constrained and an unconstrained solution (in the extreme case $\mathbf{H} = \mathbf{0}$ or $\mathbf{W} = \mathbf{0} \rightarrow \mathbf{T} = \mathbf{N}^{-1}\mathbf{N} = \mathbf{I}$ is computed as the filter matrix). The constrained solution $\hat{\boldsymbol{x}}^{\mathrm{c}}$ is, however, based and dependent on the a priori artificial observations $\boldsymbol{h}$ due to the term $\mathbf{T}\mathbf{N}^{-1}\mathbf{H}^{\mathrm{T}}\mathbf{W}\boldsymbol{h}$. If $\boldsymbol{h} = \mathbf{0}$, i.e, if a constraining to zero is performed, no shift caused by the a priori values of the constrained parameters is introduced through the artificial observations, implying that only stochastic a priori information is brought into the system, and the constrained (filtered) solution reads as

$$\hat{\boldsymbol{x}}^{\mathrm{c}} = \mathbf{T}\hat{\boldsymbol{x}} \ . \tag{3.47}$$

In an iterative LSQ process, as the non-linear formulation demands, where also the artificial observations $\boldsymbol{h}$ are reduced by the functional model evaluated at the Taylor point $\boldsymbol{f}(\boldsymbol{x}_0)$, it is pivotal that $\boldsymbol{h} = \mathbf{0}$ is set in every iteration otherwise a bias towards the solution of the preceding iteration is introduced. This means, that the right-hand side $\boldsymbol{b}$ of the normal equations has to be reduced by the a priori values $\boldsymbol{x}_0$ of the to-be-constrained parameters by

$$\boldsymbol{b}_{\mathrm{c}} = \boldsymbol{b} - \mathbf{H}^{\mathrm{T}}\mathbf{W}\boldsymbol{x}_0. \tag{3.48}$$

The bias may be easily seen in Eq. 3.44 where the part $\mathbf{N}_{\mathrm{c}}^{-1}\mathbf{H}^{\mathrm{T}}\mathbf{W}\boldsymbol{h}$ shifts the solution, and consequently, also the residuals which serve as new $O - C$ in each iteration.

The process of constraining the solution may be related with the original observations $\boldsymbol{\ell}$ by two consecutive filter

$$\begin{aligned}\hat{\boldsymbol{x}}^{\mathrm{c}} &= \mathbf{T}\mathbf{R}\boldsymbol{\ell} \\ &= \mathbf{N}_{\mathrm{c}}^{-1}\mathbf{N}\mathbf{N}^{-1}\mathbf{A}^{\mathrm{T}}\mathbf{P}\boldsymbol{\ell} \\ &= \mathbf{N}_{\mathrm{c}}^{-1}\mathbf{A}^{\mathrm{T}}\mathbf{P}\boldsymbol{\ell} \ ,\end{aligned} \tag{3.49}$$

as it follows from Eq. 3.23 with

$$\mathbf{R}^{\mathrm{c}} \coloneqq \mathbf{N}_{\mathrm{c}}^{-1}\mathbf{A}^{\mathrm{T}}\mathbf{P} \ . \tag{3.50}$$

Equation 3.49 may again be regarded as filter and the constrained solution is a linear filter applied on the observations

$$\hat{\boldsymbol{x}}^{\mathrm{c}} = \mathbf{R}^{\mathrm{c}}\boldsymbol{\ell}. \tag{3.51}$$

In the CMA the constraining of parameters is frequently adopted when extending the parameter space with so-called pseudo-stochastic parameters to account for a deficient background force modelling (see Sect. 5.1.6). A subset of the unknown parameters (the pseudo-stochastic parameters) are constrained by a stochastic model $\mathbf{W}$ which describes their a priori known stochastic behaviour. Kvas and Mayer-Gürr [2019] showed that such a set of constrained parameters may also be incorporated into the a priori covariance matrix of the observations and consequently into the weight matrix, yielding the same result as explicitly solving for all parameters. This will be further used in Sect. 3.2.6, Sect. 5.1.6 and Sect. 5.5.1.

3.2.3 Parameter pre-elimination

The time span in which parameters are valid is distinct for different parameter types. There are global parameters, which are usually the final outcome of an estimation process, and also parameters which are only valid for shorter time intervals or even epoch-wise. These parameters can be removed from the normal equation system without deleting their contribution. Depending on the formulation of the problem a gain in memory usage and computation time may be achieved because the final parameter space is reduced, and consequently, can be solved more efficiently.
Separating between two types of parameters, where $\hat{\boldsymbol{x}}$ denotes a global set of parameters which shall be kept in the system of equations, and the parameters in $\hat{\boldsymbol{y}}$, which shall be pre-eliminated on NEQ level, yields the formulation

$$\begin{bmatrix}\mathbf{N}_{\hat{x}\hat{x}} & \mathbf{N}_{\hat{x}\hat{y}} \\ \mathbf{N}_{\hat{x}\hat{y}}^{\mathrm{T}} & \mathbf{N}_{\hat{y}\hat{y}}\end{bmatrix}\begin{bmatrix}\hat{\boldsymbol{x}} \\ \hat{\boldsymbol{y}}\end{bmatrix} = \begin{bmatrix}\boldsymbol{b}_{\hat{x}} \\ \boldsymbol{b}_{\hat{y}}\end{bmatrix} \ . \tag{3.52}$$

By extracting the solution for $\hat{\boldsymbol{y}}$ and assuming that the normal equation matrix related to the to-be-eliminated parameters $\mathbf{N}_{\hat{y}\hat{y}}$ is nondegenerate, this yields

$$\hat{\boldsymbol{y}} = \mathbf{N}_{\hat{y}\hat{y}}^{-1}\left(\boldsymbol{b}_{\hat{y}} - \mathbf{N}_{\hat{x}\hat{y}}^{\mathrm{T}}\hat{\boldsymbol{x}}\right) \ . \tag{3.53}$$

The normal equations may be re-formulated to a reduced parameter space only containing the parameters in $\hat{\boldsymbol{x}}$ explicitly by

$$\left(\mathbf{N}_{\hat{x}\hat{x}} - \mathbf{N}_{\hat{x}\hat{y}}\mathbf{N}_{\hat{y}\hat{y}}^{-1}\mathbf{N}_{\hat{x}\hat{y}}^{\mathrm{T}}\right)\hat{\boldsymbol{x}} = \boldsymbol{b}_{\hat{x}} - \mathbf{N}_{xy}\mathbf{N}_{\hat{y}\hat{y}}^{-1}\boldsymbol{b}_{\hat{y}} \ . \tag{3.54}$$

Such a process is typically applied to orbit (local) and gravity field (global) parameters to allow for a pre-elimination of the orbit parameters at the level of each orbital arc.

3.2.4 Sequential least-squares adjustment

Depending on the number of observations and unknown parameters, explicitly setting up the complete design-matrix for all observations and computing normal equations for the LSQA according to Eq. 3.13 might be very costly in terms of memory usage. Under certain conditions the process of a LSQA may be broken down into smaller segments.
Assuming $\mathbf{P} = \mathbf{I}$, the normal equation matrix $\mathbf{N}$ and the right-hand side $\boldsymbol{b}$ can be set up for each observation separately by summing up each NEQ emerging from one line of the design-matrix. However, for other than diagonal weight matrices, the elements in $\mathbf{P}$ correlate observations with each other, and consequently, the NEQs cannot be stacked for each observation but only for a sequence of blocks with a length depending on the correlations described by the weight matrix. By forming K blocks the structure of the system of observation equations may be written as

$$\begin{bmatrix} \boldsymbol{\ell}_1 \\ \boldsymbol{\ell}_2 \\ \vdots \\ \boldsymbol{\ell}_K \end{bmatrix} = \begin{bmatrix} \mathbf{A}_1 \\ \mathbf{A}_2 \\ \vdots \\ \mathbf{A}_K \end{bmatrix} \boldsymbol{x} \qquad \text{with} \qquad \mathbf{P} := \begin{bmatrix} \mathbf{P}_1 & & & \mathbf{0} \\ & \mathbf{P}_2 & & \\ & & \ddots & \\ \mathbf{0} & & & \mathbf{P}_K \end{bmatrix} , \tag{3.55}$$

where the weight matrix $\mathbf{P}$ is of block diagonal structure. For each block the contribution to the normal equation system (cf. with Eq. 3.13) is computed according to

$$\mathbf{N}_k := \mathbf{A}_k^{\mathrm{T}} \mathbf{P}_k \mathbf{A}_k \ , \qquad \boldsymbol{b}_k := \mathbf{A}_k^{\mathrm{T}} \mathbf{P}_k \boldsymbol{\ell}_k \qquad \text{and} \qquad \Lambda_k := \boldsymbol{\ell}_k^{\mathrm{T}} \mathbf{P}_k \boldsymbol{\ell}_k \ . \tag{3.56}$$

Eventually, the full normal equation system may be obtained by

$$\mathbf{N} = \sum_{k=1}^{K} \mathbf{N}_k \ , \qquad \boldsymbol{b} = \sum_{k=1}^{K} \boldsymbol{b}_k \qquad \text{and} \qquad \Lambda = \sum_{k=1}^{K} \Lambda_k \ . \tag{3.57}$$

The solution is computed as described in Sect. 3.2. The choice of the block length, usually a trade-off between various factors, is a delicate matter and will be addressed in the context of Variance Component Estimation (VCE) (Sect. 5.3.2) and empirical noise modelling (Sect. 5.5.1 and 5.5.2).

3.2.5 Series of least-squares adjustments

The idea behind this process is to first apply a LSQA on the original data to determine a solution for a subset of parameters, and then to take these parameters as intermediate observations (also pseudo-observations) for a second LSQA to compute solutions for a second set of unknown parameters. Such a sequence of least-squares adjustments might be motivated by a complicated relation between the original data and the final sought-after parameters in the second adjustment. If one is able to find meaningful intermediate observations, which feature a distinct (and simple) relation to the original data and the final sought-after parameters, while preserving the information of the original observations, it might make sense to split into consecutive LSQAs. Furthermore, computation times might decrease and computational limitations might be by-passed by disregarding certain stochastic properties of the intermediate observations, especially in case the intermediate parameters are able to preserve the information of the original observations without a full covariance matrix associated with them. Additionally, the interpretation of the results could be simplified,

in particular when the intermediate observations implicate a reasonable physical meaning. A typical example in our context is the computation of kinematic positions from GNSS carrier phase observations (see Sect. 4.3) and thereof derived (reduced-)dynamic orbit and gravity field parameters.

Suppose a set of observations $\boldsymbol{\ell}^x$ with an a priori weight defined in $\mathbf{P}^x_{\ell\ell}$ and the sought-after parameter vector $\boldsymbol{x}$ for the first adjustment. This leads to a design-matrix $\mathbf{A}$

$$\mathbf{A} = \frac{\partial \boldsymbol{\ell}^x}{\partial \boldsymbol{x}} \ , \tag{3.58}$$

containing the partial derivatives of the observations to the unknown parameters $\boldsymbol{x}$. The solution then follows with Eq. 3.15 as

$$\begin{aligned} \hat{\boldsymbol{x}} &= \left(\mathbf{A}^{\mathrm{T}}\mathbf{P}^x_{\ell\ell}\mathbf{A}\right)^{-1}\mathbf{A}^{\mathrm{T}}\mathbf{P}^x_{\ell\ell}\boldsymbol{\ell}^x \\ &= \mathbf{N}^{-1}_{\hat{x}\hat{x}}\mathbf{A}^{\mathrm{T}}\mathbf{P}^x_{\ell\ell}\boldsymbol{\ell}^x \ . \end{aligned} \tag{3.59}$$

The inverse normal equation matrix corresponds to the cofactor matrix of the estimated parameters (see 3.25)

$$\mathbf{Q}_{\hat{x}\hat{x}} = \mathbf{N}^{-1}_{\hat{x}\hat{x}} \ . \tag{3.60}$$

With the quantities $\hat{\boldsymbol{x}}$ and $\mathbf{Q}_{\hat{x}\hat{x}}$ at hand, the second LSQA may be set up. The observations $\boldsymbol{\ell}^y$ are now taken from the first adjustment, hence, $\hat{\boldsymbol{x}}$ serves as the above mentioned intermediate observations. The second adjustment then only depends indirectly on the original data but makes use of pseudo-observations $\boldsymbol{\ell}^y = \hat{\boldsymbol{x}}$. The weight matrix for the pseudo-observations stems from the first adjustment as well, i.e., $\mathbf{P}^y_{\ell\ell} = \mathbf{Q}^{-1}_{\hat{x}\hat{x}} = \mathbf{N}_{\hat{x}\hat{x}}$. The unknown parameters are denoted by $\boldsymbol{y}$ and they have a formal relation with the pseudo-observations defined with the design-matrix $\mathbf{B}$

$$\mathbf{B} = \frac{\partial \boldsymbol{\ell}^y}{\partial \boldsymbol{y}} = \frac{\partial \hat{\boldsymbol{x}}}{\partial \boldsymbol{y}} \ . \tag{3.61}$$

The solution then reads as

$$\begin{aligned} \hat{\boldsymbol{y}} &= \left(\mathbf{B}^{\mathrm{T}}\mathbf{P}^y_{\ell\ell}\mathbf{B}\right)^{-1}\mathbf{B}^{\mathrm{T}}\mathbf{P}^y_{\ell\ell}\boldsymbol{\ell}^y \\ &= \left(\mathbf{B}^{\mathrm{T}}\mathbf{N}_{\hat{x}\hat{x}}\mathbf{B}\right)^{-1}\mathbf{B}^{\mathrm{T}}\mathbf{N}_{\hat{x}\hat{x}}\hat{\boldsymbol{x}} \ . \end{aligned} \tag{3.62}$$

Inserting the solution of the first LSQA into $\hat{\boldsymbol{x}}$ and expanding the first occurrence of $\mathbf{N}_{\hat{x}\hat{x}}$ gives

$$\hat{\boldsymbol{y}} = \left(\mathbf{B}^{\mathrm{T}}\mathbf{A}^{\mathrm{T}}\mathbf{P}^x_{\ell\ell}\mathbf{A}\mathbf{B}\right)^{-1}\mathbf{B}^{\mathrm{T}}\underbrace{\mathbf{N}_{\hat{x}\hat{x}}\mathbf{N}^{-1}_{\hat{x}\hat{x}}}_{\mathbf{I}}\mathbf{A}^{\mathrm{T}}\mathbf{P}^x_{\ell\ell}\boldsymbol{\ell}^x \ . \tag{3.63}$$

Simplifying Eq. 3.63 leads to

$$\hat{\boldsymbol{y}} = \left(\mathbf{B}^{\mathrm{T}}\mathbf{A}^{\mathrm{T}}\mathbf{P}^x_{\ell\ell}\mathbf{A}\mathbf{B}\right)^{-1}\mathbf{B}^{\mathrm{T}}\mathbf{A}^{\mathrm{T}}\mathbf{P}^x_{\ell\ell}\boldsymbol{\ell}^x \ . \tag{3.64}$$

It relates the original observations $\boldsymbol{\ell}^x$, their a priori weight $\mathbf{P}^y_{\ell\ell}$ with the sought-after parameters of the second LSQA $\boldsymbol{y}$. The new design-matrix defining this relation may be named

$$\mathbf{M} \coloneqq \mathbf{A}\mathbf{B} \ , \tag{3.65}$$

and accordingly, the estimation for $\hat{\boldsymbol{y}}$ reads as

$$\hat{\boldsymbol{y}} = (\mathbf{M}^{\mathrm{T}}\mathbf{P}^{x}_{\ell\ell}\mathbf{M})^{-1}\mathbf{M}^{\mathrm{T}}\mathbf{P}^{x}_{\ell\ell}\boldsymbol{\ell}^{x} \quad . \tag{3.66}$$

The new design-matrix $\mathbf{M}$ contains the partial derivatives of the original observations with respect to the unknown parameters of the second LSQA applying the chain rule

$$\begin{aligned} \mathbf{M} &= \mathbf{A}\mathbf{B} \\ &= \left[\frac{\partial \boldsymbol{\ell}_x}{\partial \boldsymbol{x}}\right]\left[\frac{\partial \hat{\boldsymbol{x}}}{\partial \boldsymbol{y}}\right] = \left[\frac{\partial \boldsymbol{\ell}_x}{\partial \boldsymbol{x}}\frac{\partial \hat{\boldsymbol{x}}}{\partial \boldsymbol{y}}\right] \quad . \end{aligned} \tag{3.67}$$

For U estimated parameters in $\hat{\boldsymbol{x}}$ and M sought-after parameters in $\boldsymbol{y}$ with N original observations in $\boldsymbol{\ell}^x$ the design-matrix $\mathbf{M}$ reads as

$$\mathbf{M} = \begin{bmatrix} \sum_{u=1}^{U}\left(\frac{\partial \ell_1^x}{\partial x_u}\frac{\partial \hat{x}_u}{\partial y_1}\right) & \cdots & \sum_{u=1}^{U}\left(\frac{\partial \ell_1^x}{\partial x_u}\frac{\partial \hat{x}_u}{\partial y_M}\right) \\ \vdots & \ddots & \vdots \\ \sum_{u=1}^{U}\left(\frac{\partial \ell_N^x}{\partial x_u}\frac{\partial \hat{x}_u}{\partial y_1}\right) & \cdots & \sum_{u=1}^{U}\left(\frac{\partial \ell_N^x}{\partial x_u}\frac{\partial \hat{x}_u}{\partial y_M}\right) \end{bmatrix}_{(N\times M)} \quad . \tag{3.68}$$

This formulation will be resumed in Sect. 4.1 and Sect. 4.3. Note that the sum over U partial derivatives may be reduced if the the corresponding partials are zero as it is the case e.g., for kinematic positions.

3.2.6 Introducing observations twice

In orbit and gravity field determination the models typically consist of several kinds of parameters which are estimated in one common adjustment process. It is tempting to separate the parameters in groups, e.g., a set of orbit parameters and a set of gravity field coefficients, where the orbit parameters are estimated first, and subsequently introduced as known into the adjustment of the gravity field parameters. Such a procedure, however, may introduce undesirable side effects.

One may assume a LSQA with one set of observations $\boldsymbol{\ell}$ and two kinds of unknown parameters $\boldsymbol{x}$ and $\boldsymbol{y}$ which compose a physical model, e.g., $\boldsymbol{x}$ denoting gravity field coefficients and $\boldsymbol{y}$ containing orbit parameters. The observation equations may be written as

$$\boldsymbol{\ell} = \begin{bmatrix}\mathbf{A} & \mathbf{B}\end{bmatrix}\begin{bmatrix}\boldsymbol{x} \\ \boldsymbol{y}\end{bmatrix} + \boldsymbol{e} \ , \tag{3.69}$$

and the corresponding normal equation system expands to

$$\begin{aligned} \begin{bmatrix}\mathbf{A}^{\mathrm{T}}\mathbf{P}\mathbf{A} & \mathbf{A}^{\mathrm{T}}\mathbf{P}\mathbf{B} \\ \mathbf{B}^{\mathrm{T}}\mathbf{P}\mathbf{A} & \mathbf{B}^{\mathrm{T}}\mathbf{P}\mathbf{B}\end{bmatrix}\begin{bmatrix}\hat{\boldsymbol{x}} \\ \hat{\boldsymbol{y}}\end{bmatrix} &= \begin{bmatrix}\mathbf{A}^{\mathrm{T}}\mathbf{P}\boldsymbol{\ell} \\ \mathbf{B}^{\mathrm{T}}\mathbf{P}\boldsymbol{\ell}\end{bmatrix} \\ \begin{bmatrix}\mathbf{N}_{\hat{x}\hat{x}} & \mathbf{N}_{\hat{x}\hat{y}} \\ \mathbf{N}^{\mathrm{T}}_{\hat{x}\hat{y}} & \mathbf{N}_{\hat{y}\hat{y}}\end{bmatrix}\begin{bmatrix}\hat{\boldsymbol{x}} \\ \hat{\boldsymbol{y}}\end{bmatrix} &= \begin{bmatrix}\boldsymbol{b}_{\hat{x}} \\ \boldsymbol{b}_{\hat{y}}\end{bmatrix} \quad . \end{aligned} \tag{3.70}$$

If the solution of the parameters in $\boldsymbol{y}$ is known a priori from a previous adjustment, which reads as

$$\boldsymbol{\ell} = \mathbf{B}\boldsymbol{y} + \boldsymbol{e} \qquad \text{and} \qquad \hat{\boldsymbol{y}} = (\underbrace{\mathbf{B}^{\mathrm{T}}\mathbf{P}\mathbf{B}}_{\mathbf{N}_{\hat{y}\hat{y}}})^{-1}\mathbf{B}^{\mathrm{T}}\mathbf{P}\boldsymbol{\ell} \ , \tag{3.71}$$

the solution $\hat{\boldsymbol{y}}$ may be inserted into Eq. 3.70

$$\begin{bmatrix} \mathbf{N}_{\hat{x}\hat{x}} & \mathbf{A}^{\mathrm{T}}\mathbf{P}\mathbf{B} \\ \mathbf{B}^{\mathrm{T}}\mathbf{P}\mathbf{A} & \mathbf{N}_{\hat{y}\hat{y}} \end{bmatrix} \begin{bmatrix} \hat{\boldsymbol{x}} \\ \mathbf{N}_{\hat{y}\hat{y}}^{-1}\mathbf{B}^{\mathrm{T}}\mathbf{P}\boldsymbol{\ell} \end{bmatrix} = \begin{bmatrix} \mathbf{A}^{\mathrm{T}}\mathbf{P}\boldsymbol{\ell} \\ \mathbf{B}^{\mathrm{T}}\mathbf{P}\boldsymbol{\ell} \end{bmatrix} \quad . \tag{3.72}$$

Expanding the matrix multiplication gives

$$\begin{bmatrix} \mathbf{N}_{\hat{x}\hat{x}}\hat{\boldsymbol{x}} + \mathbf{A}^{\mathrm{T}}\mathbf{P}\mathbf{B}\mathbf{N}_{\hat{y}\hat{y}}^{-1}\mathbf{B}^{\mathrm{T}}\mathbf{P}\boldsymbol{\ell} \\ \mathbf{B}^{\mathrm{T}}\mathbf{P}\mathbf{A}\hat{\boldsymbol{x}} + \underbrace{\mathbf{N}_{\hat{y}\hat{y}}\mathbf{N}_{\hat{y}\hat{y}}^{-1}}_{\mathbf{I}}\mathbf{B}^{\mathrm{T}}\mathbf{P}\boldsymbol{\ell} \end{bmatrix} = \begin{bmatrix} \mathbf{A}^{\mathrm{T}}\mathbf{P}\boldsymbol{\ell} \\ \mathbf{B}^{\mathrm{T}}\mathbf{P}\boldsymbol{\ell} \end{bmatrix} \quad . \tag{3.73}$$

The influence matrix $\boldsymbol{\Pi}_{\mathrm{B}}$ (see Eq. 3.28) may be introduced as

$$\boldsymbol{\Pi}_{\mathrm{B}} = \mathbf{B}\mathbf{N}_{\hat{y}\hat{y}}^{-1}\mathbf{B}^{\mathrm{T}}\mathbf{P} \tag{3.74}$$

and the system of equations (Eq. 3.73) may be simplified to

$$\begin{bmatrix} \mathbf{N}_{\hat{x}\hat{x}}\hat{\boldsymbol{x}} + \mathbf{A}^{\mathrm{T}}\mathbf{P}\boldsymbol{\Pi}_{\mathrm{B}}\boldsymbol{\ell} \\ \mathbf{B}^{\mathrm{T}}\mathbf{P}\mathbf{A}\hat{\boldsymbol{x}} + \mathbf{B}^{\mathrm{T}}\mathbf{P}\boldsymbol{\ell} \end{bmatrix} = \begin{bmatrix} \mathbf{A}^{\mathrm{T}}\mathbf{P}\boldsymbol{\ell} \\ \mathbf{B}^{\mathrm{T}}\mathbf{P}\boldsymbol{\ell} \end{bmatrix} \quad , \tag{3.75}$$

and further to

$$\begin{bmatrix} \mathbf{N}_{\hat{x}\hat{x}}\hat{\boldsymbol{x}} \\ \mathbf{B}^{\mathrm{T}}\mathbf{P}\mathbf{A}\hat{\boldsymbol{x}} \end{bmatrix} = \begin{bmatrix} \mathbf{A}^{\mathrm{T}}\mathbf{P}\boldsymbol{\ell} - \mathbf{A}^{\mathrm{T}}\mathbf{P}\boldsymbol{\Pi}_{\mathrm{B}}\boldsymbol{\ell} \\ \mathbf{0} \end{bmatrix} \quad . \tag{3.76}$$

Solving this equation for $\hat{\boldsymbol{x}}$ implicates that the formal relation between $\mathbf{B}$ and $\mathbf{A}$ is zero, thus, $\mathbf{B}^{\mathrm{T}}\mathbf{P}\mathbf{A} = \mathbf{0}$. Proceeding with the first line in Eq. 3.76 to solve for the unknown parameters in $\hat{\boldsymbol{x}}$, leads to a solution which consists of the regular solution as in Eq. 3.15 and a correction term which changes the filter according to the formal influence of $\mathbf{B}$ on the observations based on the projection with the influence matrix (see Eq. 3.28)

$$\begin{aligned} \hat{\boldsymbol{x}} &= \underbrace{\mathbf{N}_{\hat{x}\hat{x}}^{-1}\mathbf{A}^{\mathrm{T}}\mathbf{P}}_{\mathbf{R}}\boldsymbol{\ell} - \underbrace{\mathbf{N}_{\hat{x}\hat{x}}^{-1}\mathbf{A}^{\mathrm{T}}\mathbf{P}}_{\mathbf{R}}\boldsymbol{\Pi}_{\mathrm{B}}\boldsymbol{\ell} \\ &= \mathbf{R}\boldsymbol{\ell} - \mathbf{R}\boldsymbol{\Pi}_{\mathrm{B}}\boldsymbol{\ell} \\ &= (\mathbf{R} - \mathbf{R}\boldsymbol{\Pi}_{\mathrm{B}})\,\boldsymbol{\ell} \quad . \end{aligned} \tag{3.77}$$

Or formulated differently, now the observations are not only filtered but also reduced by the previously adjusted model ($\hat{\boldsymbol{\ell}}_y = \boldsymbol{\Pi}_{\mathrm{B}}\boldsymbol{\ell}$, see Eq. 3.29)

$$\begin{aligned} \hat{\boldsymbol{x}} &= \mathbf{R}\,(\boldsymbol{\ell} - \boldsymbol{\Pi}_{\mathrm{B}}\boldsymbol{\ell}) \\ &= \mathbf{R}\left(\boldsymbol{\ell} - \hat{\boldsymbol{\ell}}_y\right) \\ &= \mathbf{R}\hat{\boldsymbol{e}}_y \quad . \end{aligned} \tag{3.78}$$

Thus, the solution of $\hat{\boldsymbol{x}}$ uses the residuals of the preceding LSQA $\hat{\boldsymbol{e}}_y$ as observations. Based on the expression in 3.78 one is also able to write the residuals as being dependent from the influence matrix of $\hat{\boldsymbol{y}}$. Computing the residuals from $\hat{\boldsymbol{x}}$ (Eq. 3.77 using Eq. 3.28) leads to

$$\begin{aligned} \hat{\boldsymbol{e}}_x &= \boldsymbol{\ell} - \mathbf{A}\hat{\boldsymbol{x}} \\ &= \boldsymbol{\ell} - \mathbf{A}(\mathbf{R}\boldsymbol{\ell} - \mathbf{R}\boldsymbol{\Pi}_{\mathrm{B}}\boldsymbol{\ell}) \\ &= \boldsymbol{\ell} - \underbrace{\mathbf{A}\mathbf{R}}_{\boldsymbol{\Pi}_{\mathrm{A}}}\boldsymbol{\ell} + \underbrace{\mathbf{A}\mathbf{R}}_{\boldsymbol{\Pi}_{\mathrm{A}}}\boldsymbol{\Pi}_{\mathrm{B}}\boldsymbol{\ell} \\ &= (\underbrace{\mathbf{I} - \boldsymbol{\Pi}_{\mathrm{A}}}_{\boldsymbol{\Pi}_{\mathrm{A}}^{\mathrm{C}}})\,\boldsymbol{\ell} + (\boldsymbol{\Pi}_{\mathrm{A}}\boldsymbol{\Pi}_{\mathrm{B}})\,\boldsymbol{\ell} \quad , \end{aligned} \tag{3.79}$$

which shows that the residuals of $\hat{\boldsymbol{x}}$ are shifted by $(\boldsymbol{\Pi}_{\mathrm{A}}\boldsymbol{\Pi}_{\mathrm{B}})\,\boldsymbol{\ell}'$ and do not follow Eq. 3.30 anymore.

A regularisation towards a priori information is introduced whenever the computation of $\hat{\boldsymbol{y}}$ relies on a priori information about the parameters which are to be estimated with $\hat{\boldsymbol{x}}$ through the dependency of $\hat{\boldsymbol{y}}$ and $\hat{\boldsymbol{x}}$ on the same observations. Hence, it is questionable to change the parameter-space between subsequent adjustments which are based on the same observations. Such an idea of separating the parameter estimation process into several steps, in our context splitting into an orbit computation and a gravity field recovery thereof (a so-called two-step approach), might also be applied to a subset of parameters, hence, not introducing the full set of already solved-for orbit parameters into the second step of gravity field recovery but only a selected set. This has been investigated by Meyer et al. [2015] for a separation of a (co-)estimated stochastic model using parameter pre-elimination in contrast to fixing parameters to a priori values, where the regularisation influence could be traced down into the final gravity field solution. Such (mild) two-step approaches, where only a (small) subset of parameters is fixed, are applied in gravity field recovery, e.g., by the CSR to compute their GRACE and GRACE Follow-On gravity field solutions.

Moreover, a regularisation might not only be introduced by fixing parameters to harmful a priori values through the parameter space, as done in this section or could occur with the right-had side of the constraints' normal equations (see Sect. 3.2.2), also the weight matrix $\mathbf{P}$ or the matrix with the constraints $\mathbf{W}$ are capable of transporting a regularisation towards a priori information into the system. Kvas and Mayer-Gürr [2019] showed that the extension of the parameter-space by additional quantities and a (constrained towards zero) co-estimation of them together with all other parameters can also be represented by covariance propagation onto the cofactor matrix of the observations. Hence, a regularisation caused by the parameter-space could also be evoked by an unfavourable choice of the stochastic behaviour of the observations. Introducing a noise model which was determined by the observations in the least-squares process leads to a shift towards the a priori models used to derive the noise model. If the process of deriving the noise model contains any of the final sought-after parameters as an a priori model (e.g., the gravity field), the final solution has to be considered as regularised. An example for the latter would be to use a reduced gravity field resolution to deduce an empirical noise modelling of the observations (see Sect. 5.5.1 and Sect. 5.5.2) and extend the gravity field's resolution (enhancing the parameter-space) when introducing the empirical models. Even though such an approach could significantly decrease the computation time, it results in a regularised estimation of the gravity field parameters.

3.3 Variance component estimation

Variance Component Estimation (VCE) is a procedure to derive stochastic information about different observation groups, e.g., in terrestrial geodesy, angles and distances. Several methods of VCE have been brought up, such as Helmert types (first proposed by Helmert [1907], see e.g., Grafarend et al. [1980]), Best Invariant Quadratic Unbiased Esti-

mate (BIQUE) methods [e.g., Koch, 1997], Minimum Norm Quadratic Unbiased Estimate (MINQUE) [Rao, 1973] or Least-Squares VCE [Teunissen and Amiri-Simkooei, 2008] or the non-negative VCE from Förstner [Förstner, 1979], which is also adopted in this thesis. More recently, VCE is used in geodetic applications, e.g., by Ellmer [2018] for temporal GRACE gravity field determination, by Jean et al. [2018] to combine gravity field solutions computed at different institutions, by Zehentner and Mayer-Gürr [2016] for kinematic point positioning of LEO satellites or by Koch and Kusche [2002] for combining different observation techniques of the Earth's gravity field. VCE follows an iterative procedure where for each NEQ its contribution to the full solution is computed as a variance component, which is derived from the sum of the weighted residuals squared of this NEQ and its partial redundancy. The following reasonings about the VCE, as it is applied within the scope of this thesis, are based on the works of Förstner [1979], Koch [1997], Koch and Kusche [2002] and Niemeier [2008].

The method of VCE may be motivated by separating the stochastic model of the observations into a sum of K known individual cofactor matrices $\mathbf{Q}_k$

$$\mathbf{C}_{\ell\ell} = \sum_{k=1}^{K} \sigma_k^2 \, \mathbf{Q}_k^{\ell\ell} \quad , \tag{3.80}$$

where only a variance factor σ_k^2 for each cofactor matrix is unknown. The goal is to determine this variance factor in the context of the complete formulation of the problem to appoint a reliably estimated contribution of each observation(-group) to the solution. As a consequence, one assumes that the groups do not share the same σ_0^2. For an identity matrix as weight matrix $\mathbf{P}$ and two groups, this may be sketched in the computation of the variance of unit weight by

$$\hat{\sigma}_0^2 = \frac{\hat{\boldsymbol{e}}^{\mathrm{T}}\mathbf{P}\hat{\boldsymbol{e}}}{N-M} = \frac{\hat{\boldsymbol{e}}^{\mathrm{T}}\hat{\boldsymbol{e}}}{N-M} = \frac{\hat{e}_1^2 + \hat{e}_2^2 + ... + \hat{e}_{N_1}^2 + \hat{e}_{N_1+1}^2 + \hat{e}_{N_1+2}^2 + ... + \hat{e}_{N_1+N_2}^2}{\underbrace{r_1 + r_2 + ... + r_{N_1}}_{k=1 \rightarrow \, \sigma_1^2} + \underbrace{r_{N_1+1} + r_{N_1+2} + ... + r_{N_1+N_2}}_{k=2 \rightarrow \, \sigma_2^2}} \quad , \tag{3.81}$$

with N_1 observations in the first block, N_2 observations in the second, generally containing an arbitrary number of observations per group, however, sufficient to ensure a well-determined system of equations. Note that all correlations between the individual blocks are neglected. r indicates the partial *redundancies* [see Niemeier, 2008] for each observation, which sum up to the degree of freedom.
The variance components may be derived from the estimated minimum criterion (RSS) given in Eq. 3.22 and its expected value $\mathbb{E}\left(\hat{\Omega}\right)$, see Kendrick [2002, p. 170 et seq.], Koch [1997, p. 145] and Förstner [1979], which reads as

$$\hat{\sigma}_0^2 = \frac{\hat{\Omega}}{\mathbb{E}\left(\hat{\Omega}\right)} = \frac{\hat{\Omega}}{N-M} = \frac{\hat{\Omega}}{\mathrm{tr}\left(\mathbf{\Pi}_{\mathrm{A}}^{\mathrm{C}}\right)} = \frac{\hat{\Omega}}{\mathrm{tr}\left(\mathbf{I} - \mathbf{\Pi}_{\mathrm{A}}\right)} = \frac{\hat{\Omega}}{N - \mathrm{tr}\left(\mathbf{\Pi}_{\mathrm{A}}\right)} \quad . \tag{3.82}$$

Following Förstner [1979], the numerator and the denominator in Eq. 3.82 may be computed separately for different groups of observations with the stochastic model $\mathbf{Q}_k^{\ell\ell}$ if they are independent from each other. The RSS (see Eq. 3.22) of each group $\hat{\Omega}_k$ may then be written as

$$\hat{\Omega}_k = \Lambda_k + \hat{\boldsymbol{x}}^{\mathrm{T}}\mathbf{N}_k\hat{\boldsymbol{x}} - 2\hat{\boldsymbol{x}}^{\mathrm{T}}\boldsymbol{b}_k \qquad \text{with} \qquad \Lambda_k = \boldsymbol{\ell}_k^{\mathrm{T}}\mathbf{P}_k\boldsymbol{\ell}_k \quad , \tag{3.83}$$

and the denominator follows with

$$r_k := N_k - \mathrm{tr}\left(\mathbf{\Pi}_{\mathrm{A},k}\right) \quad , \tag{3.84}$$

where N_k denotes the number of observations in the k^{th} group. Exploiting that the trace is invariant to cyclic permutation the partial redundancies may be computed by

$$r_k = N_k - \mathrm{tr}\left(\mathbf{N}_k\mathbf{N}^{-1}\right) \quad . \tag{3.85}$$

Thereof, a variance component $\hat{\sigma}_k^2$ may be estimated for each subset of observations as introduced in Eq. 3.80 and outlined in Eq. 3.81 with

$$\hat{\sigma}_k^2 := \frac{\hat{\Omega}_k}{r_k} = \frac{\hat{\boldsymbol{e}}_k^{\mathrm{T}}\mathbf{P}_k\hat{\boldsymbol{e}}_k}{N_k - \mathrm{tr}\left(\mathbf{N}_k\mathbf{N}^{-1}\right)} \quad . \tag{3.86}$$

As it can be easily seen, the VCE requires an iterative procedure because the full solution $\hat{\boldsymbol{x}}$ and the inverse normal equation matrix $\mathbf{N}^{-1}$ is needed to compute $\hat{\Omega}_k$ and r_k. Hence, for the j^{th} iteration one may use

$$\hat{\sigma}_{k,j}^2 = \frac{\hat{\Omega}_k}{r_k} \qquad \text{with} \qquad r_k = N_k - \frac{\sigma_0^2}{\hat{\sigma}_{k,j-1}^2}\mathrm{tr}\left(\mathbf{N}_k\mathbf{N}^{-1}\right) \quad . \tag{3.87}$$

The initial stochastic model (Eq. 3.80) requires a priori information about the variance component $\hat{\sigma}_k^2$. In this work, the variance components are set to $\hat{\sigma}_k^2 = \sigma_0^2$ for the first iteration $j = 1$.

After computing the variance components, the normal equations are weighted with

$$\mathbf{N}_k = \frac{\sigma_0^2}{\hat{\sigma}_k^2}\mathbf{N}_k \quad , \qquad \boldsymbol{b}_k = \frac{\sigma_0^2}{\hat{\sigma}_k^2}\boldsymbol{b}_k \qquad \text{and} \qquad \Lambda_k = \frac{\sigma_0^2}{\hat{\sigma}_k^2}\Lambda_k \quad . \tag{3.88}$$

The solution for each iteration may be computed by using the weighted NEQs, following the sequential LSQA given by Eq. 3.56 and Eq. 3.57.

In this straight forward approach, which is used in this thesis, the computation of the matrix product $\mathbf{N}_k\mathbf{N}^{-1}$ inside the trace operator is most costly. However, exploiting the structure of the normal equation systems and that only diagonal elements contribute to the trace, it can be re-arranged into a dot product of two vectors with the dimension $M \times 1$ which has to be carried out M times. Faster methods utilise a stochastic trace estimation, for example Koch and Kusche [2002] designed a stochastic trace estimator based on Monte-Carlo experiments.

3.4 Fourier transform and analysis

This section introduces time series representation and analysis using Fourier series. Detailed derivations about the conclusions may be found in e.g., Buttkus [1991].
A signal $x(t)$ with a fundamental period of T may be written as a Fourier series in a sum of sinoids with respect to T as

$$x\left(t\right) = \frac{a_0}{2} + \sum_{i=1}^{I=\infty}\left(a_i\cos(i\omega t) + b_i\sin(i\omega t)\right) \qquad \text{with} \qquad \omega = \frac{2\pi}{T} \quad . \tag{3.89}$$

Computing the coefficients a_i and b_i from Eq. 3.89 based on a discrete realisation of $x(t)$ in $x\,[t]$ is called Discrete Fourier Transform (DFT). Taking a signal of length T, which also defines the fundamental period, the maximum degree of development is given by

$$I = \begin{cases} \frac{T}{2}, & \text{if } T \text{ even} \\ \frac{T-1}{2}, & \text{if } T \text{ odd} \end{cases} \quad . \tag{3.90}$$

As a consequence of the Nyquist–Shannon sampling theorem [Shannon, 1948] the highest frequency f_N that can be resolved by the Fourier transform reads as

$$f_N = \frac{I\omega}{2\pi} \quad . \tag{3.91}$$

Efficient methods to solve for a_i and b_i exist for evenly spaced data, like the Fast Fourier Transform (FFT), which is well suited for computers due to Cooley and Tukey [1965]. In case of non-equidistant time series methods like the LSQA (see Sect. 3.2) or least-squares spectral analysis methods like the Lomb-Scargle periodogram (or Gauss-Vaníček spectral analysis, cf. Lomb, 1976) may be utilised.
The DFT brings the signal $x\,[t]$ into the frequency domain $X\,[\omega]$ by applying the Fourier transform operator $\mathcal{F}(\cdot)$ onto the signal

$$X\,[\omega] = \mathcal{F}\left(x\,[t]\right) \quad . \tag{3.92}$$

The DFT consists of a transformation pair, and consequently, compiling the series from given Fourier coefficients is done by applying the inverse discrete Fourier transform

$$x\,[t] = \mathcal{F}^{-1}\left(X\,[\omega]\right) \quad . \tag{3.93}$$

Computing the squared sum of the estimated Fourier coefficients and referencing them to the sampling frequency f_S of the signal by forming

$$P_i^{\mathrm{PSD}} = \frac{1}{f_S}(a_i^2 + b_i^2) \qquad \text{and} \tag{3.94a}$$

$$A_i^{\mathrm{ASD}} = \sqrt{P_i^{\mathrm{PSD}}} \tag{3.94b}$$

results in the discrete Power Spectral Density (PSD) and Amplitude Spectral Density (ASD), respectively, which describes how the power of the signal is distributed in the frequency domain. The representation in ASDs retains the units of the signal per square root of the frequency, e.g., for a signal in metre, the ASD reads with $\mathrm{m}/\sqrt{\mathrm{Hz}}$.

3.4.1 Auto- and cross-covariance

The auto-covariance $c_{xx}\,(t_0, t_1)$ characterises the covariance between two elements at time t_0 and t_1 of a stochastic process. It may be defined by Eq. 3.1 where $\boldsymbol{x}$ is the realisation of a stochastic process. For a discrete signal of finite length following a stationary process, i.e., the central moments do not depend on the time [Etten, 2005], and a mean of $\mu_x = \mu(\boldsymbol{x}) = 0$, the auto-covariance only depends on the time lag Δt and can be described by a single function, which may be estimated as

$$\hat{C}_{xx}(\Delta t_k) = \frac{1}{N}\sum_{n=1}^{N-k} x_{n+k}x_n \qquad \text{with} \qquad k \in \{0, ..., M\} \leq N-1 \quad , \tag{3.95}$$

where Δt_k denotes the k^{th} lag or shift of the signal with respect to its original appearance and M is the maximum shift. It is an even function which exists for a finite length N. The scaling $1/N$ gives a biased estimate of the auto-covariance of x, whereas $1/(N-k)$ is unbiased [Percival, 1993]. The latter is dependent on the ratio of the length of the data N and the number of lags M, which means for large M the auto-correlation results in large values because the denominator converges towards $N - M \to 1$. For $N \to \infty$ the covariances of both estimates converge towards zero. The shift of $\Delta t = 0$ reduces Eq. 3.95 to the estimated variance of $\boldsymbol{x}$

$$\hat{C}_{xx}(0) = \frac{1}{N} \sum_{n=1}^{N-k} x_n^2 = \hat{\sigma}_x^2 \ . \tag{3.96}$$

The estimated normalised auto-covariance function of $\boldsymbol{x}$

$$\hat{R}_{xx}(\Delta t_k) = \frac{\hat{C}_{xx}(\Delta t_k)}{\hat{\sigma}_x^2} \ , \tag{3.97}$$

shows the correlation of the signal with itself, i.e., the correlation of each variable in $\boldsymbol{x}$ with the variable Δt lags apart. If no auto-correlation exist in $\boldsymbol{x}$ only $\hat{R}_{xx}(0) \neq 0$.

The cross-covariance between two signals $\boldsymbol{x}$ and $\boldsymbol{y}$ may be computed by

$$\mathbf{C}_{xy} = \mathbb{E}\left(\left[\boldsymbol{x} - \mu_x \right] \left[\boldsymbol{y} - \mu_y \right]^{\mathrm{T}} \right) \ . \tag{3.98}$$

As it can be seen, the auto-covariance is a special case of the cross-covariance for $\boldsymbol{y} = \boldsymbol{x}$. For a stationary process, the dependency on t_0 and t_1 vanishes for the lag $\Delta t_k = t_1 - t_0$ and the cross-covariance may then be estimated for each lag in negative and positive direction with

$$\begin{aligned} \hat{C}_{xy}(\Delta t_k) &= \frac{1}{N} \sum_{n=1}^{N-k} x_{n+k} y_n \qquad \text{with} \qquad k \in \{0, ..., M\} \leq N-1 \qquad \text{and} \\ \hat{C}_{xy}(\Delta t_{-k}) &= \frac{1}{N} \sum_{n=1}^{N-k} x_n y_{n+k} \qquad \text{with} \qquad k \in \{0, ..., M\} \leq N-1 \ , \end{aligned} \tag{3.99}$$

where

$$\hat{C}_{xy}(\Delta t_k) = \hat{C}_{yx}(\Delta t_{-k}) \ . \tag{3.100}$$

The factor $1/N$ again yields a biased estimate, whereas $1/(N-k)$ is unbiased. In analogy to Eq. 3.97, the cross-covariance may be normalised to $\hat{R}_{xy}$, which is a measure for the similarity between $\boldsymbol{x}$ and $\boldsymbol{y}$, showing at which lag the signals resemble each other best, being the same with $\hat{R}_{xy}(\Delta t_k) = 1$, not correlated with $\hat{R}_{xy}(\Delta t_k) = 0$ and anti-correlated with $\hat{R}_{xy}(\Delta t_k) = -1$.

3.4.2 Relation between PSD and auto-covariance

The PSD and the auto-covariance function with a mean of $\mu(\boldsymbol{x}) = 0$ of a stationary process are related by the Wiener–Khinchin theorem [Wiener, 1930, Khinchin, 1934], which states that the PSD of a function is the Fourier transform of the function's auto-covariance for

the lag Δt. This process may be reversed because the PSD and the auto-covariance form a transformation pair, so the auto-covariance may be derived from a given PSD. Using the inverse Fourier transform operator (Eq. 3.93) the relation may be written as

$$R_{xx}[\Delta t] = \mathcal{F}^{-1}\left(P_{xx}\left[\omega\right]\right) \quad . \tag{3.101}$$

3.5 Spherical harmonics

Spherical harmonics are a set of functions formed by harmonic and homogeneous polynomials defined on the surface of a sphere. The spherical harmonics are derived by solving Laplace' equation in spherical coordinates [see e.g., Heiskanen and Moritz, 1967]

$$\Delta f(r,\lambda,\vartheta) = \nabla^2 f = \operatorname{div}\left(\operatorname{grad}\left(f\right)\right) = 0 \quad , \tag{3.102}$$

with r denoting the radial distance, λ the longitude and ϑ the co-latitude The solution for the spherical harmonics reads as

$$C_{nm}(\lambda,\vartheta) = P_{nm}(\cos\vartheta)\cos(m\lambda) \qquad \text{and} \qquad S_{nm}(\lambda,\vartheta) = P_{nm}(\cos\vartheta)\sin(m\lambda) \quad , \tag{3.103}$$

with P_{nm} denoting the (normalised) associated Legendre functions of degree n and order m. A function f which is harmonic outside a sphere [Heiskanen and Moritz, 1967] may be expanded into a converging series of spherical harmonics by

$$f(r,\lambda,\vartheta) = \sum_{n=0}^{\infty} \frac{1}{r^{n+1}} \sum_{m=0}^{n} \left(c_{nm}C_{nm} + s_{nm}S_{nm}\right) \quad . \tag{3.104}$$

This is used in the representation of the Earth's gravity field as observed from satellites (see Sect. 4.6.1). The spherical harmonic coefficients c_{nm} and s_{nm} fully describe the function f in spectral domain. Three important sets of spherical harmonics coefficients arise, namely

- the zonal spherical harmonic coefficients with $m = 0$,
- the sectorial coefficients with $n = m$, and
- the tesseral harmonics for all other degrees and orders.

For a given degree n, there are in total $(n+1)^2$ spherical harmonic coefficients, $n+1$ zonals, $2n$ sectorials, and $n^2 - n$ tesseral harmonics.

3.5.1 Figurative representation of spherical harmonic coefficients

Synthesis on a regular grid

At a regular grid of longitudes and co-latitudes the spherical harmonic series can be efficiently evaluated for a given set of spherical harmonic coefficients c_{nm} and s_{nm} by exploiting efficient computation of sine and cosine values. Still, the full series up to the given truncation has to be synthesised for each grid point, thus, depending on the degree of the evaluation and the resolution of the grid, this might be a rather costly operation.

Triangle of coefficients

This representation structures the spherical harmonic coefficients graphically for each degree and order. A triangle of coefficients may be set up for the spherical harmonic coefficients, their formal errors or the coefficient-wise difference between two sets of spherical harmonic coefficients.

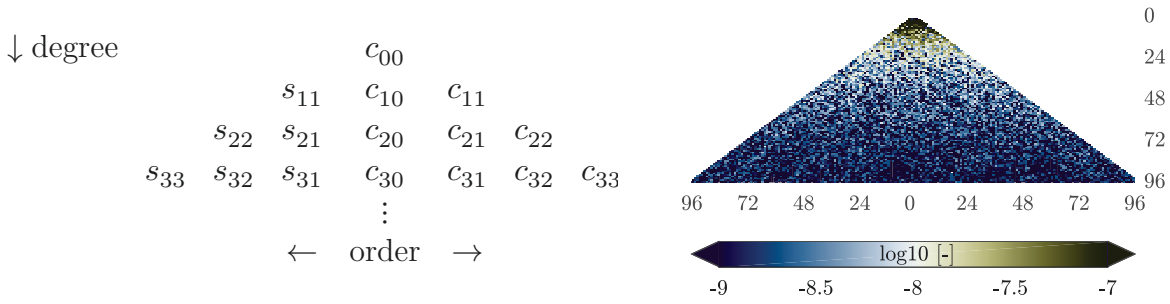

Degree amplitudes

The degree amplitudes represent the root of the squared and degree-wise added spherical harmonic coefficients. Thus, it is a representation in the spectral domain. They are formed by summing the squares of each order (Eq. 3.105a). The same computation may also be applied to the formal error of spherical harmonic coefficients (Eq. 3.105b). In order to assess two sets of spherical harmonic coefficients, difference degree amplitudes may be computed with Eq. 3.105c. An example for the spectral representation of the spherical harmonic coefficients is depicted in Fig. 3.1.

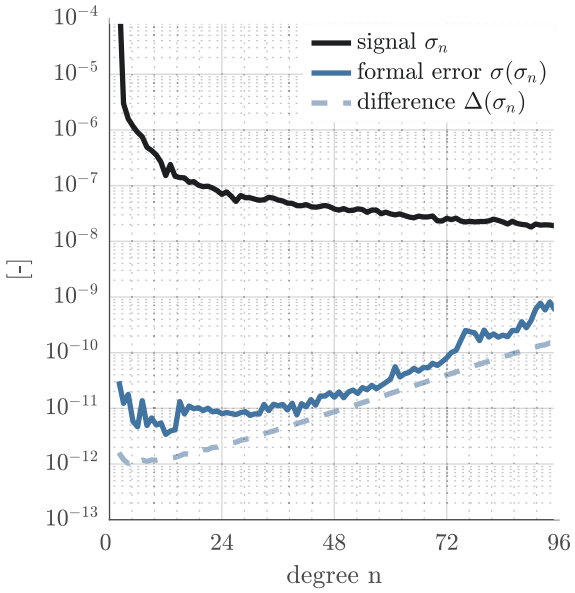

$$\sigma_n = \sqrt{\sum_{m=0}^{n} \left(c_{nm}^2 + s_{nm}^2\right)} \tag{3.105a}$$

$$\sigma\left(\sigma_n\right) = \sqrt{\sum_{m=0}^{n} \left(\sigma_{c_{nm}}^2 + \sigma_{s_{nm}}^2\right)} \tag{3.105b}$$

$$\Delta\left(\sigma_n\right) = \sqrt{\sum_{m=0}^{n} \left(\Delta c_{nm}^2 + \Delta s_{nm}^2\right)} \tag{3.105c}$$

with $\Delta_{c_{nm}} = c_{nm}^1 - c_{nm}^2$
$\Delta s_{nm} = s_{nm}^1 - s_{nm}^2$

Figure 3.1: Degree amplitudes for a signal (spherical harmonic coefficients), formal errors of the signal's degree amplitudes and difference degree amplitudes for two gravity fields.

Chapter 4

Orbit and Gravity Field Determination

This chapter outlines the concepts how the different measurements collected by the satellites (Chapter 2) and the provided mathematical tools (Chapter 3) are connected to compute orbit and gravity field models. It starts with the physical background of orbital motion and its representation, continues with the mathematical description of the satellite observations and concludes with the a priori information incorporated into the estimation process. The elementary ideas of this chapter are discussed in detail by Beutler [2005] and Beutler et al. [2010b].

4.1 Modelling satellite motion

The motion of the Centre of Mass (CoM) of a satellite around the Earth is the result of the sum of all forces $\boldsymbol{F}$ acting on the satellite. According to Newton's second law of motion the total force acting on a satellite with mass m results in an acceleration $\ddot{\boldsymbol{r}}$, pointing in the same direction as the resulting force vector

$$\sum_i \boldsymbol{F}_i = m\ddot{\boldsymbol{r}} \ . \tag{4.1}$$

The motion follows a trajectory which is called satellite orbit. First and foremost, the orbit follows Newton's law of gravity and may be described in good approximation by Kepler's laws of planetary motion for the two bodies assuming point masses.

The equation of motion is a second-order differential equation

$$\ddot{\boldsymbol{r}}(t) = \boldsymbol{f}(t, \boldsymbol{r}, \dot{\boldsymbol{r}}) \tag{4.2}$$

relating the acceleration $\ddot{\boldsymbol{r}}$ of an object at time t with its position $\boldsymbol{r}$ and velocity $\dot{\boldsymbol{r}}$, where the acceleration may be described by the function $\boldsymbol{f}$. Using Newton's law of gravity and Newton's second law of motion to solve this equation yields for the two-body problem a set of six distinct initial elements to fully describe the orbit on as conic section with the Earth in the focus at any time t

$$\begin{aligned} \boldsymbol{r}(t_0) &= \boldsymbol{r}(t_0|a, e, i, \Omega, \omega, u_0) \qquad \text{and} \\ \dot{\boldsymbol{r}}(t_0) &= \dot{\boldsymbol{r}}(t_0|a, e, i, \Omega, \omega, u_0) \ , \end{aligned} \tag{4.3}$$

with the equation of motion being

$$\ddot{\boldsymbol{r}}(t) = -\frac{GM\boldsymbol{r}}{r^3} \ , \tag{4.4}$$

where GM denotes the gravity constant times the mass of the Earth and $\boldsymbol{r}$ is the geocentric position of the satellite in (quasi-)inertial system. The equation of motion of the two-body problem (Eq. 4.4) is a function of solely the position vector $\boldsymbol{r}$. The initial elements of the orbit may be an initial position $\boldsymbol{r}(t_0)$ and velocity $\dot{\boldsymbol{r}}(t_0)$ or Keplerian orbital elements (Fig. 4.1), e.g., for an elliptical motion:

- The semi-major axis a, characterising the size of the orbit's ellipse,
- the numerical eccentricity e, characterising the shape of the ellipse,
- the inclination i as the angle between the intersection of the orbital plane and the equatorial plane, the first parameter providing the orientation of the orbital plane in space,
- the right-ascension of the ascending node Ω as the angle between the direction to the vernal equinox (x-axis) and the ascending node, thus, orienting of the orbital plane in space,
- the argument of perigee ω, which is the angle between the ascending node and the point closest to the Earth (perigee Π), thus orienting the ellipse in the orbital plane, and
- the argument of latitude u_0 which locates the satellite on the ellipse at time t_0.

Keplerian elements are constant for a two-body problem (Earth and satellite). The Keplerian orbit following the two-body problem when switching off the perturbations in the general problem at time t is called osculating orbit with the osculating elements at t_0. The coordinate system is formed by an (quasi-)inertial system originating in the centre of mass of the Earth, with the x-axis pointing to the direction of the vernal equinox (the intersection between the equatorial and ecliptic plane), the z-axis is following the Earth's rotational axis to the North and the y-axis completing an orthogonal right-handed system. One realisation of this inertial system is the J2000 reference frame [McCarthy, 1996] as CRF, which is also adopted in the BSW [Dach et al., 2009].

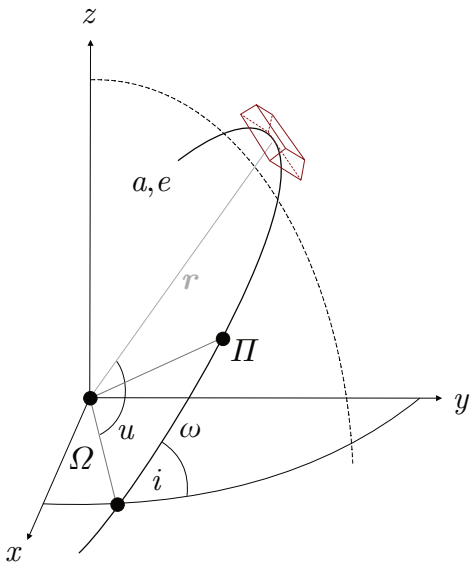

Figure 4.1: Definition of the osculating orbital elements $a, e, i, \Omega, \omega, u(t_0)$ and the position vector $\boldsymbol{r}(t)$.

Extending the formulation in Eq. 4.4 with additional accelerations acting on the satellite, e.g., further dynamic parameters describing the orbit or accelerations caused by irregularities in of the Earth's potential field due to the mass distribution or tidal effects, or

non-conservative forces like air drag perturbing the satellite's motion, leads to the general formulation of the primary equations

$$\ddot{\boldsymbol{r}}(t) = -\frac{GM\boldsymbol{r}}{r^3} + \boldsymbol{f}(t, \boldsymbol{r}, \dot{\boldsymbol{r}}, d_1, ..., d_K) = \boldsymbol{f}^{\text{total}} \quad , \tag{4.5}$$

where $\boldsymbol{f}^{\text{total}}$ is the total acceleration the satellite experiences. $\{d_1, ..., d_K\}$ denote K parameters describing the additional dynamics acting on the satellite, deviating the orbit from the Keplerian two-body solution. The full model for the equation of motion then consists of $6+K = M$ parameters in a vector $\boldsymbol{p}$. Integrating the equation of motion for a specific time interval yields the position $\boldsymbol{r}$ and velocity vector $\dot{\boldsymbol{r}}$. The CMA uses a collocation method for efficient numerical integration [Beutler, 2005].

Determining the orbital elements from observations of the satellite's trajectory is the fundamental method for gravity field recovery, where not only the orbit needs to be improved but also parts of the perturbing forces, i.e., the gravity field. Usually, the perturbing forces are known to a certain extent by a priori models and only improvements to a subset of the $\boldsymbol{p}$ parameters are sought-after, e.g., improvements to an a priori gravity field. Thus, one may assume that an a priori orbit $\boldsymbol{r}_0$ is always given from the a priori dynamic models and a numerical integration of the primary equations (Eq. 4.5), and the improvements refer to this orbit in the form of a truncated Taylor series (see Eq. 3.7) with

$$\boldsymbol{r}(t) = \boldsymbol{r}_0(t) + \sum_{i=1}^{6+K} \frac{\partial \boldsymbol{r}_0(t)}{\partial p_i}(p_i - p_{0,i}) \quad , \tag{4.6}$$

where p_i denotes the parameters, either the orbital elements or the set of perturbing accelerations $\{d_1, ..., d_K\}$, and $p_{0,i}$ are the respective a priori parameters serving as Taylor point. Setting

$$\boldsymbol{z}_{p_i} := \frac{\partial \boldsymbol{r}_0(t)}{\partial p_i} \quad , \tag{4.7}$$

$\boldsymbol{z}_{p_i}$ is the partial ascribed to the change of the orbit with respect to a change in the parameter p_i ($\boldsymbol{z}_{p_i}(p_i - p_{0,i})$). Since the initial orbit is part of the unknown parameters, an initial value problem may be formulated. Solving the latter is done by integrating the variational equations, which read for each parameter p_i as a linear differential equation system of second order

$$\ddot{\boldsymbol{z}}_{p_i} := \frac{\partial \boldsymbol{f}^{\text{total}}}{\partial \boldsymbol{r}_0}\frac{\partial \boldsymbol{r}_0}{\partial p_i} + \frac{\partial \boldsymbol{f}^{\text{total}}}{\partial \dot{\boldsymbol{r}}_0}\frac{\partial \dot{\boldsymbol{r}}_0}{\partial p_i} + \frac{\partial \boldsymbol{f}}{\partial p_i} \quad . \tag{4.8}$$

In the CMA the solution of the primary equation and the variational equations connected to the six initial conditions is separated from the variational equations for all other parameters, which are solve by numerical quadrature [Beutler et al., 2010b].

The formulation in Eq. 4.6 may be transferred to a LSQA process (Eq. 3.34) by numerical integration of the primary equations to solve for $\boldsymbol{r}_0(t)$ and of the variational equations to solve for $\boldsymbol{z}_{p_i}$. The link between the observations $\boldsymbol{\ell}$ (e.g., the satellite's position, code or

carrier-phase observations, or the inter-satellite range-rates) and the vector $\boldsymbol{r}$ may be established by a function $\boldsymbol{g}(\cdot)$, which only depends on the position vector $\boldsymbol{r}$ for the observations used in this work, as

$$\boldsymbol{\ell} = \boldsymbol{g}\left(\boldsymbol{r}\left(t\right)\right) \quad , \tag{4.9}$$

which leads together with Eq. 4.6 and linearisation to

$$\begin{aligned} \boldsymbol{\ell} &= \boldsymbol{g}\left(\boldsymbol{r}_0\left(t\right) + \sum_{i=1}^{6+K} \frac{\partial \boldsymbol{r}_0(t)}{\partial p_i}(p_i - p_{0,i})\right) \\ &= \boldsymbol{g}\left(\boldsymbol{r}_0\left(t\right)\right) + \frac{\partial \boldsymbol{g}\left(\boldsymbol{r}_0\left(t\right)\right)}{\partial \boldsymbol{r}_0(t)} \sum_{i=1}^{6+K} \frac{\partial \boldsymbol{r}_0(t)}{\partial p_i}(p_i - p_{0,i}) \quad , \end{aligned} \tag{4.10}$$

and simplifies to

$$\begin{aligned} \boldsymbol{\ell} &= \boldsymbol{\ell}_0 + \left[\frac{\partial \boldsymbol{\ell}}{\partial \boldsymbol{r}_0}\right]\left[\frac{\partial \boldsymbol{r}_0}{\partial \boldsymbol{p}}\right]\delta\boldsymbol{p} \\ \underbrace{\boldsymbol{\ell} - \boldsymbol{\ell}_0}_{\delta\boldsymbol{\ell}} &= \underbrace{\left[\frac{\partial \boldsymbol{\ell}}{\partial \boldsymbol{r}_0}\frac{\partial \boldsymbol{r}_0}{\partial \boldsymbol{x}}\right]}_{\mathbf{A}} \delta\boldsymbol{x} \quad . \end{aligned} \tag{4.11}$$

Expanding the partial derivatives to sums yields the scheme of the design-matrix as

$$\mathbf{A} = \begin{bmatrix} \sum_{u=1}^{3} \frac{\partial l_1}{\partial r_{0,u}} \frac{\partial r_{0,u}}{\partial p_1} & \cdots & \sum_{u=1}^{3} \frac{\partial l_1}{\partial r_{0,u}} \frac{\partial r_{0,u}}{\partial p_{6+K}} \\ \vdots & \ddots & \vdots \\ \sum_{u=1}^{3} \frac{\partial l_N}{\partial r_{0,u}} \frac{\partial r_{0,u}}{\partial p_1} & \cdots & \sum_{u=1}^{3} \frac{\partial l_N}{\partial r_{0,u}} \frac{\partial r_{0,u}}{\partial p_{6+K}} \end{bmatrix}_{(N\times[6+K])=(N\times M)} \tag{4.12}$$

for N observations in $\boldsymbol{\ell}$. Thus, the process might be interpreted as a special case of a series of LSQAs (see Sect. 3.2.5, Eq. 3.67 and Eq. 3.68), where the first design-matrix is predefined by the primary equation and variational equations and the intermediate observations are given by the a priori orbit. Or vice versa, one adjustment relates the observations to the a priori orbit and the other brings the conditions of the initial value problem of the variational equations into the system of equations.

4.2 Orbit representations

Three important representations of orbits are used in the context of this thesis, two referring to the equation of motion and the other one being of a geometric nature. For the sake of generalisation, the left-hand side of the orbit representations refer to the phase centre position of a satellite's antenna as it would be seen by e.g., GPS observations instead of the satellite's CoM.

4.2.1 Dynamic orbits

A dynamic orbit is a particular solution of the equation of motion (Eq. 4.5), where the satellite's state is fully described by the orbital elements $a, e, i, \Omega, \omega, u_0$ at time t_0 and the full dynamic force modelling $\boldsymbol{f}(d_1, ..., d_K)$

$$\boldsymbol{r}^{\mathrm{ant}}(t) = \boldsymbol{r}_0(t|a, e, i, \Omega, \omega, u_0, d_1, ..., d_K) + \delta\boldsymbol{r}^{\mathrm{ant}}(t) \quad . \tag{4.13}$$

The position of the antenna phase centre $\delta\boldsymbol{r}^{\text{ant}}(t)$ is usually introduced as known from external sources. A dynamic orbit is fully dependent on the initial orbital elements and the underlying force models. Any systematic deficiency directly maps into the orbit with an error increasing with the arc length as the equation of motion is integrated twice to obtain the state.

4.2.2 Reduced-dynamic orbits

A special set of additional parameters to form reduced-dynamic orbits in the CMA are the pseudo-stochastic orbit parameters. The set of additional parameters is extended by L further quantities

$$\boldsymbol{r}^{\text{ant}}(t) = \boldsymbol{r}_0(t|a, e, i, \Omega, \omega, u_0, d_1, ..., d_K, s_1, ..., s_L) + \delta\boldsymbol{r}^{\text{ant}}(t) \quad , \tag{4.14}$$

where $\{s_1, ..., s_L\}$ may be instantaneous velocity changes (pulses), Piecewise-Constant Accelerations (PCAs) set up for regular intervals or further empirical parameters, which are co-estimated together with the other parameters describing the orbit [see Jäggi, 2007]. Its name *pseudo-stochastic* stems from the application of compensating for deficiencies in the force field by providing adequate a priori information about the stochastic behaviour using constraints (see Sect. 3.2.2). Reduced-dynamic orbits follow the observations much closer than a dynamic orbit at the cost of additional parameters to be adjusted.
The partial derivatives in the variational equations for the pseudo-stochastic parameters may be set up as linear combinations of the partial derivatives with respect to the initial osculating elements and, depending on the type of pseudo-stochastic parameters, a few additional partial derivatives [cf. Jäggi, 2007]. Consequently, the computational effort for the solution of variational equations including pseudo-stochastic parameters is limited. However, estimating a full set of pseudo-stochastic parameters together with gravity field coefficients is a considerable effort.
Reduced-dynamic orbits might be seen as a trade-off between kinematic orbit positions, where position parameters are assigned to each epoch, and a dynamic orbit entirely following the underlying dynamic model. The use of (constrained) pseudo-stochastic orbit parameters is typical for the CMA [see e.g., Beutler et al., 2010a, Meyer et al., 2016]. For GRACE Follow-On orbit and gravity field recovery a sampling of 15 min is adopted in most cases.

4.2.3 Kinematic positions

Kinematic Positions (KIN) represent a discrete ephemeris of the object's trajectory. They may be computed for any moving object, not being restricted by any underlying force model. For an Earth-orbiting satellite using GNSS hl-SST they are usually given in the TRF, and therefore, may be written as

$$\boldsymbol{r}^{\text{ant}}(t_i) = \mathbf{R}^{\text{CRF}}_{\text{TRF}}\left(\boldsymbol{r}_{\text{TRF}}(t_i) + \delta\boldsymbol{r}^{\text{ant}}_{\text{TRF}}(t_i)\right) \quad . \tag{4.15}$$

The satellite's state vector $\boldsymbol{r}$ at epoch t_i is composed of a transformation from the TRF to the inertial reference frame $\mathbf{R}^{\text{CRF}}_{\text{TRF}}$ of the Earth-fixed position of the satellite's CoM $\boldsymbol{r}_{\text{TRF}}$ and the antenna phase offset $\boldsymbol{r}^{\text{ant}}_{\text{TRF}}$, also expressed in the TRF. A sufficient collection of the kinematic positions may be named kinematic orbit.

4.3 High-low SST: Kinematic point positioning

In the High-Low Satellite-to-Satellite Tracking (hl-SST) mode the low flying satellite is equipped with a GNSS receiver which records navigation signals form the GNSS. The code and phase measurements of the code's carrier on each frequencies are used to perform a kinematic Precise Point Positioning (PPP) [Zumberge et al., 1997], which is a PPP technique, a positioning method based on a single moving receiver. The procedure of kinematic PPP follows Švehla and Rothacher [2005]. The kinematic positions are a discrete representation of the satellite's position vector $\boldsymbol{r}$ at epoch t. These three dimensional coordinates are the main sought-after parameters of the kinematic PPP. Additionally, receiver clock corrections are estimated and ambiguity parameters need to be adjusted when using carrier phase measurements.
The carrier phase observation equation for a receiver i and a GNSS satellite k reads as

$$L_i^k = \rho_i^k - c\Delta t^k + c\Delta t_i - \Delta\rho_{i,\text{iono}}^k + \lambda\left(\varphi_i - \varphi^k + N_i^k\right) + e_i^k \quad , \tag{4.16}$$

where L_i^k is the carrier phase observation, expressed in units of length, hence, depending on the wavelength λ of the carrier wave and c denotes the speed of light. The formulation takes into account the offset of the receiver clock with respect to the GNSS' system time (receiver clock correction Δt_i), the clock correction Δt^k of the transmitter with respect to the GNSS' system time, and a correction due to phase advance of the electro-magnetic wave propagating through the ionosphere. The latter may be largely mitigated by forming the ionosphere-free linear combination when observing the carrier phase on two frequencies. Furthermore, there is the phase shift between the carrier phase of the transmitted signal φ^k at time t_k and the reference carrier phase φ_i generated by the receiver at time t_i and an integer number of full cycles of the carrier wave between transmitter and receiver N_i^k. This observation is linked to the coordinates of the receiver by the slant range ρ_i^k between transmitter and receiver at signal transmission and signal reception time, respectively, which is the Euclidean distance

$$\rho_i^k = |\boldsymbol{r}_i(t) - \boldsymbol{r}^k(t-\tau)| \quad , \tag{4.17}$$

where τ is the signal's travel time between the transmitter's and the receiver's antenna phase centre. When observing on two frequencies and using external products to describe the transmitter clock offset, only the coordinates of the receiver, the receiver clock error and the phase shift including the integer ambiguities remain as unknown. Directly taking the carrier phase as observation has the consequence that the elements in $\lambda\left(\varphi_i - \varphi^k + N_i^k\right)$ cannot be separated and the ambiguities have to be estimated as a float-bias term. Only when introducing high-quality bias products [e.g., Schaer et al., 2021] the ambiguities may be resolved to an integer. The ambiguity is constant over time, however, it changes its value as soon the tracking of the signal is lost (cycle slip) and the tracking of L_i^k needs to be resumed. Thus, several ambiguities have to be determined per day. The cartesian coordinates of the receiver are estimated for each observation epoch. Additionally, the receiver clock offset needs to be adjusted for each epoch as well. In total, there are four unknown parameters per epoch and ambiguities set up as soon as a cycle slip occurs, hence, the epochs are not independent from each other but the ambiguities connect several of them. Even though loosely connected, they are a discrete sampling of the satellites trajectory

expressed in terms of positions, only indirectly dependent on force models through the GNSS satellite orbits, originating from geometrical relations only. Note that the kinematic positions as formulated in Eq. 4.15 already refer to the CoM of the satellite.

The application of kinematic positions as orbit representation may be motivated by its use in the orbit and gravity field determination process. The kinematic positions $\hat{\boldsymbol{x}}_{\mathrm{KIN}}$ may be derived from the carrier phase observations by

$$\begin{aligned}\hat{\boldsymbol{x}}_{\mathrm{KIN}} &= (\mathbf{A}^{\mathrm{T}}\mathbf{P}_{\mathrm{ph}}\mathbf{A})^{-1}\mathbf{A}^{\mathrm{T}}\mathbf{P}_{\mathrm{ph}}\boldsymbol{\ell}_{\mathrm{ph}} \qquad \text{with} \qquad \mathbf{A} := \frac{\partial \boldsymbol{\ell}_{\mathrm{ph}}}{\partial \boldsymbol{x}_{\mathrm{KIN}}} \\ &= \mathbf{N}_{\mathrm{ph}}^{-1}\mathbf{A}^{\mathrm{T}}\mathbf{P}_{\mathrm{ph}}\boldsymbol{\ell}_{\mathrm{ph}} \ .\end{aligned} \tag{4.18}$$

Following Eq. 3.25 the cofactor matrix of the kinematic positions reads as $\mathbf{Q}_{\mathrm{KIN}} := \mathbf{N}_{\mathrm{ph}}^{-1}$. Note here that $\mathbf{Q}_{\mathrm{KIN}}$ refers to the variance of unit weight σ_0^2 of the original carrier phase observations. In a second step the kinematic positions are introduced as pseudo-observations (i.e., intermediate observations, see Sect. 3.2.5) $\boldsymbol{\ell}_{\mathrm{KIN}} := \hat{\boldsymbol{x}}_{\mathrm{KIN}}$ in another LSQA to estimate for orbit and gravity field parameters $\boldsymbol{p}$

$$\begin{aligned}\hat{\boldsymbol{p}} &= (\mathbf{B}^{\mathrm{T}}\mathbf{Q}_{\mathrm{KIN}}^{-1}\mathbf{B})^{-1}\mathbf{B}^{\mathrm{T}}\mathbf{Q}_{\mathrm{KIN}}^{-1}\boldsymbol{\ell}_{\mathrm{KIN}} \qquad \text{with} \qquad \mathbf{B} := \frac{\partial \boldsymbol{\ell}_{\mathrm{KIN}}}{\partial \boldsymbol{p}} \\ &= \mathbf{N}_{\mathrm{p}}^{-1}\mathbf{B}^{\mathrm{T}}\mathbf{Q}_{\mathrm{KIN}}^{-1}\hat{\boldsymbol{x}}_{\mathrm{KIN}} \ .\end{aligned} \tag{4.19}$$

Following the derivation given in Sect. 3.2.5, the solution for the orbit and gravity field parameters may be expressed as connected to the original carrier phase observations $\boldsymbol{\ell}_{\mathrm{ph}}$ by

$$\hat{\boldsymbol{p}} = (\mathbf{M}^{\mathrm{T}}\mathbf{P}_{\mathrm{ph}}\mathbf{M})^{-1}\mathbf{M}^{\mathrm{T}}\mathbf{P}_{\mathrm{ph}}\boldsymbol{\ell}_{\mathrm{ph}} \qquad \text{with} \qquad \mathbf{M} := \mathbf{AB} \ , \tag{4.20}$$

The new design-matrix $\mathbf{M}$ contains the partial derivations of the phase observations to the orbit parameters applying the chain rule

$$\begin{aligned}\mathbf{M} &= \mathbf{AB} \\ &= \left[\frac{\partial \boldsymbol{\ell}_{\mathrm{ph}}}{\partial \boldsymbol{x}_{\mathrm{KIN}}}\right]\left[\frac{\partial \boldsymbol{x}_{\mathrm{KIN}}}{\partial \boldsymbol{p}}\right] = \left[\frac{\partial \boldsymbol{\ell}_{\mathrm{ph}}}{\partial \boldsymbol{x}_{\mathrm{KIN}}}\frac{\partial \boldsymbol{x}_{\mathrm{KIN}}}{\partial \boldsymbol{p}}\right] \ ,\end{aligned} \tag{4.21}$$

which gives a similar structure to Eq. 4.11. For U estimated kinematic positions and M sought-after orbit parameters with N original carrier-phase observations $\mathbf{M}$ reads as

$$\mathbf{M} = \begin{bmatrix} \sum_{u=1}^{U}\left(\frac{\partial l_1^{\mathrm{ph}}}{\partial x_u^{\mathrm{KIN}}}\frac{\partial x_u^{\mathrm{KIN}}}{\partial p_1}\right) & \cdots & \sum_{u=1}^{U}\left(\frac{\partial l_1^{\mathrm{ph}}}{\partial x_u^{\mathrm{KIN}}}\frac{\partial x_u^{\mathrm{KIN}}}{\partial p_{\mathrm{M}}}\right) \\ \vdots & \ddots & \vdots \\ \sum_{u=1}^{U}\left(\frac{\partial l_N^{\mathrm{ph}}}{\partial x_u^{\mathrm{KIN}}}\frac{\partial x_u^{\mathrm{KIN}}}{\partial p_1}\right) & \cdots & \sum_{u=1}^{U}\left(\frac{\partial l_N^{\mathrm{ph}}}{\partial x_u^{\mathrm{KIN}}}\frac{\partial x_u^{\mathrm{KIN}}}{\partial p_{\mathrm{M}}}\right) \end{bmatrix}_{(N\times M)} \ . \tag{4.22}$$

The derivatives in $\mathbf{A}$ express the change of the phase observation with respect to a change in the kinematic positions. This is, however, zero unless the kinematic position and phase observations refer to the same epoch. Consequently, only three terms in the sums in Eq. 4.22 are unequal to zero for each line in $\mathbf{M}$. Comparing this result to Eq. 4.12 shows that the result may be interpreted that for the computation of the orbit and gravity field parameters

only a different a priori orbit was eventually used, namely the kinematic orbit positions instead of the numerically integrated a priori orbit $\boldsymbol{r}_0$.

When using kinematic positions as pseudo-observations for the orbit and gravity field recovery, the set of unknown parameters is split into two groups, local (orbit) parameters $\boldsymbol{o}$ which only refer to one arc of the satellite and global parameters $\boldsymbol{g}$ which are valid for several arcs (e.g., the gravity field coefficients)

$$\boldsymbol{x} = \begin{bmatrix} \boldsymbol{o}^{\mathrm{T}} & \boldsymbol{g}^{\mathrm{T}} \end{bmatrix}^{\mathrm{T}} \quad . \tag{4.23}$$

The kinematic positions may be directly used as pseudo-observations of the satellite's position as described by Eq. 4.6 in the primary equation

$$\boldsymbol{r}^{\mathrm{ant}}(t) - \delta\boldsymbol{r}^{\mathrm{ant}}(t) = \boldsymbol{r}_0(t) + \sum_{i=1}^{6+K} \frac{\partial \boldsymbol{r}_0(t)}{\partial p_i}(p_i - p_{0,i}) + \boldsymbol{e} \quad , \tag{4.24}$$

where p_i denote the unknown parameters of the dynamic force model, composed of local and global parameters. Re-formatting to the formulation of non-linear least squares (Eq. 3.34), Eq. 4.24 reads as

$$\begin{aligned} \boldsymbol{r}^{\mathrm{ant}}(t) - \delta\boldsymbol{r}^{\mathrm{ant}}(t) - \boldsymbol{r}_0(t) &= \sum_{i=1}^{6+K} \frac{\partial \boldsymbol{r}_0(t)}{\partial p_i}(p_i - p_{0,i}) + \boldsymbol{e} \\ \delta\boldsymbol{\ell} &= \begin{bmatrix} \mathbf{A}_{\boldsymbol{o}} & \mathbf{A}_{\boldsymbol{g}} \end{bmatrix} \begin{bmatrix} \delta\boldsymbol{o} \\ \delta\boldsymbol{g} \end{bmatrix} + \boldsymbol{e} \quad . \end{aligned} \tag{4.25}$$

The satellite's position vector $\boldsymbol{r}_0(t)$ may be obtained by numerical integration of the initial value problem of the primary equations, and the partial derivatives with respect to the unknown parameters to compile $\mathbf{A}$ may be computed by numerical quadrature of the initial value problem of the variational equations.

4.4 Low-low SST: Inter-satellite ranging

GRACE and GRACE Follow-On are both equipped with a dual one-way microwave ranging system to measure the inter-satellite distance d^{m}. Differential carrier phase observations on K- and Ka-band are time-tagged to the GPS observations and adjusted for ionospheric effects in the data pre-processing resulting in biased ranges ρ. Since they refer to the distance between the antenna phase centres of the satellites, they have to be corrected for the antenna phase centre offset to the CoM of each satellite and also a light-time correction has to be applied to account for the travel time of the microwaves between the two spacecraft, so the ranges then refer to the Euclidean distance between the satellites' centres of mass at the same time [Kim, 2000].
The biased ranges are converted to range-rates $\dot{\boldsymbol{\rho}}$ and range-accelerations $\ddot{\boldsymbol{\rho}}$ by numerical differentiation using a linear filter $\mathbf{F}$. It filters the data with a window length of 70.7 s from the original 0.1 s sampling of $\boldsymbol{d}^{\mathrm{m}}$ to a 5 s sampling while also computing the time derivatives of the biased range as

$$\boldsymbol{\rho} = \mathbf{F}\boldsymbol{d}^{\mathrm{m}} \quad , \qquad \dot{\boldsymbol{\rho}} = \dot{\mathbf{F}}\boldsymbol{d}^{\mathrm{m}} \qquad \text{and} \qquad \ddot{\boldsymbol{\rho}} = \ddot{\mathbf{F}}\boldsymbol{d}^{\mathrm{m}} \quad . \tag{4.26}$$

The definition of the filter coefficients is given by Thomas [1999]. Assuming white noise in the biased range, the filter process leads to coloured noise in the range-rates and range-accelerations.

The (pseudo-)observable of the biased range may be linked with the unknown parameters by

$$\rho(t) \mathrel{\hat{=}} d(t) = |\Delta \boldsymbol{r}_0(t)| = \Delta \boldsymbol{r}_0 \boldsymbol{e}_{\Delta \boldsymbol{r}_0} \ , \tag{4.27}$$

where $d(t)$ demotes the Euclidean distance between GF1 and GF2 and $\Delta \boldsymbol{r}_0(t)$ is the difference vector of the position vector between the two satellites

$$\Delta \boldsymbol{r}_0(t) = \boldsymbol{r}_{0,\mathrm{GF2}}(t) - \boldsymbol{r}_{0,\mathrm{GF1}}(t) \ . \tag{4.28}$$

$\boldsymbol{e}_{\Delta \boldsymbol{r}_0}$ denotes its unit vector

$$\boldsymbol{e}_{\Delta \boldsymbol{r}_0} = \frac{\Delta \boldsymbol{r}_0}{|\Delta \boldsymbol{r}_0|} = \frac{\Delta \boldsymbol{r}_0}{d} \ . \tag{4.29}$$

For the sake of simplicity the time argument (t) will be dropped in the following.
The observation equations for the inter-satellite range observations may then be written as

$$\delta \boldsymbol{\ell} := \boldsymbol{\rho} - \boldsymbol{d} = \begin{bmatrix} \mathbf{A}^{\rho}_{\boldsymbol{o},\mathrm{GF1}} & \mathbf{A}^{\rho}_{\boldsymbol{o},\mathrm{GF2}} & \mathbf{A}^{\rho}_{\boldsymbol{g}} \end{bmatrix} \begin{bmatrix} \delta \boldsymbol{o}_{\mathrm{GF1}} \\ \delta \boldsymbol{o}_{\mathrm{GF2}} \\ \delta \boldsymbol{g} \end{bmatrix} + \boldsymbol{e} \ . \tag{4.30}$$

The notation follows the description of the kinematic PPP (Sect. 4.3), i.e., $\boldsymbol{o}$ refers to local (usually orbit) parameters which are related to one satellite only, and $\boldsymbol{g}$ denote global parameters. The vector of unknowns consists of three components

$$\boldsymbol{x} = \begin{bmatrix} \boldsymbol{o}^{\mathrm{T}}_{\mathrm{GF1}} & \boldsymbol{o}^{\mathrm{T}}_{\mathrm{GF2}} & \boldsymbol{g}^{\mathrm{T}} \end{bmatrix}^{\mathrm{T}} \ , \tag{4.31}$$

corresponding to the design-matrix

$$\mathbf{A} = \begin{bmatrix} \mathbf{A}^{\rho}_{\boldsymbol{o},\mathrm{GF1}} & \mathbf{A}^{\rho}_{\boldsymbol{o},\mathrm{GF2}} & \mathbf{A}^{\rho}_{\boldsymbol{g}} \end{bmatrix} \ . \tag{4.32}$$

The elements of each line in the design-matrix then read as

$$\begin{aligned} \boldsymbol{a}^{\rho}_{\boldsymbol{o},\mathrm{GF1}} &= -\ \boldsymbol{e}_{\Delta \boldsymbol{r}_0} \frac{\partial \boldsymbol{r}_{0,\mathrm{GF1}}}{\partial \boldsymbol{o}_{\mathrm{GF1}}} \ , \\ \boldsymbol{a}^{\rho}_{\boldsymbol{o},\mathrm{GF2}} &= +\ \boldsymbol{e}_{\Delta \boldsymbol{r}_0} \frac{\partial \boldsymbol{r}_{0,\mathrm{GF2}}}{\partial \boldsymbol{o}_{\mathrm{GF2}}} \qquad \text{and} \\ \boldsymbol{a}^{\rho}_{\boldsymbol{g}} &= -\ \boldsymbol{e}_{\Delta \boldsymbol{r}_0} \frac{\partial \boldsymbol{r}_{0,\mathrm{GF1}}}{\partial \boldsymbol{g}} + \boldsymbol{e}_{\Delta \boldsymbol{r}_0} \frac{\partial \boldsymbol{r}_{0,\mathrm{GF2}}}{\partial \boldsymbol{g}} \ . \end{aligned} \tag{4.33}$$

Each $\boldsymbol{a}^{\rho}$ forms one row of the respective design-matrix. The elements between GF1 and GF2 are related by a multiplication of -1 (but evaluated at a different a priori orbit $\boldsymbol{r}_{0,\mathrm{GF1}}$ and $\boldsymbol{r}_{0,\mathrm{GF2}}$) and the global parameters contain the influence of both GF1 and GF2 in a differential way. This symmetry is the result of the one-dimensional inter-satellite measurement which yields that only relative parameters may be reliably determined and the

absolute location needs to be augmented by GPS. Since the observations contain a biased range, the bias has to be co-estimated as well, being determined by GF1 and GF2 with the respective partial being 1. All partials in the design-matrix may be easily derived from the a priori orbit of each satellite $\boldsymbol{r}_{0,\mathrm{GF1}}$ and $\boldsymbol{r}_{0,\mathrm{GF2}}$. Note that the velocity $\dot{\boldsymbol{r}}_0$ does not appear in the partials for the range observable, but only for range-rates (see below).

The step from ranges to range-rates is done by projecting the differential velocity vector between the two spacecraft to the Line of Sight (LoS). The magnitude of the relative velocity vector between the satellites reads as

$$\dot{d} = |\Delta\dot{\boldsymbol{r}}_0| = |\dot{\boldsymbol{\rho}}\boldsymbol{e}_{\Delta\boldsymbol{r}_0}| \ , \tag{4.34}$$

which is connected to the range-rates by the projection into the LoS with

$$\begin{aligned} \dot{\rho} &\mathrel{\hat{=}} \Delta\dot{\boldsymbol{r}}_0\boldsymbol{e}_{\Delta\boldsymbol{r}_0} \\ &= \dot{d}\cos\varphi \ , \end{aligned} \tag{4.35}$$

where φ denotes the angle between the velocity vector and the LoS vector. Hence, the range-rates do not have the same magnitude as the velocity differences. One may note that an efficient implementation is using the vector operations instead of the trigonometric function which is stated here for the sake of better readability. The range-rate observation equations may then be formulated as

$$\delta\boldsymbol{\ell} := \dot{\boldsymbol{\rho}} - \dot{\boldsymbol{d}}\cos\boldsymbol{\varphi} = \begin{bmatrix} \mathbf{A}^{\dot{\rho}}_{\boldsymbol{o},\mathrm{GF1}} & \mathbf{A}^{\dot{\rho}}_{\boldsymbol{o},\mathrm{GF2}} & \mathbf{A}^{\dot{\rho}}_{\boldsymbol{g}} \end{bmatrix} \begin{bmatrix} \delta\boldsymbol{o}_{\mathrm{GF1}} \\ \delta\boldsymbol{o}_{\mathrm{GF2}} \\ \delta\boldsymbol{g} \end{bmatrix} + \boldsymbol{e} \ , \tag{4.36}$$

using the same separation between local and global parameters. Each row of the design-matrices reads as

$$\begin{aligned} \boldsymbol{a}^{\dot{\rho}}_{\boldsymbol{o},\mathrm{GF1}} &= +\ \frac{1}{d}\left(\Delta\dot{\boldsymbol{r}}_0 - \boldsymbol{e}_{\Delta\boldsymbol{r}_0}\dot{d}\cos\varphi\right)\frac{\partial\boldsymbol{r}_{0,\mathrm{GF1}}}{\partial\boldsymbol{o}_{\mathrm{GF1}}} \ + \ \boldsymbol{e}_{\Delta\boldsymbol{r}_0}\frac{\partial\dot{\boldsymbol{r}}_{0,\mathrm{GF1}}}{\partial\boldsymbol{o}_{\mathrm{GF1}}} \ , \\ \boldsymbol{a}^{\dot{\rho}}_{\boldsymbol{o},\mathrm{GF2}} &= -\ \frac{1}{d}\left(\Delta\dot{\boldsymbol{r}}_0 - \boldsymbol{e}_{\Delta\boldsymbol{r}_0}\dot{d}\cos\varphi\right)\frac{\partial\boldsymbol{r}_{0,\mathrm{GF2}}}{\partial\boldsymbol{o}_{\mathrm{GF2}}} \ - \ \boldsymbol{e}_{\Delta\boldsymbol{r}_0}\frac{\partial\dot{\boldsymbol{r}}_{0,\mathrm{GF2}}}{\partial\boldsymbol{o}_{\mathrm{GF2}}} \qquad \text{and} \\ \boldsymbol{a}^{\dot{\rho}}_{\boldsymbol{g}} &= +\ \frac{1}{d}\left(\Delta\dot{\boldsymbol{r}}_0 - \boldsymbol{e}_{\Delta\boldsymbol{r}_0}\dot{d}\cos\varphi\right)\frac{\partial\boldsymbol{r}_{0,\mathrm{GF1}}}{\partial\boldsymbol{g}} - \frac{1}{d}\left(\Delta\dot{\boldsymbol{r}}_0 - \boldsymbol{e}_{\Delta\boldsymbol{r}_0}\dot{d}\cos\varphi\right)\frac{\partial\boldsymbol{r}_{0,\mathrm{GF2}}}{\partial\boldsymbol{g}} \\ &\quad + \ \boldsymbol{e}_{\Delta\boldsymbol{r}_0}\frac{\partial\dot{\boldsymbol{r}}_{0,\mathrm{GF1}}}{\partial\boldsymbol{g}} \ - \ \boldsymbol{e}_{\Delta\boldsymbol{r}_0}\frac{\partial\dot{\boldsymbol{r}}_{0,\mathrm{GF2}}}{\partial\boldsymbol{g}} \ . \end{aligned} \tag{4.37}$$

Since range-rates are unbiased, no additional offset parameter has to be estimated within the global parameters. For a more detailed derivation of the formulations for the KBR observables see Kim [2000].
The same formulas of processing the inter-satellite link observables may in principle be transferred to the range measurement provided by the LRI. Only the phase centre offset correction is not necessary since the LRI observations refer geometrically already to the satellite's CoM.

The linear filter $\mathbf{F}$ and $\dot{\mathbf{F}}$ in Eq. 4.26 could be seen as additional filter before the LSQA,

thus, applying two[1] consecutive LSQAs (see Sect. 3.2.5). However, when using range-rates as observations without any dedicated weighting, in fact, introducing them as pseudo- or intermediate observations, this comes at the cost that the correlations induced by the filter process are neglected. Thus, the processing of ranges and range-rates cannot be considered as equivalent anymore. As Beutler et al. [2010a] showed, including the coloured noise due to the filter process leads to a weighting of the observations which is centred around the length these correlations are included. Consequently, varying the length of these correlations (e.g., 30 min or 90 min or 1 d) samples a different signal through a subsequent weighting in a sequential LSQ process (see Sect. 3.2.4), where each block is treated as being independent.

4.5 Joint orbit and gravity field determination

As already explained, the unknown parameters are separated into local and global parameters $\boldsymbol{x} = \begin{bmatrix} \boldsymbol{o}_{\mathrm{GF1}}^{\mathrm{T}} & \boldsymbol{o}_{\mathrm{GF2}}^{\mathrm{T}} & \boldsymbol{g}^{\mathrm{T}} \end{bmatrix}^{\mathrm{T}}$ and for each satellite NEQs according to Eq. 3.13 are set up based on the solution of the ordinary differential equations related to the primary equation (Eq. 4.5) and the variational equations (Eq. 4.8), resulting in three NEQs

$$\mathrm{NEQ}_{\mathrm{GF1}}^{\mathrm{KIN}} \rightarrow \boldsymbol{o}_{\mathrm{GF1}} \quad \boldsymbol{g} \ , \quad \mathrm{NEQ}_{\mathrm{GF2}}^{\mathrm{KIN}} \rightarrow \boldsymbol{o}_{\mathrm{GF2}} \quad \boldsymbol{g} \ \text{and} \quad \mathrm{NEQ}^{\mathrm{Kb}} \rightarrow \boldsymbol{o}_{\mathrm{GF1}} \quad \boldsymbol{o}_{\mathrm{GF2}} \quad \boldsymbol{g} \ .$$

Combining these NEQs to a solution for all local and global parameters poses the question of the relative weighting between the kinematic positions and the KBR observations. The latter are more precise by orders of magnitude (see Beutler et al. [2010b] for an outline) and in this thesis a fixed ratio of $\sigma_0^{\dot{\rho}} = 3 \times 10^{-7}\,\mathrm{m\,s^{-1}}$ and $\sigma_0^{\mathrm{KIN}} = 10 \cdot \sigma_0^{\mathrm{ph}} \approx 15\,\mathrm{mm}$ is adopted. A short overview about the influence of such weighting schemes on the recovered gravity field will be given in Sect. 5.1.5.

4.5.1 Orbit parameter transformation

For relative measurements between two satellites which are orbiting the Earth only a few hundred kilometres separated from each other at the same trajectory, the elements of the local parameters in the design-matrix (Eq. 4.33 or Eq. 4.37) will be very similar [Beutler et al., 2010b], i.e.,

$$\boldsymbol{a}_{\boldsymbol{o},\mathrm{GF1}} \approx -\boldsymbol{a}_{\boldsymbol{o},\mathrm{GF2}} \ . \tag{4.38}$$

This implies that the absolute position of each satellite is not well captured by the inter-satellite observable. The CMA makes use of this structure to perform a transformation of the orbit parameters to the mean, denoted as Summation (SUM), and difference, labelled as Difference (DIFF), between the two satellites for all observations (kinematic positions and inter-satellite measurements), thus, introducing a new set of parameters, which instead of referring to the individual spacecraft, are linked to a position and velocity in space, see Fig. 4.2. The transformation is accomplished for each satellite-specific parameter by

$$\boldsymbol{o}_{\mathrm{SUM}} := \frac{\boldsymbol{o}_{\mathrm{GF1}} + \boldsymbol{o}_{\mathrm{GF1}}}{2} \qquad \text{and} \qquad \boldsymbol{o}_{\mathrm{DIFF}} := \frac{\boldsymbol{o}_{\mathrm{GF1}} - \boldsymbol{o}_{\mathrm{GF1}}}{2} \ , \tag{4.39}$$

[1] Three, in case the orbit and gravity field determination is also seen as series of LSQAs.

or conversely

$$\boldsymbol{o}_{\mathrm{GF1}} = \boldsymbol{o}_{\mathrm{SUM}} + \boldsymbol{o}_{\mathrm{DIFF}} \qquad \text{and} \qquad \boldsymbol{o}_{\mathrm{GF2}} = \boldsymbol{o}_{\mathrm{SUM}} - \boldsymbol{o}_{\mathrm{DIFF}} \ . \tag{4.40}$$

The SUM-part mainly refers to the absolute parameter value, each of the parameters set up

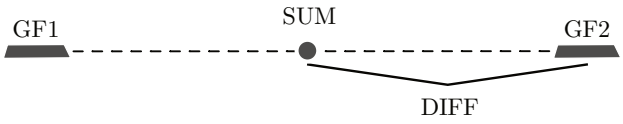

Figure 4.2: Illustration of the orbit parameter transformation to SUM- and DIFF-components.

is averaged: The mean osculating Keplerian elements between the two satellites, the mean ACC parameters between the two satellites and the the mean pseudo-stochastic parameters between the two satellites. Thus, the SUM-parameters refer to a mean orbit between the two spacecraft after the transformation. As the SUM-part belongs to absolute (mean) parameters, it is considered to be driven by the absolute observations, such as the kinematic positions. The DIFF-component on the other hand denotes the relative difference between each parameter, thus, e.g., between each Keplerian element of the two spacecraft or the variation of the pseudo-stochastic parameters as the two spacecraft experience a slightly different environment being at the same time over hundred kilometre apart. Consequently, this set of parameters is considered to be best-determined by the relative measurement between the two spacecraft, i.e., the inter-satellite link observations. All of that is represented in the magnitude of the NEQs. The NEQs of the kinematic positions referring to the SUM-part is several orders of magnitude larger than the DIFF-part of the same NEQ. Vice versa the range-rate-NEQ has a much higher power in the DIFF-components. For all subsequent interpretations this transformation is performed and in general it is assumed that the SUM-part is mostly driven by the kinematic positions and the DIFF components are associated with the inter-satellite link. This is of particular relevance when considering the meaning of the pseudo-stochastic parameters.

4.5.2 Residuals in the joint orbit and gravity field recovery

In non-linear LSQ problems it is common to distinguish between pre-fit and post-fit residuals, those being computed from all a priori introduced models including the Taylor point approximations for the unknown parameters, thus, evaluating the left-hand side of Eq. 3.34. Post-fit residuals on the other hand refer to the estimated residuals (Eq. 3.16), which may be derived after a common solution for all sought-after parameters has been obtained. It is important to note that intermediate adjustments, such as computing an a priori orbit $\boldsymbol{r}_0(t)$ for faster convergence of a following orbit and gravity field recovery process, result in pre-fit residuals because the finally sought-after gravity field parameters have not been estimated (yet). Only after a joint orbit and gravity field solution post-fit residuals may be derived.

The post-fit residuals may be computed in two ways: A first one, named *non-linear* in this context, is to calculate the solution for all parameters and to use the estimated gravity

field together with the background force models to evaluate the estimated orbit parameters at the given observation epochs, hence, computing adjusted observations, and subsequently, post-fit residuals with

$$\hat{\boldsymbol{e}}_{\text{non-lin}} = \boldsymbol{\ell} - \boldsymbol{f}(\hat{\boldsymbol{x}}) \quad , \tag{4.41}$$

The other approach, denoted as *linearised*, is to only solve for the gravity field parameters explicitly while pre-eliminating all orbit parameters on arc-wise level (see Sect. 3.2.3). This procedure provides a more efficient handling of the NEQs, since the amount of parameters to be solved for is reduced. The post-fit residuals may then be obtained by a back-substitution process, thus, taking the estimated gravity field as part of the a priori force field and setting up and solving NEQs for the previously pre-eliminated orbit parameters. The residuals of this adjustment process yield the joint post-fit residuals by computing

$$\hat{\boldsymbol{e}}_{\text{lin}} = \delta\boldsymbol{\ell} - \mathbf{A}\delta\hat{\boldsymbol{x}} \quad . \tag{4.42}$$

The difference between the non-linear and linearised post-fit residuals is displayed in Fig. 4.3a. It is a least two orders of magnitude below the signal of post-fit residuals with a clear jump at the period corresponding to the maximum degree of the gravity field solution ($\mathrm{d/o} = 96$). The vertical black lines at 0.18 mHz and 18 mHz indicate the frequency range in which gravity field signal is expected for a polar-orbiting mission like GRACE Follow-On for spherical harmonic degrees of $\mathrm{d/o} \in \{2, ..., 96\}$. These lines will be plotted as a reference in all upcoming ASD-graphs. The difference between two gravity field solutions

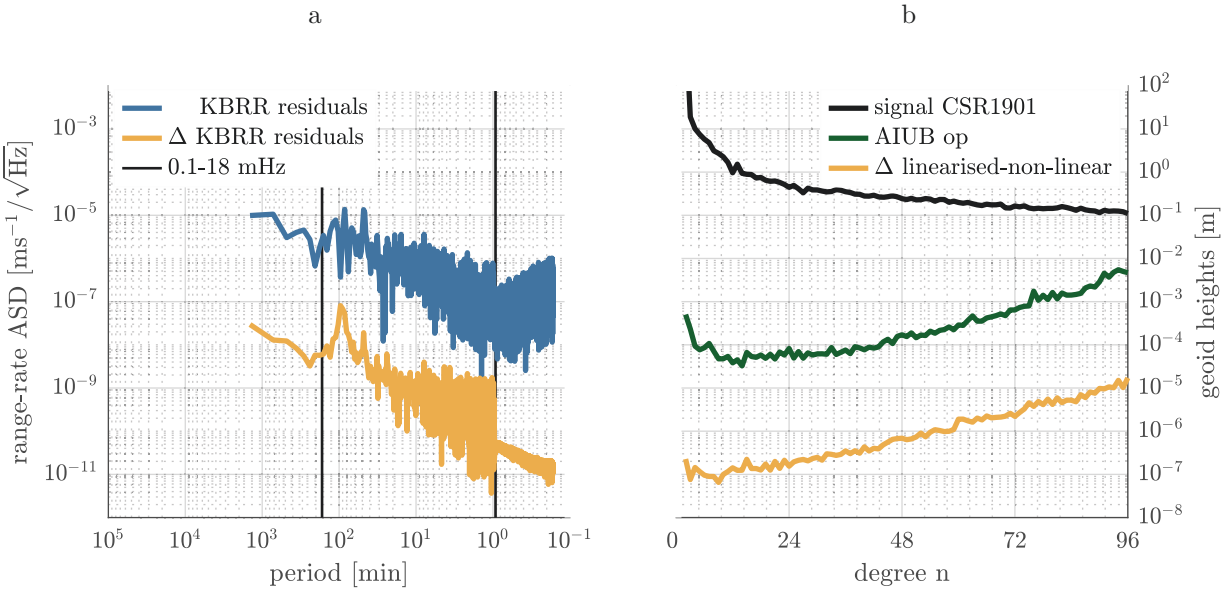

Figure 4.3: ASDs of KBRR post-fit residuals and their difference when using the non-linear or linearised computation method (a) and the same comparison expressed in resulting gravity field's degree amplitudes (b).

resulting from a linearised or non-linear setup, obtained by computing a further iteration of the non-linear LSQA where the respective residuals serve as new $O-C$ vector ($\delta\boldsymbol{\ell}$), leads to results about three orders of magnitude below the expected differences in all degrees

between monthly gravity field solutions (Fig. 4.3b). This is an improvement of at least one order of magnitude compared to Jäggi et al. [2012]. As a reference the GRACE Follow-On monthly gravity field solution computed at CSR [Save, 2019] is taken, which may be considered as slightly superior to the AIUB solutions. The green line depicts the degree amplitude differences (see Sect. 3.5.1 between the reference and an AIUB solution to evaluate the level of difference that may be expected. Hence, the conclusion is drawn that both computations methods are suited to compute post-fit residuals and the linearisation error is sufficiently small. In the processing environment at the AIUB normally linearised post-fit residuals are computed because the local orbit parameters are usually pre-eliminated on arc-wise level to allow for a more efficient usage of the computational resources.

4.6 Background force modelling

The formulation of the equation of motion (Eq. 4.5) may contain any kind of known force models to correctly describe the total acceleration. It is advisable to use all kinds of a priori known models which are sufficiently well known to reduce the accelerations introduced in the orbit and gravity field determination process to the extent possible. Thus, all improvements (estimations) are only happening on top of the a priori force field. For temporal gravity field modelling several a priori forces have to be taken into account, especially those which model changes in the Earth's gravity field due to mass re-distributions which are not sufficiently covered by the satellite's ground-track [see e.g., Han et al., 2004, Thompson et al., 2004]. The following description covers the background forces applied within the scope of temporal gravity field recovery. A summary may be found in Lasser et al. [2020c]. A description of the important non-tidal effects, i.e., gravitational forces caused by Earth's internal processes, including mathematical derivations may be found in Dobslaw et al. [2014]. Eventually, a sum of such variations (namely those which are not reduced by the a priori force model) are reflected by the computed monthly gravity fields. In particular, this is the total mass change induced by the continental water cycle and the cryosphere.
To illustrate the nature of the accelerations Fig. 4.4 shows the norm of perturbing gravitational accelerations considered for one day of GRACE in June 2008 based on the benchmark data set used in Lasser et al. [2020c]. The mean orbital altitude is 466 km. The accelerations are arranged by their magnitude. The Earth's gravity field in Fig. 4.4 is resolved starting from d/o = 2.

All formulae given in the following sections correspond to the International Earth Rotation and Reference Systems Service (IERS) 2010 conventions [Petit and Luzum, 2010], however, they are provided in the way they are implemented in the BSW. All constants can be found in the IERS 2010 conventions and the corresponding model descriptions. When referring to the equations from the IERS 2010 conventions, the notation *Eq.*^{IERS} *(n.n)* is used.

4.6.1 Earth's Gravity field

The most important a priori force field is the accelerations caused by the Earth's gravity field. It is by far the largest force, explained to 99.9 % by the Kepler-term (cf. Eq. 4.4). Its

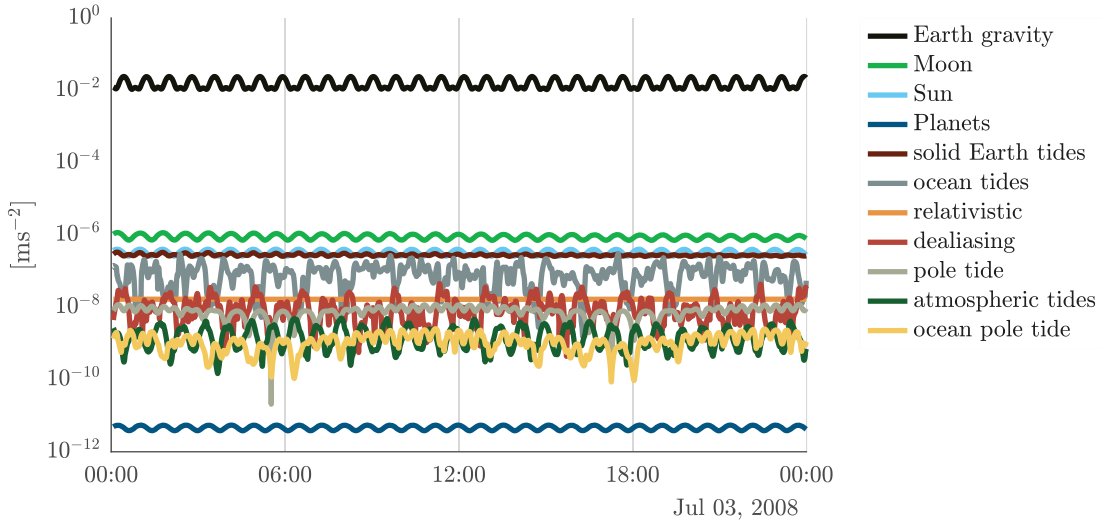

Figure 4.4: Magnitude of the background perturbing accelerations for July 3rd, 2008 as appearing in a mean orbital altitude of 466 km for a GRACE satellite.

parameters not only describe an a priori force but are also contained in the dynamic model which is introduced as part of the sought-after quantities ($\{d_1, ..., d_K\}$ in Eq. 4.5). Therefore, the sought-after quantities are split into a known component from the a priori force field and an unknown increment, which is estimated in the gravity field recovery process. It is crucial that the information of the a priori gravity field does not leak into the solution of the increments to provide for an unbiased solution. In particular when estimating only orbit parameters, the complete a priori force field (including the gravity field) is present in these parameters. Thus, any quantities derived subsequently, already contain information from the a priori gravity field (see e.g., the effect of observations being introduced twice to estimate for different sets of parameters in Sect. 3.2.6).

The Earth's surface may be described by an equipotential surface, where each point refers to the same potential. For any point (r, λ, ϑ) above the Earth's surface the potential V may be developed into a spherical harmonic series [Heiskanen and Moritz, 1967, see Sect. 3.5] expressed as

$$V(r,\lambda,\vartheta) = \frac{GM_\mathrm{E}}{r}\sum_{n=0}^{N}\left(\frac{a_\mathrm{E}}{r}\right)^n \sum_{m=0}^{n}\left(c_{nm}\cos(m\lambda) + s_{nm}\sin(m\lambda)\right) P_{nm}(\cos\vartheta) \quad , \tag{4.43}$$

where c_{nm} and s_{nm} denote the normalised spherical harmonic coefficients of degree n and order m and P_{nm} are the normalised associated Legendre functions. The series is truncated at degree and order N, which is later referred to as d/o (*degree and order*). a_E defines the equatorial radius of the Earth, GM_E the gravitational constant multiplied with the mass of the Earth, both are directly associated with the gravity field model. Equation 4.43 corresponds to *Eq.^{IERS} (6.1)*. For a detailed derivation of the expression of the Earth's gravity field in spherical harmonics one may consult Heiskanen and Moritz [1967].

The accelerations and the potential are related by the gradient

$$\boldsymbol{a}_{r,\lambda,\vartheta} = \nabla V \quad , \tag{4.44}$$

with ∇ being the gradient operator. The accelerations in cartesian coordinates may be obtained by a transformation of Earth-fixed (r, λ, ϑ)-frame to (x, y, z)-frame. Note that the observables of a satellite's orbit through positions and ranges do not directly observe the Earth's potential but only its spatial derivatives. This concept was and is employed in the missions dedicated to sensing the Earth's gravity field CHAMP, GRACE, GOCE[2] and GRACE Follow-On.

The a priori gravity field model used in this thesis is AIUB-GRACE03S [Jaeggi et al., 2011] computed from seven years of GRACE data. It contains a set of dimensionless, fully-normalised spherical harmonic coefficients representing the static and time-variable part of the Earth's gravity field up to d/o = 160. In this work only the static part is considered.

4.6.2 3rd body perturbations

The other celestial bodies in the solar system induce a n-body problem because not only Earth and the satellite are interacting with each other but all other massive objects perturb the satellite's orbit. The accelerations caused by the attraction of other celestial bodies (labelled with the subscript cb) than the Earth are computed with positions derived from the JPL DE421 [Folkner et al., 2009] ephemeris. The Moon and the Sun have the largest impact, all other planets play a minor role. All bodies are treated as point masses, thus,

$$\boldsymbol{a}_{\mathrm{cb}} = -GM_{\mathrm{cb}} \left(\frac{\boldsymbol{r} - \boldsymbol{r}_{\mathrm{cb}}}{|\boldsymbol{r} - \boldsymbol{r}_{\mathrm{cb}}|^3} + \frac{\boldsymbol{r}_{\mathrm{cb}}}{r_{\mathrm{cb}}^3} \right) \tag{4.45}$$

expresses the accelerations caused by a celestial body. $\boldsymbol{r}$ and $\boldsymbol{r}_{\mathrm{cb}}$ denote the geocentric position vector of the satellite and the celestial body in the quasi inertial frame. The constants of GM_{cb} are given by the ephemerides. All planets including the dwarf planet Pluto are taken into account. The positions of Sun and Moon, which are derived from the ephemerides, are also used for the computation of the solid Earth tides and the relativistic corrections.

4.6.3 Solid Earth tides

Solid Earth tides are computed according to the IERS 2010 conventions using the anelastic model. They account for the deformation of the solid Earth due to Sun and Moon. They affect the spherical harmonic spectrum up to degree 4 and make use of the Love numbers to describe the rigidity of the Earth as elastic deformation when exposed to a tidal potential. The computation is split into two steps. Step 1 computes the coefficients due to the tide generating potential for degree 2 and 3, as well as the effect of degree 2 on degree 4 coefficients. Step 1 is frequency independent, whereas step 2 states frequency dependent corrections for degree two.

[2]Together with satellite gravity gradiometry.

Step 1 - corresponds with *Eq.^{IERS} (6.6)* and *Eq.^{IERS} (6.7)*:

$$\begin{aligned}
c_{2m} &= \left(\left(k^{\Re}_{2m}\cos(m\lambda_{\mathrm{M}}) + k^{\Im}_{2m}\sin(m\lambda_{\mathrm{M}})\right) P_{2m}(\cos\vartheta_{\mathrm{M}}) \frac{GM_{\mathrm{M}}}{5GM_{\mathrm{E}}} \left(\frac{a_{\mathrm{E}}}{r_{\mathrm{M}}}\right)^3 \right) \; + \\
&\quad \left(\left(k^{\Re}_{2m}\cos(m\lambda_{\mathrm{S}}) + k^{\Im}_{2m}\sin(m\lambda_{\mathrm{S}})\right) P_{2m}(\cos\vartheta_{\mathrm{S}}) \frac{GM_{\mathrm{S}}}{5GM_{\mathrm{E}}} \left(\frac{a_{\mathrm{E}}}{r_{\mathrm{S}}}\right)^3 \right) \; , \\
s_{2m} &= \left(\left(k^{\Re}_{2m}\sin(m\lambda_{\mathrm{M}}) - k^{\Im}_{2m}\cos(m\lambda_{\mathrm{M}})\right) P_{2m}(\cos\vartheta_{\mathrm{M}}) \frac{GM_{\mathrm{M}}}{5GM_{\mathrm{E}}} \left(\frac{a_{\mathrm{E}}}{r_{\mathrm{M}}}\right)^3 \right) \; + \\
&\quad \left(\left(k^{\Re}_{2m}\sin(m\lambda_{\mathrm{S}}) - k^{\Im}_{2m}\cos(m\lambda_{\mathrm{S}})\right) P_{2m}(\cos\vartheta_{\mathrm{S}}) \frac{GM_{\mathrm{S}}}{5GM_{\mathrm{E}}} \left(\frac{a_{\mathrm{E}}}{r_{\mathrm{S}}}\right)^3 \right) \; , \\
&\qquad\qquad m \in \{0,1,2\}
\end{aligned} \tag{4.46}$$

$$\begin{aligned}
c_{4m} &= \left(\left(k^{(+)}_{2m}\cos(m\lambda_{\mathrm{M}})\right) P_{2m}(\cos\vartheta_{\mathrm{M}}) \frac{GM_{\mathrm{M}}}{5GM_{\mathrm{E}}} \left(\frac{a_{\mathrm{E}}}{r_{\mathrm{M}}}\right)^3 \right) \; + \\
&\quad \left(\left(k^{(+)}_{2m}\cos(m\lambda_{\mathrm{S}})\right) P_{2m}(\cos\vartheta_{\mathrm{S}}) \frac{GM_{\mathrm{S}}}{5GM_{\mathrm{E}}} \left(\frac{a_{\mathrm{E}}}{r_{\mathrm{S}}}\right)^3 \right) \; , \\
s_{4m} &= \left(\left(k^{(+)}_{2m}\sin(m\lambda_{\mathrm{M}})\right) P_{2m}(\cos\vartheta_{\mathrm{M}}) \frac{GM_{\mathrm{M}}}{5GM_{\mathrm{E}}} \left(\frac{a_{\mathrm{E}}}{r_{\mathrm{M}}}\right)^3 \right) \; + \\
&\quad \left(\left(k^{(+)}_{2m}\sin(m\lambda_{\mathrm{S}})\right) P_{2m}(\cos\vartheta_{\mathrm{S}}) \frac{GM_{\mathrm{S}}}{5GM_{\mathrm{E}}} \left(\frac{a_{\mathrm{E}}}{r_{\mathrm{S}}}\right)^3 \right) \; , \\
&\qquad\qquad m \in \{0,1,2\}
\end{aligned} \tag{4.47}$$

$$\begin{aligned}
c_{3m} &= \left(\left(k^{\Re}_{3m}\cos(m\lambda_{\mathrm{M}}) + k^{\Im}_{3m}\sin(m\lambda_{\mathrm{M}})\right) P_{3m}(\cos\vartheta_{\mathrm{M}}) \frac{GM_{\mathrm{M}}}{7GM_{\mathrm{E}}} \left(\frac{a_{\mathrm{E}}}{r_{\mathrm{M}}}\right)^4 \right) \; + \\
&\quad \left(\left(k^{\Re}_{3m}\cos(m\lambda_{\mathrm{S}}) + k^{\Im}_{3m}\sin(m\lambda_{\mathrm{S}})\right) P_{3m}(\cos\vartheta_{\mathrm{S}}) \frac{GM_{\mathrm{S}}}{7GM_{\mathrm{E}}} \left(\frac{a_{\mathrm{E}}}{r_{\mathrm{S}}}\right)^4 \right) \; , \\
s_{3m} &= \left(\left(k^{\Re}_{3m}\sin(m\lambda_{\mathrm{M}}) - k^{\Im}_{3m}\cos(m\lambda_{\mathrm{M}})\right) P_{3m}(\cos\vartheta_{\mathrm{M}}) \frac{GM_{\mathrm{M}}}{7GM_{\mathrm{E}}} \left(\frac{a_{\mathrm{E}}}{r_{\mathrm{M}}}\right)^4 \right) \; + \\
&\quad \left(\left(k^{\Re}_{3m}\sin(m\lambda_{\mathrm{S}}) - k^{\Im}_{3m}\cos(m\lambda_{\mathrm{S}})\right) P_{3m}(\cos\vartheta_{\mathrm{S}}) \frac{GM_{\mathrm{S}}}{7GM_{\mathrm{E}}} \left(\frac{a_{\mathrm{E}}}{r_{\mathrm{S}}}\right)^4 \right) \; . \\
&\qquad\qquad m \in \{0,1,2,3\}
\end{aligned} \tag{4.48}$$

$k^{\Re}_{nm}$, $k^{\Im}_{nm}$, $k^{(+)}_{nm}$ are the Love numbers (*Table^{IERS} 6.3*), r_{S} and r_{M} is the norm of the geocentric vector to Sun and Moon. The Legendre functions P_{nm} were already introduced in Sect. 3.5. They depend on the co-latitude $\vartheta_{\mathrm{S,M}}$ of Sun and Moon in the TRF. $\lambda_{\mathrm{S,M}}$ is the geographical longitude of Sun and Moon in the Earth-fixed frame.

Step 2:
Corrections on c_{20} - correspond to *Eq.^{IERS} (6.8a)* and uses *Table^{IERS} 6.5b*:

$$\Delta c^{\mathrm{corr}}_{20} = \sum_{f_{\mathrm{long\ periodic}}} \left(A^{\mathrm{ip}}_f \cos\theta - A^{\mathrm{op}}_f \sin\theta\right) \; . \tag{4.49}$$

Corrections on c_{21}, c_{22}, s_{21} and s_{22} - correspond to *Eq.^{IERS} (6.8b)* and uses *Table^{IERS} 6.5a* and *Table^{IERS} 6.5c*:

$$\begin{aligned} \Delta c_{21}^{\text{corr}} &= \sum_{f_{\text{diurnal}}} \left(A_f^{\text{ip}} \sin\theta + A_f^{\text{op}} \cos\theta\right) \ , & \Delta c_{22}^{\text{corr}} &= \sum_{f_{\text{semi diurnal}}} +A_f^{\text{ip}} \cos\theta_f \ , \\ \Delta s_{21}^{corr} &= \sum_{f_{\text{diurnal}}} \left(A_f^{\text{ip}} \cos\theta - A_f^{\text{op}} \sin\theta\right) \ , & \Delta s_{22}^{\text{corr}} &= \sum_{f_{\text{semi diurnal}}} -A_f^{\text{ip}} \sin\theta_f \ . \end{aligned} \tag{4.50}$$

The amplitudes for the frequency dependent corrections for A_f^{ip} and A_f^{op} are listed in *Table^{IERS} 6.5a*, *Table^{IERS} 6.5b* and *Table^{IERS} 6.5c*.

The Doodson angle argument reads as

$$\theta_f = \boldsymbol{n}_f \boldsymbol{\beta} \ , \tag{4.51}$$

where θ_f may be derived from the fundamental six Doodson arguments $\boldsymbol{\beta}$ and the respective tidal frequency $\boldsymbol{n}_f$. The computation of the fundamental Doodson arguments $\boldsymbol{\beta} = \begin{bmatrix} \tau & s & h & p & N' & p_{\text{s}} \end{bmatrix}^{\text{T}}$ stems from the fundamental arguments of lunisolar nutation l, l', F, D, Ω (Delaunay variables, see Doodson and Lamb [1921], *Eq.^{IERS} (5.43)*) and reads as

$$\begin{aligned} l &= 134.963\,402\,51^\circ + 1\,717\,915\,923.2178''t + 31.8792''t^2 \\ &\quad + 0.051\,635''t^3 - 0.000\,244\,70''t^4 \ , \\ l' &= 357.529\,109\,18^\circ + 129\,596\,581.0481''t - 0.5532''t^2 \\ &\quad + 0.000\,136''t^3 - 0.000\,011\,49''t^4 \ , \\ F &= 93.272\,090\,62^\circ + 1\,739\,527\,262.8478''t - 12.7512''t^2 \\ &\quad - 0.001\,037''t^3 + 0.000\,004\,17''t^4 \ , \\ D &= 297.850\,195\,47^\circ + 1\,602\,961\,601.2090''t - 6.3706''t^2 \\ &\quad + 0.006\,593''t^3 - 0.000\,031\,69''t^4 \qquad \text{and} \\ \Omega &= 125.044\,555\,01^\circ - 6\,962\,890.5431''t + 7.4722''t^2 \\ &\quad + 0.007\,702''t^3 - 0.000\,059\,39''t^4 \ , \end{aligned} \tag{4.52}$$

where t is the time interval in Julian centuries between the current epoch and J2000.0, both expressed in the Modified Julian Date (MJD), i.e.,

$$t = \frac{t_{\text{MJD}} - t_{\text{MJD}_{2000}}}{36\,525} \qquad \text{with} \qquad t_{\text{MJD}_{2000}} = 51\,544.5 \ . \tag{4.53}$$

Finally, the Doodson arguments read as

$$\boldsymbol{\beta} = \begin{bmatrix} \tau \\ s \\ h \\ p \\ N' \\ p_{\text{s}} \end{bmatrix} = \begin{bmatrix} \theta_{\text{g}} + \pi - s \\ F + \Omega \\ s - D \\ s - l \\ -\Omega \\ s - D - l' \end{bmatrix} \ , \tag{4.54}$$

where θ_{g} denotes the Greenwich Mean Sidereal Time (GMST). Each digit in the tidal frequency vector $\boldsymbol{n}_f$ makes up one element of the multipliers $n_{f,i}$. An example for the long periodic om1-tide with a frequency of 00.010 would be $\boldsymbol{n}_{om1} = \begin{bmatrix} 0 & 5 & 5 & 5 & 6 & 5 \end{bmatrix}$. The

first element of the vector tells the periodicity of the tide, all other elements have to be computed by adding 5.
The final coefficients c_{2m}^{total} and s_{2m}^{total} are obtained by adding together step 1 and step 2

$$c_{2m}^{\text{total}} = c_{2m} + \Delta c_{2m}^{\text{corr}} \qquad \text{and} \qquad s_{2m}^{\text{total}} = s_{2m} + \Delta s_{2m}^{\text{corr}} \ . \tag{4.55}$$

The Doodson arguments and fundamental arguments of nutation are also used in the computation of oceanic tides and atmospheric tides. The accelerations caused by the solid Earth tides are eventually computed using Eq. 4.43 and Eq. 4.44.

4.6.4 Ocean tides

The ocean tides represent the responses of the ocean to the attraction of Sun and Moon, which induce a gravitational signal due to the mass re-distribution of water. In this thesis the model FES2014b [Carrere et al., 2016] is applied, based on the conversion of the corresponding grids to dimensionless and fully-normalised prograde $\{c_{nm,f}^{\cos}, s_{nm,f}^{\cos}\}$ and retrograde $\{c_{nm,f}^{\sin}, s_{nm,f}^{\sin}\}$ spherical harmonic coefficients done by TUG. The spherical harmonic coefficients may be compiled from the given coefficients in a sum over all tidal frequencies f by

$$\begin{aligned} c_{nm} &= \sum_f \left(c_{nm,f}^{\cos} \cos(\theta_f) + c_{nm,f}^{\sin} \sin(\theta_f) \right) \qquad \text{and} \\ s_{nm} &= \sum_f \left(s_{nm,f}^{\cos} \cos(\theta_f) + s_{nm,f}^{\sin} \sin(\theta_f) \right) \ . \end{aligned} \tag{4.56}$$

In this representation the Doodson-Warburg correction (see *Table*^{IERS} *6.6*) is already applied. To complete the tidal spectrum, admittances between the major tides may be computed using linear interpolation

$$\begin{aligned} c_{nm,f}^{\cos} &= c_{nm,1}^{\cos} \frac{\theta_2 - t_f}{\theta_2 - t_1} \frac{H_f}{H_1} + c_{nm,2}^{\cos} \frac{\theta_f - \theta_1}{\theta_2 - \theta_1} \frac{H_f}{H_2} \ , \\ s_{nm,f}^{\cos} &= s_{nm,1}^{\cos} \frac{\theta_2 - \theta_f}{\theta_2 - \theta_1} \frac{H_f}{H_1} + s_{nm,2}^{\cos} \frac{\theta_f - \theta_1}{\theta_2 - \theta_1} \frac{H_f}{H_2} \ , \\ c_{nm,f}^{\sin} &= c_{nm,1}^{\sin} \frac{\theta_2 - t_f}{\theta_2 - t_1} \frac{H_f}{H_1} + c_{nm,2}^{\sin} \frac{\theta_f - \theta_1}{\theta_2 - \theta_1} \frac{H_f}{H_2} \qquad \text{and} \\ s_{nm,f}^{\sin} &= s_{nm,1}^{\sin} \frac{\theta_2 - \theta_f}{\theta_2 - \theta_1} \frac{H_f}{H_1} + s_{nm,2}^{\sin} \frac{\theta_f - \theta_1}{\theta_2 - \theta_1} \frac{H_f}{H_2} \ . \end{aligned} \tag{4.57}$$

The subscripts 1 and 2 denote the main waves, f the interpolated wave. H is the astronomic amplitude of the wave. Accelerations resulting from ocean tides are eventually obtained by Eq. 4.43 and Eq. 4.44.

4.6.5 Relativistic corrections

Because the satellite is orbiting in a low altitude around a massive object (the Earth), three effects of general relativity have to be taken into account, the Schwarzschild-term, the geodetic precession due to the curvature of space-time (de Sitter effect), and the

Lense-Thirring effect (frame-dragging) due to the Earth's rotation. Relativistic corrections are computed according to the IERS 2010 conventions for General Relativity using *Eq.^{IERS} (10.12)*

$$\boldsymbol{a}_{\text{Schwarzschild}} = \frac{GM_{\text{E}}}{c^2 r^3}\left(4\,\frac{GM_{\text{E}}\boldsymbol{r}}{r} - (\dot{\boldsymbol{r}}\dot{\boldsymbol{r}})\boldsymbol{r} + 4\,(\boldsymbol{r}\dot{\boldsymbol{r}})\,\dot{\boldsymbol{r}}\right) \quad , \tag{4.58a}$$

$$\boldsymbol{a}_{\text{Lense Thirring}} = 2\frac{GM_{\text{E}}}{c^2 r_{sat}^3}\left(\frac{3}{r^2}(\boldsymbol{r}\times\dot{\boldsymbol{r}})\,(\boldsymbol{r}\boldsymbol{J}) + (\dot{\boldsymbol{r}}\times\boldsymbol{J})\right) \qquad \text{and} \tag{4.58b}$$

$$\boldsymbol{a}_{\text{de Sitter}} = 3\left(-\dot{\boldsymbol{r}}_{\text{S}}\times\frac{GM_{\text{S}}\boldsymbol{r}_{\text{S}}}{c^2 r_{\text{S}}^3}\right)\times\dot{\boldsymbol{r}} \quad , \tag{4.58c}$$

where c is the speed of light and $\boldsymbol{J}$ is the Earth's angular momentum per unit mass. It may be set to $\begin{bmatrix}0 & 0 & 9.8\times10^8\end{bmatrix}^{\text{T}}\,\text{m}\,\text{s}^{-2}$ [Petit and Luzum, 2010]. The vectors $\boldsymbol{r}_{\text{S}}$ and $\dot{\boldsymbol{r}}_{\text{S}}$ describe the geocentric position and velocity of the Sun in the CRF. The relativistic accelerations in Fig. 4.4 are the sum of the three components

$$\boldsymbol{a}_{\text{relativistic}} = \boldsymbol{a}_{\text{Schwarzschild}} + \boldsymbol{a}_{\text{Lense Thirring}} + \boldsymbol{a}_{\text{de Sitter}} \quad . \tag{4.59}$$

4.6.6 Short-term mass variations of atmosphere and ocean

The Atmospheric and Oceanic De-aliasing (AOD) is a model of great importance for time-variable gravity field recovery. The satellite is subject to the gravitational attraction caused by the full gravity field, however, it is only able to correctly measure gravitational signal based on the traversed area, thus, only along its ground track. When sufficiently dense ground tracks are reached a full snapshot of the state of the Earth's gravity field may be provided. For GRACE and GRACE Follow-On this is usually each month. Any mass re-distributions (causing a change in the gravitational potential at this location) occurring in shorter time intervals lead to an aliasing in the recovered monthly gravity field. The effect of tides is already treated with the respective models, however, non-tidal short-term changes have to considered as well. Therefore, the AOD1B RL06 [Dobslaw et al., 2017] is used as a de-aliasing product. Is contains the sum of atmospheric and oceanic contributions to short-term mass changes, and is given in spherical harmonic coefficients valid for certain time spans.

The spherical harmonic synthesis of the de-aliasing model follows Eqs. 4.43 and 4.44. As the data set is given for time intervals, a linear interpolation between the neighbouring sets at time t_1 and t_2 is carried out on the level of spherical harmonic coefficients to obtain the spherical harmonic coefficients at time t_i $(t_1 \le t_i \le t_2)$ by

$$\begin{aligned} c_{nm} &= c_{nm}(t_1)\,\frac{t_2 - t_i}{t_2 - t_1} + c_{nm}(t_2)\,\frac{t_i - t_1}{t_2 - t_1} \qquad \text{and} \\ s_{nm} &= s_{nm}(t_1)\,\frac{t_2 - t_i}{t_2 - t_1} + s_{nm}(t_2)\,\frac{t_i - t_1}{t_2 - t_1} \quad . \end{aligned} \tag{4.60}$$

Accelerations resulting from the de-aliasing model are eventually computed with Eq. 4.43 and Eq. 4.44.

4.6.7 Pole tide

"The pole tide of the solid Earth is generated by the centrifugal effect of polar motion" [Petit and Luzum, 2010, ch. 6.4] and affects only the coefficients c_{21} and s_{21}. It is derived from the polar motion parameters and the mean pole definition via

$$\begin{aligned} c_{21} &= -1.333 \times 10^{-9} \left((x_P - \bar{x}_P) - 0.0115 \, (y_P - \bar{y}_P) \right) \qquad \text{and} \\ s_{21} &= +1.333 \times 10^{-9} \left((y_P - \bar{y}_P) + 0.0115 \, (x_P - \bar{x}_P) \right) \quad . \end{aligned} \tag{4.61}$$

x_P, y_P, $\bar{x}_P$ and $\bar{y}_P$ form the wobble parameters (*Eq.^{IERS} (7.24)*) via

$$m_1 = (x_P - \bar{x}_P) \qquad \text{and} \qquad m_2 = -(y_P - \bar{y}_P) \quad . \tag{4.62}$$

The pole tide and ocean pole tide make use of the most recent secular pole model [IERS, 2018] with

$$\bar{x}_P = 55.0 \times 10^{-3} + 1.677 \times 10^{-3} \, t \qquad \text{and} \qquad \bar{y}_P = 320.5 \times 10^{-3} + 3.460 \times 10^{-3} \, t \quad , \tag{4.63}$$

in units of arc seconds and arc seconds per year, respectively, with t denoting the time interval between the current epoch and J2000.0 in Julian years, thus,

$$t = \frac{t_{\mathrm{MJD}} - t_{\mathrm{MJD}_{2000}}}{365.25} \qquad \text{with} \qquad t_{\mathrm{MJD}_{2000}} = 51\,544.5 \quad . \tag{4.64}$$

Accelerations resulting from the pole tide model are again derived with Eq. 4.43 and Eq. 4.44.

4.6.8 Atmospheric tides

Atmospheric tides are modelled using the AOD1B RL06 product and contain all twelve tidal constituents. The evaluation of the atmospheric tides reads as

$$\begin{aligned} c_{nm} &= \sum_f \left(c^{\cos}_{nm,f} \cos(\theta_f + \chi_f) + c^{\sin}_{nm,f} \sin(\theta_f + \chi_f) \right) \qquad \text{and} \\ s_{nm} &= \sum_f \left(s^{\cos}_{nm,f} \cos(\theta_f + \chi_f) + s^{\sin}_{nm,f} \sin(\theta_f + \chi_f) \right) \quad , \end{aligned} \tag{4.65}$$

where the coefficients $c^{\cos}_{nm,f}$, $c^{\sin}_{nm,f}$, $s^{\cos}_{nm,f}$, $s^{\sin}_{nm,f}$ are given by the model for each tidal frequency f. The angle argument θ_f may be obtained from Eq. 4.51 and the Doodson-Warburg phase correction χ_f may be looked up for each tidal frequency. To compute the accelerations, the spherical harmonic coefficients may be evaluated with Eq. 4.43 and Eq. 4.44.

4.6.9 Ocean pole tide

Similar to the solid Earth pole tide, the ocean pole tide is a result of the centrifugal effect of polar motion on the oceans. The implementation follows the IERS 2010 conventions, using the Desai model [Desai, 2002], which is given in spherical harmonic coefficients, representing a self-consistent equilibrium model. The formulae follow *Eq.^{IERS} (6.23a)* and *Eq.^{IERS} (6.23b)*.

$$\begin{aligned} c_{nm} &= R_n \left(A^{\Re}_{nm} \left(m_1 \gamma_2^{\Re} + m_2 \gamma_2^{\Im} \right) + A^{\Im}_{nm} \left(m_2 \gamma_2^{\Re} - m_1 \gamma_2^{\Im} \right) \right) \qquad \text{and} \\ s_{nm} &= R_n \left(B^{\Re}_{nm} \left(m_1 \gamma_2^{\Re} + m_2 \gamma_2^{\Im} \right) + B^{\Im}_{nm} \left(m_2 \gamma_2^{\Re} - m_1 \gamma_2^{\Im} \right) \right) \quad , \end{aligned} \tag{4.66}$$

where $A_{nm}^{\Re}$, $A_{nm}^{\Im}$, $B_{nm}^{\Re}$,$B_{nm}^{\Im}$ are the coefficients from the model, m_1 and m_2 are the wobble parameters (Eq. 4.62), $\gamma_2^{\Re} = 0.6870$, $\gamma_2^{\Im} = 0.0036$ and the factor R_n is given by

$$R_n = \frac{\omega_{\mathrm{E}}^2 a_{\mathrm{E}}^4 4\pi G\rho}{GM_{\mathrm{E}} g_{\mathrm{eq}}} \left(\frac{1+k_n'}{2n+1}\right) \quad , \tag{4.67}$$

with ω_{E} being the nominal mean Earth's rotation velocity, G the gravitational constant, ρ the density of sea water, g_{eq} the gravity at the equator and k_n' the Love numbers. Accelerations resulting from the ocean pole tide model are again computed by Eq. 4.43 and Eq. 4.44.

Chapter 5

GRACE Follow-On Data Processing

This chapter details the processing of GRACE Follow-On Level 1B data as it is realised at the time of writing (Spring 2022) at the AIUB. The basic processing scheme follows the implementations made by Beutler et al. [2010a,b], Jäggi et al. [2009a, 2011a,b, 2012] and Meyer et al. [2012a,b, 2015, 2016], where they rigorously applied the CMA not only to process kinematic positions but added KBR observables from GRACE to enable high accuracy in temporal gravity field determination.
Based on this processing, several developments concerning a more accurate description of the observation noise have been accomplished in this thesis, namely the use of empirically derived covariances characterising the observation noise [Lasser et al., 2020a], the incorporation of theoretical (pre-launch) noise models, and the application of VCE in different processing steps to either detect and down-weight outliers, or to improve the co-estimated pseudo-stochastic model.

5.1 Operational GRACE Follow-On processing

Monthly GRACE Follow-On gravity fields are operationally computed at the AIUB and released to the public [Lasser et al., 2020b] at the International Centre for Global Earth Models[1][ICGEM, Ince et al., 2019]. The operational routines make use of the processing of GRACE data as it is done a the AIUB since 2009 [Jäggi et al., 2010]. These solutions follow the CMA as adopted by Meyer et al. [2016] with minor updates regarding the background force modelling. They will serve as a reference for the developments made within this thesis and will be denoted subsequently with *classical* approach or the identifier *op*.

The computation scheme for GRACE Follow-On makes use of Level-1B data published by the JPL [Wen et al., 2019]. These are K-band Range-Rate (KBRR), linear accelerations collected by the ACC and attitude information mainly composed of SCA observations, together with in-house computed kinematic positions [Arnold and Jäggi, 2022]. The latter are obtained from the dual-frequency GPS carrier phase observations using the BSW. The procedure of kinematic point positioning is outlined in Sect. 4.3 and follows Švehla and Rothacher [2005] using GPS satellite orbits and clock corrections generated at the Center for Orbit Determination Europe [CODE, Dach et al., 2009, Bock et al., 2009].

[1] `http://icgem.gfz-potsdam.de/`

5.1.1 Parametrisation

The parametrisation for the operational GRACE Follow-On processing essentially continues to adopt the settings from GRACE [Meyer et al., 2016]. The orbit is split into daily arcs in which all orbit parameters are estimated. Only the gravity field coefficients are adjusted on a monthly basis. The orbit is parametrised for each arc and satellite with six initial osculating Keplerian elements (initial conditions), and additionally, by parameters characterising the ACC (see Sect. 5.1.3), which are a bias set up in a Local Orbit Frame (RSW), being composed of radial (R), along-track (S) and cross-track (W) directions and a scaling factor for each of the axes. To compensate for shortcomings in the background force field, be it either noise stemming from the ACCs or the adopted background force models, PCAs are set up in a regular interval of 15 min in R, S and W directions. These empirical accelerations extend the parameter space (significantly) and allow to absorb force model deficiencies to a certain extent, which is driven by the PCA sampling rate and the adopted constraints. PCAs are always constrained to zero, not introducing any regularisation and not provoking singularities due to the co-estimated bias of the ACC. Table 5.1 lists the complete set of orbit parameters for the operational processing of one daily arc.

Table 5.1: Orbit parametrisation for the operational gravity field solutions for each arc (24 h) and satellite.

parameter	# of parameters	remark
osculating elements	6	a, e, i, Ω, ω, u_0
ACC parameters	6	bias and scale in RSW
PCAs	288	every 15 min in RSW
in total	300	per satellite
	600	per 24 h arc for both spacecraft

5.1.2 A priori force field

Temporal gravity field determination from satellite orbit data, where the satellite orbits serve as the primary observations, is governed by the fact that not only non-conservative forces (e.g., atmospheric drag) and conservative forces (e.g., the sought after gravity field) act on the satellite, but also the conservative forces that may not be resolved by the satellites' observation sampling in space and time. Thus, such forces have to be considered beforehand in the orbit integration as known, stemming from various models. Table 5.2 lists the background models used in the operational processing together with orders of magnitude of the modelled accelerations. The resulting accelerations for a GRACE-like orbit are illustrated in Fig. 4.4, where the individual contributions are discussed in more detail.

A special case of background model in the CMA are the linear accelerations measured by the onboard ACCs on each satellite. They are a crucial component of the gravity field recovery process because they provide precise information about the non-conservative forces acting on the satellite due to the space environment along the orbit [Touboul et al., 1999]. This is

Table 5.2: Background models used in the operational GRACE Follow-On data processing. The list is ordered according to the magnitude of the accelerations.

force	model	remark	magnitude
Earth's gravity field	AIUB-GRACE03S static[2]	d/o = 2..160	$\sim 1 \times 10^{-2}\,\mathrm{m\,s^{-2}}$
3rd body attractions	DE421[3]	Sun, Moon Planets	$\sim 1 \times 10^{-6}\,\mathrm{m\,s^{-2}}$
solid Earth tides	IERS 2010 conventions[4]	elastic	$\sim 1 \times 10^{-7}\,\mathrm{m\,s^{-2}}$
ocean tides	FES2014b[5] with linearly interpolated admittances	d/o = 2..100	$\sim 1 \times 10^{-7}\,\mathrm{m\,s^{-2}}$
relativistic corrections	IERS 2010 conventions		$\sim 1 \times 10^{-8}\,\mathrm{m\,s^{-2}}$
dealiasing	AOD1B RL06[6]	d/o = 2..100	$\sim 1 \times 10^{-8}\,\mathrm{m\,s^{-2}}$
pole tide	IERS 2010 conventions		$\sim 1 \times 10^{-8}\,\mathrm{m\,s^{-2}}$
atmospheric tides	AOD1B RL06	d/o = 2..100	$\sim 1 \times 10^{-9}\,\mathrm{m\,s^{-2}}$
ocean pole tide	IERS 2010 conventions[7]	d/o = 2..100	$\sim 1 \times 10^{-9}\,\mathrm{m\,s^{-2}}$

required to separate the non-gravitational accelerations from the gravitational signal, which is ultimately sought-after. Even though the ACC measurements are not models, they are introduced as part of the force model in the orbit and gravity field recovery process, which means there is no way of directly considering their stochastic behaviour in a weight matrix connected to the ACC measurements. The following section gives an overview about the modelling of systematic components of the ACC data with a bias and scale.

5.1.3 Modelling accelerometer data

The ACC data is applied on the right-hand side of the equation of motion (Eq. 4.5) as part of the complete a priori force model, and not on the observation side of the system of equations. ACC data are thus assumed to be free of errors. Still, systematic and stochastic deficiencies of the measuring system need to be compensated. Therefore, in a first step the ACC observations are centred by removing the mean for each axis i

$$\tilde{\boldsymbol{a}}_i := \boldsymbol{a}_i^{\mathrm{org}} - \mathrm{mean}(\boldsymbol{a}_i^{\mathrm{org}}) \quad . \tag{5.1}$$

The measured accelerations are much higher sampled (1 Hz) than the kinematic positions (0.1 Hz) or inter-satellite range-rates (0.2 Hz for the KBR, 0.5 Hz for the LRI). In the data processing always the nearest neighbouring acceleration is taken into account.
The vector of unknown parameters $\boldsymbol{x}$ is extended by satellite-specific parameters characterising the low-frequency ACC behaviour. In the CMA the ACC parameters are estimated in RSW frame. The formulation for the accelerations $\boldsymbol{a}^{\mathrm{RSW}}(t)$ in RSW frame reads as

$$\boldsymbol{a}^{\mathrm{RSW}}(t) = \boldsymbol{b} + \mathbf{S}\ \mathbf{R}_{\mathrm{SRF}}^{\mathrm{RSW}}(t)\ \tilde{\boldsymbol{a}}(t) \quad , \tag{5.2}$$

[2] Jaeggi et al. [2011]
[3] Folkner et al. [2009]
[4] Petit and Luzum [2010]
[5] Carrere et al. [2016]
[6] Dobslaw et al. [2017]
[7] Desai [2002]

where the bias $\boldsymbol{b}$ is an unknown constant shift in the measurements (e.g., due to temperature variations) and $\mathbf{R}_{\mathrm{SRF}}^{\mathrm{RSW}}$ is the transformation matrix from the Science Reference Frame (SRF) into the RSW, which is realised by the satellite's position and velocity vectors ($\boldsymbol{r}$, $\dot{\boldsymbol{r}}$) and the ATT measurements with the SCA. $\mathbf{S}$ denotes the scaling matrix of the accelerations

$$\mathbf{S} = \begin{bmatrix} s_{\mathrm{R}} & \alpha+\zeta & \beta-\varepsilon \\ \alpha-\zeta & s_{\mathrm{S}} & \gamma+\delta \\ \beta+\varepsilon & \gamma-\delta & s_{\mathrm{W}} \end{bmatrix} \quad . \tag{5.3}$$

Ideally, $\mathbf{S}$ is an identity matrix, but at least the magnitude of the accelerations needs to be scaled by the diagonal elements of the scale matrix in the analysis of the ACC data. Additionally, the off-diagonal elements, represented as infinitesimal rotations, may be adjusted, where the symmetric components $\{\alpha, \beta, \gamma\}$ describe a shear of the ACC axes, thus, that they do not form a strictly orthogonal coordinate system, and the skew-symmetric components $\{\zeta, \varepsilon, \delta\}$ define a mis-alignment between the ACC axes and the reference frame of the satellite which should be perfectly parallel [Kim, 2000]. As Klinger and Mayer-Gürr [2016] showed, the co-estimation of a full scale matrix for the ACC significantly improves the low degree spherical harmonics, especially the c_{20} coefficient.

In the CMA the ACC parameters are estimated on arc-wise level. This seems to be a reasonable choice for the bias, however, the scaling should be more stable. Nevertheless, best results are achieved with a arc-wise scaling, even though the estimates are strongly fluctuating (see Fig. 5.2, Fig. 5.3 and Fig. 5.4).
For GRACE Follow-On the challenge arises to correctly deal with the degraded ACC data due to the instruments under-performance on GF2 [Bandikova et al., 2019, Landerer et al., 2020]. This motivated the generation of a so-called Accelerometer Transplant (ACT) product released by the JPL (named *JPL-ACT*) to 'transplant' the accelerations captured by GF1 in space and time to GF2 to have a best-possible characterisation of the non-conservative forces on GF2. The approach is only data driven and explained in detail in Bandikova et al. [2019]. The second ACT product available at the time of writing (Spring 2022), named *TUG-ACT*, uses a remove-restore approach based on a priori force models to first remove all known signal from the accelerations and applying the transplant from GF1 and GF2 in space and time only to the residual signal, see Behzadpour et al. [2021].
When co-estimating the bias and scale factors with the CMA, significant differences arise when adopting the two different ACT products in the data processing. Three scenarios are discussed here. The first one is to use the remove-restore transplant data (TUG-ACT), which is also used in the the operational processing, and estimate only a diagonal scale matrix. In the second and third scenario the JPL-ACT accelerations are introduced for GF2, either estimating only a diagonal scale matrix or a full scale matrix. The fourth option of estimating a full scale matrix when using the TUG-ACT product is not shown because it does not improve the solution any further. It is in fact a good indicator of quality for the TUG-ACT product that no additional shear and mis-alignment parameters are required.
All figures showing the estimated ACC parameters contain the estimates for GF2. The estimates for GF1 look alike because due to the orbit parameter transformation (see Sect. 4.5.1), which includes the ACC parameters, the mean and difference between the two spacecraft of each parameter is determined and the solutions of the parameters for the

individual satellites are computed by a back-transformation.

The estimated bias parameters (Fig. 5.1) in R and W directions do not show significant differences between the three cases. It may be noted that the W bias is very susceptive to the β' angle, i.e., the position of the Sun above the orbital place, thus, the geometry with respect to the position of the Sun, which has a period of 322 days. This may be related to the mentioned temperature variations. The bias in radial direction on other hand features

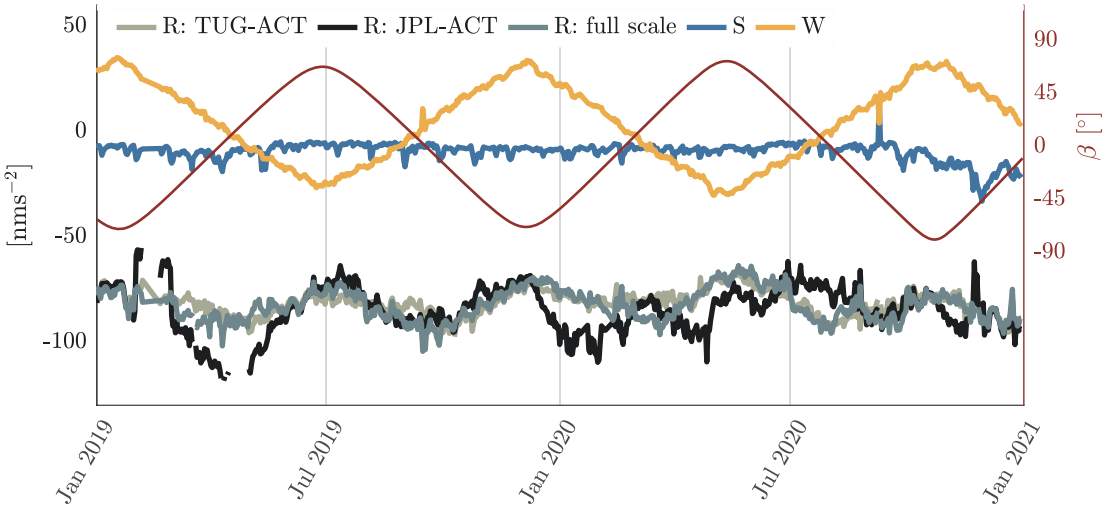

Figure 5.1: Daily ACC biases for two years of GF2 co-estimated in the monthly gravity field recovery for the TUG-ACT and the JPL-ACT products.

large variations, in particular for the JPL-ACTs. Estimating a diagonal scale matrix for these observations is not sufficient to absorb the deficiencies of the transplant product. Extending the parametrisation by the off-diagonal elements of the scale matrix significantly improves the result, which can be seen in Fig. 5.5.

The scale elements exhibit a similar pattern for the R axis (Fig. 5.2), where the TUG-ACT is slightly nosier than the full scale matrix, however, both being close to one. It shows a significant improvement due to a change of the parametrisation when using the poorer JPL-ACTs. The scaling factors in S direction, depicted in Fig. 5.3, are stable with a mean

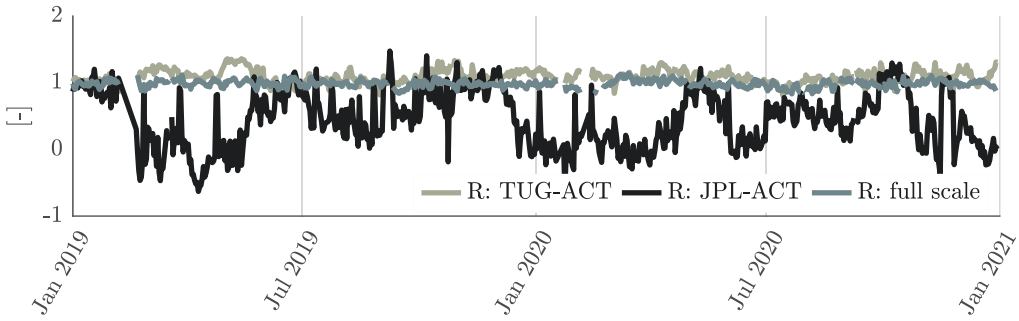

Figure 5.2: Daily ACC scale in R direction for two years of GF2 estimated in the monthly gravity field recovery for the TUG-ACT and the JPL-ACT products.

of about 1 for the TUG-ACTs, while the two others are close to each other, which implies that the S behaviour might actually be caused by the different nature of the transplant products, not only by the parametrisation. The W scale factors (Fig. 5.4) feature the oppo-

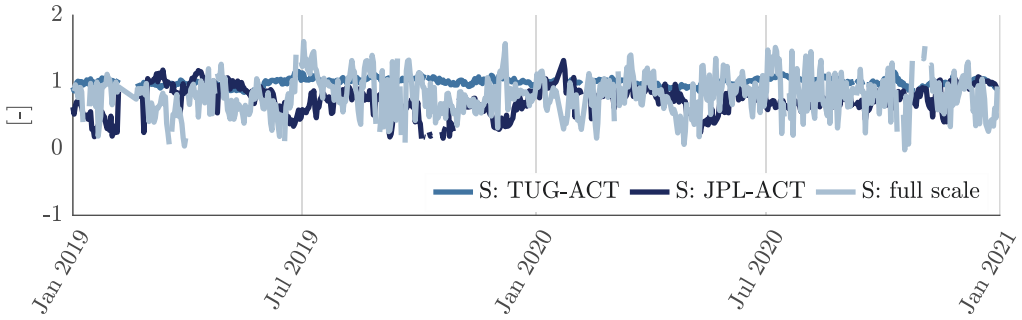

Figure 5.3: Daily ACC scale in S for two years of GF2 estimated in the monthly gravity field recovery for the TUG-ACT and the JPL-ACT products.

site behaviour than the S scale factors. Here, the full scale matrix provides the most stable estimates, being centred around 1, while the other two approaches provide the same but less stable results. Thus, the estimates in W direction are clearly influenced by the parametrisation, but they do not depend on the quality of the ACT product. All those investigations

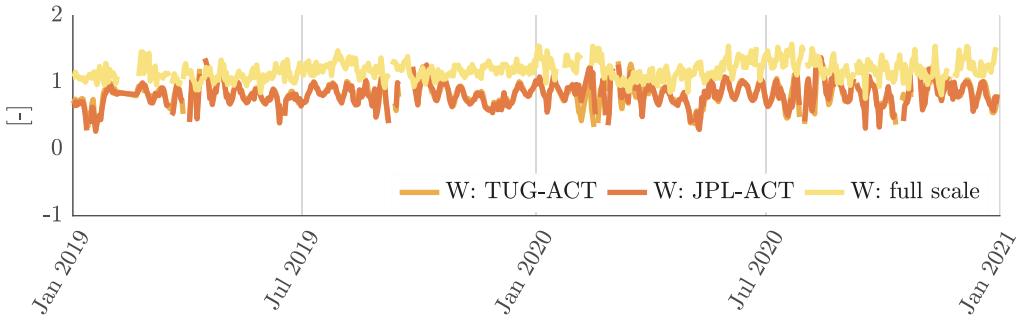

Figure 5.4: Daily ACC scale in W direction for two years of GF2 estimated in the monthly gravity field recovery for the TUG-ACT and the JPL-ACT products.

are most relevant for a full gravity field solution. Figure 5.5 shows the Root Mean Square (RMS) over the oceans for the three investigated scenarios. The RMS over the oceans is a method of globally assessing the noise in gravity field solutions. It should be small since all oceanic signals causing changes in the gravity field are supposed to be reduced by the tidal and non-tidal de-aliasing models. Therefore, the remaining signal over the oceans is a widely used indicator for the quality of a solution. The RMS over the oceans is referenced to a mean signal model from GRACE Follow-On and a 400 km Gauss filter [Wahr et al., 1998] is applied to emphasise the low-frequency signal contained in the solution. It clearly displays the best performance with the lowest RMS for the remove-restore ACT product from TUG. Co-estimating a full scale matrix is a crucial piece of the parametrisation when using the JPL-ACT data. One may note that these investigations refer to a period of low solar activity. Since accelerometers are very sensitive to the environment [see e.g., Meyer et al., 2016], the model-based approach might deteriorate when models start to deviate.

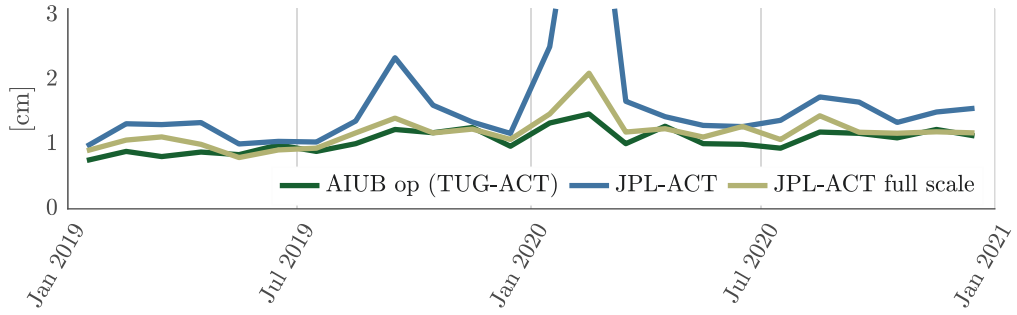

Figure 5.5: Monthly RMS over the oceans for two years of GRACE Follow-On using the TUG-ACT product and the JPL-ACT product as ACC data for GF2, including a change of the parametrisation to a full scale matrix for the JPL-ACTs.

5.1.4 Processing chain

The operational processing is realised by the application of three main programmes of a development version of the BSW: *GRAVDET2*, *ORBDIFF* and *ADDNEQ2*. These programmes are called in the sequence depicted in Fig. 5.6. First, the programme GRAVDET2

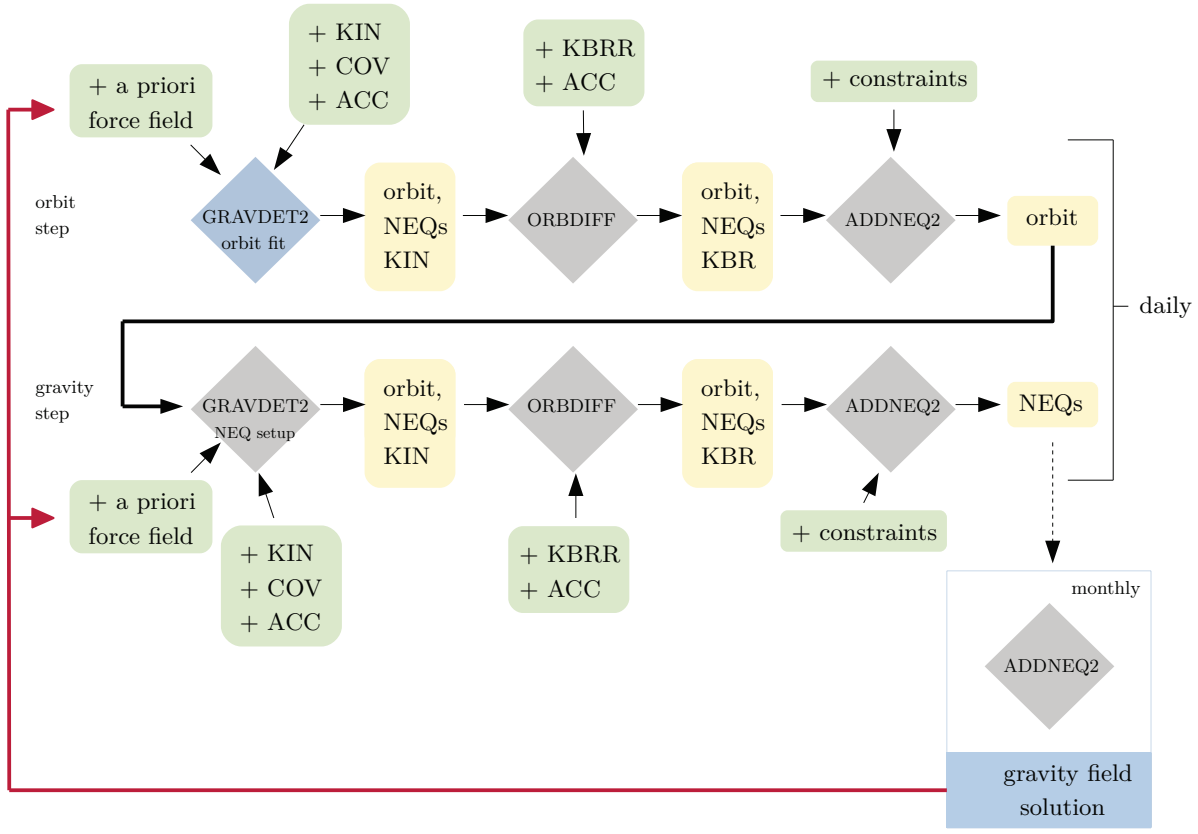

Figure 5.6: Flowchart of the operational GRACE Follow-On processing. Starting point is the blue GRAVDET2 square. The red line indicates an iteration loop (if necessary).

is called for each arc and satellite to process kinematic positions (upper left blue square in Fig. 5.6). In this step, the kinematic positions of each satellite are taken as (pseudo-)ob-

servations in a 10 s sampling to fit an a priori reduced-dynamic orbit for each spacecraft. The background force models applied are listed in Table. 5.2 and include ACC and ATT observations. The parametrisation of the reduced-dynamic orbit may be found in Table 5.1. To guarantee an invertible normal equation matrix, loose constraints are applied on the pseudo-stochastic parameters (see Sect. 3.2.2, the numbers are given in Table 5.3). The magnitudes of the constraints are deliberately chosen to characterise a loose constraining in order to also enable the use of a priori gravity field models from the pre-CHAMP era, e.g., the Earth Gravitational Model from 1996 [EGM96, Lemoine et al., 1998].

Table 5.3: Constraints applied for the operational solution for each pseudo-stochastic parameter when using kinematic positions as observations.

satellite	direction	constraint [$\mathrm{m\,s^{-2}}$]	satellite	direction	constraint [$\mathrm{m\,s^{-2}}$]
	R	1×10^{-8}		R	1×10^{-8}
GF1	S	1×10^{-8}	GF2	S	1×10^{-8}
	W	1×10^{-8}		W	1×10^{-8}

The next programme called is named ORBDIFF (first grey square in the upper row of Fig. 5.6). It deals with two separate tasks. The first one is to set up NEQs along the a priori orbits from the previous GRAVDET2 run by applying Eq. 4.36 and Eq. 4.37 based on the KBRR. The parametrisation is taken over from the a priori orbits. If biased ranges are processed instead of KBRR, the K-band bias parameters are set up as well. Secondly, ORBIDIFF performs the orbit transformation of all orbit parameters to the SUM between the two satellites and the DIFF, which is explained in Sect. 4.5.1. This is done on normal equation level for the NEQs based on kinematic positions and for the NEQs based on the inter-satellite ranging data.

The last programme of the processing chain, ADDNEQ2, covers normal equation handling [Brockmann, 1996]. It allows for an efficient manipulation of NEQs. In the context of its call in the first row of the flowchart (upper right grey square) it is used to accumulate NEQs for each arc, thus combining the NEQ based on the kinematic positions and the NEQ based on the KBRR. After combining the two NEQs, constraints for the pseudo-stochastic parameters are applied (see Table 5.4, second row) and the solution for the reduced-dynamic a priori orbit (now based on kinematic positions and KBRR observations) is computed. The constraints are tightened compared to the GRAVDET2 solution, as now the KBRR play a major role in determining the solution.

Table 5.4: Constraints applied for the operational solution for each pseudo-stochastic parameter when using kinematic positions and KBRR observations.

type	direction	constraint [$\mathrm{m\,s^{-2}}$]	type	direction	constraint [$\mathrm{m\,s^{-2}}$]
	R	3×10^{-9}		R	3×10^{-11}
SUM	S	3×10^{-9}	DIFF	S	3×10^{-11}
	W	3×10^{-9}		W	3×10^{-11}

The NEQ based on the kinematic positions - mainly influencing the SUM component of

parameters because of the sensitivity of kinematic positions to absolute parameters - is down-weighted by a factor of 100 as described in Sect. 5.1.5. This implies that the pseudo-stochastic SUM parameters are in fact constrained by

$$\sigma_{\mathrm{R}}^{\mathrm{SUM}} = \sigma_{\mathrm{S}}^{\mathrm{SUM}} = \sigma_{\mathrm{W}}^{\mathrm{SUM}} = \frac{1}{\sqrt{100}} \cdot 3 \times 10^{-9} = 3 \times 10^{-10}\,\mathrm{m\,s^{-2}} \quad , \tag{5.4}$$

a number roughly characterising the ACC noise (see Sect. 5.5.2).
With this, the a priori orbits for each arc and satellite based on kinematic positions and KBRR are established.

The second row in the flow chart (Fig. 5.6) now refers to the *gravity-step*, where the previously determined a priori orbits are used to call the same sequence of programmes not only to set up the orbit-related parameters $\boldsymbol{o}$, but to extend the parameter space with the gravity field coefficients $\boldsymbol{g}$. In accordance with the SDS [e.g., Save, 2019] the spherical harmonic expansion of the unknown gravity field coefficients is truncated at $\mathrm{d/o} = 96$ for a monthly solution.
In contrast to the generation of the a priori orbit, ADDNEQ2 additionally pre-eliminates (see Sect 3.2.3) the orbit parameters on the level of each arc after having combined the daily NEQs based on kinematic positions and KBRR data to allow for an efficient solution of the monthly gravity field. This reduces the dimensions of the NEQ to be solved drastically. Before the pre-elimination the constraints on the pseudo-stochastic parameters have to be applied. It is important to note that they are constrained to zero and not to the a priori values from the a priori orbit. Otherwise, a regularisation towards the underlying a priori orbit (and consequently, the a priori force field - including the a priori gravity field) would be introduced into the solution. The arc-wise ADDNEQ2 (second row) does not compute a solution of the normal equation system because the arc-wise gravity field coefficients are neither of interest nor is the corresponding normal equation matrix regular due to the insufficient ground-track coverage.

Eventually, the programme ADDNEQ2 is called again after the arcs are processed to accumulate all (daily) NEQs together to compute a monthly gravity field solution.

It is important to emphasise that this sort of a two-step approach, where the a priori orbit generation is separated from the NEQ setup of the joint orbit and gravity field solution, does not introduce any bias since all parameters are jointly estimated eventually in one common adjustment where all constrained parameters are constrained to zero. In principle the first and second step (orbit-step and gravity-step) could be executed in one common process. It turned out, however, that the a separation into an a priori orbit, which serves as a Taylor point, and a gravity field step is more efficient [see e.g., Prange, 2010, Beutler et al., 2010b].

After having computed a monthly gravity field solution, iterations may be applied by using the just-estimated gravity field as the new a priori gravity field in the background force field to repeat the orbit- and gravity-step in order to compute a new solution (indicated by the red arrow in the flowchart). Such an iterative procedure is necessary if certain quantities shall be derived in the estimation process without introducing a regularisation

towards the a priori gravity field as the latter then already stems from an independent solution. The iterative procedure is applied for the block-wise VCE (Sect. 5.3.2) and the derivation of empirical covariances (Sect. 5.5.1 and Sect. 5.5.2).

5.1.5 Relative weighting between observation types

Even though both observation types (KIN and KBRR) are supposed to contribute with their own precision to the overall gravity field solution, it turns out that assigning a weight to the kinematic positions based on a rough estimate of the original carrier phase observations is detrimental [see e.g., Meyer et al., 2016]. This has been suggested already in Sect. 4.5. Thus, by empirical fine tuning, the contribution of the kinematic positions is down-weighted with a $\sigma_\mathrm{e} = 10$ by

$$\mathbf{N}_\mathrm{KIN}^\mathrm{dwn} = \frac{1}{\sigma_\mathrm{e}^2}\mathbf{N}_\mathrm{KIN} = \frac{1}{100}\mathbf{N}_\mathrm{KIN} \quad . \tag{5.5}$$

The a priori variance of the kinematic positions is taken from the daily a posteriori estimation of the variance of unit weight $\hat{\sigma}_{0,\mathrm{KIN}}^2$ of the kinematic point positioning (see Sect. 4.3), where the a priori variance of the L1 and L2 carrier phase observations was chosen to be $\sigma_{0,\mathrm{ph}}^2 = 1\,\mathrm{mm}$. The KBRR observation are assumed to have a fixed precision of $\sigma_{0,\mathrm{KBRR}} = 3 \times 10^{-7}\,\mathrm{m\,s^{-1}}$. The relative weighting between kinematic positions and KBRR is applied when the corresponding NEQs are accumulated (cf. Fig. 5.6 upper right grey square) by

$$\mathbf{N}_\mathrm{full} = \frac{\sigma_0^2}{\hat{\sigma}_{0,\mathrm{KIN}}^2}\frac{1}{\sigma_\mathrm{e}^2}\mathbf{N}_\mathrm{KIN} + \frac{\sigma_0^2}{\sigma_{0,\mathrm{KBRR}}}\mathbf{N}_\mathrm{KBRR} \quad , \tag{5.6}$$

where σ_0^2 may be arbitrarily chosen, e.g., set to the a priori variance of the KBRR observations. Such a down-weighting also affects the effect of the adopted constraints since the latter act relative to the magnitude of the normal equation matrix (Eq. 3.43). Another way of down-weighting the contribution of the kinematic positions is to use them at a reduced sampling, e.g., instead of 10 s only every 5 min as it was done e.g., by Mayer-Gürr et al. [2018]. This, however, might be problematic for the estimation of the PCAs with 15 min spacing.

A negative impact of GPS information is visible in the post-fit residuals. Figure 5.7a-e shows ASDs (see Sect. 3.4) of KBRR post-fit residuals for January 2019 where no down-weighting is adopted and the gravity field is estimated up to $\mathrm{d/o} \in \{30, 60, 70, 96, 120\}$. A clear jump appears at the frequency corresponding to the maximum degree of the estimated gravity field for $\mathrm{d/o} > 60$, which one may assign to the insufficient contribution of the kinematic positions to the high degrees of the gravity field. Figure 5.7f is the reference case where a down-weighting is performed according to Eq. 5.5. Estimating gravity fields up do $\mathrm{d/o} = 96$ for different weighting ratios, shows the best agreement with the monthly CSR solution for $\sigma_e = 10$ (Fig. 5.8a). Note that adapting the pseudo-stochastic model using VCE (see Sect. 5.3.3) allows for an adequate estimation of the gravity field in all but one cases where no down-weighting of the kinematic positions is applied. Between an empirical variance of $\sigma_e = 1$ and $\sigma_e = 5$ the detrimental contribution of the kinematic positions cannot be suppressed by the pseudo-stochastic parameters anymore.

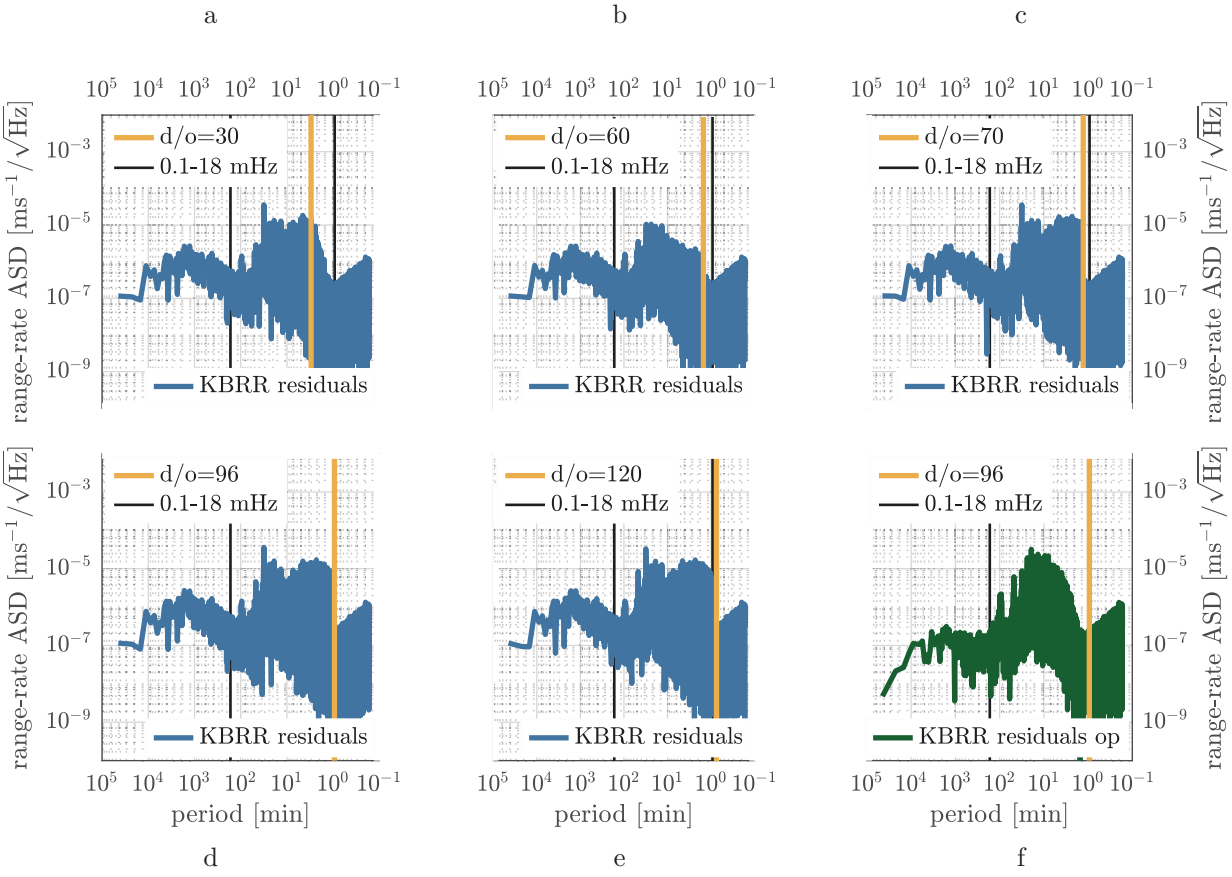

Figure 5.7: ASDs of post-fit residuals of gravity field estimations up to d/o $\in \{30, 60, 70, 96, 120\}$ without down-weighting the kinematic positions (a-e) and the corresponding post-fit residuals of the operational solution (f).

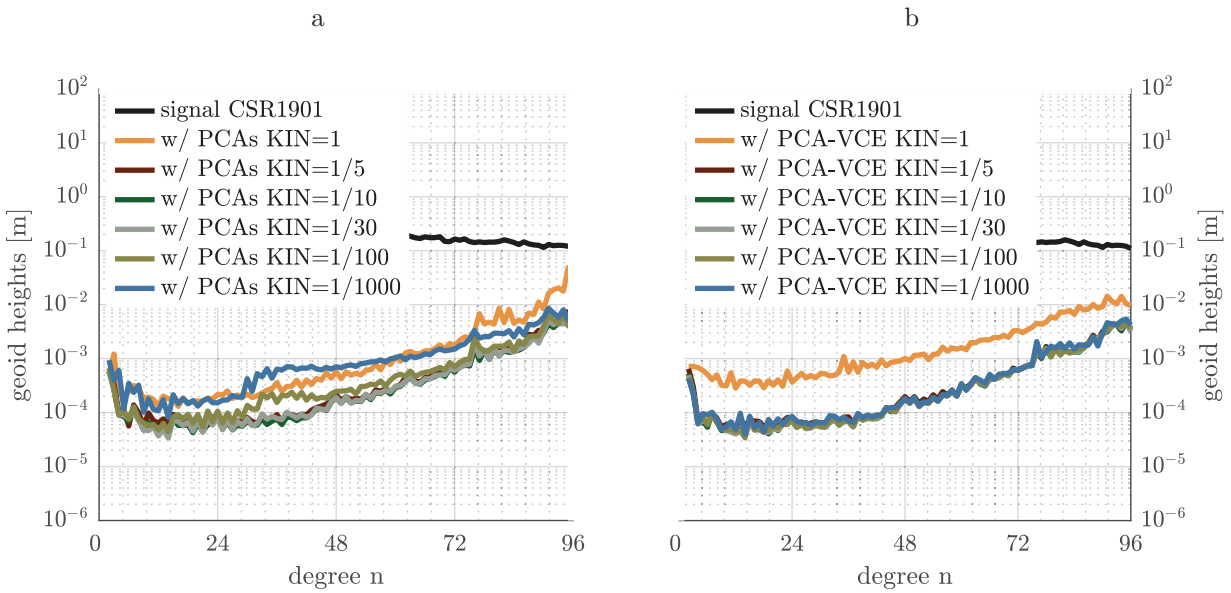

Figure 5.8: Difference degree amplitudes for different down-weighting ratios of the NEQs based on the kinematic position (a) and using an accordingly adapted co-estimated pseudo-stochastic model (b).

5.1.6 Pseudo-stochastic modelling with PCAs

GRACE Follow-On gravity field recovery is not only affected by the observation noise of the KBR observations and kinematic positions. The background force field is composed of models (see Sect. 4.6), which are prone to deficiencies and may, therefore, describe the true signals only to a certain extent. Furthermore, the ACC and ATT data is introduced as noise free on the right-hand side of the equation of motion (Eq. 4.5). Even though a bias and scaling factor are estimated to reduce ACC measurement's shortcomings, the stochastic noise of these observations is not taken into account. Several options of dealing with such deficiencies are introduced later in this thesis for the different observations types (Sect. 5.5).
The focus of the following remarks is on the extension of the parameter space by co-estimating additional artificial parameters [Jäggi, 2007, Beutler et al., 2010b] to compensate for various deficiencies emerging in the formulation of the problem of gravity field recovery from GRACE Follow-On. This method is applied in the operational GRACE Follow-On processing scheme and is commonly used in the gravity field determination with the CMA, e.g., Jäggi et al. [2011a, 2016], Meyer et al. [2016] or [Prange et al., 2009]. As already out-

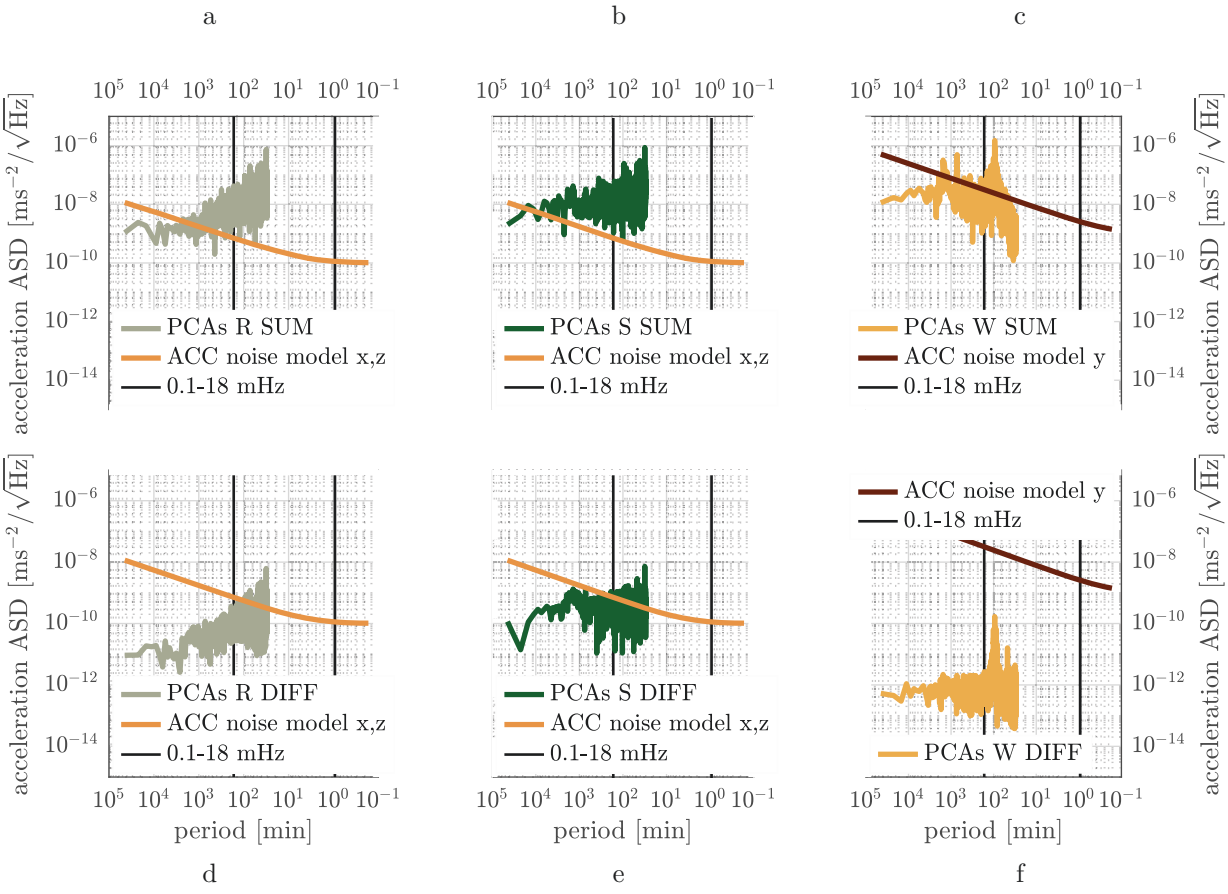

Figure 5.9: ASDs of co-estimated PCAs of the classical solution for January 2019 for each direction and parameter type (first row SUM, second row DIFF). For comparison a theoretical pre-launch ACC model is depicted in each graph.

lined in Sect. 5.1.4, Piecewise-Constant Accelerations (PCAs) are set up in regular intervals of 15 min, with expected values of zero and a priori known (empirically derived) standard

deviations (Table 5.4), and co-estimated together with the other orbit and gravity field parameters. These additional parameters are supposed to absorb noise contained in the system of equations - be it observation noise or due to the deficient background force field. Figure 5.9a-f shows the ASDs of the co-estimated PCAs of the operational solution for January 2019 for each direction and parameter type (SUM and DIFF). The vertical black lines denote the frequencies related to a gravity field solution setup from d/o $\in \{2, ..., 96\}$ (0.1 mHz - 18 mHz). As a reference a simple theoretical model for the ACC noise from Kim [2000] is also given, it will be introduced in more detail later in Sect. 5.5.2. The agreement with the model is rather limited, especially in the W axis of the SUM-parameters. This, however, may be explained by the fact that DIFF-parameters are dominated by the KBRR observations, which are not directly sensitive to cross-track signals. The other axes show that not only the ACC noise, as described by the model, is absorbed by the PCAs but further noise sources as well. Only the along-track DIFF-PCAs seem to more or less reflect the modelled ACC noise, to be seen even more clearly in Fig. 5.10a, where the accelerations are integrated to velocities. The extension of the parameter space by the PCAs causes a flatter spectrum in the post-fit residuals compared to the case of not estimating for PCAs (Fig. 5.10b) because the model is able to better fit the observations (depending on the PCAs' sampling and adopted constraining). The PCAs, even though they are valid for an interval of 15 min, affect the entire spectrum of post-fit residuals with a clear impact on periods greater than 30 min (the Nyquist period). Consequently, an influence on the whole spectral domain of the gravity field is to be expected, not only on coefficients which are sampled with the 15 min interval ($\sim$ d/o $\in \{2, ..., 10\}$). The $1/f^2$-noise of the ACC is still

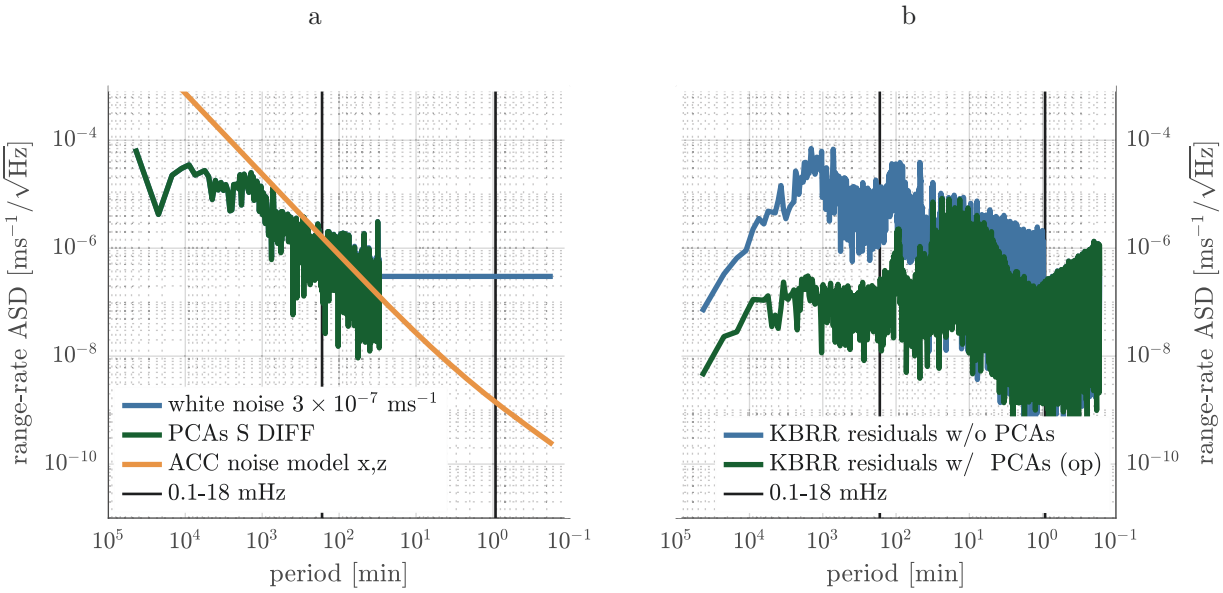

Figure 5.10: ASDs of the co-estimated pseudo-stochastic model compared to a theoretical pre-launch ACC characterisation, expressed in velocities (a) and ASDs of KBRR post-fit residuals of a solution with PCAs and a solution without PCAs for January 2019 (b).

dominating the lower frequencies, even though partly absorbed by PCAs with effects on the entire spectrum.

A comparison of the resulting gravity fields using the pseudo-stochastic parameters

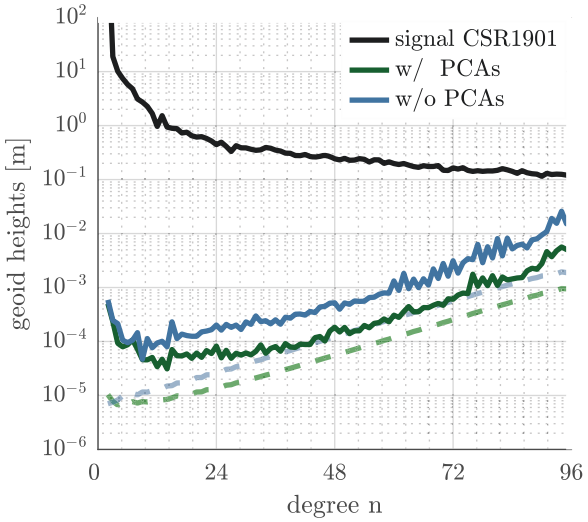

Figure 5.11: Difference degree amplitudes for a monthly solution (January 2019) when applying the co-estimation of PCAs to account for deficiencies in the system of equations (light blue curve) and omitting any noise treatment (dark blue curve).

as a noise model and omitting any further noise modelling reveals the large impact of the PCAs (Fig. 5.11). The solution without any noise modelling is severely degraded because the gravity field coefficients absorb a significant part of the noise in the observations and background force models. The extension of the parameter space with the PCAs allows for an effective absorption of noise, depending on the magnitude of the adopted constraints. If constraints are set very loose the PCAs will absorb gravity field signal as well. This can be seen e.g., in Fig. 5.8a (orange curve) when the down-weighting was too weak.

5.2 Computational efficiency

Efficient and fast computing is a prerequisite for up-to-date gravity field recovery since data is manifold and decade long observation series are available. The processing routines in the gravity-branch of the BSW software have been updated to make use of the Basic Linear Algebra Subprograms [BLAS, Lawson et al., 1979] and the Linear Algebra Package [LAPACK, Anderson et al., 1999] for fast and efficient computing. The software uses Intel's Fortran compiler (ifort), therefore, the native Math Kernel Library (MKL) is adopted to perform low-level linear algebra operations (BLAS), as well as higher level computations, such as solving systems of linear equations (LAPACK).

A special emphasis is given to the efficient handling when setting up and dealing with NEQs. The time consuming matrix-matrix multiplication $\mathbf{N} = \mathbf{A}^{\mathrm{T}}\mathbf{P}\mathbf{A}$ is separated into two parts, one being the operation

$$\mathbf{P}\mathbf{A} = \mathbf{P} \cdot \mathbf{A} \ , \tag{5.7}$$

where in case of $\mathbf{P} = \mathbf{I}$ this reduces to

$$\mathbf{P}\mathbf{A} = \mathbf{A} \ . \tag{5.8}$$

If $\mathbf{P}$ is a diagonal matrix, the elements p_{ii} are applied accordingly. Only when having a full weight matrix at hand, the BLAS Level-3 routine DSYMM[8] is used to compute the product of the two matrices, where the symmetry of $\mathbf{P}$ is exploited.

[8]Double precision SYmmetrical Matrix-Matrix multiplication

Note that due to internal storage structures of the software the characteristic of certain matrices of being triangular or sparse is not yet fully taken into account and no BLAS routine for triangular matrices is applied (e.g., DTRMM[9] and DTRMV[10]).
Afterwards, the full normal equation matrix $\mathbf{N} = \mathbf{A}^{\mathrm{T}} \cdot \mathbf{PA}$ is calculated by general matrix-matrix multiplication with the BLAS Level-3 DGEMM[11]-subroutine. This part takes most of the computational resources as it demands $\mathcal{O}(N \cdot M^2)$ floating point operations with N being the number of observations and M the number of unknown parameters.
The right-hand side of the normal equations $\boldsymbol{b}$ is calculated by matrix-vector multiplication, first applying the BLAS Level-2 routine DGEMV[12] to

$$\boldsymbol{b} = \mathbf{A}^{\mathrm{T}}\mathbf{P}\boldsymbol{\ell} = (\mathbf{PA})^{\mathrm{T}} \cdot \boldsymbol{\ell} \ , \tag{5.9}$$

where the product $\mathbf{PA}$ is already known from the computation of the normal equation matrix $\mathbf{N}$ and needs only to be used in its transposed form in DGEMV.
The sum of the squared and weighted observations Λ is calculated by matrix-vector multiplication, first applying the BLAS Level-2 routine DSYMV[13] to

$$\mathbf{P}\boldsymbol{\ell} = \mathbf{P} \cdot \boldsymbol{\ell} \ . \tag{5.10}$$

If $\mathbf{P} = \mathbf{I}$, $\mathbf{P}\boldsymbol{\ell} = \boldsymbol{\ell}$ holds, and in case of $\mathbf{P}$ being a diagonal matrix $\mathbf{P}\boldsymbol{\ell}$ is computed as the Schur product (element-wise product) between the two vectors

$$\mathbf{Pl} = \mathrm{diag}(\mathbf{P}) \circ \boldsymbol{\ell} \ . \tag{5.11}$$

Finally applying the inner product using BLAS's Level-1 DDOT[14] routine

$$\Lambda = \boldsymbol{\ell}^{\mathrm{T}}\mathbf{P}\boldsymbol{\ell} = \langle \boldsymbol{\ell}, \mathbf{P}\boldsymbol{\ell} \rangle \tag{5.12}$$

the weighted sum of the observations squared is efficiently computed.

The possibility of directly using the BLAS routines (DGEMM and DGEMV) for an efficient stacking of the NEQs ($\mathbf{N}$ and $\boldsymbol{b}$) as explained in Sect. 3.2.4 is not utilised as it would interfere with a VCE on block-wise observation level (see Sect. 5.3.2).

Solving large normal equation systems, which (temporal) gravity field solutions usually are, with the number of parameters easily ranging from 10'000 (only gravity field coefficients) up to 70'000 (including orbit and pseudo-stochastic parameters), is very time consuming. The general inversion (Gauss-Jordan elimination) requires $\mathcal{O}(M^3)$ operations, with M denoting the rank of the normal equation matrix. Exploiting that $\mathbf{N}$ is a symmetric, positive-definite matrix a Cholesky decomposition may be applied, i.e.,

$$\mathbf{N} = \mathbf{L}\mathbf{L}^{\mathrm{T}} \tag{5.13}$$

[9] Double precision TRiangular Matrix-Matrix multiplication
[10] Double precision TRiangular Matrix-Vector multiplication
[11] Double precision GEneral Matrix-Matrix multiplication
[12] Double precision GEneral Matrix-Vector multiplication
[13] Double precision SYmmetrical Matrix-Vector multiplication
[14] Double DOT product

holds, where $\mathbf{L}$ is a lower triangular matrix. The solution may then be computed by forward and backward substitution (as in a Gaussian elimination) with

$$\mathbf{L}\boldsymbol{y} = \boldsymbol{b} \qquad \text{and} \qquad \mathbf{L}^{\mathrm{T}}\boldsymbol{x} = \boldsymbol{y} \ , \tag{5.14}$$

where $\boldsymbol{y}$ is an intermediate solution and $\boldsymbol{x}$ is the final solution. These steps are efficiently computed with the LAPACK subroutines DPOTRF[15] (Cholesky factorisation in Eq. 5.13), DPOTRS[16] (forward and backward substitution in Eq. 5.14).

For several applications, such as VCE or the estimation of the formal errors of the gravity field coefficients, $\mathbf{N}^{-1}$ has to be known explicitly. Therefore, the LAPACK routine DPOTRI[17] is utilised to calculate the corresponding inverse from the Cholesky-factorised lower triangular matrix $\mathbf{L}$.

The optimisation of computing the inverse via LAPACK's DPOTRF and DPOTRI is also utilised in the computation of the weight matrix $\mathbf{P}$ from a cofactor matrix $\mathbf{Q}$, derived either from theoretical values, covariance propagation, or empirical modelling.

Processing one iteration of a monthly gravity field solution (thus, a classical solution) with all these changes in the handling of the NEQs, the computation time for all parameters is reduced by about 90 % from more than five hours to about 40 min on the current aiub-nodes at the UBELIX[18] cluster, a partition with seven nodes and 20 sCPUs (cores) each, providing 823 GB of memory[19]. The largest gain in run time stems from GRAVDET2 and ORBDIFF (from the processes of setting up the corresponding NEQs) and the more efficient way of computing the solution in ADDNEQ2. Table 5.5 gives a comparison of the run time and peak memory usage between two processing settings of a 30-day classical gravity field solution, either by pre-eliminating the local orbit-related parameters on arc-wise level (denoted as case a.), or keeping all parameters explicitly in the NEQs (case b.), when running with and without BLAS and LAPACK optimisations. The two computation methods yield the numerically same results, however, the computation times for the final solution differ. The drawback of using the BLAS and LAPACK routines as implemented in the development version of the BSW lies in the memory handling as for almost every step in the computation the peak memory usage doubles due to the additional memory required to store interim results.
A further point of optimisation in the processing scheme may be added here as well. BLAS and LAPACK routines are best performing for large matrices. For small arrays, the straightforward implementation using loops (and/or Fortran's intrinsic procedures) may be even faster. Thus, by e.g., reducing the block length in the sequential least squares (see Sect. 3.2.4) a high computational efficiency may be achieved. This comes with the drawback that only correlations between observations within one block may be taken into account in the weight matrix $\mathbf{P}$. Naturally, smaller blocks in the LSQA are less demanding in terms of memory consumption. Fortunately, the current CPUs mounted in the aiub-nodes provide

[15] Double precision PO→symmetric matrix TRiangular Factorisation
[16] Double precision PO→symmetric matrix in TRiangular structure to Solve
[17] Double precision PO→symmetric matrix in factorised TRiangular structure to compute its Inverse
[18] University of Bern Linux Cluster `http://www.id.unibe.ch/hpc`
[19] AMD EPYC microprocessors

Table 5.5: Comparison of memory consumption (peak memory usage) and run time for a 30-day classical monthly gravity field solution with and without making use of BLAS and LAPACK.

	#-parameters	peak memory [MB] w/o BLAS	peak memory [MB] w/ BLAS	run time [hh:mm:ss] w/o BLAS	run time [hh:mm:ss] w/ BLAS
case a.					
a priori orbit	300	134	137	00:08:30	00:06:30
NEQ setup (KIN)	9705	768	1520	00:44:30	00:11:00
NEQ setup (KBRR)	10005	718	1500	00:16:40	00:04:10
solution	9405	1326	1687	00:14:30	00:05:40
				$\sum$ 01:14:10	$\sum$ 00:27:20
case b.					
a priori orbit	·	·	·	·	·
NEQ setup (KIN)	·	·	*see case a.*	·	·
NEQ setup (KBRR)	·	·	·	·	·
solution	27405	4012	9243	04:02:00	00:17:20
				$\sum$ 05:14:10	$\sum$ 00:39:00

enough capacity that memory consumption is not hindering the computation with large blocks. Typically, at maximum up to 16 GB of RAM per arc may be occupied.

The processing itself is executed arc-wise for each month. All arcs are computed in parallel and when finished the final script accumulates the arc-wise NEQs to allow for the calculation of a monthly gravity field solution. With the current settings of the aiub-queue maximum 64 jobs per user may be processed at the same time, hence, for a month with 31 days (arcs) and the two GRACE Follow-On satellites this limit is just about enough for a perfect parallelisation on arc-wise level. Using the BLAS/LAPACK routines the processing time for each arc with the classical parametrisation and gravity field coefficients up to d/o = 96 scatters around 20 min (including waiting time), thus, any non-parallel arc increases the overall run time by this number.

5.3 Variance component estimation in GRACE Follow-On data processing

The method of Variance Component Estimation (VCE) may be applied for different tasks in the process of gravity field recovery. Its ability to derive information about the unknown stochastic behaviour of observables, which are interacting with each other, makes it a valuable tool for automated processing of large data sets. The mathematical background for the application of VCE in the LSQA is described in Sect. 3.3. Different groups of observations (represented by corresponding NEQs) may be treated with VCE as long as the prerequisite of independence is assumed and a common (sub)-set of unknown parameters is addressed. The following sections present three practical applications of VCE in the gravity field processing scheme incorporated to the CMA, namely the adoption on arc-wise level,

on block-wise level, and on constraints.

5.3.1 Arc-wise level

Not only different types of observations resulting in different NEQs, e.g., satellite gravimetry and terrestrial gravimetry, may be considered with VCE, but all kinds of NEQs where the underlying data can be assumed to be independent. Relying on this assumption for each orbital arc, i.e., only the observations of each arc share the same a priori variance of unit weight σ_0^2, the corresponding NEQs may be used in a VCE to estimate a weight for each individual arc. Consisting of K arcs, for a monthly processing $K \in \{28, 29, 30, 31\}$, each NEQ (composed of $\mathbf{N}_k, \boldsymbol{b}_k$ and Λ_k) is used to evaluate Eq. 3.87 and then apply Eq. 3.88. In this sense VCE might be seen as a form of arc-wise outlier screening, which does not discard individual observations but down-weights an arc polluted by bad observations in the estimation process.
The processing of the CMA is usually applied - however not restricted - to an arc-length of one day because NEQs containing orbit parameters and gravity field parameters are set up on a daily basis. All arcs of one month are then accumulated and a solution is eventually computed (for arc-wise orbit parameters and monthly gravity field parameters). Utilising VCE in this context leads to a weight for each daily NEQ, which results in a coarse quantification of the observation data noise based on the functional and stochastic model.

The behaviour of the estimated arc-wise variance components is depicted in Fig. 5.12 for the years 2019 and 2020. The variance components as computed with an implementation of Eq. 3.87 are an estimation for the implicit variance of unit weight of each arc, which is dependent on the choice of the a priori variance of unit weight. For a more clear interpretation all variance components in the graphs are scaled by the median of the time series of variance components. The arc-wise variance components feature several outliers,

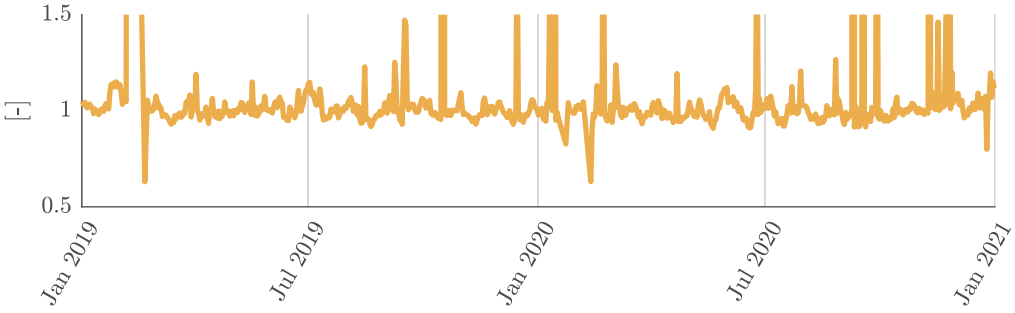

Figure 5.12: Two years of arc-wise variance components estimated with the operational GRACE Follow-On solution. The variance components are referenced to their median.

correspond to arcs with poor data quality. An example is given in Fig. 5.13b for September 2020, where three days are corrupted: By an orbit manoeuvre[20] on 9 Sep, and by KBR calibration manoeuvres on 17 Sep and 28 Sep. Also note the slight increase on 24 Sep, mostly likely due to an impact[20]. The VCE is able to detect arcs with poor data quality and to automatically down-weight the corresponding contributions to ensure a good gravity field

[20] According to the spacecraft events log `TN-01a_SCE.txt` of the operator.

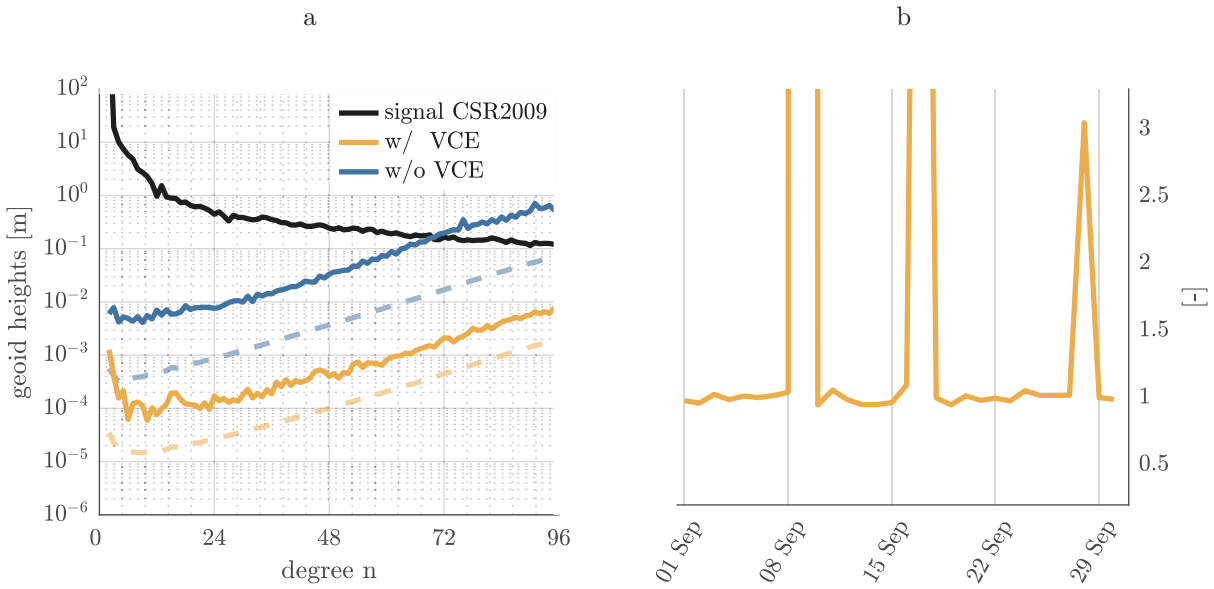

Figure 5.13: Difference degree amplitudes for September 2020 for the operational gravity field solution with and without VCE (a) and the corresponding arc-wise variance components (b).

solution, see Fig. 5.13a for the effect of VCE on a gravity field solution. One should keep in mind that this procedure only provides a rough outlier treatment because entire arcs are down-weighted although only a few epochs of the arc may have been affected by poor data quality. A refined method of using VCE as outlier treatment will be addressed in Sect. 5.3.2.

Since VCE is an iterative procedure, the variance components change with each iteration based on the previously determined solution $\mathbf{N}^{-1}$. The convergence of the variance components is shown in Fig. 5.14a for January 2019. The graph depicts four iterations because afterwards no further changes occur. For a month without gross outliers, the vari-

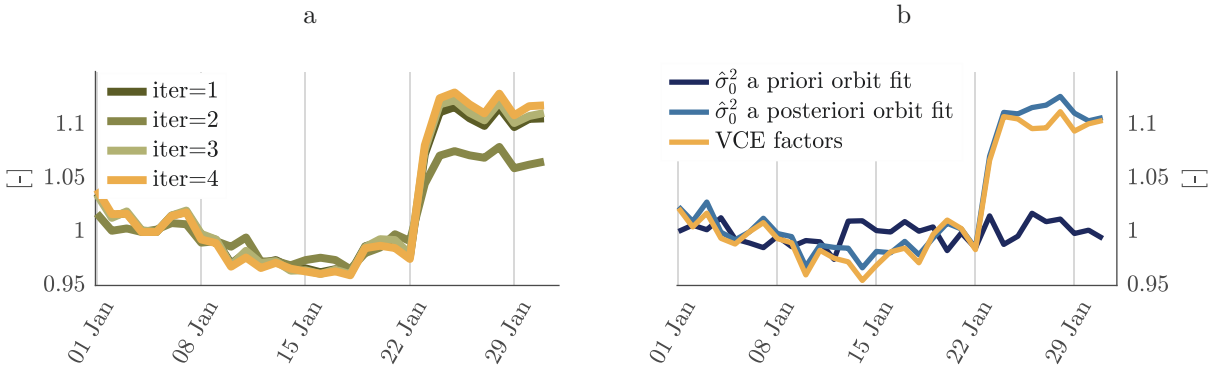

Figure 5.14: Convergence behaviour of arc-wise variance components in January 2019 for four iterations (a) and a comparison of the variance components with the variances of daily a priori orbit-fits and variances of daily orbit-fits after the gravity field recovery (b).

ance components may be related to the a posteriori variance of unit weight of an orbit fit (Fig. 5.14b). The a priori orbit fit refers to the full a priori force field (including the a pri-

ori gravity field), the a posteriori orbit fit is done with a corresponding estimated monthly gravity field. The latter is very similar to the variance components because both relate to the improved gravity field. Thus, the VCE may be seen as being capable of incorporating the estimated variance of unit weight $\hat{\sigma}_0$ of the a posteriori orbit fits as a quality indication into in the full orbit and gravity field recovery process.

As the CMA relies on the use of additional pseudo-stochastic parameters, which are co-estimated to compensate for a deficient force field (and which are absorbing observation noise as well), some additional remarks have to be made. With Eq. 3.88 the NEQs are weighted by the estimated variance components (the implicit σ_0^2 in each NEQ is determined). However, the pseudo-stochastic parameters are characterised by a priori stochastic information in the form of a priori standard deviations. One has to keep in mind that the impact of the adopted constraints depends on the relative magnitude between constraint and NEQ (cf. Eq. 3.42 where the matrix containing the constraints is accumulated with the normal equation matrix). The question arises, whether the variance component shall refer to

$$\mathbf{N}_k = \frac{\sigma_0^2}{\hat{\sigma}_k^2}\mathbf{N}_k + \mathbf{W} \quad , \tag{5.15}$$

where $\mathbf{W}$ defines the constraints (see Eq. 3.38 et seq.), or if it shall refer to

$$\mathbf{N}_k = \frac{\sigma_0^2}{\hat{\sigma}_k^2}\left(\mathbf{N}_k + \mathbf{W}\right) \quad . \tag{5.16}$$

If the latter case is realised, e.g., by pre-eliminating all constrained parameters before the VCE is applied, no further thoughts have to be made. However, the case of Eq. 5.15 needs some additional consideration, as it may occur when the to-be-constrained parameters cannot be pre-eliminated before the VCE is applied (e.g., because they belong to the global parameters). Down-weighting the NEQ's contribution due to a high $\hat{\sigma}_k^2$ from the VCE leads to a higher relative magnitude between constraint $\mathbf{W}$ and $\mathbf{N}_k$, i.e., in fact a tighter constraint (this also happens to the constraints referring to the NEQ based on the kinematic positions, see Sect. 5.1.5). To overcome this change in the stochastic model of the pseudo-stochastic parameters, the constraints have to be adjusted according to the variance components as well. Four options of correcting the constraints are presented here:

a. Choosing an appropriate a priori σ_0^2.
b. Correcting the constraint based on the estimated variance component $\hat{\sigma}_k^2$.
c. Taking the median of the estimated variance components.
d. Apply VCE for the constraints as well.

A fifth option would be to apply the constraint directly after setting up and before storing the NEQ, which, however, would violate the principle of the BSW of only storing unconstrained NEQs. Moreover, it not possible to use this strategy for global parameters.
The idea of scaling the constraint is sketched in Fig. 5.15. It shall indicate that the constraints depend on the σ_0^2 of the observations (to be seen in the definition of $\mathbf{W}$ in Eq. 3.38 as well). If σ_0^2 changes due to the VCE also the effect of the stochastic model applied through the constraints will alter, and an appropriate method of taking this implication into account has to be chosen.

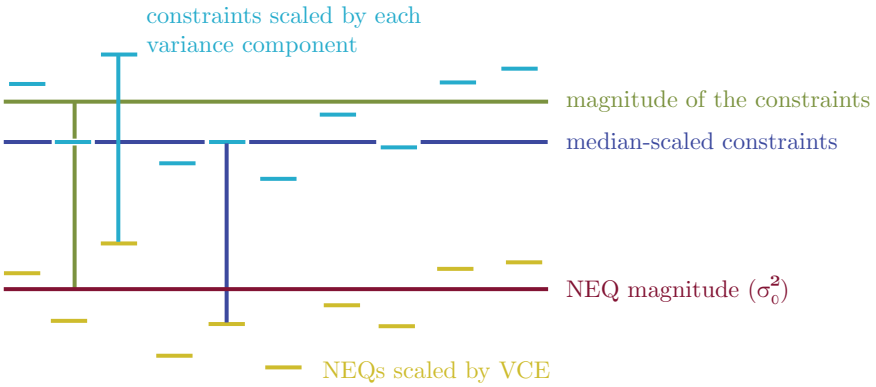

Figure 5.15: Illustration of the constraints acting relative to σ_0^2. The blue lines show the change of the constraint magnitudes relative to the weighted NEQs based on the adopted correcting scheme.

Case a. This option is only possible when computing the variance components relative to an a priori σ_0^2 as in Eq. 3.87 and Eq. 3.88. In principle this violates the assumption that the groups of observations for which the variance components are sought-after do not share a common σ_0^2, however, one is free to factor out an arbitrary number to scale the complete stochastic model. This may be done to ensure a correct contribution of the a priori stochastic model due to the constraints since they are defined relative to σ_0^2 (Eq. 3.38).

Case b. The second idea of correcting the magnitude of each constraint based on the estimated variance component $\hat{\sigma}_k^2$ valid in the interval, in which the constrained parameter is valid, demands a more complex implementation. It allows, however, for a fully comparable application of the constraints as without using VCE. All constraints in each group are scaled based on the respective group's variance component $\hat{\sigma}_k^2$. Consequently, the stochastic model of the constrained parameters reads as

$$\mathbf{W} = \begin{bmatrix} \frac{\hat{\sigma}_1^2}{\sigma_1^{c\,2}} & & & & & \mathbf{0} & \\ & \frac{\hat{\sigma}_1^2}{\sigma_2^{c\,2}} & & & & & \\ & & \frac{\hat{\sigma}_1^2}{\sigma_3^{c\,2}} & & & & \\ & & & \frac{\hat{\sigma}_2^2}{\sigma_4^{c\,2}} & & & \\ & & & & \frac{\hat{\sigma}_2^2}{\sigma_5^{c\,2}} & & \\ & \mathbf{0} & & & & \ddots & \\ & & & & & & \frac{\hat{\sigma}_K^2}{\sigma_P^{c\,2}} \end{bmatrix} \begin{matrix} \} \text{ block } k=1 \\ \\ \} \text{ block } k=2 \\ \\ \vdots \\ \} \text{ block } k=K \end{matrix} \tag{5.17}$$

for K variance components and P constrained parameters. This is only possible for local parameters.

Case c. It represents a trade-off between the first two. It takes into account that the NEQs are scaled, however, referencing them to the median. The median shall take into account that gross outliers do not deteriorate the variance components due to unnoticed

data problems (which may easily occur as they indicate a bad arc). Consequently, they do not degrade the model applied with the constraints on the good arcs. For arcs contaminated with outliers, however, $\mathbf{N}_k$ gets down-weighted, whereas $\mathbf{W}$ keeps its magnitude relative to the good arcs, i.e., the constraints get tighter and in case of the pseudo-stochastic PCAs they are allowed to follow the observations to a lesser extent, implying the orbit gets more dynamic.

Case d. A further option of taking into account the constraints as additional NEQs

$$\mathbf{N} = \sum_{k}^{K} \frac{\sigma_0^2}{\hat{\sigma}_k^2}\mathbf{N}_k + \frac{\sigma_0^2}{\hat{\sigma}_c^2}\mathbf{W} \ , \tag{5.18}$$

and deriving a corresponding variance component $\hat{\sigma}_c^2$ as well, which will be explained in more detail in Sect. 5.3.3.

The operational processing of GRACE Follow-On data makes use of the VCE on arc-wise level to realise a data weighting (kinematic positions and KBRR) in the first iteration. The VCE is applied for each arc-wise NEQ when the accumulation of the daily arcs to a monthly solution is perfomred. It avoids the aforementioned scaling problems by pre-eliminating all pseudo-stochastic parameters on the level of each arc before the VCE. The constraining is applied before the pre-elimination, hence, simply a fixed a priori stochastic model for the pseudo-stochastic parameters is applied.

5.3.2 Block-wise level

Adopting the NEQ to daily arcs is a very coarse approach to detect and down-weight outliers. As one daily arc consists of about 50'000 observations of kinematic positions and in addition more than 17'000 KBRR observations, assigning only one variance component will usually not reflect the complete behaviour of the observations (in fact, of the combination of kinematic positions and KBRR observations) and one single outlier may dominate the respective variance component, which is not a favourable behaviour for outlier screening. To assign variance components more precisely, shorter time spans of the NEQs may be taken into account. When setting up the NEQs, each arc is already divided into several independent blocks which are building up the entire normal equation system (see Sect. 3.2.4). For each such block, which again forms a complete NEQ $(\mathbf{N}_k, \boldsymbol{b}_k, \Lambda_k)$ VCE may be applied, which leads to a large number of NEQs contributing to a monthly solution. For a month with 30 d and blocks of 3 h this sums up to 240 variance components that may be estimated. Pre-elimination is not easily possible on the level of each block individually because the local parameters refer to one daily arc. As a consequence, the computation of a full orbit and gravity field solution with several iterations of VCE is becoming very time consuming. To overcome this issue, the VCE is only applied to the orbit parameters in a back-substitution process, as applied in the determination of the linearised residuals (Sect. 4.5.2). In a first iteration a gravity field solution is estimated and introduced as part of the new a priori force field. Based on this force field the NEQs for the new a priori orbit are set up for each arc, which is split into several blocks of NEQs. VCE is then applied on these blocks of NEQs, i.e., only on arc-wise orbit parameters which implicitly refer to the full monthly

gravity field solution through the underlying force model. Obviously, introducing an a priori gravity field instead of computing an independent monthly solution as first step leads to a regularisation towards the a priori gravity field because the blocks are weighted according to their observation's contribution to the dynamic parameters in the full force field.

Using this formulation, the VCE has been broken down to the level of each arc where for blocks of 3 h only 8 variance components need to be adjusted. This procedure may be applied to estimate separate variance components for the kinematic positions and the KBR observable without estimating a relative weight between the two observation types, which is kept fixed to $\sigma_{\mathrm{KIN}} \approx 1\,\mathrm{cm}$ and $\sigma_{\mathrm{KBRR}} = 3 \times 10^{-7}\,\mathrm{m\,s^{-1}}$ (see Sect. 5.1.5). When applying the parameter-transformation (Sect. 4.5.1), even a constrained KBRR-only solution may be used for the VCE by constraining the SUM-parameters tightly to the a priori orbit (based on the kinematic positions and the new force field from the previous iteration). Otherwise, the arc-wise NEQs consisting of the SUM and DIFF contributions of the kinematic positions and KBRR have to be taken into account. The latter, however, is more complicated to be incorporated in the programme flow of GRAVDET2, ORBDIFF and ADDNEQ2 since a loop between ORBDIFF to set up the blocks of NEQs and performing the VCE for each block and ADDNEQ2 to combine and solve the corresponding NEQs would have to be established. The procedure of restricting the block-wise VCE to the level of each arc and not storing each block and running the VCE on all blocks of a month provides a fast and efficient way of computing, even though an iteration with the gravity field solution has to be introduced.

As expounded in Sect. 5.3.1, the scaling of blocks of observations in the normal equation matrix leads to a wrong magnitude between the a priori constraints and the normal equation matrix. Since it is not possible to pre-eliminate parameters on block-wise level within one arc for only one type of observations, the magnitude of the constraints has to be scaled relative to the variance component (see Figure 5.16). The scaling may be applied

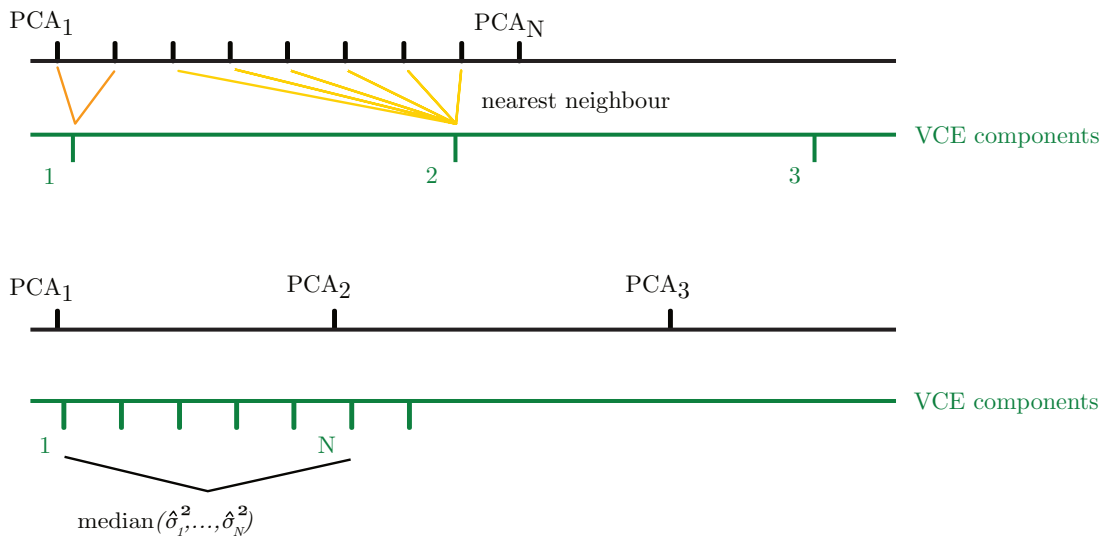

Figure 5.16: Illustration of the scaling of the constraints based on block-wise variance components.

by taking into account the median (case c. in Sect. 5.3.1) or correcting each constraint based on the estimated variance component (case b. in Sect. 5.3.1). This is done by correcting the constraints of the parameters valid in the time interval of each block based on the estimated variance component σ_k^2 of the respective block. In case a parameter is valid longer than a variance component, all corresponding variance components are averaged by the median to account for outliers. The other (more frequent) case, where the parameter is valid for a shorter time interval than the corresponding variance component is treated by taking the respective variance component for scaling. At boundaries of two variance components where a parameter is potentially valid within the time range of two variance components the value of the variance component closest in time is taken for the re-scaling (nearest neighbour). The time series of block-wise estimated variance for a block length of 50 min is shown in Fig. 5.17 for the years 2019 and 2020. Additionally, an outlier screening is applied on a monthly basis, which is used and discussed in Sect. 5.5.2. Naturally, the

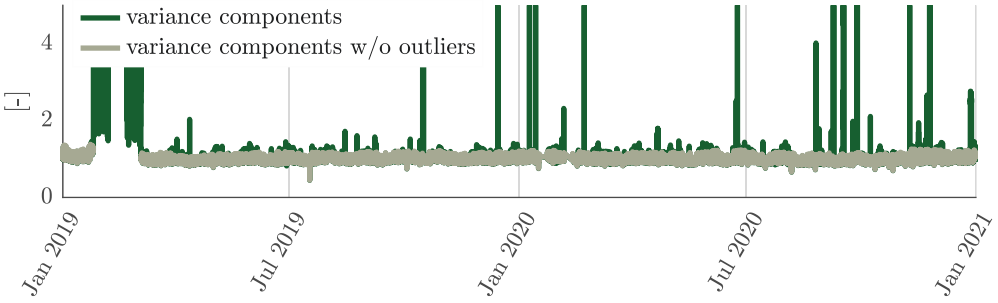

Figure 5.17: Two years of block-wise variance components estimated with the operational GRACE Follow-On solution. The variance components are referenced to their median and outliers are marked.

block-wise variance components provide a much higher resolution and outliers are better identified. For September 2020 the comparison between arc-wise and block-wise variance components is shown in Fig. 5.18a. The outlier due to the manoeuvre, which lasted only a few seconds, is much better resolved and data from that day could still be incorporated. Another good example, how VCE adopted on daily arcs smooths the variance components, is the outlier due to the suspected impact on 24 Sep, 2020. The difference degree amplitudes in Fig. 5.18b compare the influence of the estimation of arc-wise and block-wise variance components on the gravity field solution for September 2020.

The operational processing of GRACE Follow-On data makes use of the VCE on block-wise level. It is only applied to the KBRR data, however, there is no impediment to use it for the kinematic positions as well. For the latter it simply turned out not to be necessary because GRACE Follow-On kinematic positions are affected by only a few outliers. Moreover, the impact of the kinematic positions on the gravity field is much lower than for the KBR data, which are the main observable.

5.3.3 Variance component estimation on constraints

The CMA applied to GRACE Follow-On data makes use of the co-estimation of additional empirical accelerations set up in regular intervals. Estimating a large amount of pseudo-

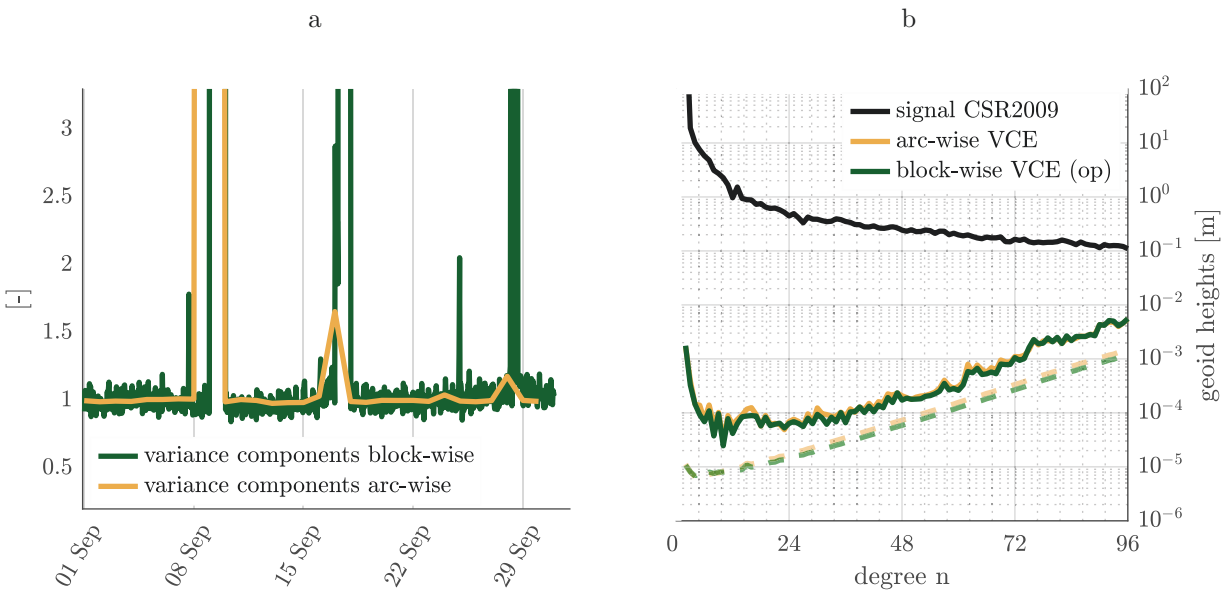

Figure 5.18: Comparison of arc-wise and block-wise variance components for September 2020 (a), also expressed in degree amplitudes of a resulting gravity field solution (b).

stochastic parameters requires not only an elaborated method of solving the variational equations, but also a delicate choice of constraints applied to them to ensure an invertible normal equation matrix on one hand and not to absorb the sought-after gravity field information on the other. Obviously, the magnitude of the constraints needs to be adapted based on the choice of the background force field (and/or observation noise modelling), in order to (only) account for noise signal. Not using ACC data or an outdated de-aliasing product, e.g., results in unmodelled signal, ideally to be absorbed by more moderately constrained pseudo-stochastic parameters.

As mentioned in Eq. 5.18, the matrix containing the constraints may be regarded as an additional normal equation system. The constraints may be interpreted as the stochastic model to additional artificial observations $\boldsymbol{h}$ which are related to the to-be-constrained parameters by $\mathbf{H}$, next to the observed set of observations $\boldsymbol{\ell}$ (Eq. 3.39). The artificial observations are of the parameters and it follows $\mathbf{H} = \mathbf{I}$. In the case of pseudo-stochastic orbit parameters, it is crucial that these parameters are constrained to zero $\boldsymbol{h} = \mathbf{0}$, such that no bias to the a priori force field is introduced. Expanding the system of equations leads to the normal equation system

$$(\mathbf{N} + \mathbf{W})\,\hat{\boldsymbol{x}} = \boldsymbol{b} \quad , \tag{5.19}$$

where $\mathbf{W}$ defines the weight of the additional pseudo-observations $\boldsymbol{h}$ (Eq. 3.38). As a consequence of Eq. 5.19, the matrix with the constraints may be regarded as an additional normal equation system to be considered in the sequential LSQA (Eq. 3.57)

$$\mathbf{N} = \sum_{k=1}^{K} \mathbf{N}_k + \mathbf{W} \quad , \qquad \boldsymbol{b} = \sum_{k=1}^{K} \boldsymbol{b}_k \qquad \text{and} \qquad \Lambda = \sum_{k=1}^{K} \Lambda_k \quad . \tag{5.20}$$

It is not necessary to set up all constraints in one normal equation matrix $\mathbf{W}$. It may be divided into sub-groups, e.g., different NEQs for the constraints acting on different

parameters, so the full normal equation matrix may be accumulated by K NEQs containing the relation with the observations and I NEQs taking into account the stochastic model for I different to-be-constrained parameters

$$\mathbf{N} = \sum_{k=1}^{K} \mathbf{N}_k + \sum_{i=1}^{I} \mathbf{W}_i \quad . \tag{5.21}$$

As a consequence of this formulation, one might understand $\mathbf{W}_i$ as a further observation group (where the observations are zero) with an unknown variance factor $(\sigma_k^{\mathrm{c}})^2$ such that VCE may be applied. This idea was used by Koch and Kusche [2002] for the determination of regularisation quantities of static gravity field solutions stemming from multiple observation types and satellite missions and terrestrial data. Transferring the procedure to PCAs allows for an estimation of the constraints of the co-estimated pseudo-stochastic model together with the gravity field. As a matter of fact, the cumbersome process of manually tuning the magnitude of the constraints is avoided. The basic idea of treating the artificial observations, which are introduced with the constraints, as further observation group with an unknown σ_0^2 (thus, the basic assumption of VCE) stands insofar to reason as the artificial observations are actually of a completely different nature, i.e., PCAs, than the observations which are kinematic positions and KBRR.

The constraining matrix $\mathbf{W}_i$ is of diagonal structure if for each to-be-constrained parameter no correlations are mapped into the a priori stochastic model. As a consequence, the variance component $\hat{\sigma}_{i,\mathrm{c}}^2$ applied to $\mathbf{W}_i$

$$\mathbf{N} = \sum_{k=1}^{K} \frac{\sigma_0^2}{\hat{\sigma}_k^2} \mathbf{N}_k + \sum_{i=1}^{I} \frac{\sigma_0^2}{\hat{\sigma}_{i,\mathrm{c}}^2} \mathbf{W}_i \tag{5.22}$$

directly steers the magnitude of each co-estimated pseudo-stochastic parameter. Even though VCE is applied to the constraints $\mathbf{W}_i$ and the NEQs of the observations $\mathbf{N}_k$, it is important that the relative magnitude is not changed during the estimation process. The constraints - also when determined by VCE - refer in their magnitude to the full normal equation system $\mathbf{N}$, which is eventually inverted to compute the redundancy factors $r_{k,i}$ (Eq. 3.85). Thus, scaling the normal equation matrix $\mathbf{N}_{k,j}$ in iteration j by $\sigma_0^2/\hat{\sigma}_{k,j}^2$ must be compensated in the constraints because they refer to $\mathbf{N}_{j-1}$, which is constituted of $\sigma_0^2/\hat{\sigma}_{k,j-1}^2$. This can be achieved by either setting the weight of the first normal equation matrix $\mathbf{N}_1$ to one or by e.g., taking the median of the variance components $\hat{\sigma}_{k,j}^2$ to scale $\mathbf{N}_k$ accordingly. When applying the VCE as defined in Eq. 3.87 and Eq. 3.88, the a posteriori variance of unit weight $\hat{\sigma}_0^2$ will converge towards the a priori variance of unit weight σ_0^2 which was factorised from the weight matrix in the NEQs. This means that the denominator in Eq. 3.86, the group-wise redundancy r_k (Eq. 3.85), represents the formal contribution of the formulated problem to the estimated variance component and the numerator $\hat{\Omega}_k$ the *residual-contribution*, i.e., the influence of the interplay between observations and (to-be-) estimated model. In other words, the VCE considers the residual-contribution together with the formal contribution by adapting the stochastic model accordingly. By compensating the scaling of the normal equation matrix $\mathbf{N}_k$, the residual-contribution is harmonised with the a priori stochastic model (or referred to it) and the VCE process converges in the context of the implicit σ_0^2 of the combined NEQs, thus, around the first iteration's a posteriori

variance of unit weight $\hat{\sigma}^2_{0,j=1}$. As a consequence, each normal equation matrix $\mathbf{N}_k$ receives a proper weight according to the contribution to the full solution and the stochastic model of the pseudo-stochastic parameters $\mathbf{W}_i$ is allowed to leverage in the correct magnitude. One may also say, such an approach accounts for the (median) residual-contribution of the actual observations in the magnitude of the constraints, thus, propagating observation information due to an insufficient knowledge of their σ_0^2 to the constraints. To put it in other words, the matrix with the constraints $\mathbf{W}$ depends on σ_0^2. In the VCE σ_0^2 is iteratively improved (and changed), therefore, this has to be taken into account when defining $\mathbf{W}$ in each iteration step of the VCE.

Experiments with VCE on constraints

Three main experiments on the application of VCE are conducted to determine adequate constraints:

a. Estimating two variance components, one for the SUM[21]-PCAs and one for the DIFF-PCAs.
b. Estimating six variance components by setting up a constraining NEQ for each direction (R, S, W) and parameter-relation (SUM, DIFF).
c. Estimating six variance components as in b. but instead of a monthly estimation setting up constraining NEQs for each daily arc.

The PCAs are set up in analogy to the operational solution for intervals of 15 min.

Case a. The most simple case to use VCE for the PCAs corresponds to the two parameter-relations SUM and DIFF. As stated in Sect. 5.1.4, the empirically determined constraints are not the same for SUM and DIFF, the PCAs corresponding to the latter are tightened by a factor of 100 (see Table 5.4). The NEQs used in this scenario are listed in Table 5.6. A variance component for the pseudo-stochastic parameters for each parameter-relation is estimated, as well as one for NEQ-1.

NEQ-#	type	contains
1		actual observations & all parameters
2	SUM	constraints for PCAs
3	DIFF	constraints for PCAs

Table 5.6: NEQs set up for the VCE applied to determine the constraints of SUM- and DIFF-PCAs.

All estimations take place on monthly level. Consequently, a monthly mean model is computed using the constraints. Starting from a loose a priori constraint of $1 \times 10^{-8}\,\mathrm{m\,s^{-2}}$, the VCE considerably tightens the range for the PCAs by about two orders of magnitude (see Table 5.7).

The results may be compared with the empirically determined constraints of the operational solution (Table 5.4 and Eq. 5.4), which are of a similar order of magnitude for both the SUM and DIFF-PCAs. The differences to the operational gravity field solution

[21] see Sect. 4.5.1

Table 5.7: Constraints applied when using VCE for the pseudo-stochastic parameters set up as SUM and DIFF parameters for January 2019.

type	a priori constraint [$\mathrm{m\,s^{-2}}$]		VCE constraint [$\mathrm{m\,s^{-2}}$]
SUM	1×10^{-8}	$\rightarrow$	5.7×10^{-9}
DIFF	1×10^{-8}	$\rightarrow$	5.2×10^{-11}

are negligible. However, it may be emphasised that in contrast to the operational solution the a priori constraint was very loose.

The VCE to determine only the magnitude of constraints based on a diagonal constraining matrix $\mathbf{W}_i$ and the observation information being comprised in one NEQ may be set up efficiently by computing the numerator of Eq. 3.86 as

$$\begin{aligned} \hat{\Omega}_i &= \hat{\boldsymbol{e}}_i^{\mathrm{T}} \mathbf{W}_i \hat{\boldsymbol{e}}_i \\ &= (-\hat{\boldsymbol{x}}_i^{\mathrm{T}}) \mathbf{W}_i (-\hat{\boldsymbol{x}}_i) \\ &= \sum_{m=1}^{M_i} w_{mm} \hat{x}_m^2 \quad , \end{aligned} \tag{5.23}$$

where $\hat{\boldsymbol{e}}_i = -\hat{\boldsymbol{x}}_i$ because $\boldsymbol{h} = \mathbf{0}$ and M_i are the number of parameters corresponding to $\mathbf{W}_i$. The trace in the denominator $t = \mathrm{tr}\left(\mathbf{W}_i \mathbf{N}^{-1}\right)$ may be computed as a dot product of

$$t = \mathrm{diag}\left(\mathbf{W}_i\right) \cdot \mathrm{diag}\left(\mathbf{N}^{-1}\right) \quad . \tag{5.24}$$

In this case it is not necessary to compute the full inverse normal equation matrix $\mathbf{N}^{-1}$ but only its diagonal elements. Thus, when applying a Cholesky decomposition (see Eq. 5.13), the back-substitution process may be stopped at the diagonal elements of $\mathbf{N}^{-1}$ when computing the inverse normal equation matrix from $\mathbf{L}$. Finally, fixing the weight of NEQ-1 to 1, enables to disregard the residual-contribution of NEQ-1.

Case b. For the following results 37 NEQs are set up (see Table 5.8), the NEQs from 31 daily arcs of January 2019 and six NEQs for the SUM- and DIFF-PCAs in each axes. This case takes into account that not every direction of a set of PCAs will have to absorb the same magnitude of noise and mis-modelled signal.
The a priori constraints are set to $1 \times 10^{-8}\,\mathrm{m\,s^{-2}}$ for all six groups of PCAs and are tightened due to the VCE (see Table 5.9), in particular in along-track for DIFF where the KBRR observations have their highest contribution, compare with Table 5.4 and Eq. 5.4
The VCE is iteratively applied and after five iterations convergence is reached, which is shown in Fig. 5.19 for a loose a priori constraint of $1 \times 10^{-8}\,\mathrm{m\,s^{-2}}$ (a) and a tight a priori constraints of $1 \times 10^{-12}\,\mathrm{m\,s^{-2}}$.

Table 5.8: NEQs set up for the VCE with constraints in each axis and parameter type.

NEQ-#	type	direction	contains
1,..., 31			actual observations & all parameters
32		R	constraints for PCAs
33	SUM	S	constraints for PCAs
34		W	constraints for PCAs
35		R	constraints for PCAs
36	DIFF	S	constraints for PCAs
37		W	constraints for PCAs

Table 5.9: Constraints applied when using VCE for the pseudo-stochastic parameters transformed to SUM and DIFF in each axis for January 2019.

type	direction	a priori constraint $[\mathrm{m\,s^{-2}}]$		VCE constraint $[\mathrm{m\,s^{-2}}]$
SUM	R	$1 \times 10^{-8} \mid 1 \times 10^{-12}$	$\rightarrow$	1.5×10^{-9}
	S	$1 \times 10^{-8} \mid 1 \times 10^{-12}$	$\rightarrow$	2.6×10^{-10}
	W	$1 \times 10^{-8} \mid 1 \times 10^{-12}$	$\rightarrow$	6.2×10^{-9}
DIFF	R	$1 \times 10^{-8} \mid 1 \times 10^{-12}$	$\rightarrow$	3.3×10^{-11}
	S	$1 \times 10^{-8} \mid 1 \times 10^{-12}$	$\rightarrow$	9.7×10^{-12}
	W	$1 \times 10^{-8} \mid 1 \times 10^{-12}$	$\rightarrow$	1.7×10^{-10}

A comparison of the spectra of the co-estimated pseudo-stochastic model (Fig. 5.21a-f) reveals that not every axis is affected in the same manner. SUM-cross-track, which is mostly defined by the kinematic positions is rather accurately described by the loose a priori constraint, whereas the PCAs of all other axes require a tighter constraint. The difference between the loose a priori constraints is also clearly visible in the KBRR post-fit residuals (Fig. 5.22a) and the degree amplitudes of the corresponding gravity field solution (Fig. 5.22b). The KBRR post-fit residuals derived from a solution with VCE on the constraints get flattened in the spectrum for periods >30 min, which is the Nyquist frequency for a 15 min sampling of PCAs. Especially, the peak at 90 min is suppressed. For periods <30 min the spectrum is dominated by a $1/f^2$-noise and then changing to f^2-noise in both the solutions, which is in line with simple theoretical assumptions about the noise behaviour in post-fit residuals (see Sect. 5.5.2). As it can be seen in the difference degree amplitudes, the PCAs with loose constraints absorb signal from the gravity field, however, the VCE is able to correctly scale the constraints to retain the signal in the gravity field.

Comparing solutions with VCE on constraints on a larger scale for two years of GRACE Follow-On by the means of a RMS over the oceans (Fig. 5.23) with the classical operational GRACE Follow-On model with fixed constraints shows that the VCE is able to deliver slightly better results in half of the inspected months. In months with challenging data, e.g., January 2020, where a lot of data is missing it exhibits its drawback of being de-

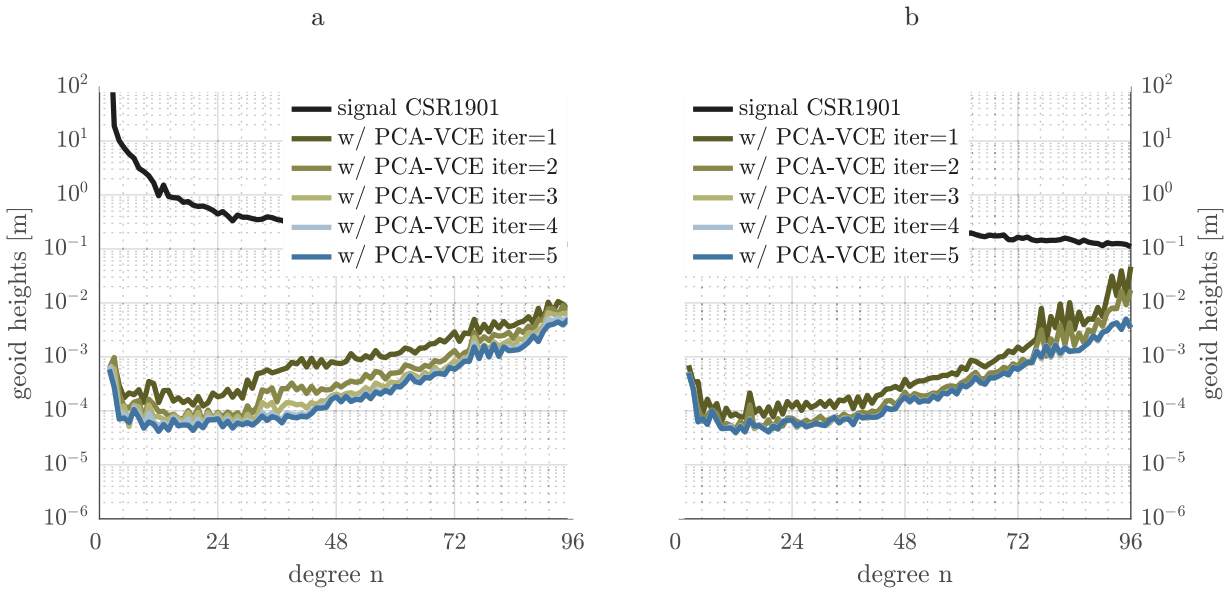

Figure 5.19: Convergence of gravity field solutions in the VCE process for monthly constraints per axis when starting from $1 \times 10^{-8}\,\mathrm{m\,s^{-2}}$ (a) or $1 \times 10^{-12}\,\mathrm{m\,s^{-2}}$ (b).

pendent on the data quality as well, i.e., for a lot of poor data the VCE for the constraints ensures to some extent that the PCAs follow the (poor) observations.

Case c. The last test scenario tries to mitigate noise with the PCAs not by co-estimating a monthly mean model with VCE but at the level of each daily arc. The NEQs for the constraints are set up as in case b. but for each arc, resulting in much higher numbers of NEQs to be addressed in the VCE. The total number of NEQs $N_{\text{total}}^{\text{NEQs}}$ is put together as

$$N_{\text{total}}^{\text{NEQs}} = \#\text{days/month} \cdot 6 + \#\text{days/month} = 217 \text{ NEQs for January 2019} \quad . \tag{5.25}$$

The co-estimated daily constraints (Fig. 5.20) feature variations, especially in cross-track

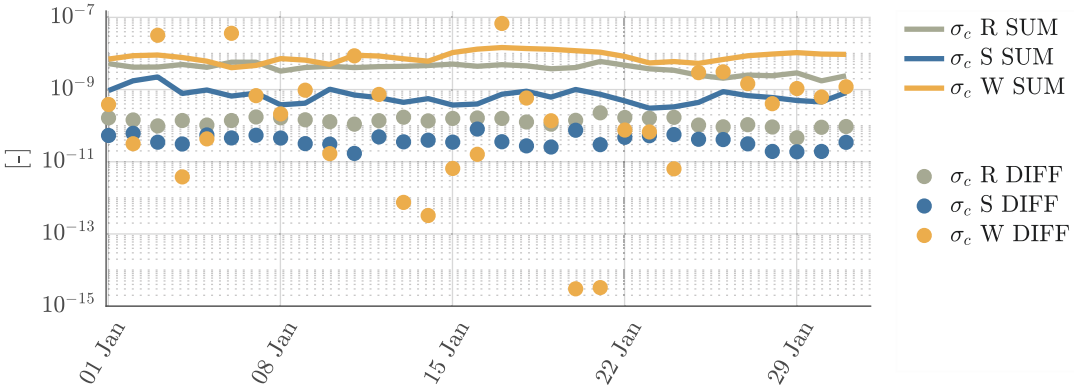

Figure 5.20: Daily constraints estimated with VCE for January 2019.

for the DIFF-PCAs which are weakly determined by the KBRR observations. In the gravity field no additional benefit can be seen from increasing the number of variance components to a daily level. However, it may be noted that this experiment was only performed for a month with good data quality.

Discussion about VCE on constraints

The use of VCE on constraints is generally beneficial for a gravity field solution, at least it is not harmful (see Fig. 5.23). However, the data-dependency bears some drawbacks as well. Additionally, the whole process is rather costly in terms of computational effort and memory. In the operational processing all orbit related parameters are pre-eliminated on arc-wise level after accumulating the NEQs for kinematic positions and KBRR, and only global parameters are explicitly kept. For adopting the VCE to the constraints the full parameter space of the global parameters and the to-be-constrained parameters (PCAs) has to be retained and consequently, the normal equation matrix for one month easily reaches dimesions of (30000×30000). This ultimately results in long computation times with high demands on the memory, even though the routines of LAPACK are employed. The operational processing of GRACE Follow-On data does not yet include any VCE on the constraints due to its rather limited impact and high consumption of computational resources. This may change in future, depending on the Level-1B data quality, improved background force models and availability of computing power. At least it might be applied to find reasonable numbers for the constraints which then may be used in a fixed setting.

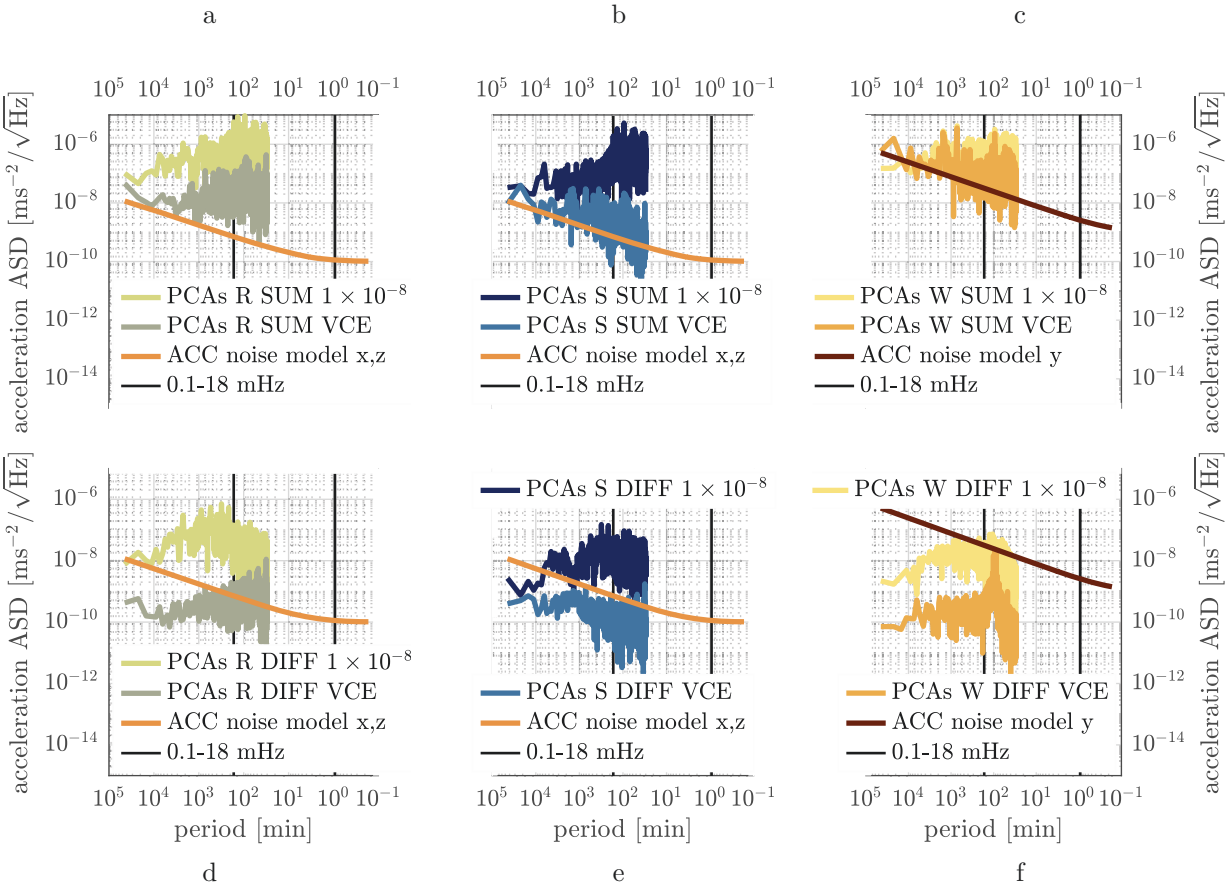

Figure 5.21: Co-estimated PCAs for a solution using VCE to determined their constraints, exemplarily for January 2019, in each direction (each column) and parameter type (first row SUM, second row column DIFF), including a comparison with the PCAs based on the a priori constraints of $1 \times 10^{-8}\,\mathrm{m\,s^{-2}}$. For reasons of simple comparison of magnitudes also a theoretical pre-launch ACC model is depicted in each graph.

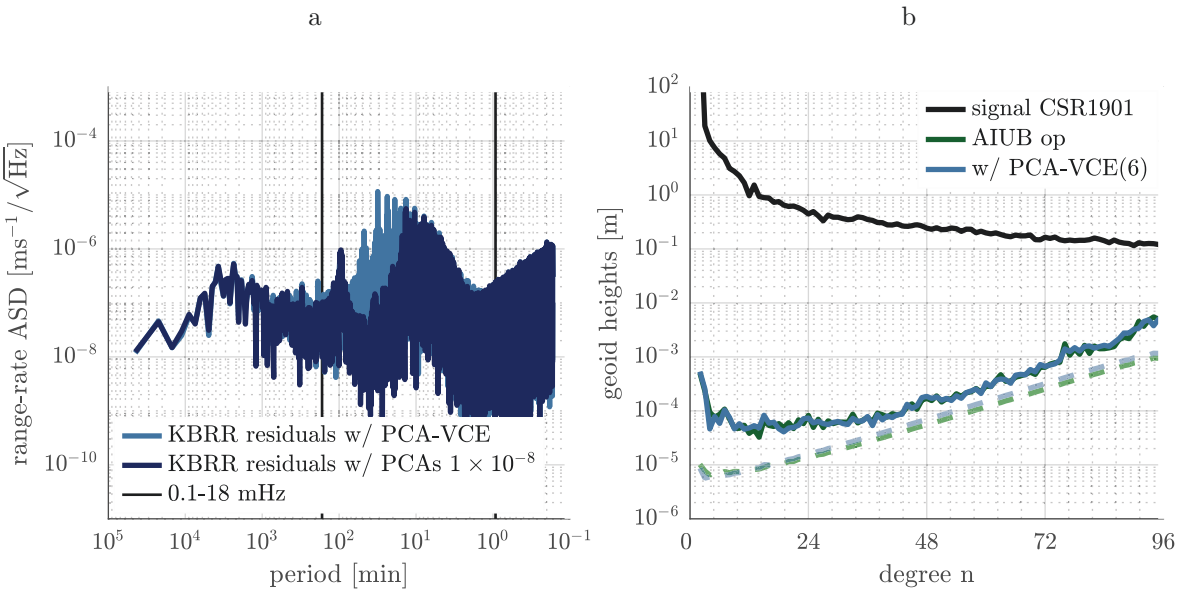

Figure 5.22: Comparison of KBRR post-fit residuals when using loose priori constraints for the PCAs and the result from the VCE, exemplarily for January 2019 (a), and difference degree amplitudes for the two corresponding monthly solutions (b).

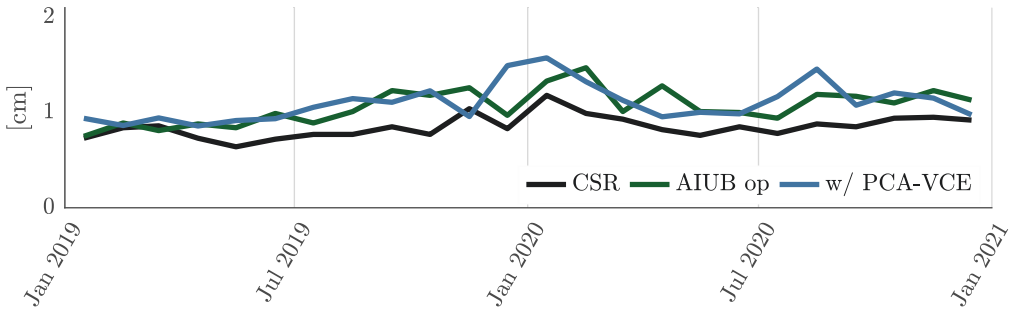

Figure 5.23: RMS over the oceans for two years of GRACE Follow-On comparing the solutions from CSR, the operational AIUB contributions and additionally applying VCE for the constraints on a monthly scale.

5.4 Epoch definition of a monthly gravity field

The epoch of each monthly gravity field of the operational solution, as it is provided in the header of the files, is computed from the K-band observation time tag t^{KBR} and the weight w, as it is derived and applied by the block-wise VCE in the KBRR observations, by

$$t_{\text{epoch}} = \frac{\sum_{i=1}^{N} w_i t_i^{\text{KBR}}}{\sum_{i=1}^{N} w_i} \quad , \tag{5.26}$$

with N denoting the total number of observations per month. As the weight for the k-th block w_k is applicable for several KBRR observations at times t_i^{KBR}, w_i corresponds to the weight w_k valid at t_i^{KBR}. Consequently, several epochs t_i^{KBR} obtain the same weight

(depending on the length of each block k). Such a weight usually corresponds to the middle day of each month (end of the 14^{th}, the 15^{th} or beginning of the 16^{th} day), with very little deviations. Only months with exceptional time spans due to missing data in 2018 may have a epoch which does not correspond to mid-month.
One may note that only the main observable of GRACE Follow-On contributes to the definition in Eq. 5.26. Other components, such as other observations (e.g., kinematic positions) or background force model data are neglected in this epoch definition. Thus, it is a somewhat arbitrarily chosen definition declaring the main observable to be the pivotal element. When trying to restore the full observed monthly gravity signal by adding back all applied background forces this definition might not suffice and additional products about the applied background forces in respective month might be necessary. Such products are already available for e.g., the operational GRACE Follow-On solution from TUG [Kvas et al., 2019].

5.5 Stochastic modelling for GRACE Follow-On observables

The stochastic noise modelling of kinematic positions and KBR measurements is a crucial part in high-precision gravity field recovery. The noise treatment of the observations influences the quality of the result (e.g., in terms of formal errors) significantly, and it will also affect the solution itself. The correct characterisation of noise in the data helps to retain the full signal content and separates signal from noise through a modelling of the latter - provided that the signal component is also adequately modelled.

The main findings about the stochastic modelling of kinematic positions in following section may be found in Lasser et al. [2020a].

5.5.1 Stochastic modelling of kinematic positions

In case of kinematic positions, which are introduced as pseudo-observations in the CMA, the process of computing the kinematic positions may be incorporated into the stochastic modelling. The original observations are the GPS dual-frequency carrier phases and the kinematic positions of the LEO satellite are determined by a PPP (see Sect. 4.3). GPS satellite orbits and clocks are introduced as error-free, i.e., correlations due to the GPS satellite orbits, clocks and underlying GPS tracking network errors are neglected. Only the carrier phase ambiguities correlate the kinematic positions in time, "implying that degraded estimates of carrier phase ambiguities may affect the estimation of the kinematic positions for more than one hour." [Jäggi et al., 2011b]. Consequently, the positions referring to different epochs are no longer uncorrelated. The correlation depends on the constellation of the GPS satellites and the number of carrier phase ambiguities.
The investigations to this subject were mainly performed before GRACE Follow-On data was released. Hence, they rely on GRACE, in particular the data from April 2007. The ideas presented here may be transferred to GRACE Follow-On without any loss of generality. For all experiments two orbit parametrisation scenarios are included, the first only using a dynamic orbit including ACC data and the estimation of respective bias and scale factor.

The second scenario follows the classical CMA approach by additionally estimating for constrained PCAs in a 15 min sampling (see table 5.1) to form reduced-dynamic orbits. The constraints are set to $1 \times 10^{-8}\,\mathrm{m\,s^{-2}}$ (Table 5.3). A static a priori gravity field is introduced up to d/o = 160, and the gravity field solutions are estimated up to d/o = 70.

Formal covariance propagation

Covariance information about the kinematic positions $\mathbf{C}^{\mathrm{KIN}}$ may be derived from a formal covariance propagation of the stochastic model of the carrier phase measurement to the kinematic positions according to Eq. 3.25 and Eq. 3.26. White noise is generally assumed for the stochastic model of the carrier phase measurements.

The correlations derived from $\mathbf{C}^{\mathrm{KIN}}$ mainly feature a twice-per-revolution signal (see Fig. 5.24), which is related to the satellite crossings of the poles and the weaker observation geometry in the polar regions since GPS satellite orbits are inclined at 55° with respect to the Earth's equator. The better tracking geometry in the equatorial regions generally leads to a smaller number of interruptions, thus fewer ambiguities, and consequently, to a better determination of each ambiguity and more correlated kinematic positions [Jäggi et al., 2011b]. Generally, the correlations are positive and decreasing for a growing distance in time. However, jumps may occur due to the set up of new ambiguities, which indicates changes in the observed constellation or data problems, e.g., causing cycle slips.
The GPS carrier phase ambiguities are the only parameters which are connecting kinematic positions referring to different epochs when using GPS carrier phase data. Consequently, deficiencies in the modelling of the GPS phase observations may be propagated through the ambiguities over several epochs. Since the formal covariance matrix of the kinematic positions $\mathbf{C}^{\mathrm{KIN}}$ only depends on the observation scenario, but not on the actual observations, any degradation of positions due to GPS data quality issues (including issues with GPS orbits and clocks introduced as known) is not reflected by this type of covariance information. An outlier in the carrier phase observations, e.g., affects the individual kinematic position and through the ambiguities neighbouring positions as well, but not the formal covariance of the respective positions.
Introducing the kinematic positions as pseudo-observations together with their full covariance matrix $\mathbf{C}^{\mathrm{KIN}}$ in the LSQA for the gravity field recovery would be equivalent to starting directly with carrier phase observations, as it is a series of LSQAs. This was shown, e.g., for the application of orbit determination from carrier phase observations and from kinematic positions used as pseudo-observations in Jäggi et al. [2011b]. Facing the large number of kinematic pseudo-observations, e.g., 3×8640 for one day with a 10 s sampling of GPS data, this would require a huge computational effort and would demand high storage requirements. Two ways how to deal with these issues are presented in the next sub-sections.

Epoch-wise covariance information The epoch-wise covariance information is a subset of the covariance matrix from the formal covariance propagation, which may be easily derived in the kinematic point positioning process using pre-elimination and back-substitution techniques. Focusing only on the kinematic positions, the epoch-wise covariances, assembled in Eq. 5.27, consist of six distinct elements, which comprise the variances of the three coordinates ($c_{xx}, c_{yy}, c_{zz} > 0$) and the off-diagonal elements c_{xy}, c_{xz}, c_{yz}, which

contain information about the correlation between the x,y,z components of the kinematic positions in the Earth-fixed coordinate system,

$$\mathbf{C}_{\text{epo}}^{\text{KIN}} = \begin{bmatrix} c_{xx} & c_{xy} & c_{xz} \\ c_{xy} & c_{yy} & c_{yz} \\ c_{xz} & c_{yz} & c_{zz} \end{bmatrix} \quad . \tag{5.27}$$

Any correlations between adjacent epochs due to the ambiguities are neglected. Taking into account epoch-wise covariances demands only little memory capacity and the weight matrix may be set up easily (Eq. 5.27 and Eq. 3.11).
The epoch-wise covariance information mainly features the twice-per-revolution behaviour of polar satellite orbits (the orbital period for GRACE was T =96 min), which reflects the observation scenario (weaker geometry over the poles). Figure 5.24 displays all elements of the epoch-wise covariance matrix for GRACE-A of day 091, 2007 in frequency domain. The elements are rotated to a RSW frame consisting of radial (R), along-track (S) and cross-track (W) direction, based on the unit vectors derived from a reduced-dynamic orbit fit. The twice-per-revolution signal is clearly visible in the radial component and also in the covariance between R and S axis. The information from the formal covariance propagation

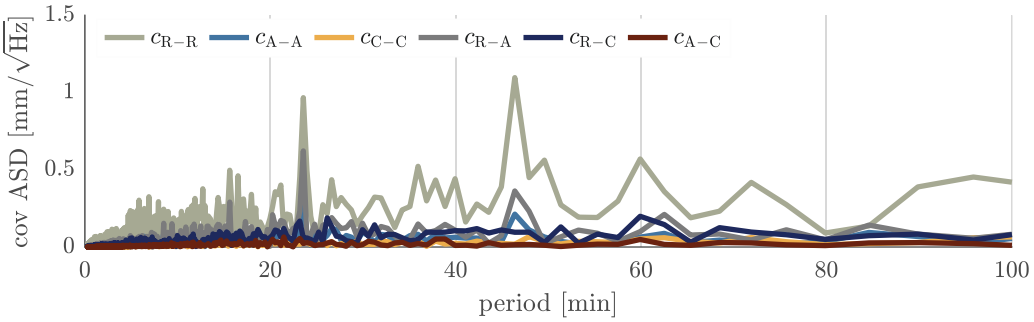

Figure 5.24: Independent components of the epoch-wise covariance matrix of GRACE-A for one arc on April 1st, 2007, in R, S and W direction expressed in ASDs.

cannot be neglected in the orbit reconstruction and gravity field recovery process without significantly degrading the recovered gravity field solutions when using the classical CMA, see Prange [2010].

Impact of epoch-wise covariance information on orbit reconstruction and gravity field recovery The post-fit residuals of the reconstructed orbit (Fig. 5.25a-c) with respect to the kinematic positions are characterised by the underlying orbit parametrisation and the noise in the kinematic positions. The reduced-dynamic orbit residuals feature less long-periodic variations than the dynamic orbit residuals, because a deficient force modelling can be absorbed by the PCAs. Thus, the reduced-dynamic orbit follows the observations to a large extent. In contrast, the post-fit residuals of the dynamic orbit feature mainly systematic signals caused by the deficient force model, which are mainly visible as once-per-revolution signatures. The flattening for periods above the the Nyquist-frequency of 30 min due to the PCAs sampling is especially prominent in cross-track.

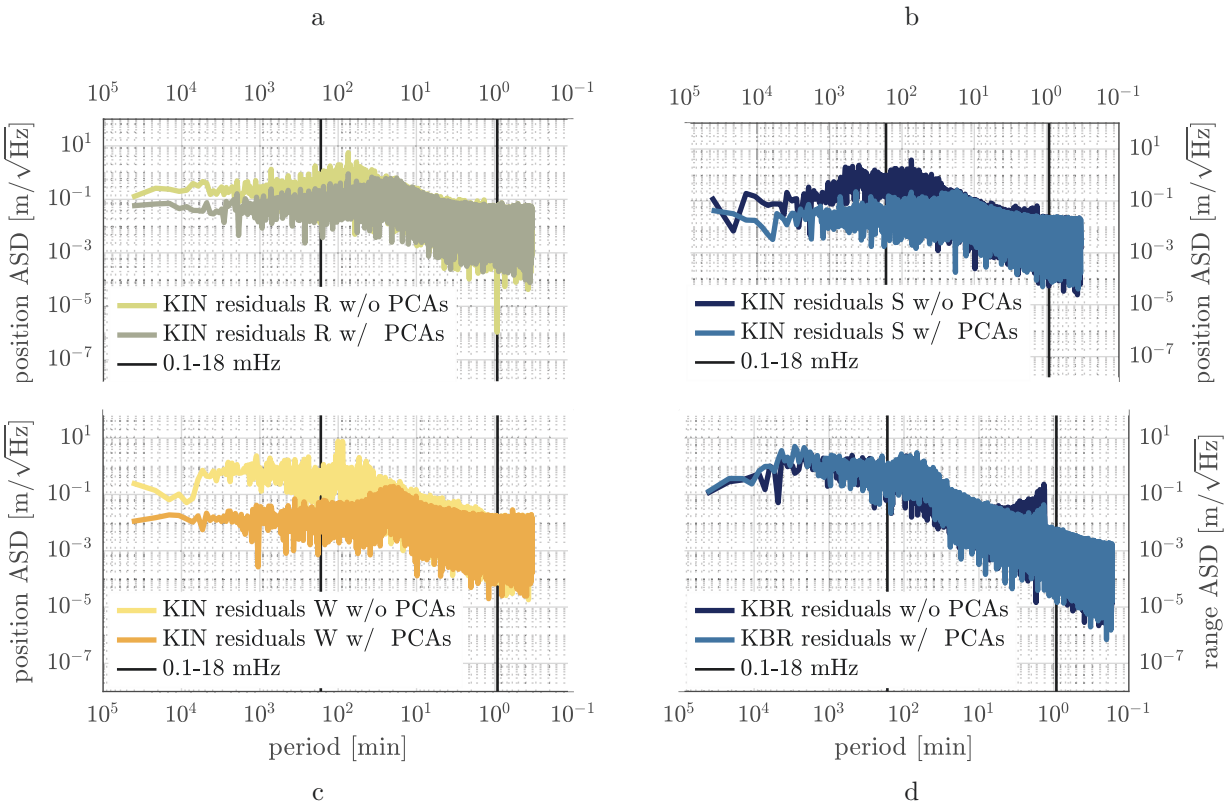

Figure 5.25: ASD of the post-fit residuals in R (a) S (b) and W (c) direction for April 2007, as well as KBR ranges (d) with an underlying dynamic and reduced-dynamic parametrisation when using epoch-wise covariances.

The KBR range validation of both solutions is rather similar for higher frequencies, however systematically different for long periods, see Table 5.10. In the high frequencies of the

parametrisation	RMS
reduced-dynamic	1.8 cm
dynamic	0.8 cm

Table 5.10: KBR range validation RMS over all days using epoch-wise covariances in the orbit reconstruction for April 2007.

spectrum both show a clear cut-off jump at the period corresponding to the resolution of the co-estimated gravity field at d/o = 70. This indicates that the high degrees and orders cannot be resolved properly by the observations with respect to the a priori gravity field which was introduced to a higher degree and order (d/o = 160). The KBR range validation of the reduced-dynamic orbit does not reflect the same level of accuracy as using directly GPS carrier phase observations for orbit determination, which is accounted for by the insufficient stochastic model, see Jäggi et al. [2011b] for a detailed investigation. This means that the fitted reduced-dynamic orbit is less precise when being computed from kinematic positions with epoch-wise covariance information than a corresponding orbit being computed directly from GPS carrier phase observations, where no degradation due to the automatically correctly modelled correlations is occurring.
The gravity field solutions based on the epoch-wise covariance information when either using the reduced-dynamic or the dynamic orbit parametrisations are shown in Fig. 5.26a. The solution based on the dynamic orbit parametrisation is degraded because of an insufficient treatment of force model and observation errors. The gravity field solution based

on the co-estimation of constrained PCAs is of good quality and represents the classical parametrisation used so far in the context of the CMA. In all further degree amplitude figures it will serve as a reference. Any further reference such as *classical* approach refers to the use of epoch-wise covariance information. For a better comparison with the next sec-

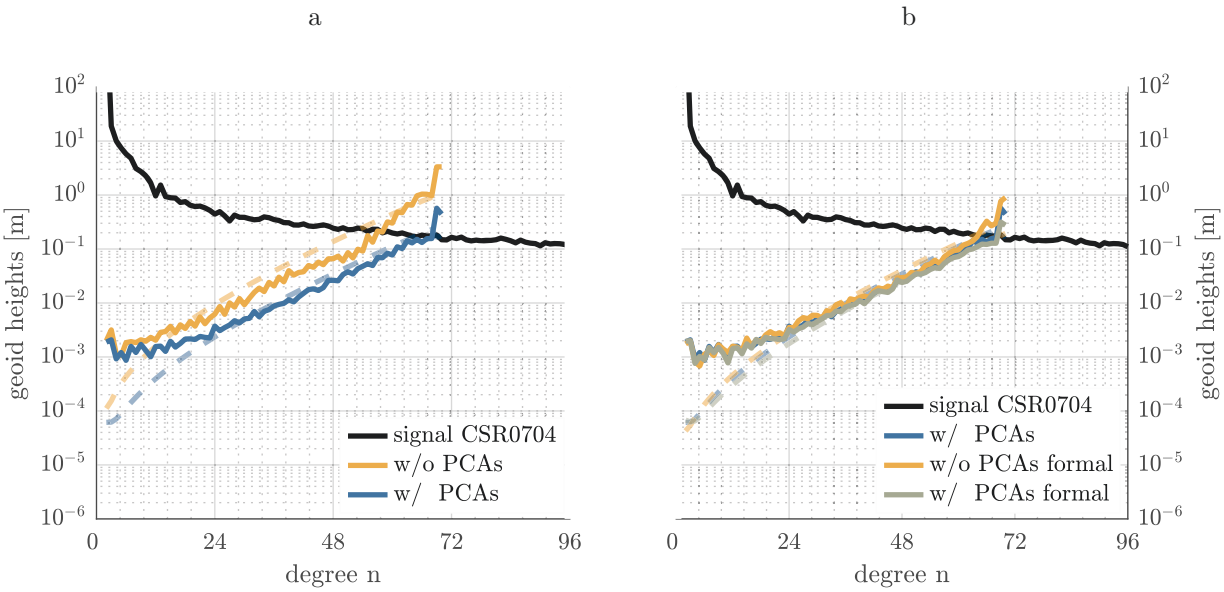

Figure 5.26: GRACE GPS-only gravity field solution for April 2007. Formal covariances from the determination of the kinematic positions considering correlations over 50 min are introduced in the gravity field determination process.

tion, using the formal covariance information over several epochs is depicted in Fig. 5.26b. In both cases the resulting formal errors of the solutions still not reflect the accuracy assessed by the differences to the (superior) monthly GRACE gravity field model from CSR, especially in the low degrees. Hence, the stochastic description of the pseudo-observations needs to be expanded.

Covariance information covering several epochs Apart from the epoch-wise covariance information from the formal covariance propagation, the formal covariances connecting a certain number of epochs may be taken into account as well. Their behaviour reflects the presence of the carrier phase ambiguities because only these parameters connect different epochs in a kinematic point positioning. They comprise the observation geometry, thus the influence of the constellation on the correlation between epochs.
The computation of the covariances is in principle straightforward, however, depending on the number of correlated epochs that are of interest, memory consumption may become an issue (e.g., for one day of 10 s kinematic positions and correlations up to two hours >53 million elements need to be stored, which consumes in a 64 bit notation about 500 MB memory). The covariance matrix is fully populated and nondegenerate if all epochs are considered. However, when taking only correlations for a certain time interval into account, the matrix is band-diagonal and not necessarily invertible anymore. A simple approach of obtaining an invertible matrix is slicing fully populated blocks of the matrix and inverting these blocks individually since the block diagonal matrix is invertible [cf. Jäggi et al., 2011b]. The block length defines the number of epochs that are considered. Correlations

between individual blocks are neglected, however, when applying a sufficiently long correlation time the impact on the solution is insignificant. For the results shown here the formal covariance matrices are used for a length of 50 min, which is about twice the time the observed constellation takes to vary completely (the maximum time interval an individual ambiguity is valid is about 25–30 min. Only ambiguities overlapping each other may propagate covariance information for longer time spans. The influence is decreasing with time.

Impact of formal covariances over 50 min **on orbit reconstruction and gravity field recovery** Figure 5.27 shows the elements of the covariance function for the first 50 min of the day 091, 2007, rotated to a RSW frame based on a fit using the reduced-dynamic orbit parametrisation. In addition the post-fit residuals of the respective axis are shown as well. For a clearer picture, the off-diagonal elements are drawn together with the KBR range validation and only one set of covariances over time is depicted (i.e., R-S, R-W and S-W). The other three covariances (S-R etc.) are of very similar shape and magnitude. Observe that all elements, including the off-diagonal ones, are of considerable magnitude and that neglecting them in the case of only considering epoch-wise covariances discards this information completely. Introducing the formal covariances model the (pseudo-)obser-

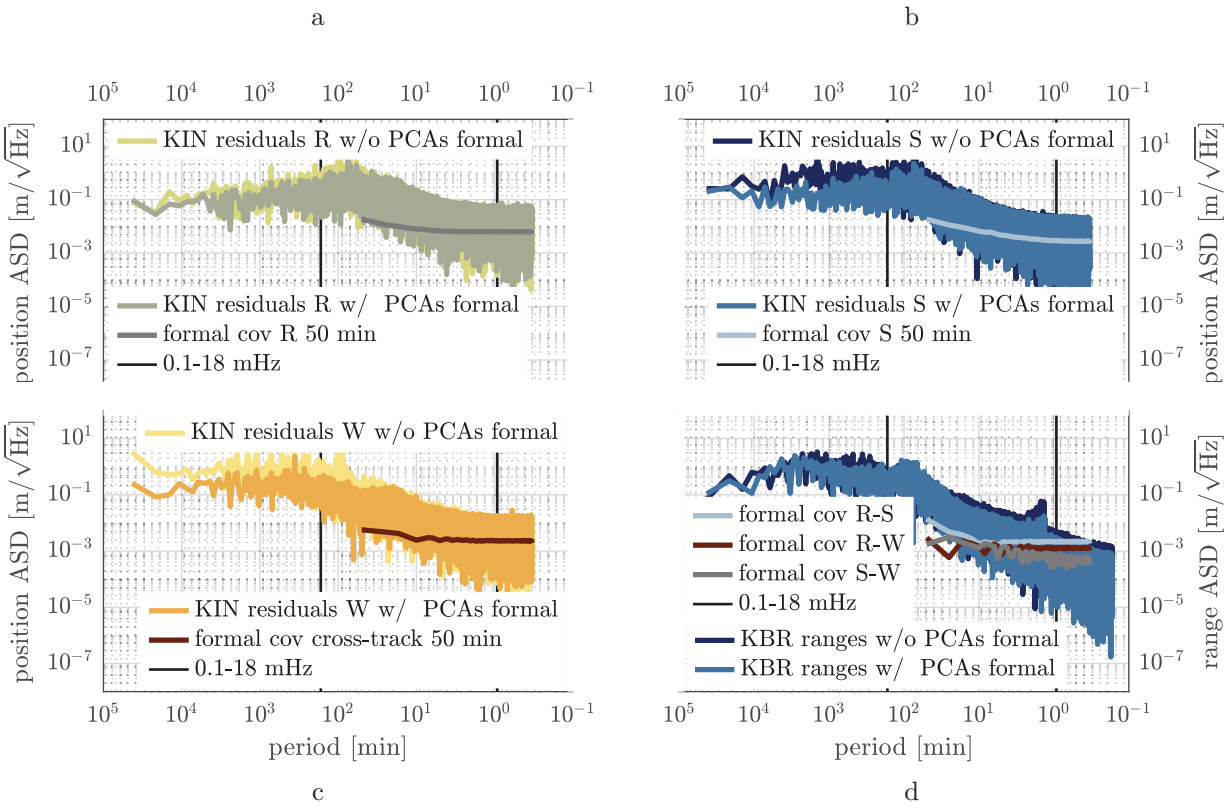

Figure 5.27: ASDs of the post-fit residuals in R (a) S (b) and W (c) directions for April 2007, as well as KBR ranges (d) with an underlying dynamic and reduced-dynamic parametrisation when using formal covariances covering 50 min. Additionally, the averaged first 50 min of the formal covariances are shown.

vations, the distinct difference in the post-fit residuals between the dynamic and reduced-

dynamic parametrisation is reduced in all axes. Note that the jump at d/o = 70 is only visible in the range-validation but not in the along-track post-fit residuals of the dynamic orbit case anymore (compare with Fig. 5.25). The dynamic orbit is still subject to the deficient a priori force model, however long-periodic variations induced by the observation geometry and ambiguity setup of the original phase observations are no longer allowed to be absorbed by orbit parameters. That accounts for both parametrisations and is visible in particular in the reduced-dynamic orbit residuals, which show a more coloured noise (pink) than in the case of only using the epoch-wise covariance information. The KBR range validation for the reduced-dynamic orbit is significantly lower than in the classical approach of weighting (cf. Table 5.11 and Table 5.10) since long-periodic variations of the pseudo-observations are no longer (erroneously) fitted by the parameters of the orbit model but (correctly) interpreted as a consequence of the ambiguity-induced correlations in time [Jäggi et al., 2011b]. In contrast to the epoch-wise covariance weighting, the KBR range validation is now at the same level as using directly GPS carrier phase observations for orbit determination. Experiments substantiating this behaviour are presented in [Jäggi et al., 2011b]. Weighting the kinematic positions by taking into account 50 min of correla-

parametrisation	RMS
reduced-dynamic	0.8 cm
dynamic	0.8 cm

Table 5.11: KBR range validation RMS using covariances over 50 min in the orbit reconstruction for April 2007.

tions leads to more realistic formal errors of the high degrees in the gravity field recovery process (Fig. 5.26b). The low degrees, however, still reveal deficiencies in the stochastic modelling. The dynamic solution profits most from taking the formal covariances over several epochs into account (compare to Fig. 5.26a), however, it cannot fully compete with the reduced-dynamic solution in the higher degrees. One may conclude that the perturbing noise therefore stems from different sources. The original carrier-phase observation uncertainty on one hand, the geometry and tracking scenario of the pseudo-observations on the other, which could be modelled by the formal covariance information, and a deficient a priori force modelling used to reduce the full gravitational and non-gravitational signal.

Empirical modelling for kinematic positions

The residuals $\hat{\boldsymbol{e}}$ (see Eq. 3.16) of a LSQ fit of kinematic positions are obtained as the difference between the pseudo-observations $\boldsymbol{\ell}$ and the adjusted observations $\hat{\boldsymbol{\ell}}$, which are computed from the estimated model parameters $\hat{\boldsymbol{x}}$. They reflect functional and stochastic modelling and data deficiencies of the orbit and gravity field recovery process. Consequently, deriving covariances from the residuals leads to a description of the physical system, and respectively, a description of the entire process of the residuals.

When the errors $\boldsymbol{e}$ of the LSQ formulation (Eq. 3.9) are disturbed by a process which is not explained in the stochastic model $\mathbf{P}$, the estimation of the cofactors of the unknown parameters $\mathbf{Q}_{\hat{x}\hat{x}}$ is scaled because $\mathbf{Q}_{ee}\mathbf{P} \neq \mathbf{I}$ (cf. Eq. 3.25). However, the residuals $\hat{\boldsymbol{e}}$ of the adjustment process, which are an estimation for the errors $\mathbf{e}$, reflect the behaviour of the errors. Therefore, they may be analysed to derive information about the disturbance. It is not possible to estimate a fully populated error covariance matrix from the residuals because the number of elements in the covariance matrix ($N \times N$) largely exceeds the number

of residuals N. However, assuming that the errors follow a (weak) stationary process [Etten, 2005] with a mean of zero and a variance constant over time, the error covariance matrix may be described by an estimated covariance function (see Sect. 3.4.1). Such a function, also named *empirical* covariance function, describes the stochastic process of the errors in a single function rather than in a full covariance matrix. The covariance function for a certain time interval Δt_k, with k denoting the sampling interval of the pseudo-observations, is defined by the auto-covariance (cf. Eq. 3.96) between the respective estimated residuals $\hat{\boldsymbol{e}}$ according to

$$\begin{aligned}
\hat{C}_{xx}(\Delta t_k) &= \frac{1}{N}\sum_{n=1}^{N-k} \hat{e}_x(t_{n+k})\hat{e}_x(t_n) \ , \\
\hat{C}_{yy}(\Delta t_k) &= \frac{1}{N}\sum_{n=1}^{N-k} \hat{e}_y(t_{n+k})\hat{e}_y(t_n) \qquad \text{and} \\
\hat{C}_{zz}(\Delta t_k) &= \frac{1}{N}\sum_{n=1}^{N-k} \hat{e}_z(t_{n+k})\hat{e}_z(t_n) \ .
\end{aligned} \tag{5.28}$$

Observe, that the biased estimate of the auto-covariance function is used here to guarantee that the estimates converge towards zero for larger lags. The covariances between the axes are obtained by computing the cross-covariance between the residuals of the respective axes:

$$\begin{aligned}
\hat{C}_{xy}(\Delta t_k) &= \frac{1}{N}\sum_{n=1}^{N-k} \hat{e}_y(t_{n+k})\hat{e}_x(t_n) \ , \qquad \hat{C}_{xz}(\Delta t_k) = \frac{1}{N}\sum_{n=1}^{N-k} \hat{e}_z(t_{n+k})\hat{e}_x(t_n) \ , \\
\hat{C}_{yx}(\Delta t_k) &= \frac{1}{N}\sum_{n=1}^{N-k} \hat{e}_x(t_{n+k})\hat{e}_y(t_n) \ , \qquad \hat{C}_{yz}(\Delta t_k) = \frac{1}{N}\sum_{n=1}^{N-k} \hat{e}_z(t_{n+k})\hat{e}_y(t_n) \ , \\
\hat{C}_{zx}(\Delta t_k) &= \frac{1}{N}\sum_{n=1}^{N-k} \hat{e}_x(t_{n+k})\hat{e}_z(t_n) \ , \qquad \hat{C}_{zy}(\Delta t_k) = \frac{1}{N}\sum_{n=1}^{N-k} \hat{e}_y(t_{n+k})\hat{e}_z(t_n) \ .
\end{aligned} \tag{5.29}$$

Assembling a covariance matrix from the covariance function leads to a (block) Toeplitz structure, which may be populated by

$$\hat{\mathbf{C}}_{ee}^{\text{kin}}(\Delta t_k) = \begin{bmatrix} \hat{C}_{xx}(\Delta t_k) & \hat{C}_{xy}(\Delta t_k) & \hat{C}_{xz}(\Delta t_k) \\ \hat{C}_{yx}(\Delta t_k) & \hat{C}_{yy}(\Delta t_k) & \hat{C}_{yz}(\Delta t_k) \\ \hat{C}_{zx}(\Delta t_k) & \hat{C}_{zy}(\Delta t_k) & \hat{C}_{zz}(\Delta t_k) \end{bmatrix} \ , \tag{5.30}$$

and

$$\hat{\mathbf{C}}_{ee}^{\text{kin,full}} = \begin{bmatrix} \hat{\mathbf{C}}_{ee}^{\text{kin}}(\Delta t_0) & \hat{\mathbf{C}}_{ee}^{\text{kin}}(\Delta t_1) & \hat{\mathbf{C}}_{ee}^{\text{kin}}(\Delta t_2) \\ \left(\hat{\mathbf{C}}_{ee}^{\text{kin}}\right)^{\text{T}}(\Delta t_1) & \hat{\mathbf{C}}_{ee}^{\text{kin}}(\Delta t_0) & \hat{\mathbf{C}}_{ee}^{\text{kin}}(\Delta t_1) \\ \left(\hat{\mathbf{C}}_{ee}^{\text{kin}}\right)^{\text{T}}(\Delta t_2) & \left(\hat{\mathbf{C}}_{ee}^{\text{kin}}\right)^{\text{T}}(\Delta t_1) & \hat{\mathbf{C}}_{ee}^{\text{kin}}(\Delta t_0) \\ & \ddots & \ddots & \ddots \end{bmatrix} \ . \tag{5.31}$$

Typically, the auto- and cross-covariance to compute the covariance functions is applied for a subset of lags until the correlations become negligible (e.g., a few hours) using the residuals of one month. In case of correlating less than all epochs, the matrix is band diagonal. Note that only for Δt_0 the symmetry relation for the off-diagonal elements of

$\bar{c}_{xy} = \bar{c}_{yx}$, $\bar{c}_{xz} = \bar{c}_{zx}$, $\bar{c}_{yz} = \bar{c}_{zy}$ holds, in case of $\Delta t_k, k \geq 1$ the covariance block $\hat{\mathbf{C}}_{ee}^{\text{kin}}(\Delta t_k)$ is composed of nine different elements.
The estimated covariance matrix $\hat{\mathbf{C}}_{ee}^{\text{kin,full}}$ may then be inserted into Eq. 3.11 as the new stochastic model

$$\mathbf{P} \triangleq \sigma_0^2 \left(\hat{\mathbf{C}}_{ee}^{\text{kin,full}}\right)^{-1} \quad , \tag{5.32}$$

and the LSQA computed according to Eq. 3.13 and Eq. 3.15.

Such an approach to empirically derive accurate covariance information is already successfully implemented in the gravity field recovery performed at TUG [see e.g., Ellmer, 2018]. The method used in this work is a simplified version suited for the CMA. In contrast to TUG, the biased estimate for the computation of the covariance function is used, because it yields a nondegenerate covariance matrix $\hat{\mathbf{C}}_{ee}^{\text{kin,full}}$. Furthermore, partial redundancies referring to the estimation of the auto-covariances are neglected. Both simplification cause a small bias, however, given the number of observations largely exceeds the number of unknown parameters and a limited number of lags is sufficient to estimate the covariance function, this bias will not be visible. In contrast, the approach employed at TUG takes both sources for a bias into account by estimating an unbiased covariance function and applying VCE to assign a variance factor to each frequency appearing in the covariance function.

In practical sense, the residuals depend on the a priori force field. Thus, first a full orbit and gravity field solution is estimated and then re-introduced as new a priori gravity field in an iterative procedure, to become independent from the a priori gravity field when computing the residuals from which the empirical covariances are derived. Otherwise, information about the a priori gravity field is trapped in the empirical covariances. Additionally, the shape of the residuals is driven by the underlying parametrisation. Consequently, the time until the correlations become negligible is highly dependent on the a priori force modelling and the parametrisation. Even under the assumption that there are no outliers (a prerequisite) in the data, the parametrisation of the underlying orbit affects the magnitude of the empirical models significantly, see Fig. 5.29 for the dynamic and reduced-dynamic parametrisations adopted there.

The noise modelling technique used in this thesis fully relies on the assumption of a stationary process. In orbit and gravity field recovery, however, the residuals are composed of both stationary and non-stationary noise. Thus, the estimated empirical covariance function is subject to an aliasing from the non-stationary components. In this work, such non-stationary noise sources are not specifically addressed, the long-periodic part may be attenuated by the PCAs. Including non-stationary noise into the stochastic model has been investigated in detail by Ellmer [2018] for SCA uncertainties on GRACE and by Kvas and Mayer-Gürr [2019] for background model uncertainties in GRACE gravity field recovery.

Impact of empirical covariances on orbit reconstruction and gravity field recovery The first two scenarios investigate the effect of empirical covariances on the gravity field recovery in the context of a dynamic orbit parametrisation. Introducing white noise as most simple assumption to weight the kinematic positions in the a priori gravity field

and orbit recovery, requires at least two iterations to compute a reasonable gravity field solution (Fig. 5.28a). Based on the expectation that the residuals better fulfil the assumption of stationarity in a RSW frame, as periodic behaviours due to the satellites' orbit will be reflected cleaner and easier to interpret, the empirical covariances are derived from residuals rotated to a RSW frame. The impact in the gravity field recovery when computing the empirical covariance functions in CRF and applying them accordingly is significant (see Fig. 5.28b). When the epoch-wise covariance information from the formal covariance

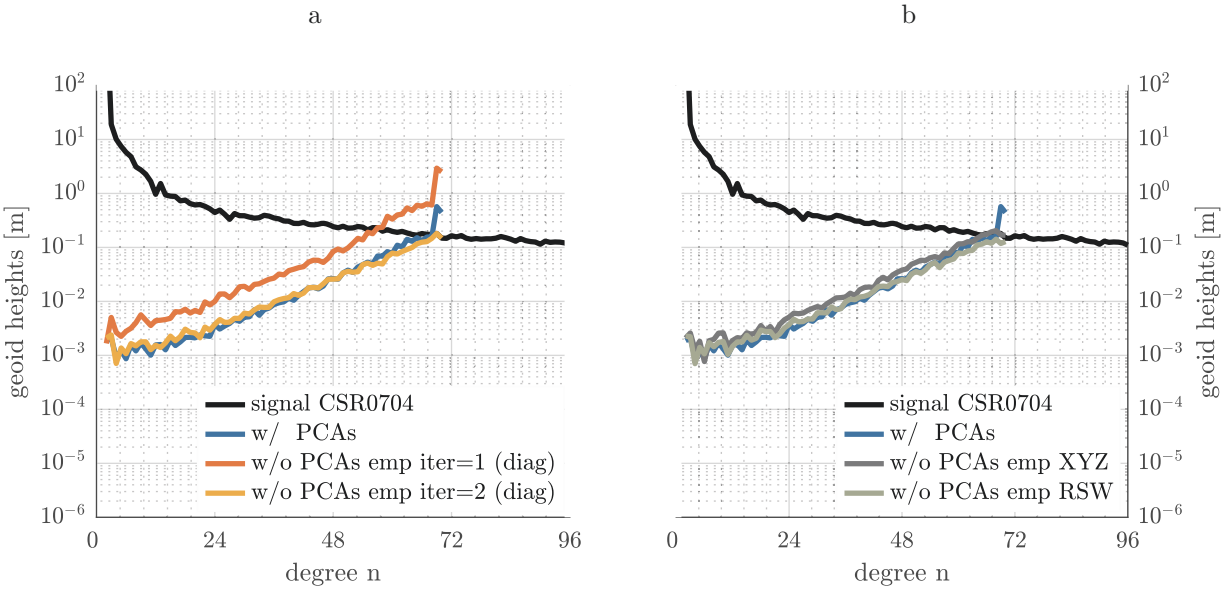

Figure 5.28: GRACE GPS-only gravity field solutions for April 2007 where the first iteration's gravity field is based an a diagonal weight matrix with equal weights for each observation and a thereof derived empirically weighted solution (a) and empirically weighted solutions where the covariance function was derived in inertial frame and RSW frame considering correlations over 50 min (b).

propagation is used in the a priori gravity field and orbit recovery, on which the empirical covariance function is built, one iteration is sufficient to estimate a reasonable gravity field solution (see in Fig. 5.30) because the epoch-wise covariances already incorporate information about the tracking scenario (inferior constellation over polar regions). For all further investigation the empirical covariances are derived in RSW frame based on an initial orbit and gravity field recovery process which applied epoch-wise covariances in the weighting of the kinematic positions.

The empirical covariance functions and the respective post-fit residuals are depicted in Fig. 5.29a-c, with a KBR range validation in Fig. 5.29d, where the cross-covariance functions are shown as a sum of all six individuals functions. The empirical models reflect the behaviour of the post-fit residuals to some extent, especially the prominent once-per-revolution peak at around 90 min is caught by the empirical covariance function of the dynamic case. This frequencies is damped by the PCAs in the reduced-dynamic orbit parametrisation, and therefore, barely contained in the respective empirical covariance functions. Noteworthy are the large correlations between the axis. For both orbit parametrisations a weight matrix derived from empirical covariances covering correlations

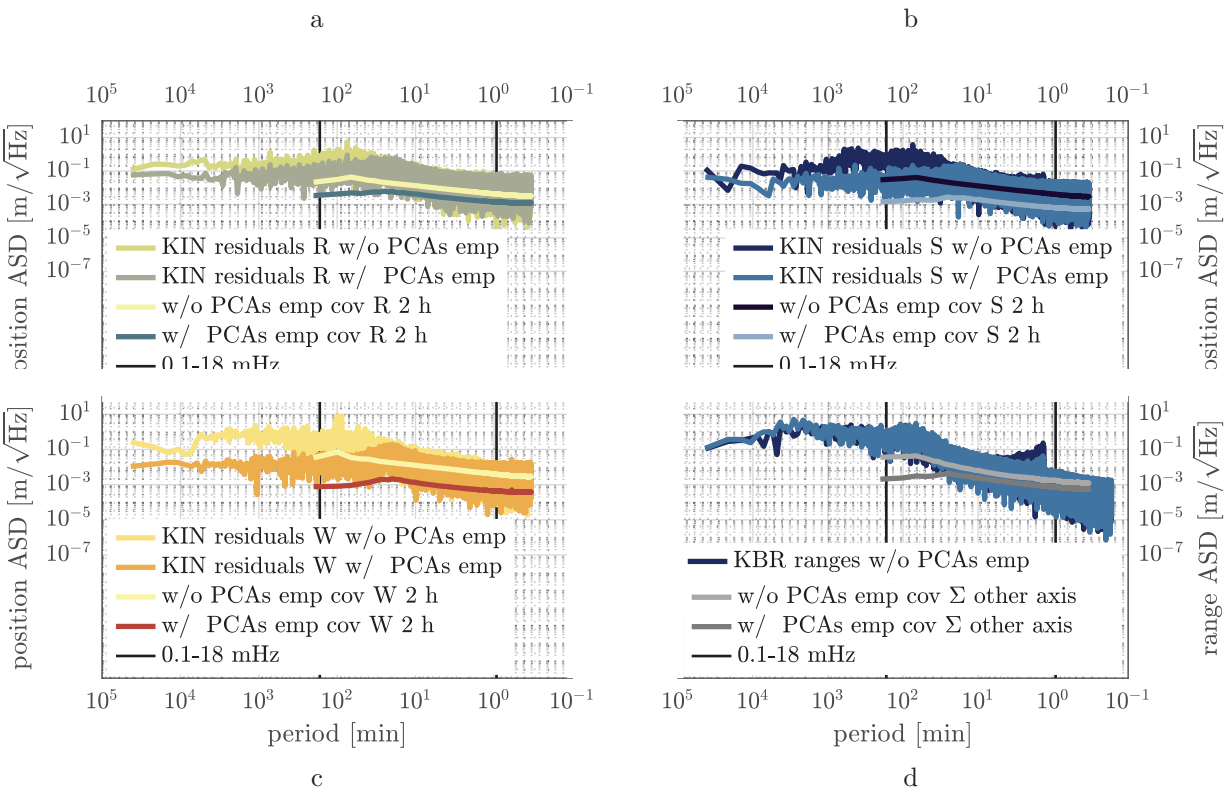

Figure 5.29: ASDs of the post-fit residuals in R (a) S (b) and W (c) direction, as well as KBR ranges (d) with an underlying dynamic and reduced-dynamic parametrisation and corresponding empirical covariance functions.

up to 50 min and 200 min was introduced in the LSQA. Likewise to the formally propagated covariances, the band diagonal structure is broken up for the sake of simple computation to a block-wise treatment in the LSQ problem, where one block is invertible and the blocks are independent from each other. The block length depends on the length of the auto-correlation of the residuals. If the correlations would be modelled such that only one block remains (e.g., one day for a daily arc), $\mathbf{C}_{\ell\ell}$ would be fully populated and nondegenerate. The block-wise treatment disregards correlations between subsequent blocks including the large correlations between the old block's end and the new block's beginning. Correlations between subsequent blocks do not vanish, however, correlations within a block tend to zero. The orbit residuals of the fit with empirical covariances and the KBR range validation (Fig. 5.29) show almost the same behaviour as in the classical approach (Fig. 5.25), an indication that the empirical covariances do not introduce systematic behaviour into the physical system. The KBR range validation RMS over one month is 1.8 cm for the reduced-dynamic and 0.8 cm for the dynamic parametrisation.

Using the empirical covariances to weight the kinematic positions in the gravity field recovery process, one can find formal errors much closer to the degree variance differences (Fig. 5.30). The low to medium degree terms, which are prone to systematic errors (e.g., antenna phase centre variations, cf. Jäggi et al. [2009b]), still feature discrepancies between the theoretically expected formal errors and the differences to the superior solution.

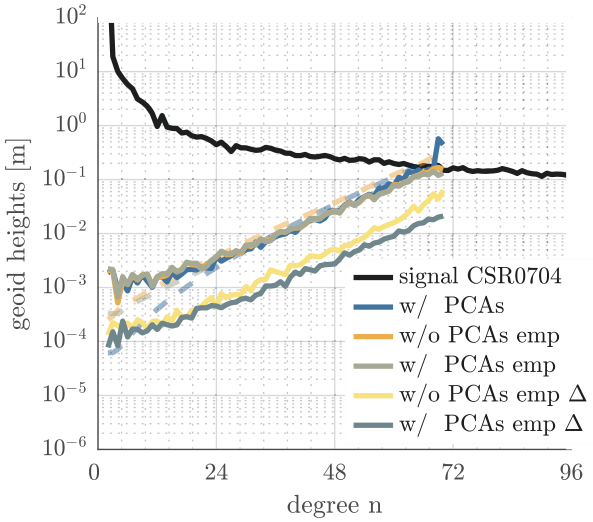

Figure 5.30: GRACE GPS-only gravity field solutions for April 2007. Empirical covariances based on the observation residuals are introduced in the gravity field determination process for lengths of 50 min and 200 min.

Empirical covariances perform better than formally propagated ones because knowledge about model and data deficiencies is both transferred into the LSQA. Degrees 10 to 26 are slightly degraded compared to the classical solution. The influence of the PCAs is still visible in the low degrees, however, the dynamic solution is not degraded in the higher degrees anymore (compare with Fig. 5.26a) because the empirical covariances are capable of dealing with noise that is absorbed by the PCAs. The difference between deriving and applying empirical covariances for 50 min or 200 min is about one order of magnitude smaller than the noise level of the individual solutions, hence, 50 min seems to be a sufficient for the application as it also allows for a faster processing. Memory consumption is not an issue for the usage of empirical covariances because they are valid over one month and are fully described by nine functions from which the covariance matrix may be compiled according to Eq. 5.31.

5.5.2 Stochastic modelling for range-rates

In the classical CMA, as it is also employed for the operational GRACE Follow-On solution computed as AIUB, the noise of the KBRR is treated as being white with a $\sigma_{\mathrm{rr}} = 3 \times 10^{-7}\,\mathrm{m\,s^{-1}}$, which was determined from an residuals analysis [Meyer et al., 2016]. The process of deriving the range-rates from the measured ranges or even the dual-frequency K-band ranging computation is not considered any further in its impact on the range-rates yet, even though there have been investigations by Beutler et al. [2010b] on the stochastic behaviour of range-rates due to the filter process to convert the range measurements to range-rates. Also the ACC is treated as noise free. The only measure in the classical CMA to account for noise in these two observation types are the constrained pseudo-stochastic parameters. Since some knowledge about the linear accelerations and the range-rates is known a priori, the next two sections make an attempt to incorporate such information into the gravity field recovery process of the CMA. This is followed by a method of empirically modelling the noise in the range-rates by examining their post-fit residuals in a process similar to the empirical covariances described in Sect. 5.5.1 for kinematic positions.

Theoretical noise models for KBRR

Using theoretical models for the observation noise emerging from the measurement system itself is a first step towards a better of mapping these deficiencies through the LSQA to the final solution. Such models are usually defined before launch (pre-launch models) by

systematically testing the performance of the instruments on ground. Indeed, the behaviour in space might be different due to the harsh space conditions and the zero-g environment, but a ground truth may serve as an initial guess about the observation noise.
The theoretical modelling has been implemented for two instruments, namely the ACC and the KBR system, but only as the combined effect affecting the observation type of range-rates. Still, the ACC noise is also affecting the NEQs based on the kinematic positions as it is contained in the background force field. One might assume it to be of rather low impact because for a kinematic-positions-only gravity field solution the noise in the observations superposes the ACC noise.

Noise model for the KBR K-band Dual One-Way Ranging (DOWR) noise consists of several components, mostly the noise of the ultra-stable oscillator which is highly dependent on its frequency stability, mainly acting on low frequencies of the range spectrum, and the system noise, which is mainly visible in the higher frequencies [Kim et al., 2002]. In addition, there is noise due to time tagging errors or multipath effects, which are, however, rather small. Kim [2000] and Thomas [1999] have performed detailed pre-launch simulations for GRACE on these different noise sources, Frommknecht [2007] gives a detailed description of the actual behaviour of the different instruments and their data pre-processing. For the application as a theoretical noise model only the system noise is considered as relevant since the noise of the oscillator is superimposed by the ACC noise by several orders of magnitude in the low frequency range (see Fig. 5.31a). Furthermore, Ko [2008] showed for GRACE that the ranging errors due to the oscillator noise is two orders of magnitude lower than the system requirement. Consequently, neither the low frequencies nor the high frequencies of the spectrum are dominated by the oscillator noise and it might be omitted for the noise model formulation. For the system noise a simple model is adopted. It assumes white noise

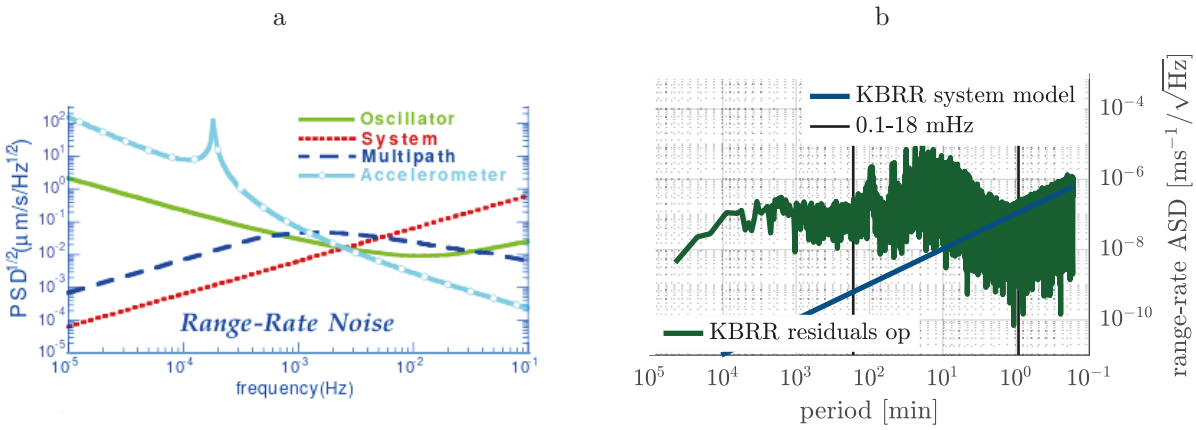

Figure 5.31: Theoretical noise models expressed in range-rates for the main observation noise sources from Kim [2000] (a) and ASDs of the system noise and of KBRR post-fit residuals for a classical solution, exemplarily for January 2019, expressed in range-rates (b).

with $\sigma = 1\,\mu\mathrm{m}/\sqrt{\mathrm{Hz}}$ for the measured biased range between the two spacecraft, thus, a flat spectrum [Thomas, 1999]. The relation between ranges and range-rates is established by numerical differentiation. In frequency domain, this differentiation may be easily expressed

by a multiplication with the vector $\boldsymbol{z}$

$$\boldsymbol{z} = 2\pi \boldsymbol{f} \ , \tag{5.33}$$

and by the element-wise product

$$\boldsymbol{P}_{\mathrm{rr}}^{\mathrm{system}} = \boldsymbol{z}^2 \circ \boldsymbol{P}_{\mathrm{r}}^{\mathrm{system}} \ , \tag{5.34}$$

where $\boldsymbol{P}_{\mathrm{r}}^{\mathrm{system}}$ denotes the PSD of the range noise, $\boldsymbol{P}_{\mathrm{rr}}$ the PSD of the range-rate noise and $\boldsymbol{f}$ a frequency vector containing all frequencies of the spectrum $\boldsymbol{P}$. This differentiation leads to coloured noise for the range-rates. The noise contained in the post-fit range-rate residuals of the operational solution (Fig. 5.31b) is well characterised by the model of the system noise for periods <2 min, differentiated from white noise in ranges to range-rates.

Noise model for the ACC The ACC noise used in this context is defined by the pre-launch specifications published for GRACE, see e.g., Kim [2000]. It stems from the ACC design precision of 0.1 nm s^{-2} at 10 Hz [Kim et al., 2002]. In contrast to the original attempt of Kim [2000], which makes use of Hill's equation to analytically solve for the influence on range-rates, only a simple integration from accelerations to velocities is adopted at the level of the PSD by using $(\boldsymbol{z}^2)^{-1}$. As a consequence, the major peak at 1 cycle-per-revolution as seen in Fig. 5.31a is not reproduced, but the general slope is well preserved. The noise model is generated for the different axes of the ACC, distinguishing between the two high-sensitivity axes (x, z, Eq. 5.35a) and the low-sensitivity axis (y, Eq. 5.35b)

$$\boldsymbol{P}_{x,z}^{\mathrm{acc}} = \left(1 + \frac{0.005}{\boldsymbol{f}}\right) \cdot 1 \times 10^{-20} \ (\mathrm{m\,s^{-2}}\sqrt{\mathrm{Hz}})^2 \qquad \text{and} \tag{5.35a}$$

$$\boldsymbol{P}_{y}^{\mathrm{acc}} = \left(1 + \frac{0.1}{\boldsymbol{f}}\right) \cdot 1 \times 10^{-18} \ (\mathrm{m\,s^{-2}}\sqrt{\mathrm{Hz}})^2 \ . \tag{5.35b}$$

The noise model is supposed to reflect noise in the range-rate observations, thus, only the high-sensitivity axis' model defined in Eq. 5.35a is taken into consideration in the combined noise model of system and ACC noise. The ACC noise model expressed as ASDs is depicted in Fig. 5.32a for accelerations and in Fig. 5.32b for range-rates, where the accelerations are integrated to velocities by inverting Eq. 5.34. The model is in good agreement for frequencies between 10 min and 1 min when taking the KBRR post-fit residuals of the operational solution as a reference for the actual noise in the system.

Combining the noise models for the ACC and the KBR The two noise models are not used separately because each covers only one part of the spectrum. Thus, the sum of the two is used

$$\boldsymbol{P}_{\mathrm{rr}}^{\mathrm{full}} = \boldsymbol{P}_{\mathrm{rr}}^{\mathrm{system}} + \boldsymbol{P}_{\mathrm{rr}}^{\mathrm{acc,x}} \ . \tag{5.36}$$

The full noise model $\boldsymbol{P}_{\mathrm{rr}}^{\mathrm{full}}$ (depicted in Fig. 5.33a) is converted to a covariance function by the relation between the PSD and the auto-correlation for stationary signals given with the Wiener-Khinchin theorem, see Sect. 3.4.2.

The inverse Fourier transformation ($\mathcal{F}^{-1}$) needs to be applied to obtain the auto-covariance function $\boldsymbol{c}_{\mathrm{rr}}^{\mathrm{theor}}(\Delta\boldsymbol{t})$, thus, the covariance function from the theoretical models by

$$\boldsymbol{c}_{\mathrm{rr}}^{\mathrm{theor}}(\Delta\boldsymbol{t}) = \mathcal{F}^{-1}\left(\boldsymbol{P}_{\mathrm{rr}}^{\mathrm{full}}\right) \quad . \tag{5.37}$$

$\Delta\boldsymbol{t}$ denotes a vector of time lags between t_0 and the time t_K corresponding to the lowest frequency in $\boldsymbol{f}$. The covariance function may be used to compile a covariance matrix. It

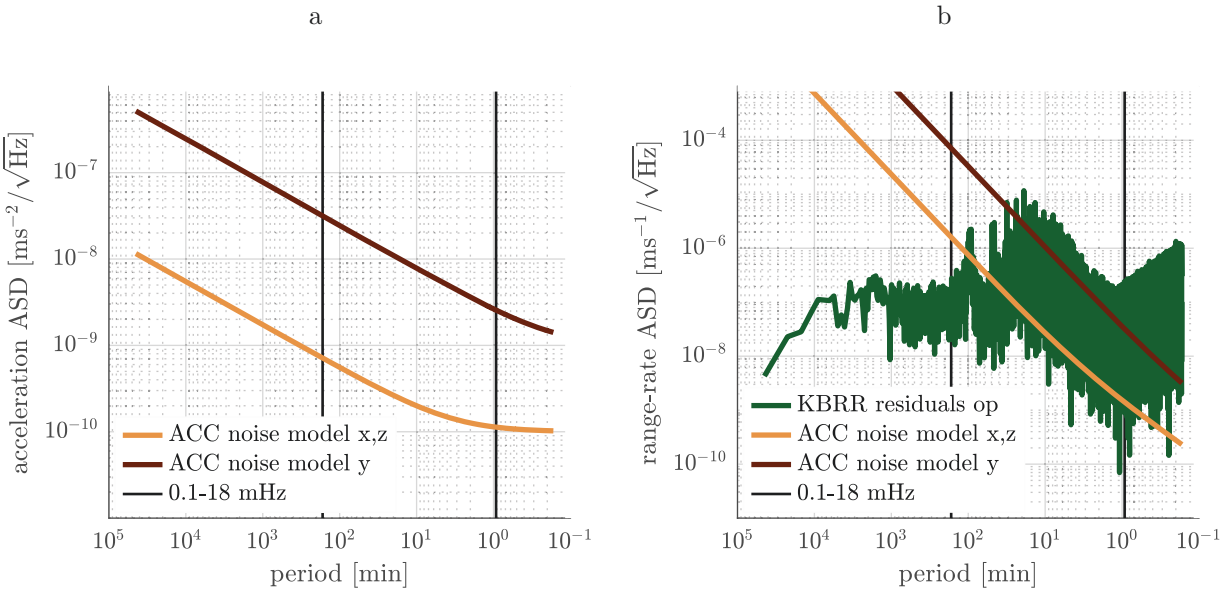

Figure 5.32: ASDs of the ACC noise (a) and the projected noise together with KBRR post-fit residuals for a classical solution, exemplarily for January 2019 (b).

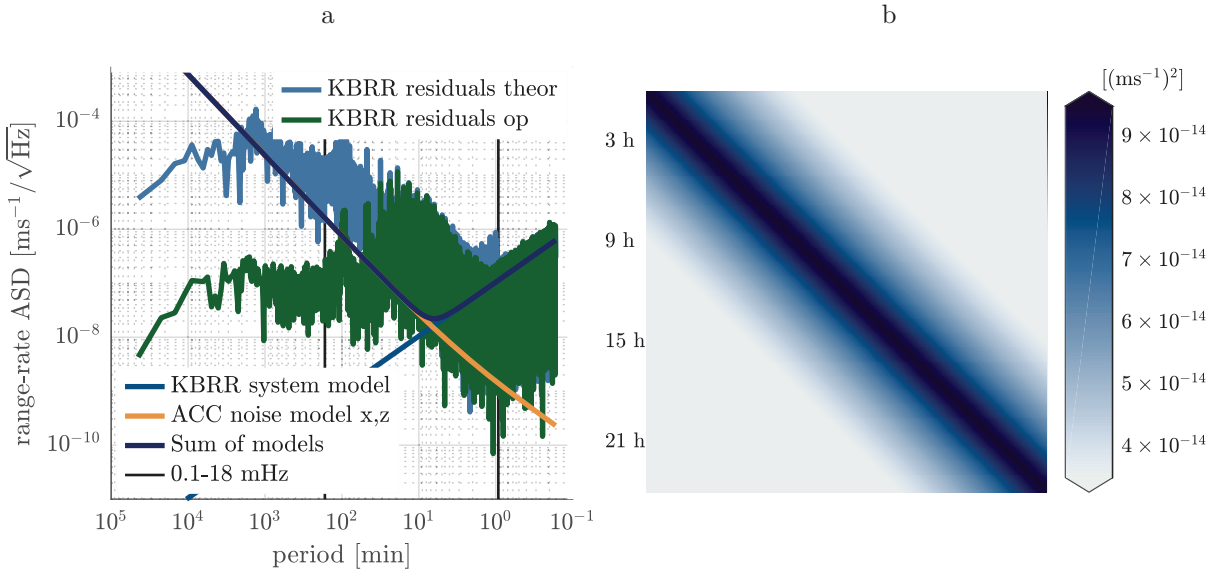

Figure 5.33: ASDs of the system noise and the ACC noise together with KBRR post-fit residuals for a classical solution, exemplarily for January 2019, and the covariance matrix for derived from the noise model for one day (b).

is of a symmetric (block) Toeplitz structure and may be easily set up as

$$\mathbf{C}^{\mathrm{rr}}_{\mathrm{theor}} = \begin{bmatrix} c^{\mathrm{theor}}_{\mathrm{rr}}(\Delta t_0) & c^{\mathrm{theor}}_{\mathrm{rr}}(\Delta t_1) & c^{\mathrm{theor}}_{\mathrm{rr}}(\Delta t_2) & \dots & c^{\mathrm{theor}}_{\mathrm{rr}}(\Delta t_K) \\ c^{\mathrm{theor}}_{\mathrm{rr}}(\Delta t_1) & c^{\mathrm{theor}}_{\mathrm{rr}}(\Delta t_0) & c^{\mathrm{theor}}_{\mathrm{rr}}(\Delta t_1) & \dots & c^{\mathrm{theor}}_{\mathrm{rr}}(\Delta t_{K-1}) \\ c^{\mathrm{theor}}_{\mathrm{rr}}(\Delta t_2) & c^{\mathrm{theor}}_{\mathrm{rr}}(\Delta t_1) & c^{\mathrm{theor}}_{\mathrm{rr}}(\Delta t_0) & \dots & c^{\mathrm{theor}}_{\mathrm{rr}}(\Delta t_{K-2}) \\ \vdots & \vdots & \vdots & \ddots & \vdots \\ c^{\mathrm{theor}}_{\mathrm{rr}}(\Delta t_K) & c^{\mathrm{theor}}_{\mathrm{rr}}(\Delta t_{K-1}) & c^{\mathrm{theor}}_{\mathrm{rr}}(\Delta t_{K-2}) & \dots & c^{\mathrm{theor}}_{\mathrm{rr}}(\Delta t_0) \end{bmatrix} . \quad (5.38)$$

The covariance matrix is shown for one day in Fig. 5.33b. It may then serve as weight matrix $\mathbf{P}$ for the range-rate observations in the LSQA by applying Eq. 3.11. $\mathbf{C}^{\mathrm{rr}}_{\mathrm{theor}}$ may easily be set up as full matrix, however, due to the processing of daily arcs, it is cut to shorter blocks (daily or even shorter), thus being of a block Toeplitz kind.

Impact of the theoretical noise model Applying the theoretical noise model (Eq. 5.38) to describe the stochastic behaviour of the KBRR observations for each arc without additionally estimating constrained PCAs, i.e., only using a dynamic orbit parametrisation of six initial conditions and the ACC bias and scale, leads to gravity field solutions of reasonably good quality. The RMS over the oceans for such a time series covering the years 2019 and 2020 is shown in Fig. 5.34 and compared to the operational solution. It is

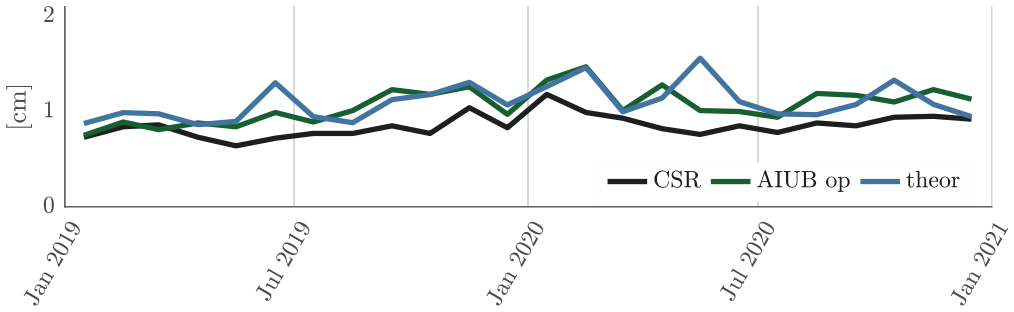

Figure 5.34: RMS over the oceans for two years of GRACE Follow-On comparing the CSR solutions, the operational AIUB model and solution when the theoretical noise model for the KBRR data is applied.

interesting to note that the theoretical model has a similar capability in dealing with the noise caused by the ACC and the KBRR as the constrained and co-estimated PCAs. Since the parameter space for the local parameters consists of only twelve elements, the solutions demand are hardly any computational resources compared with the solution based on PCAs. The main disadvantage may be attributed to the fact the theoretical models are not very flexible compared to the PCAs and they might need to be adapted to a changing instrument behaviour.

Empirical modelling for range-rates

As with the kinematic positions, the post-fit residuals of KBRR of an orbit and gravity field fit reflect model (functional and stochastic) and data deficiencies. Hence, using them as the basis for modelling the noise is supposed to provide an accurate description of the entire definition of the problem. The empirical modelling of range-rates corresponds with the one of the kinematic positions (see Sect. 5.5.1) to a large extent. Again, as the residuals depend

on the a priori force field, first a full orbit and gravity field solution is estimated without empirical noise modelling and then re-introduced as new a priori gravity field to become independent from the a priori gravity field when computing the residuals and the empirical covariances. This procedure may be applied iteratively by taking the solution computed using empirical covariances as new a priori gravity field. The number of iterations is largely depending on the quality of the initial stochastic model, see in Fig. 5.37a. It is important to note that the parameter space is not allowed to be changed within the iterations, e.g., deriving the empirical model from a reduced set of parameters. This leads to a bias of the final solution towards the solution which is computed with the parametrisation used to obtain the empirical model. In the extreme case of using two completely different sets of parameters, one to estimate the empirical stochastic model for the observations, the other to obtain the sought-after solution from the same (now accordingly weighted) observations, the bias may be expressed as using the residuals of the first adjustment as observation (see Sect. 3.2.6, Eq. 3.78).

Even though similar to the process of deriving an empirical covariance function for the kinematic positions, several modifications for range-rates need to be considered. First of all, the one dimensional nature of the range-rate observations simplifies the estimation of the empirical covariance function to computing only the auto-covariance. No cross-covariance functions as in Eq. 5.29 exist. The covariance function for a certain time interval Δt_k may be estimated in analogy to Eq. 5.28 as

$$\hat{C}_{\mathrm{rr}}(\Delta t_k) = \frac{1}{N}\sum_{n=1}^{N-k} \hat{e}(t_{n+k})\hat{e}(t_n) \qquad \text{with} \qquad k \in \{0, ..., K\} \ , \tag{5.39}$$

where K defines the maximum lag. Again, the assumption of a (weak) stationary process underlying and characterising the stochastic behaviour of the residuals is made. The covariance matrix from the covariance function may be set up as

$$\hat{\mathbf{C}}_{ee}^{\mathrm{rr}} = \begin{bmatrix} \hat{C}_{\mathrm{rr}}(\Delta t_0) & \hat{C}_{\mathrm{rr}}(\Delta t_1) & \hat{C}_{\mathrm{rr}}(\Delta t_2) & ... & \hat{C}_{\mathrm{rr}}(\Delta t_K) \\ \hat{C}_{\mathrm{rr}}(\Delta t_1) & \hat{C}_{\mathrm{rr}}(\Delta t_0) & \hat{C}_{\mathrm{rr}}(\Delta t_1) & ... & \hat{C}_{\mathrm{rr}}(\Delta t_{K-1}) \\ \hat{C}_{\mathrm{rr}}(\Delta t_2) & \hat{C}_{\mathrm{rr}}(\Delta t_1) & \hat{C}_{\mathrm{rr}}(\Delta t_0) & ... & \hat{C}_{\mathrm{rr}}(\Delta t_{K-2}) \\ \vdots & \vdots & \vdots & \ddots & \vdots \\ \hat{C}_{\mathrm{rr}}(\Delta t_K) & \hat{C}_{\mathrm{rr}}(\Delta t_{K-1}) & \hat{C}_{\mathrm{rr}}(\Delta t_{K-2}) & ... & \hat{C}_{\mathrm{rr}}(\Delta t_0) \end{bmatrix} \ , \tag{5.40}$$

which again leads to a symmetric matrix in (block) Toeplitz structure. The processing with daily arcs implies that the covariance matrix is split into blocks with a maximum length of one day, thus for a 5 s KBRR sampling this is corresponding to 17 280 epochs. The full covariance matrix for M blocks, with $M \in \{28, 29, 30, 31\}$ for monthly solutions, reads as

$$\hat{\mathbf{C}}_{ee}^{\mathrm{rr,full}} = \begin{bmatrix} \hat{\mathbf{C}}_{ee}^{\mathrm{rr},1} & & & \mathbf{0} \\ & \hat{\mathbf{C}}_{ee}^{\mathrm{rr},2} & & \\ & & \ddots & \\ \mathbf{0} & & & \hat{\mathbf{C}}_{ee}^{\mathrm{rr,M}} \end{bmatrix} \ , \tag{5.41}$$

with the superscript denoting the block number. However, the processing may be performed sequentially for each block (see Sect. 3.2.4). Shorter block lengths may be chosen, e.g., in case the block-wise VCE (see in Sect. 5.3.2) is used. Based on the given formulation

of the problem, trade-offs between the block length for VCE and the empirical modelling may be necessary, e.g., a short block length would be interesting for the outlier treatment with VCE, but to catch the correlations longer blocks may be required for a more accurate empirical modelling. For the GRACE Follow-On processing block lengths of 3 h turned out to be reasonable (or a sensible balance), mostly driven by the signal to be described by the empirical modelling to sample at least one revolution of the satellites.
A covariance function for January 2019, which is based on the KBRR post-fit residuals from the operational processing, is shown in Fig. 5.35. To better illustrate its behaviour a length of 6 h is plotted, even tough only 3 h are used in the processing. It mainly features peak frequencies linked to the satellites' revolution period, the most prominent being at once-per-revolution. The sign flip between at the first lag between Δt_0 and Δt_1 (Fig. 5.35b) is caused by the differentiation of the original ranges to range-rates. The empirical model

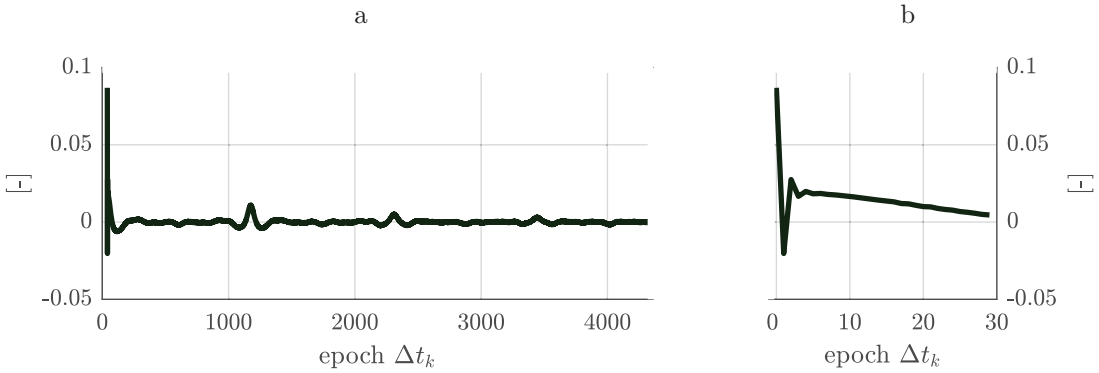

Figure 5.35: Empirical covariance function in time domain derived from KBRR post-fit residuals (a) with a zoom to the first 30 epochs (b).

is supposed to reflect the general stochastic behaviour of the underlying force model and the observations in the modelled physical system. It is important that the residuals fulfil the assumption of following a stationary process. In particular outliers will distort the estimation of the covariance function because Eq. 5.39 is not a robust estimator. To attenuate for these effects, the variance components from a block-wise VCE are considered to screen the residuals by excluding all residuals corresponding to a block with a large variance component. Whether a variance component corresponds to an outlier or not is determined by a simple outlier detection in each monthly time series of variance components ($\hat{\boldsymbol{\sigma}}$) by adopting the Median Absolute Deviation (MAD) outlier screening. This method is a simple robust estimator of a time series' standard deviation [see Hampel, 1974, Huber, 1981] and checks if each component of the time series lies within an interval of three times the estimated standard deviation around the median. Such outliers appear on a regular basis as no other screening of the KBRR observations is applied. For the GRACE Follow-On time series of 38 months (June 2018 until September 2021) about 6 % of the variance components are found to be an outlier (see Fig. 5.17).
The dependency on the a priori gravity field is mitigated to the extent possible by estimating an independent gravity field solution first and by computing the covariance function from post-fit residuals. The interdependency between the orbit parametrisation and the shape of the residuals, however, strongly impacts the basic assumption of stationarity. Any parameter set up to compensate for remaining signal in the system (be it noise or sought-

after gravity field signal) leads to a flatter spectrum of the residuals and a smaller amount of noise to be compensated by the empirically determined covariances which are only accounting for (stationary) stochastic noise on the level of observation weighting. Thus, it is advisable to treat systematic and non-stationary signal either with co-estimated parameters and/or an accurate a priori stochastic model [Ellmer, 2018, Kvas and Mayer-Gürr, 2019].
In contrast to the kinematic positions, the frame of the observations does not need to be addressed because a scalar, one dimensional differential observable is processed. Likewise, memory consumption is not a problem for applying empirical covariances since they are fully described by one function which is valid over one month. The relation between the covariance matrix set up in Eq. 5.41 and the weight matrix $\mathbf{P}$ introduced into the LSQA follows

$$\mathbf{P} \triangleq \sigma_0^2 \left(\hat{\mathbf{C}}_{ee}^{\mathrm{rr}} \right)^{-1} \quad . \tag{5.42}$$

For reasons of efficiency, the inverse may be computed for each block of $\hat{\mathbf{C}}_{ee}^{\mathrm{rr}}$ separately. The LSQA then continues with Eq. 5.42, and a block-wise treatment to set up the system of equations as introduced in Sect. 3.2.4 is adopted.
One may note that modelling the noise in the observations by analysing the correlations of the post-fit residuals over time, thus, treating them as a univariate time series, is only part of the full information content in the post-fit residuals. This may be suited to cover instrument errors, which only affect measurements taken within a certain interval, generally combined with a decreasing influence over time. Geographically distributed errors, e.g., induced by a deficient de-aliasing model, which may first be sampled after several ground track passes, cannot be treated adequately with a univariate view on the post-fit residuals. Kvas and Mayer-Gürr [2019] provide elaborated methods of including background model uncertainties of GRACE gravity field recovery into the stochastic model of the observations.

Impact of range-rate empirical covariances The empirical model is reflected in the post-fit residuals from which it is derived. Figure 5.36a shows the post-fit residuals from the operational solution and the corresponding empirical model in the spectral domain. The same empirical model in time domain is depicted in Fig. 5.35. The two main types of coloured noise i.e., $1/f^2$-noise and f^2-noise where the latter dominates in periods of 2 min and less, are very well captured by the empirical model, also the prominent peak at once-per-revolution is reflected. Introducing artefacts into the post-fit residuals by e.g., cutting the monthly a priori gravity field solution at d/o = 60 (Fig. 5.36b), which results in a spike at the corresponding frequency, is also mapped by the empirical covariance function. Observe that any information (also a bias) transported to the post-fit residuals will be absorbed in the thereof derived empirical noise model. In case of using constrained pseudo-stochastic parameters, only one iteration is required because the PCAs absorb a good portion of the noise in the system. On the contrary, without any additional noise parameters, up to at least two or three iterations are needed to come up with a reasonable solution. This solution, however, lacks the modelling of certain deficiencies which are covered by co-estimated PCAs (see Fig. 5.37a).

An empirical model may be derived for kinematic positions and KBRR observations (Fig. 5.37b). Separating the influence of these two components (Fig. 5.38) shows that the

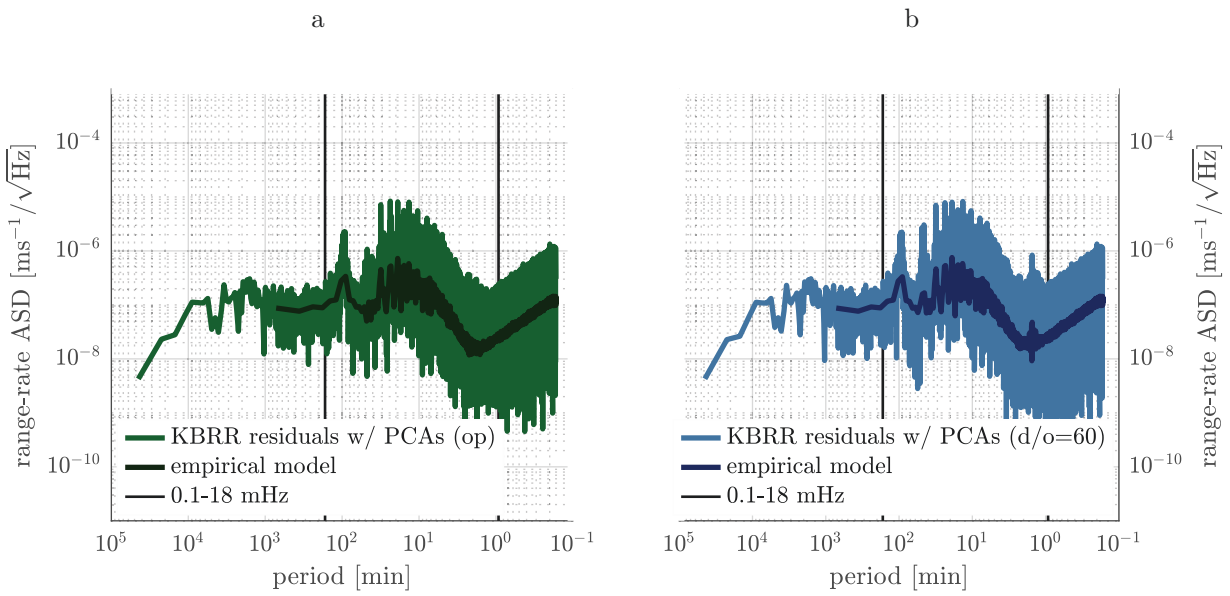

Figure 5.36: ASD of KBRR post-fit residuals for January 2019 together with the thereof derived empirical model for d/o = 96 (a) and d/o = 60 (b).

formal errors are shifted towards a more realistic noise level, assessed with an external solution from CSR, by the contribution of the empirical noise modelling of the kinematic positions. Thus, modelling the stochastic behaviour of the kinematic positions in a more adequate way bears a large contribution to the estimation of the formal errors of the gravity field solution. The empirical covariances of the KBRR additionally change the shape

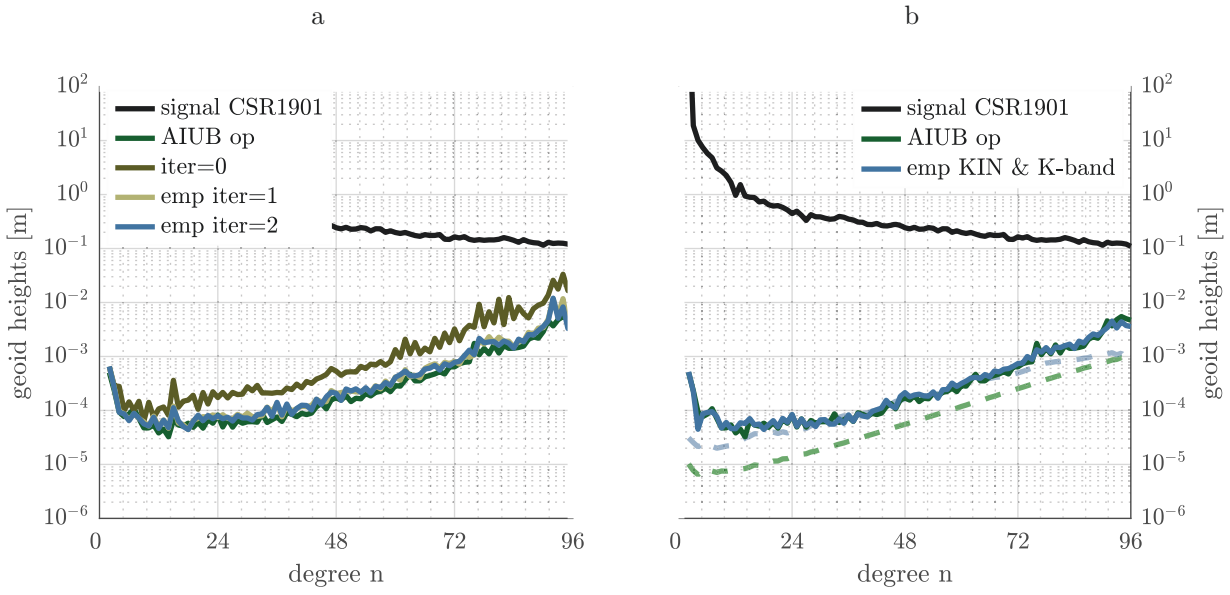

Figure 5.37: Development of a gravity field solution without pseudo-stochastic modelling when deriving empirical noise models (a) and difference degree amplitudes for a monthly solution (January 2019) using an empirical noise model for both the kinematic positions and KBRR (b).

of the formal errors, now featuring the resonance orders as well and closely following the

difference degree amplitudes in the mid-degrees. The small bend in the high degrees is an indication that more information from the high degrees of the static background gravity field went into the solution with empirical noise modelling than in the classical solution. The differences be particularly well seen in a triangle of coefficients (Fig. 5.39), where the

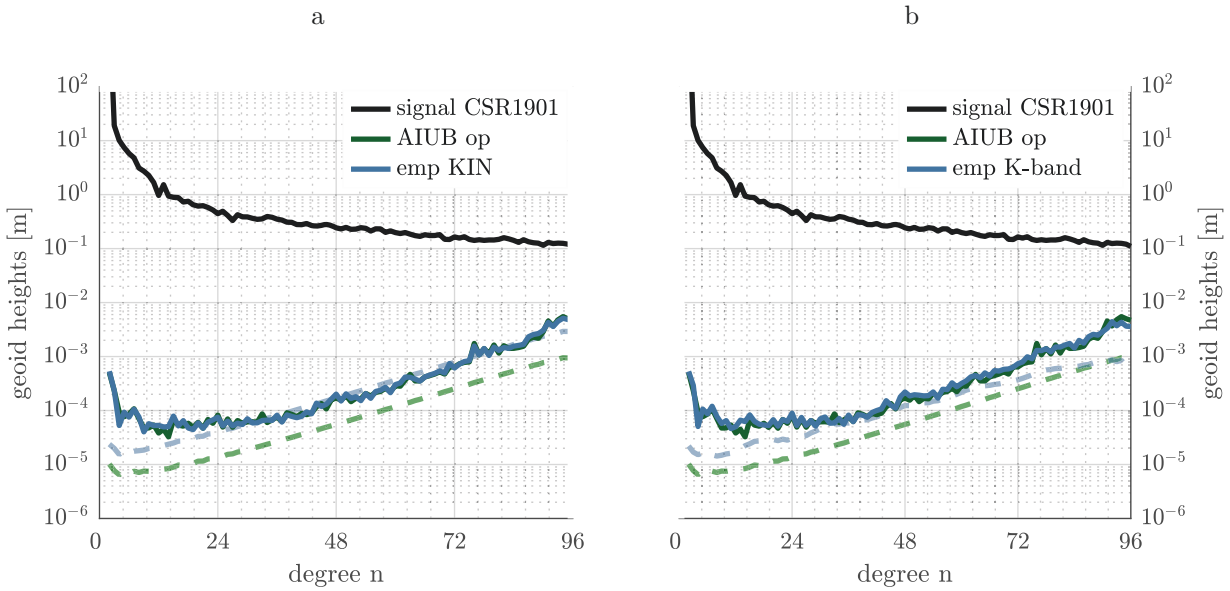

Figure 5.38: Difference degree amplitudes for a monthly solution (January 2019) using an empirical noise model for the kinematic positions (a) and KBRR (b).

stripes in the resonance orders appear. Applying the empirical modelling for longer time

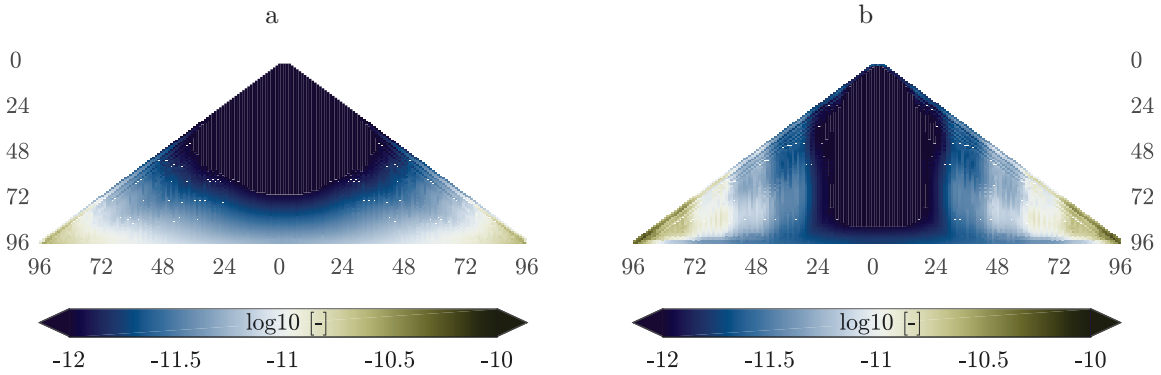

Figure 5.39: Triangle of coefficients for the formal errors of the operational solution (a) and the solution with empirical noise modelling for KBRR (b).

spans shows that the RMS over the oceans can be significantly lowered (see Fig. 5.40), indicating that this modelling technique is capable of absorbing noise. Thus, adapting the stochastic model of the observations based on the information contained in the post-fit residuals is beneficial to suppress noise leaking into the gravity field solution.

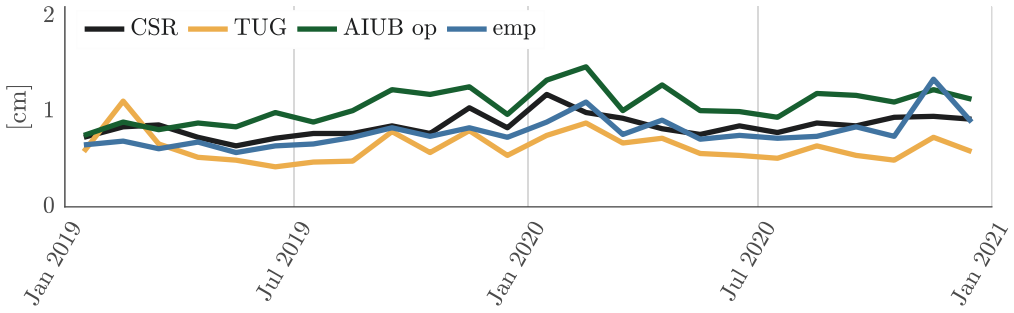

Figure 5.40: RMS over the oceans for two years of GRACE Follow-On comparing the CSR solutions, the operational AIUB model and applying empirical noise modelling based on the post-fit residuals.

5.5.3 Combination of noise modelling techniques

It is straightforward to make use of the pseudo-stochastic modelling including a VCE to obtain optimal constraints and to additionally derive empirical covariances from the post-fit residuals. This procedure may be simply applied iteratively to obtain a gravity field. The post-fit residuals including the empirical covariance function for KBRR after the first iteration is shown in Fig. 5.41. The spectrum for periods larger than the Nyquist-frequency of the pseudo-stochastic parameters with a 15 min sampling is significantly flattened compared to the one of the operational solution where a clear once-per-revolution peak is visible. Additionally, the transition from the flat to the coloured spectrum features a more pronounced edge (compare with the ASDs of the operational solution in Fig. 5.36a). One may assume that the modelling for the frequencies directly affected by the PCAs is accurate and the weighting through the empirical covariance function mainly acts on higher frequencies, because, in contrast to the classical solution, the constraining of the parameters is optimised in the framework of VCE. The RMS over the oceans (Fig. 5.42) is very similar to the solution with only empirical noise modelling, with a few months, e.g., the already mentioned September 2020, distorting the solution with the combination of noise modelling techniques.

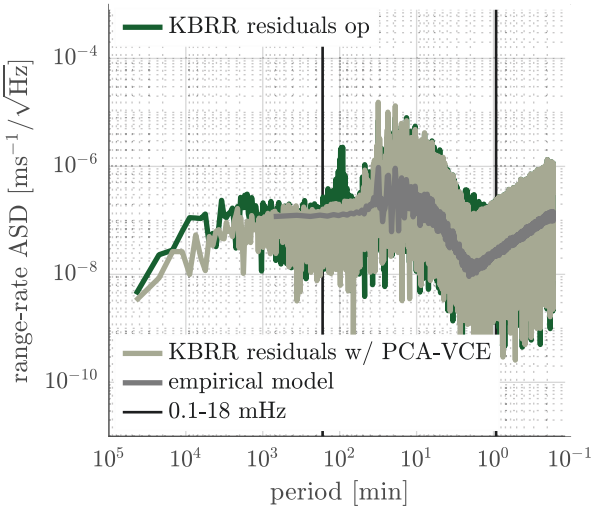

Figure 5.41: ASD of KBRR post-fit residuals for January 2019 together with the thereof derived empirical model when additionally using VCE to determine the constraints for the PCAs.

5.5.4 Combination of gravity field models

Combining gravity field models derived from different ACs, computed with different software and approaches is based on the idea to bring the strengths of each individual solution to an optimal combined product.

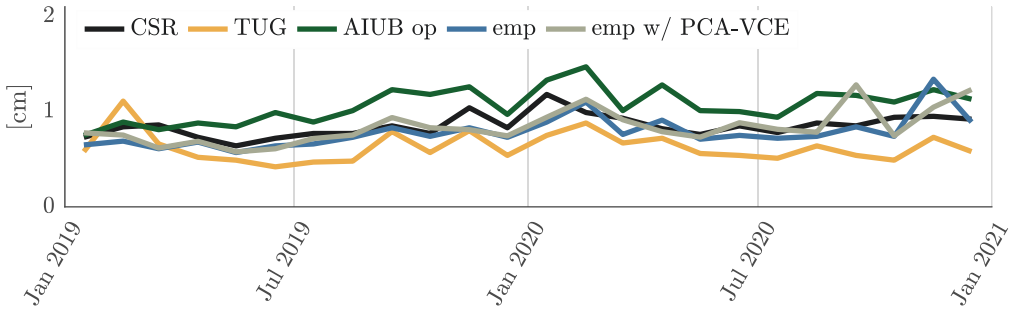

Figure 5.42: RMS over the oceans for two years of GRACE Follow-On comparing the solutions from CSR, the operational AIUB solution, the solution with empirical modelling and combining empirical modelling with a VCE on the constraints.

The operational GRACE Follow-On solution is contributing to COST-G's combined GRACE Follow-On solution, comprised of seven individual solutions computed with different software packages and each employing a different approach on gravity field recovery. As the analysis centre coordinator of the COST-G service is located at the AIUB, the chance of not only using the operational solution but also various test solutions in the combination process is taken. This provides the opportunity to access COST-G's internal validation tools, and furthermore, holds a good indication on the overall performance of a test scenario in the chain of different independent gravity field solutions.

The COST-G performance of two solutions is investigated in more detail:

a. The operational GRACE Follow-On solution. It will also serve as a reference whether additional processing methods turn out to be beneficial.
b. This case investigates the use of empirically derived noise models for kinematic positions and range-rates.

As the previous sections have shown, additionally estimating the constraints through VCE or using the pre-launch noise models, does not result in large improvements of the gravity field solutions. Therefore, only the operational processing and empirical noise modelling, which is significantly improving the noise level of the solutions, are covered here.

The weights assigned by the VCE used to combine the individual gravity field solution are indicating the contribution of each solution to the full model. Introducing the operational solution (Fig. 5.43) shows that the AIUB time series receives the highest weights, even though - based on the comparison with the RMS over the ocean, e.g., in Fig. 5.40 - the solution is not best performing among the ACs. For some months the contribution reaches up to 40 %, this may only be explained that the AIUB solutions balances in between all other solutions, which is favoured by the combining VCE. Even though providing for a solution with the lowest noise level [see Kvas et al., 2019], the solution from TUG contributes only to a minor extent. Using the solutions with empirical noise modelling for the kinematic positions and KBRR instead of the operational AIUB model, displayed in Fig. 5.44, yields weights which follow closer the expectations indicated by the noise over the oceans. Still, the AIUB shows rather high weights, but drastically dropped compared to the operational solution. Furthermore, the contributions from TUG and CSR, which

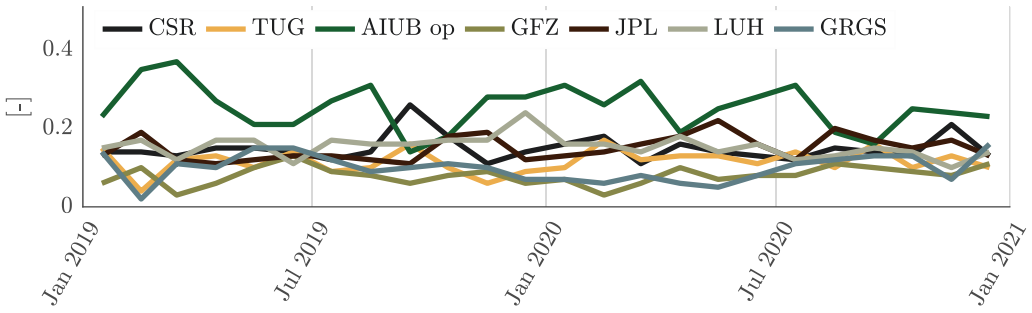

Figure 5.43: Normalised weights derived in the COST-G combination process for all ACs including the operational AIUB solution.

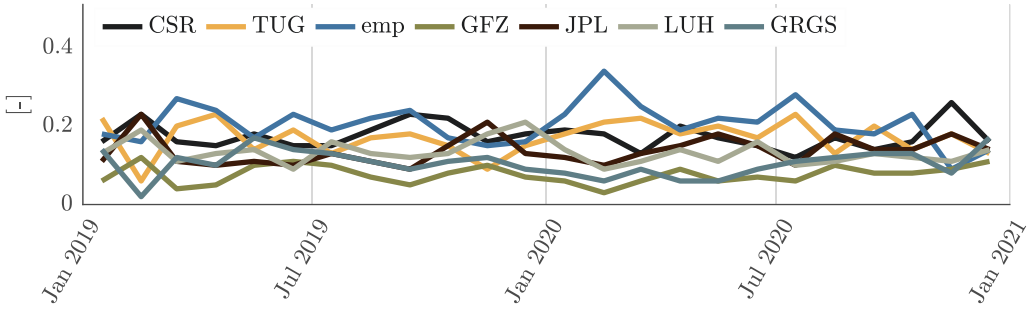

Figure 5.44: Normalised weights derived in the COST-G combination process for all ACs when exchanging the operational AIUB solution for the one using empirical noise models.

feature a low noise level, receive a higher weighting.

Expressed as RMS over the ocean (Fig. 5.45) including the solution which employs empirical modelling improves the combined solution compared to the one with the operational AIUB contribution. As a reference the individual CSR, TUG, AIUB operational and AIUB empirical solutions are depicted as well. In conclusion, the empirical modelling is benefi-

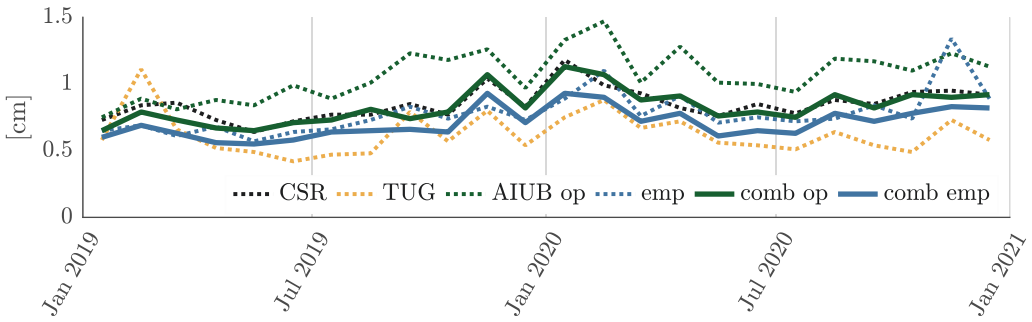

Figure 5.45: RMS over the oceans for two years of GRACE Follow-On comparing the solutions from CSR, TUG and the COST-G combination when using the operational AIUB solution or the solution with empirical modelling in the combination process.

cial not only for the quality of the individual solution but the combined product benefits noticeably as well.

Chapter 6

Summary

This thesis presented the state of modelling the stochastic noise of kinematic positions and KBRR observations for GRACE Follow-On together with unknown deficiencies in the background force field in the context of the CMA of orbit and gravity field determination at the AIUB. Several methods of noise treatment have been investigated:

- The well established pseudo-stochastic parameters in the form of PCAs of the dynamic force model. This approach is tailored and restricted to the usage of the equation of motion, thus, to a physical representation of the satellite's orbit dynamics. It has been extended to estimate an optimal constraining for the PCAs with VCE. This improved constraining enables a co-estimation of PCAs which flatten the spectrum of the post-fit residuals to (almost) white noise in the respective frequencies, which indicates a plausible consideration of the unknown noise propagating to these frequencies. It is to be further investigated if this method is also suited for other gravity field recovery satellite missions, or any type of constrained parameter in the CMA in general.

- Additionally, the method of VCE is introduced as a powerful and efficient tool of automated data weighting to account for outliers on the level of arc-wise normal equations as well as on the level of the sequential LSQA. This outlier detection and weighting yields good results and for the operational GRACE Follow-On processing no additional data inspection had to be carried out with the data analysed so far. However, this method strongly depends on the chosen arc length or block length of the sequential LSQA. This may lead to a (undesired) trade-off between the stochastic model of the observations and the outlier detection and weighting.

- The noise in the kinematic positions is examined by considering the formal covariance propagation of the a priori noise of the carrier phase observations through the kinematic PPP. It turned out that covering 50 min of formal correlations between the kinematic positions improves the estimation of gravity field coefficients, compared to the common treatment with only epoch-wise covariances. However, this noise may also be treated with PCAs or an empirical modelling based on post-fit residuals.

- The stochastic model of the observations represented by theoretical noise models based on a given PSD. This is investigated for the accumulation of two noise sources

propagated to the stochastic model of the KBRR observations, which are the system noise of the KBR and noise introduced by the ACC. The theoretical noise models deliver surprisingly good results while being of a very simple nature and allowing to completely discard the pseudo-stochastic modelling.

- An empirical modelling derived from post-fit residuals. Such a model is introduced for the kinematic positions as well as the KBRR observations. It significantly improves the quality of the estimated gravity field solutions in terms of a lower RMS over the oceans. Furthermore, the formal errors of the estimated gravity field coefficients become more realistic when assessed with GRACE Follow-On gravity field solutions computed by other institutions. Using the empirical modelling of the observations noise in the AIUB solutions contributing to the COST-G combined product results in an improved combined solution. The empirical modelling based on post-fit residuals is universally usable, being applicable to any least-squares problem where post-fit residuals transport stochastic information about the formulation of the problem. However, assumptions about underlying processes, e.g., following stationarity, have to be made.

It has been shown how different noise modelling techniques and orbit and gravity field recovery approaches may be prone to estimate a biased solution, where a priori information about the unknown gravity field is transported through parameters or the stochastic model to the adjusted gravity field.

In conclusion, all methods of dealing with observation and background model noise are well suited for GRACE Follow-On gravity field recovery, each providing certain advantages and restrictions, especially if the computational resources are limited. They perform best in the interplay with each other, so an empirical modelling based on the post-fit residuals together with a pseudo-stochastic parametrisation and a VCE to determine their constraints in the CMA.

Furthermore, the processing schemes of GRACE Follow-On data were expanded to an efficient normal equation handling with BLAS and LAPACK routines, resulting in a reduction of computation time up to 90 %.

The future potential of this study is on one hand to incorporate the empirical modelling of the GRACE Follow-On observables to the operational processing routines to provide the improved products to the COST-G and a broad user community, and on the other hand to extend the analysis of the empirical modelling to other observation types, e.g., carrier phase observations. Additionally, the statistical methods of the empirical modelling may be refined in future by extending the treatment of the post-fit residuals from a univariate to a multivariate consideration.
Furthermore, the VCE to determine the magnitude of constraints in the CMA may be applied to and investigated with other parameter types, other satellite missions which are capable of sensing the Earth's gravity field like Swarm, or even with different observation concepts such as SLR.

Scientific environment and publications

The research conducted in scope of thesis has been carried out at the Astronomical Institute of the University of Bern (AIUB). It has been supported by the Swiss National Science Foundation (SNSF, grant no. 200021_175942 Assessment of Noise Models for GRACE and GRACE-FO). Results were presented at the occasion of several international conferences and symposia. Moreover, the following scientific publications are related to it.

Lead author

Stochastic noise modelling of kinematic orbit positions in the Celestial Mechanics Approach. Martin Lasser, Ulrich Meyer, Daniel Arnold and Adrian Jäggi. *Advances in Geosciences*, volume 50, 101–113, 2020. doi:10.5194/adgeo-50-101-2020.
`https://adgeo.copernicus.org/articles/50/101/2020`

Benchmark data for verifying background model implementations in orbit and gravity field determination software. Martin Lasser, Ulrich Meyer, Adrian Jäggi, Torsten Mayer-Gürr, Andreas Kvas, Karl Hans Neumayer, Christoph Dahle, Frank Flechtner, Jean-Michel Lemoine, Igor Koch, Matthias Weigelt, and Jakob Flury. *Advances in Geosciences*, volume 55, 1–11, 2020. doi:10.5194/adgeo-55-1-2020.
`https://adgeo.copernicus.org/articles/55/1/2020`

AIUB-GRACE-FO_operational — Operational GRACE Follow-On monthly gravity field solutions. Martin Lasser, Ulrich Meyer, Daniel Arnold and Adrian Jäggi. *GFZ Data Services*, dataset, 2020. doi:10.5880/icgem.2020.001.
`https://dataservices.gfz-potsdam.de/icgem/showshort.php?id=4c95fc04-fd9d-11ea-9603-497c92695674`

Co-authorship

Determination and combination of monthly gravity field time series from kinematic orbits of GRACE, GRACE-FO and Swarm. Thomas Grombein, Martin Lasser, Daniel Arnold, Ulrich Meyer and Adrian Jäggi. *International Association of Geodesy Symposia*, 1–11, Springer Berlin-Heidelberg, Germany, 2022. doi:10.1007/1345_2022_163.
https://link.springer.com/content/pdf/10.1007/1345_2022_163.pdf

COST-G gravity field models for precise orbit determination of Low Earth Orbiting Satellites. Heike Peter, Ulrich Meyer, Martin Lasser and Adrian Jäggi. *Advances in Space Research*, volume 69(12), 4155–4168, 2022. doi:10.1016/j.asr.2022.04.005.
https://www.sciencedirect.com/science/article/pii/S0273117722002551

Assessing reduced-dynamic parametrizations for GRAIL orbit determination and the recovery of independent lunar gravity field solutions. Stefano Bertone, Daniel Arnold, Valère Girardin, Martin Lasser, Ulrich Meyer and Adrian Jäggi. *Earth and Space Science*, volume 8, issue 6, 1–21, 2021. doi:10.1029/2020EA001454.
https://agupubs.onlinelibrary.wiley.com/doi/10.1029/2020EA001454

International Combination Service for Time-Variable Gravity Fields (COST-G) – Start of Operational Phase and Future Perspectives. Adrian Jäggi, Ulrich Meyer, Martin Lasser, Barbara Jenny, Teodolina Lopez, Frank Flechtner, Christoph Dahle, Christoph Förste, Torsten Mayer-Gürr, Andreas Kvas, Jean-Michel Lemoine, Stéphane Bourgogne, Matthias Weigelt and Andreas Groh. *International Association of Geodesy Symposia: Beyond 100: The Next Century in Geodesy*, editor J. Freymueller and L. Sánchez, volume 152, 1–9, Springer Cham, Switzerland, 2020. doi:10.1007/1345_2020_109.
https://link.springer.com/chapter/10.1007/1345_2020_109

International Combination Service for Time-variable Gravity Fields (COST-G) Monthly GRACE-FO Series. V. 01. Ulrich Meyer, Martin Lasser, Adrian Jäggi, Christoph Dahle, Frank Flechtner, Andreas Kvas, Saniya Behzadpour, Torsten Mayer-Gürr, Jean-Michel Lemoine, Igor Koch, Jakob Flury, and Stéphane Bourgogne. *GFZ Data Services*, dataset, 2020. doi:10.5880/ICGEM.COST-G.002.
https://dataservices.gfz-potsdam.de/icgem/showshort.php?id=6234ca2d-29ce-11eb-9603-497c92695674

Bibliography

K. Abich, A. Abramovici, B. Amparan, A. Baatzsch, B. B. Okihiro, D. C. Barr, M. P. Bize, C. Bogan, C. Braxmaier, M. J. Burke, K. C. Clark, C. Dahl, K. Dahl, K. Danzmann, M. A. Davis, G. de Vine, J. A. Dickson, S. Dubovitsky, A. Eckardt, T. Ester, G. F. Barranco, R. Flatscher, F. Flechtner, W. M. Folkner, S. Francis, M. S. Gilbert, F. Gilles, M. Gohlke, N. Grossard, B. Guenther, P. Hager, J. Hauden, F. Heine, G. Heinzel, M. Herding, M. Hinz, J. Howell, M. Katsumura, M. Kaufer, W. Klipstein, A. Koch, M. Kruger, K. Larsen, A. Lebeda, A. Lebeda, T. Leikert, C. C. Liebe, J. Liu, L. Lobmeyer, C. Mahrdt, T. Mangoldt, K. McKenzie, M. Misfeldt, P. R. Morton, V. Müller, A. T. Murray, D. J. Nguyen, K. Nicklaus, R. Pierce, J. A. Ravich, G. Reavis, J. Reiche, J. Sanjuan, D. Schütze, C. Seiter, D. Shaddock, B. Sheard, M. Sileo, R. Spero, G. Spiers, G. Stede, M. Stephens, A. Sutton, J. Trinh, K. Voss, D. Wang, R. T. Wang, B. Ware, H. Wegener, S. Windisch, C. Woodruff, B. Zender, and M. Zimmermann. In-Orbit Performance of the GRACE Follow-on Laser Ranging Interferometer. *Physical Review Letters*, 123:1–7, 2019. doi: 10.1103/PhysRevLett.123.031101. 5

A. C. Aitken. On Least Squares and Linear Combination of Observations. *Proceedings of the Royal Society of Edinburgh*, 55:42—48, 1936. doi: 10.1017/S0370164600014346. 14

Z. Altamimi, P. Rebischung, L. Métivier, and X. Collilieux. ITRF2014: A new release of the International Terrestrial Reference Frame modeling nonlinear station motions. *Journal of Geophysical Research: Solid Earth*, 121(8):6109–6131, 2016. doi: 10.1002/2016JB013098. 7

E. Anderson, Z. Bai, C. Bischof, S. Blackford, J. Demmel, J. Dongarra, J. DuCroz, A. Greenbaum, S. Hammarling, A. McKenney, and D. Sorensen. *LAPACK Users' Guide*. Society for Industrial and Applied Mathematics, third edition, 1999. ISBN 0-89871-447-8. 66

D. Arnold and A. Jäggi. AIUB GRACE-FO kinematic orbits, release 02. *Astronomical Institute, University of Bern*, dataset, 2022. doi: 10.48350/169040. 53

D. Arnold, S. Bertone, A. Jäggi, G. Beutler, and L. Mervart. GRAIL gravity field determination using the Celestial Mechanics Approach. *Icarus*, 261:182–192, 2015. ISSN 0019-1035. doi: 10.1016/j.icarus.2015.08.015. 8

D. Arnold, O. Montenbruck, S. Hackel, and K. Sośnica. Satellite laser ranging to low Earth orbiters: orbit and network validation. *Journal of Geodesy*, 93(11):2315–2334, 2019. ISSN 1432-1394. doi: 10.1007/s00190-018-1140-4. 8

T. Bandikova, C. McCullough, G. L. Kruizinga, H. Save, and B. Christophe. GRACE accelerometer data transplant. *Advances in Space Research*, 64(3):623–644, 2019. ISSN 0273-1177. doi: 10.1016/j.asr.2019.05.021. 5, 56

S. Behzadpour, T. Mayer-Gürr, and S. Krauss. GRACE Follow-On Accelerometer Data Recovery. *Journal of Geophysical Research: Solid Earth*, 126(5), 2021. ISSN 2169-9313. doi: 10.1029/2020JB021297. 56

S. Bertone, D. Arnold, V. Girardin, M. Lasser, U. Meyer, and A. Jäggi. Assessing Reduced-Dynamic Parametrizations for GRAIL Orbit Determination and the Recovery of Independent Lunar Gravity Field Solutions. *Earth and Space Science*, 8(6), 2021. doi: 10.1029/2020EA001454. 8

G. Beutler. *Methods of Celestial Mechanics*. Springer, Berlin-Heidelberg, Germany, 2005. ISBN 978-3-642-10529-6. 8, 31, 33

G. Beutler, A. Jäggi, L. Mervart, and U. Meyer. The celestial mechanics approach: application to data of the GRACE mission. *Journal of Geodesy*, 84(11):661–681, 2010a. ISSN 1432-1394. doi: 10.1007/s00190-010-0402-6. 35, 41, 53

G. Beutler, A. Jäggi, L. Mervart, and U. Meyer. The celestial mechanics approach: theoretical foundations. *Journal of Geodesy*, 84(10):605–624, 2010b. ISSN 1432-1394. doi: 10.1007/s00190-010-0401-7. 31, 33, 41, 53, 61, 64, 96

H. Bock, R. Dach, A. Jäggi, and G. Beutler. High-rate GPS clock corrections from CODE: support of 1 Hz applications. *Journal of Geodesy*, 83(11):1083–1094, 2009. ISSN 1432-1394. doi: 10.1007/s00190-009-0326-1. 53

E. Brockmann. *Combination of Solutions for Geodetic and Geodynamic Applications of the Global Positioning System (GPS)*. PhD thesis, University of Bern, Bern, Switzerland, 1996. 60

B. Buttkus. *Spektralanalyse und Filtertheorie in der angewandten Geophysik*. Springer, Berlin-Heidelberg, Germany, 1991. ISBN 978-3-662-09971-1. 26

L. Carrere, F. Lyard, M. Cancet, A. Guillot, and N. Picot. FES 2014, a new tidal model – Validation results and perspectives for improvements. In *ESA Living Planet Conference*, Prague, Czech Republic, 2016. 49, 55

B. Christophe, D. Boulanger, B. Foulon, P.-A. Huynh, V. Lebat, F. Liorzou, and E. Perrot. A new generation of ultra-sensitive electrostatic accelerometers for GRACE Follow-on and towards the next generation gravity missions. *Acta Astronautica*, 117:1–7, 2015. ISSN 0094-5765. doi: 10.1016/j.actaastro.2015.06.021. 5

J. Cooley and J. Tukey. An Algorithm for the Machine Calculation of Complex Fourier Series. *Mathematics of Computation*, 19(90):297–301, 1965. doi: 10.1090/S0025-5718-1965-0178586-1. 27

R. Dach, E. Brockmann, S. Schaer, G. Beutler, M. Meindl, L. Prange, H. Bock, A. Jäggi, and L. Ostini. GNSS processing at CODE: status report. *Journal of Geodesy*, 83(3):353–365, 2009. ISSN 1432-1394. doi: 10.1007/s00190-008-0281-2. 8, 32, 53

C. Dahle, M. Murböck, F. Flechtner, H. Dobslaw, G. Michalak, K. H. Neumayer, O. Abrykosov, A. Reinhold, R. König, R. Sulzbach, and C. Förste. The GFZ GRACE RL06 Monthly Gravity Field Time Series: Processing Details and Quality Assessment. *Remote Sensing*, 11(18):1–22, 2019. ISSN 2072-4292. doi: 10.3390/rs11182116. 8

F. N. David and J. Neyman. Extension of the Markoff theorem on least squares. *Statistical Research Memoirs II, 1*, 105(16), 1938. 14

S. D. Desai. Observing the pole tide with satellite altimetry. *Journal of Geophysical Research: Oceans*, 107(C11):1–13, 2002. doi: 10.1029/2001JC001224. 51, 55

H. Dobslaw, I. Bergmann-Wolf, R. Dill, E. Forootan, V. Klemann, J. Kusche, and I. Sasgen. *Updating ESA's Earth System Model for Gravity Mission Simulation Studies: 1. Model Description and Validation.* Deutsches GeoForschungsZentrum, Potsdam, Germany, 2014. doi: 10.2312/GFZ.b103-14079. 44

H. Dobslaw, I. Bergmann-Wolf, R. Dill, L. Poropat, M. Thomas, C. Dahle, S. Esselborn, R. König, and F. Flechtner. A new high-resolution model of non-tidal atmosphere and ocean mass variability for de-aliasing of satellite gravity observations: AOD1B RL06. *Geophysical Journal International*, 211(1):263–269, 2017. ISSN 0956-540X. doi: 10.1093/gji/ggx302. 50, 55

A. T. Doodson and H. Lamb. The harmonic development of the tide-generating potential. *Proceedings of the Royal Society (London)*, Series A(100):305–329, 1921. doi: 10.1098/rspa.1921.0088. 48

M. Drinkwater, R. Haagmans, D. Muzi, A. Popescu, R. Floberghagen, M. Kern, and M. Fehringer. The GOCE gravity mission: ESA's first core explorer. *Proceedings of Third GOCE User Workshop*, pages 1–7, 2006. 1

C. Dunn, W. Bertiger, Y. Bar-Sever, S. Desai, B. Haines, D. Kuang, G. Franklin, I. Harris, G. Kruizinga, T. Meehan, S. Nandi, D. Nguyen, T. Rogstad, J. B. Thomas, J. Tien, L. Romans, M. M. Watkins, S.-C. Wu, S. Bettadpur, and J. R. Kim. Instrument of Grace: GPS augments gravity measurements. *GPS World*, 14:16–28, 2003. 4

M. Ellmer. *Contributions to GRACE Gravity Field Recovery: Improvements in Dynamic Orbit Integration Stochastic Modelling of the Antenna Offset Correction, and Co-Estimation of Satellite Orientations.* PhD thesis, Graz University of Technology, In *Monographic Series TU Graz*, number 1, Verlag der Technischen Universität Graz, Graz, Austria, 2018. 25, 93, 103

M. Ellmer and T. Mayer-Gürr. High precision dynamic orbit integration for spaceborne gravimetry in view of GRACE Follow-on. *Advances in Space Research*, 60(1):1–13, 2017. ISSN 0273-1177. doi: 10.1016/j.asr.2017.04.015. 7

W. v. Etten. *Introduction to Random Signals and Noise.* John Wiley & Sons, New York, NY, USA, 2005. ISBN 978-0-470-02411-9. 27, 92

A. L. Fey, D. Gordon, and C. S. Jacobs. *The Second Realization of the International Celestial Reference Frame by Very Long Baseline Interferometry, IERS Technical Note*

No. 35. Verlag des Bundesamts für Kartographie und Geodäsie, Frankfurt am Main, 2009. ISBN 3-89888-918-6. 7

F. Flechtner, C. Reigber, R. Rummel, and G. Balmino. Satellite Gravimetry: A Review of Its Realization. *Surveys in Geophysics*, 42(5):1029–1074, 2021. ISSN 1573-0956. doi: 10.1007/s10712-021-09658-0. 1

W. M. Folkner, J. G. Williams, and D. H. Boggs. The Planetary and Lunar Ephemeris DE 421. *Interplanetary Network Progress Report*, 41-178(1), 2009. 46, 55

E. Friis-Christensen, H. Lühr, D. Knudsen, and R. Haagmans. Swarm – An Earth Observation Mission investigating Geospace. *Advances in Space Research*, 41(1):210–216, 2006. ISSN 0273-1177. doi: 10.1016/j.asr.2006.10.008. 1

B. Frommknecht. *Integrated Sensor Analysis of the GRACE Mission*. PhD thesis, Technical University of Munich, Munich, Germany, 2007. 97

W. Förstner. Ein Verfahren zur Schätzung von Varianz- und Kovarianzkomponenten. *Allgemeine Vermessungsnachrichten*, Heft 11-12:446–453, 1979. 14, 25

C. F. Gauß. *Theoria Motus Corporum Coelestium in sectionibus conicis solem ambientium*. Hamburgi: sumtibus Frid. Perthes et I. H. Besser, Göttingen, Germany, 1809. 12

E. Grafarend, A. Kleusberg, and B. Schaffrin. An introduction to the variance-covariance-component estimation of Helmert type. *Zeitschrift für Vermessungswesen*, 105(4): 161–180, 1980. 24

F. R. Hampel. The Influence Curve and its Role in Robust Estimation. *Journal of the American Statistical Association*, 69(346):383–393, 1974. doi: 10.1080/01621459.1974.10482962. 102

S.-C. Han, C. Jekeli, and C. K. Shum. Time-variable aliasing effects of ocean tides, atmosphere, and continental water mass on monthly mean GRACE gravity field. *Journal of Geophysical Research: Solid Earth*, 109(B4), 2004. doi: 10.1029/2003JB002501. 44

N. Harvey and C. Sakumura. Results from a GRACE/GRACE-FO attitude reconstruction Kalman filter. *Journal of Geodesy*, 93(10):1881–1896, 2019. ISSN 1432-1394. doi: 10.1007/s00190-019-01289-z. 5

W. A. Heiskanen and H. Moritz. *Physical geodesy*. W. H. Freeman and Company, San Francisco, CA, USA, 1967. 29, 45

F. R. Helmert. *Die Ausgleichung nach der Methode der kleinsten Quadrate*. 2nd edition, Teubner, Leipzig, Berlin, 1907. 24

A. E. Hoerl and R. W. Kennard. Ridge Regression: Biased Estimation for Nonorthogonal Problems. *Technometrics*, 12(1):55–67, 1970. ISSN 00401706. doi: 10.2307/1267351. 17

P. J. Huber. *Robust Statistics*. John Wiley & Sons, New York, NY, USA, 1981. ISBN 0471418056 9780471418054. 102

IEEE-754. IEEE Standard for Binary Floating-Point Arithmetic. *ANSI/IEEE Std 754-1985*, pages 1–20, 1985. 9

IERS. *Update IERS 2010 Conventions ch. 7.1.4.* IERS, 2018. URL `http://iers-conventions.obspm.fr/content/chapter7/icc7.pdf`. 51

E. S. Ince, F. Barthelmes, S. Reißland, K. Elger, C. Förste, F. Flechtner, and H. Schuh. ICGEM – 15 years of successful collection and distribution of global gravitational models, associated services, and future plans. *Earth System Science Data*, 11(2):647–674, 2019. doi: 10.5194/essd-11-647-2019. 53

A. Jaeggi, U. Meyer, G. Beutler, L. Prange, R. Dach, and L. Mervart. AIUB-GRACE03S: A static gravity field model computed with simultaneously solved-for time variations from 6 years of GRACE data using the Celestial Mechanics Approach. *Paper in preparation*, 2011. URL `http://icgem.gfz-potsdam.de/tom_longtime`. 46, 55

Y. Jean, U. Meyer, and A. Jäggi. Combination of GRACE monthly gravity field solutions from different processing strategies. *Journal of Geodesy*, 92(11):1313–1328, 2018. ISSN 1432-1394. doi: 10.1007/s00190-018-1123-5. 25

G. Johnston, A. Riddell, and G. Hausler. The International GNSS Service. In P. J. Teunissen and O. Montenbruck, editors, *Springer Handbook of Global Navigation Satellite Systems*, page 179 pp. Springer, Cham, Switzerland, 2017. ISBN 978-3-319-42926-7. doi: 10.1007/978-3-319-42928-1_33. 6

A. Jäggi. *Pseudo-Stochastic Orbit Modeling of Low Earth Satellites Using the Global Positioning System.* PhD thesis, University of Bern, In *Geodätisch-geophysikalische Arbeiten in der Schweiz*, volume 73, Schweizerische Geodätische Kommission, Institut für Geodäsie und Photogrammetrie, Eidg. Technische Hochschule Zürich, Switzerland, 2007. 35, 64

A. Jäggi, G. Beutler, L. Prange, R. Dach, and L. Mervart. Assessment of GPS-only observables for Gravity Field Recovery from GRACE. In M. G. Sideris, editor, *International Association of Geodesy Symposia: Observing our Changing Earth*, volume 133, pages 113–123. Springer, Berlin-Heidelberg, Germany, 2009a. ISBN 978-3-540-85425-8. doi: 10.1007/978-3-540-85426-5_14. 53

A. Jäggi, R. Dach, O. Montenbruck, U. Hugentobler, H. Bock, and G. Beutler. Phase center modeling for LEO GPS receiver antennas and its impact on precise orbit determination. *Journal of Geodesy*, 83(12):1145–1162, 2009b. ISSN 1432-1394. doi: 10.1007/s00190-009-0333-2. 95

A. Jäggi, G. Beutler, and L. Mervart. GRACE Gravity Field Determination Using the Celestial Mechanics Approach - First Results. In S. P. Mertikas, editor, *International Association of Geodesy Symposia: Gravity, Geoid and Earth Observation*, volume 135, pages 177–184. Springer, Berlin-Heidelberg, Germany, 2010. ISBN 978-3-642-10633-0. doi: 10.1007/978-3-642-10634-7_24. 53

A. Jäggi, H. Bock, L. Prange, U. Meyer, and G. Beutler. GPS-only gravity field recovery with GOCE, CHAMP, and GRACE. *Advances in Space Research*, 47(6):1020–1028, 2011a. ISSN 0273-1177. doi: 10.1016/j.asr.2010.11.008. 53, 64

A. Jäggi, L. Prange, and U. Hugentobler. Impact of covariance information of kinematic positions on orbit reconstruction and gravity field recovery. *Advances in Space Research*, 47(9):1472–1479, 2011b. ISSN 0273-1177. doi: 10.1016/j.asr.2010.12.009. 53, 85, 86, 88, 89, 91

A. Jäggi, G. Beutler, U. Meyer, L. Prange, R. Dach, and L. Mervart. AIUB-GRACE02S - Status of GRACE Gravity Field Recovery using the Celestial Mechanics Approach. In S. Kenyon, M. C. Pacino, and U. Marti, editors, *International Association of Geodesy Symposia: Geodesy for Planet Earth*, volume 136, pages 161–170. Springer, Berlin-Heidelberg, Germany, 2012. ISBN 978-3-642-20337-4. doi: 10.1007/978-3-642-20338-1_20. 44, 53

A. Jäggi, C. Dahle, D. Arnold, H. Bock, U. Meyer, G. Beutler, and J. van den IJssel. Swarm kinematic orbits and gravity fields from 18 months of GPS data. *Advances in Space Research*, 57(1):218–233, 2016. ISSN 0273-1177. doi: 10.1016/j.asr.2015.10.035. 64

A. Jäggi, M. Weigelt, F. Flechtner, A. Güntner, T. Mayer-Gürr, S. Martinis, S. Bruinsma, J. Flury, S. Bourgogne, H. Steffen, U. Meyer, Y. Jean, A. Sušnik, A. Grahsl, D. Arnold, K. Cann-Guthauser, R. Dach, Z. Li, Q. Chen, T. van Dam, C. Gruber, L. Poropat, B. Gouweleeuw, A. Kvas, B. Klinger, J.-M. Lemoine, R. Biancale, H. Zwenzner, T. Bandikova, and A. Shabanloui. European Gravity Service for Improved Emergency Management (EGSIEM) – from concept to implementation. *Geophysical Journal International*, 218(3):1572–1590, 2019. ISSN 0956-540X. doi: 10.1093/gji/ggz238. 6

A. Jäggi, U. Meyer, M. Lasser, B. Jenny, T. Lopez, F. Flechtner, C. Dahle, C. Förste, T. Mayer-Gürr, A. Kvas, J.-M. Lemoine, S. Bourgogne, M. Weigelt, and A. Groh. International Combination Service for Time-Variable Gravity Fields (COST-G) – Start of Operational Phase and Future Perspectives. In J. Freymueller and L. Sánchez, editors, *International Association of Geodesy Symposia: Beyond 100: The Next Century in Geodesy*, volume 152, pages 1–9. Springer, Cham, Switzerland, 2020. ISBN 978-3-031-09859-8. doi: 10.1007/1345_2020_109. 6

D. Kendrick. *Stochastic control for economic models*. 2nd edition, The University of Texas, Austin, TX, USA, 2002. 25

A. Khinchin. Korrelationstheorie der stationären stochastischen Prozesse. *Mathematische Annalen*, 109(1):604–615, 1934. ISSN 1432-1807. doi: 10.1007/BF01449156. 28

J. R. Kim. *Simulation study of a low-low satellite-to-satellite tracking mission*. PhD thesis, University of Texas at Austin, Austin, TX, USA, 2000. VI, 38, 40, 56, 65, 97, 98

J. R. Kim, P. J. Roesset, S. V. Bettadpur, B. D. Tapley, and M. M. Watkins. Error Analysis of the Gravity Recovery and Climate Experiment (GRACE) Mission. In M. G. Sideris, editor, *International Association of Geodesy Symposia: Gravity, Geoid and Geodynamics*

2000, volume 123, pages 103–108. Springer, Berlin-Heidelberg, Germany, 2002. ISBN 978-3-642-07634-3. doi: 10.1007/978-3-662-04827-6_17. 97, 98

B. Klinger and T. Mayer-Gürr. The role of accelerometer data calibration within GRACE gravity field recovery: Results from ITSG-Grace2016. *Advances in Space Research*, 58 (9):1597–1609, 2016. ISSN 0273-1177. doi: 10.1016/j.asr.2016.08.007. 56

U. D. Ko. *Analysis of the characteristics of the GRACE dual one-way ranging system*. PhD thesis, University of Texas at Austin, Austin, TX, USA, 2008. 97

I. Koch, J. Flury, M. Naeimi, and A. Shabanloui. LUH-GRACE2018: A New Time Series of Monthly Gravity Field Solutions from GRACE. In J. Freymueller and L. Sánchez, editors, *International Association of Geodesy Symposia: Beyond 100: The Next Century in Geodesy*, volume 152, pages 1–9. Springer, Cham, Switzerland, 2020. doi: 10.1007/1345_2020_92. 8

K.-R. Koch. *Parameterschätzung und Hypothesentests in Linearen Modellen*. Ferd. Dümmlers Verlag, Bonn, 1997. 11, 13, 14, 25

K.-R. Koch and J. Kusche. Regularization of geopotential determination from satellite data by variance components. *Journal of Geodesy*, 76(5):259–268, 2002. ISSN 1432-1394. doi: 10.1007/s00190-002-0245-x. 25, 26, 78

R. P. Kornfeld, B. W. Arnold, M. A. Gross, N. T. Dahya, W. M. Klipstein, P. F. Gath, and S. Bettadpur. GRACE-FO: The Gravity Recovery and Climate Experiment Follow-On Mission. *Journal of Spacecraft and Rockets*, 56(3):931–951, 2019. doi: 10.2514/1.A34326. 4

A. Kvas and T. Mayer-Gürr. Grace gravity field recovery with background model uncertainties. *Journal of Geodesy*, 93(12):2543–2552, 2019. ISSN 1432-1394. doi: 10.1007/s00190-019-01314-1. 19, 24, 93, 103

A. Kvas, S. Behzadpour, M. Ellmer, B. Klinger, S. Strasser, N. Zehentner, and T. Mayer-Gürr. ITSG-Grace2018: Overview and evaluation of a new GRACE-only gravity field time series. *Journal of Geophysical Research: Solid Earth*, 2019. ISSN 2169-9313. doi: 10.1029/2019JB017415. 9, 85, 107

A. Kvas, J. M. Brockmann, S. Krauss, T. Schubert, T. Gruber, U. Meyer, T. Mayer-Gürr, W.-D. Schuh, A. Jäggi, and R. Pail. GOCO06s – a satellite-only global gravity field model. *Earth System Science Data*, 13(1):99–118, 2021. 9

F. W. Landerer, F. M. Flechtner, H. Save, F. H. Webb, T. Bandikova, W. I. Bertiger, S. V. Bettadpur, S. H. Byun, C. Dahle, H. Dobslaw, E. Fahnestock, N. Harvey, Z. Kang, G. L. H. Kruizinga, B. D. Loomis, C. McCullough, M. Murböck, P. Nagel, M. Paik, N. Pie, S. Poole, D. Strekalov, M. E. Tamisiea, F. Wang, M. M. Watkins, H.-Y. Wen, D. N. Wiese, and D.-N. Yuan. Extending the Global Mass Change Data Record: GRACE Follow-On Instrument and Science Data Performance. *Geophysical Research Letters*, 47 (12), 2020. doi: 10.1029/2020GL088306. 1, 3, 5, 56

M. Lasser, U. Meyer, D. Arnold, and A. Jäggi. Stochastic noise modelling of kinematic orbit positions in the Celestial Mechanics Approach. *Advances in Geosciences*, 50:101–113, 2020a. doi: 10.5194/adgeo-50-101-2020. 53, 85

M. Lasser, U. Meyer, D. Arnold, and A. Jäggi. AIUB-GRACE-FO-operational — Operational GRACE Follow-On monthly gravity field solutions. *GFZ Data Services*, dataset, 2020b. doi: 10.5880/icgem.2020.001. 53

M. Lasser, U. Meyer, A. Jäggi, T. Mayer-Gürr, A. Kvas, K. H. Neumayer, C. Dahle, F. Flechtner, J.-M. Lemoine, I. Koch, M. Weigelt, and J. Flury. Benchmark data for verifying background model implementations in orbit and gravity field determination software. *Advances in Geosciences*, 55:1–11, 2020c. doi: 10.5194/adgeo-55-1-2020. 6, 44

C. L. Lawson, R. J. Hanson, D. R. Kincaid, and F. T. Krogh. Basic Linear Algebra Subprograms for Fortran Usage. *ACM Transactions on Mathematical Software*, 5(3): 308–323, 1979. ISSN 0098-3500. doi: 10.1145/355841.355847. 66

A. M. Legendre. *Nouvelles méthodes pour la détermination des orbites des comètes*. Firmin Didot, Paris, France, 1805. 12

F. G. Lemoine, S. C. Kenyon, J. K. Factor, R. G. Trimmer, N. K. Pavlis, D. S. Chinn, C. M. Cox, S. M. Klosko, S. B. Luthcke, M. H. Torrence, Y. M. Wang, R. G. Williamson, E. C. Pavlis, R. H. Rapp, and T. R. Olson. *The Development of the Joint NASA GSFC and NIMA Geopotential Model EGM96*. NASA Goddard Space Flight Center, NASA Goddard Space Flight Center, Greenbelt, MD, USA, 1998. 60

K. Levenberg. A method for the solution of certain problems in least-squares. *Quarterly of Applied Mathematics*, 2(2):164–168, 1944. doi: 10.1090/qam/10666. 17

N. R. Lomb. Least-squares frequency analysis of unequally spaced data. *Astrophysics and Space Science*, 39(2):447–462, 1976. ISSN 1572-946X. doi: 10.1007/BF00648343. 27

D. W. Marquardt. An Algorithm for Least-Squares Estimation of Nonlinear Parameters. *Journal of the Society for Industrial and Applied Mathematics*, 11(2):431–441, 1963. doi: 10.1137/0111030. 17

T. Mayer-Gürr, S. Behzadpur, M. Ellmer, A. Kvas, B. Klinger, S. Strasser, and N. Zehentner. ITSG-Grace2018 - Monthly, Daily and Static Gravity Field Solutions from GRACE. *GFZ Data Services*, dataset, 2018. doi: 10.5880/ICGEM.2018.003. 9, 62

T. Mayer-Gürr, S. Behzadpour, A. Eicker, M. Ellmer, B. Koch, S. Krauss, C. Pock, D. Rieser, S. Strasser, B. Süsser-Rechberger, N. Zehentner, and A. Kvas. GROOPS: A software toolkit for gravity field recovery and GNSS processing. *Computers & Geosciences*, 155:1–9, 2021. ISSN 0098-3004. doi: 10.1016/j.cageo.2021.104864. 7, 9

D. McCarthy. *IERS Conventions (1996), IERS Technical Note No. 21.* Central Bureau of IERS - Observatoire de Paris, Paris, France, 1996. 32

U. Meyer, A. Jäggi, and G. Beutler. Monthly gravity field solutions based on GRACE observations generated with the Celestial Mechanics Approach. *Earth and Planetary*

Science Letters, 345–348:72–80, 2012a. ISSN 0012-821X. doi: 10.1016/j.epsl.2012.06.026. 53

U. Meyer, A. Jäggi, and G. Beutler. The Impact of Attitude Control on GRACE Accelerometry and Orbits. In S. Kenyon, M. C. Pacino, and U. Marti, editors, *International Association of Geodesy Symposia: Geodesy for Planet Earth*, volume 136, pages 139–146. Springer, Berlin-Heidelberg, Germany, 2012b. ISBN 978-3-642-20337-4. doi: 10.1007/978-3-642-20338-1_17. 53

U. Meyer, A. Jäggi, G. Beutler, and H. Bock. The impact of common versus separate estimation of orbit parameters on GRACE gravity field solutions. *Journal of Geodesy*, 89(7):685–696, 2015. ISSN 1432-1394. doi: 10.1007/s00190-015-0807-3. 24, 53

U. Meyer, A. Jäggi, Y. Jean, and G. Beutler. AIUB-RL02: an improved time-series of monthly gravity fields from GRACE data. *Geophysical Journal International*, 205(2): 1196–1207, 2016. ISSN 0956-540X. doi: 10.1093/gji/ggw081. 8, 35, 53, 54, 58, 62, 64, 96

U. Meyer, A. Jaeggi, C. Dahle, F. Flechtner, A. Kvas, S. Behzadpour, T. Mayer-Gürr, J.-M. Lemoine, and S. Bourgogne. International Combination Service for Time-variable Gravity Fields (COST-G) Monthly GRACE Series. V. 01. *GFZ Data Services*, dataset, 2020a. doi: 10.5880/ICGEM.COST-G.001. 6

U. Meyer, M. Lasser, A. Jaeggi, C. Dahle, F. Flechtner, A. Kvas, S. Behzadpour, T. Mayer-Gürr, J.-M. Lemoine, I. Koch, J. Flury, and S. Bourgogne. International Combination Service for Time-variable Gravity Fields (COST-G) Monthly GRACE-FO Series. V. 01. *GFZ Data Services*, dataset, 2020b. doi: 10.5880/ICGEM.COST-G.002. 6

W. Niemeier. *Ausgleichungsrechnung: Statistische Auswertemethoden*. De Gruyter, 2008. ISBN 978-3110190557. doi: doi:10.1515/9783110206784. 11, 25

M. R. Pearlman, J. J. Degnan, and J. M. Bosworth. The International Laser Ranging Service. *Advances in Space Research*, 30(2):135–143, 2002. ISSN 0273-1177. doi: 10.1016/S0273-1177(02)00277-6. 6

D. B. Percival. Three Curious Properties of the Sample Variance and Autocovariance for Stationary Processes with Unknown Mean. *The American Statistician*, 47(4):274–276, 1993. doi: 10.1080/00031305.1993.10475997. 28

H. Peter, U. Meyer, M. Lasser, and A. Jäggi. COST-G gravity field models for precise orbit determination of Low Earth Orbiting Satellites. *Advances in Space Research*, 69 (12):4155–4168, 2022. ISSN 0273-1177. doi: 10.1016/j.asr.2022.04.005. 6

G. Petit and B. Luzum. *IERS Conventions (2010), IERS Technical Note No. 36*. Verlag des Bundesamts für Kartographie und Geodäsie, Frankfurt am Main, Germany, 2010. ISBN 3-89888-989-6, 2010. 44, 50, 51, 55

L. Prange. *Global Gravity Field Determination Using the GPS Measurements Made Onboard the Low Earth Orbiting Satellite CHAMP*. PhD thesis, University of Bern, In *Geodätisch-geophysikalische Arbeiten in der Schweiz*, volume 81, Schweizerische Geodätische Kommission, Institut für Geodäsie und Photogrammetrie, Eidg. Technische Hochschule Zürich, Switzerland, 2010. 61, 87

L. Prange, A. Jäggi, G. Beutler, R. Dach, and L. Mervart. Gravity Field Determination at the AIUB - the Celestial Mechanics Approach. *Observing our Changing Earth*, 133: 353–362, 2009. doi: 10.1007/978-3-540-85426-5_42. 64

L. Prange, E. Orliac, R. Dach, D. Arnold, G. Beutler, S. Schaer, and A. Jäggi. CODE's five-system orbit and clock solution—the challenges of multi-GNSS data analysis. *Journal of Geodesy*, 91(4):345–360, 2017. ISSN 1432-1394. doi: 10.1007/s00190-016-0968-8. 8

C. R. Rao. *Linear Statistical Inference and its Applications*. John Wiley & Sons, New York, NY, USA, 1973. doi: 10.1002/9780470316436. 25

C. Reigber, H. Lühr, and P. Schwintzer. Status of the CHAMP Mission. In R. Rummel, H. Drewes, W. Bosch, and H. Hornik, editors, *International Association of Geodesy Symposia: Towards an Integrated Global Geodetic Observing System (IGGOS)*, volume 120, pages 63–65. Springer, Berlin-Heidelberg, Germany, 1998. ISBN 978-3-642-64107-7. doi: 10.1007/978-3-642-59745-9_9. 1

R. Savcenko and W. Bosch. EOT11a - a new tide model from Multi-Mission Altimetry. In *OSTST Meeting 2011*, San Diego, CA, USA, 2011. 7

H. Save. *CSR Level-2 Processing Standards Document For Level-2 Product Release 06*. Processing Standards Document, The University of Texas at Austin, Austin, TX, USA, 2019. 44, 61

S. Schaer, A. Villiger, D. Arnold, L. Prange, and A. Jäggi. The CODE ambiguity-fixed clock and phase bias analysis products: generation, properties, and performance. *Journal of Geodesy*, 95(7):81–105, 2021. ISSN 1432-1394. doi: 10.1007/s00190-021-01521-9. 36

C. E. Shannon. A mathematical theory of communication. *The Bell System Technical Journal*, 27(4):623–656, 1948. doi: 10.1002/j.1538-7305.1948.tb00917.x. 27

S. Strasser, T. Mayer-Gürr, and N. Zehentner. Processing of GNSS constellations and ground station networks using the raw observation approach. *Journal of Geodesy*, 93(7): 1045–1057, 2019. ISSN 1432-1394. doi: 10.1007/s00190-018-1223-2. 9

B. Süsser-Rechberger, S. Krauss, S. Strasser, and T. Mayer-Gürr. Improved precise kinematic LEO orbits based on the raw observation approach. *Advances in Space Research*, 69(10):3559–3570, 2022. ISSN 0273-1177. doi: 10.1016/j.asr.2022.03.014. 9

B. D. Tapley, S. Bettadpur, M. M. Watkins, and C. Reigber. The gravity recovery and climate experiment: Mission overview and early results. *Geophysical Research Letters*, 31(9), 2004. doi: 10.1029/2004GL019920. 1

P. Teixeira Encarnação, J. and. Visser, A. Jaeggi, A. Bezdek, T. Mayer-Gürr, C. K. Shum, D. Arnold, E. Doornbos, M. Ellmer, J. Guo, J. van den IJssel, J. Iorfida, E. and; Klokocnik, S. Krauss, X. Mao, U. Meyer, J. Sebera, C. Zhang, Y. Zhang, and C. Dahle. Multi-approach Gravity Field Models from Swarm GPS data. *GFZ Data Services*, dataset, 2019. doi: 10.5880/ICGEM.2019.006. 6

P. J. Teunissen and A. R. Amiri-Simkooei. Least-squares variance component estimation. *Journal of Geodesy*, 82(2):65–82, 2008. ISSN 1432-1394. doi: 10.1007/s00190-007-0157-x. 25

J. B. Thomas. *An Analysis of Gravity-Field Estimation Based on Intersatellite Dual-1-Way Biased Ranging*. Jet Propulsion Laboratory (JPL), Pasadena, CA, USA, 1999. 39, 97

P. F. Thompson, S. V. Bettadpur, and B. D. Tapley. Impact of short period, non-tidal, temporal mass variability on GRACE gravity estimates. *Geophysical Research Letters*, 31(6), 2004. doi: 10.1029/2003GL019285. 44

A. N. Tikhonov. Solution of Incorrectly Formulated Problems and the Regularization Method. *Soviet Mathematics Doklady*, 1963. 17

P. Touboul, E. Willemenot, B. Foulon, and V. Josselin. Accelerometers for CHAMP, GRACE and GOCE space missions: Synergy and evolution. *Bollettino di Geofisica Teorica ed Applicata*, 40(3–4):321–327, 1999. 10, 54

J. Wahr, M. Molenaar, and F. Bryan. Time variability of the Earth's gravity field: Hydrological and oceanic effects and their possible detection using GRACE. *Journal of Geophysical Research: Solid Earth*, 103(B12):30205–30229, 1998. doi: 10.1029/98JB02844. 58

M. Weigelt, T. van Dam, A. Jäggi, L. Prange, M. J. Tourian, W. Keller, and N. Sneeuw. Time-variable gravity signal in Greenland revealed by high-low satellite-to-satellite tracking. *Journal of Geophysical Research: Solid Earth*, 118(7):3848–3859, 2013. doi: 10.1002/jgrb.50283. 8

H. Y. Wen, G. Kruizinga, M. Paik, F. Landerer, W. Bertiger, C. Sakumura, T. Bandikova, and C. McCullough. *Gravity Recovery and Climate Experiment Follow-On (GRACE-FO) Level-1 Data Product User Handbook*. Technical Report JPL D-56935 (URS270772), NASA Jet Propulsion Laboratory/California Institute of Technology, Pasadena, CA, USA, 2019. 4, 53

N. Wiener. Generalized harmonic analysis. *Acta Mathematica*, 55:117–258, 1930. doi: 10.1007/BF02546511. 28

M. Wolff. Direct measurements of the Earth's gravitational potential using a satellite pair. *Journal of Geophysical Research*, 74(22):5295–5300, 1969. doi: 10.1029/JB074i022p05295. 1

N. Zehentner. *Kinematic orbit positioning applying the raw observation approach to observe time variable gravity*. PhD thesis, Graz University of Technology, Graz, Austria, 2017. 9

N. Zehentner and T. Mayer-Gürr. Precise orbit determination based on raw GPS measurements. *Journal of Geodesy*, 90(3):275–286, 2016. ISSN 1432-1394. doi: 10.1007/s00190-015-0872-7. 9, 25

S. Zhu, C. Reigber, and R. König. Integrated adjustment of CHAMP, GRACE, and GPS data. *Journal of Geodesy*, 78(1):103–108, 2004. ISSN 1432-1394. doi: 10.1007/s00190-004-0379-0. 8

J. F. Zumberge, M. B. Heflin, D. C. Jefferson, M. M. Watkins, and F. H. Webb. Precise point positioning for the efficient and robust analysis of GPS data from large networks. *Journal of Geophysical Research: Solid Earth*, 102(B3):5005–5017, 1997. doi: 10.1029/96JB03860. 36

D. Švehla and M. Rothacher. Kinematic precise orbit determination for gravity field determination. In F. Sansò, editor, *International Association of Geodesy Symposia: A Window on the Future of Geodesy*, volume 128, pages 181–188. Springer, Berlin-Heidelberg, Germany, 2005. ISBN 978-3-540-24055-6. doi: 10.1007/3-540-27432-4_32. 36, 53

Declaration

I declare herewith that this thesis is my own work and that I have not used any sources other than those stated. I have indicated the adoption of quotations as well as thoughts taken from other authors as such in the thesis. I am aware that the Senate pursuant to Article 36 paragraph 1 litera r of the University Act of September 5th, 1996 and Article 69 of the University Statute of June 7th, 2011 is authorized to revoke the doctoral degree awarded on the basis of this thesis. For the purposes of evaluation and verification of compliance with the declaration of originality and the regulations governing plagiarism, I hereby grant the University of Bern the right to process my personal data and to per-form the acts of use this requires, in particular, to reproduce the written thesis and to store it permanently in a database, and to use said database, or to make said database available, to enable comparison with theses submitted by others.